Bridging the Gap between Post-Newtonian Theory and Numerical Relativity in Gravitational-Wave Data Analysis

Dissertation

zur Erlangung des wissenschaftlichen Grades
doctor rerum naturalium
(Dr. rer. nat.)

eingereicht an der
Universität Potsdam, Mathematisch-Naturwissenschaftliche Fakultät

von

Frank Ohme

11. April 2012
(finale Version vom 16. Juli 2012)

Max-Planck-Institut für Gravitationsphysik/Albert-Einstein-Institut

Gutachter & Betreuer: Prof. Bernard Schutz
Betreuer: Dr. Badri Krishnan
Gutachter: Prof. Bernd Brügmann
Gutachter: Ass. Prof. Deirdre Shoemaker

Published online at the
Institutional Repository of the University of Potsdam:
URL http://opus.kobv.de/ubp/volltexte/2012/6034/
URN urn:nbn:de:kobv:517-opus-60346
http://nbn-resolving.de/urn:nbn:de:kobv:517-opus-60346

Allgemeinverständliche Zusammenfassung

Wenn sich eines der kompaktesten Objekte unseres Universums, ein Schwarzes Loch, im Wirkungsbereich eines anderen Schwarzen Lochs befindet, kommt es zu einem spektakulärem Schauspiel. Durch die gegenseitige Anziehung, oder *Gravitation*, beginnen beide sich zu umkreisen, immer schneller und näher, bis sie am Ende zu einem einzigen Schwarzen Loch verschmelzen.

Bei diesem Prozess wird der umgebende Raum und die Zeit derart stark gekrümmt, dass die Auswirkungen, sogenannte *Gravitationswellen*, selbst hier auf der Erde im Prinzip messbar sind. Dafür benötigt man unvorstellbar sensible Detektoren und ein Netzwerk dieser Gravitationswellendetektoren ist bereits in Betrieb, um solche Signale erstmals direkt zu messen.

Ein wichtiger Beitrag, um tatsächlich Binärsysteme von Schwarzen Löchern zu „hören", sind theoretische Modelle der Signale, schließlich lässt sich ein bekanntes Geräusch deutlich leichter und genauer aus dem Rauschen der Detektoren herausfiltern als das völlig Unbekannte. Ausgehend von Einsteins Allgemeiner Relativitätstheorie, die zu kompliziert ist, um sie direkt zu lösen, wurden in dieser Arbeit sowohl analytische Näherungen auf dem Papier als auch numerische Simulationen mit Supercomputern vereint, um erstmals das gesamte Signal von einspiralenden und verschmelzenden Schwarzen Löchern vorherzusagen.

Die Resultate geben nicht nur einen Einblick, was von Gravitationswellenmessungen zu erwarten ist, sie ermitteln auch die Ungenauigkeiten, die in den analytischen und numerischen Lösungen vorhanden sind, und die im schlimmsten Fall zur Nichtentdeckung oder Fehlinterpretation von Signalen führen könnten. Die Schlussfolgerungen der vorliegenden Arbeit sind dabei positiv: Die theoretischen Vorhersagen von verschmelzenden Schwarzen Löchern sind genau genug, um eine neue Ära der Astronomie einzuleiten. Für fundamentale Fragen, z.B. ob Einsteins Theorie wirklich allumfassend unser Universum beschreibt, sind die Gravitationswellenmodelle womöglich noch zu ungenau, aber bis die ersten Daten mit einer neuen Generation von Detektoren erhoben werden, sind auch noch ein paar Jahre Zeit, um auch auf theoretischer Seite alles für den wissenschaftlichen Durchbruch vorzubereiten.

Abstract

One of the most exciting predictions of Einstein's theory of gravitation that have not yet been proven experimentally by a direct detection are *gravitational waves*. These are tiny distortions of the spacetime itself, and a world-wide effort to directly measure them for the first time with a network of large-scale laser interferometers is currently ongoing and expected to provide positive results within this decade. One potential source of measurable gravitational waves is the inspiral and merger of two compact objects, such as binary black holes. Successfully finding their signature in the noise-dominated data of the detectors crucially relies on accurate predictions of what we are looking for.

In this thesis, we present a detailed study of how the most complete waveform templates can be constructed by combining the results from

(A) analytical expansions within the post-Newtonian framework and

(B) numerical simulations of the full relativistic dynamics.

We analyze various strategies to construct complete *hybrid waveforms* that consist of a post-Newtonian inspiral part matched to numerical-relativity data. We elaborate on exsisting approaches for nonspinning systems by extending the accessible parameter space and introducing an alternative scheme based in the Fourier domain. Our methods can now be readily applied to multiple spherical-harmonic modes and precessing systems.

In addition to that, we analyze in detail the accuracy of hybrid waveforms with the goal to quantify how numerous sources of error in the approximation techniques affect the application of such templates in real gravitational-wave searches. This is of major importance for the future construction of improved models, but also for the correct interpretation of gravitational-wave observations that are made utilizing any complete waveform family. In particular, we comprehensively discuss how long the numerical-relativity contribution to the signal has to be in order to make the resulting hybrids accurate enough, and for currently feasible simulation lengths we assess the physics one can potentially do with template-based searches.

Acronyms and symbols

BH	black hole
EOB	effective one body
FFT	fast Fourier transform
GW	gravitational wave
IMR	inspiral-merger-ringdown
NR	numerical relativity
PN	post-Newtonian
SNR	signal-to-noise ratio

Frequently used symbols

$h_+, h_\times$	plus and cross polarization of the gravitational wave
h	gravitational-wave strain, $h = h_+ - i\,h_\times$
Ψ_4	Newman-Penrose scalar, $\Psi_4 = \partial^2 h/\partial t^2$
A, ϕ	amplitude and phase of h, $h = A\,e^{i\phi}$
$\phi_{\rm orb}$	orbital phase of a binary inspiral
$\omega_{\rm orb}$	time-domain frequency of the orbital movement, $\omega_{\rm orb} = \lvert d\phi_{\rm orb}/dt\rvert$
v	relative velocity in an orbiting black-hole binary
$\tilde{h}$	Fourier transform of h
$\tilde{A}$, $\tilde{\phi}$	amplitude and phase of $\tilde{h}$, $\tilde{h} = \tilde{A}\,e^{i\tilde{\phi}}$
R, $r_{\rm ex}$	distance between source and observer, also extraction radius
m_1, m_2	individual masses of the black holes in a binary
M	total mass of the binary, $M = m_1 + m_2$
q	mass ratio of the binary, $q = m_1/m_2$
η	symmetric mass ratio of the binary, $\eta = m_1\,m_2/M^2$
$\boldsymbol{S}_1, \boldsymbol{S}_2$	individual spins of the black holes
$\boldsymbol{L}$	angular momentum of the binary
$\boldsymbol{L}_N$	Newtonian angular momentum of the binary
$\hat{\boldsymbol{L}}_N$	unit vector of the Newtonian angular momentum, $\hat{\boldsymbol{L}}_N = \boldsymbol{L}_N/\lVert\boldsymbol{L}_N\rVert$
χ_1, χ_2	dimensionless spin projections, $\chi_i = \boldsymbol{S}_i \cdot \hat{\boldsymbol{L}}_N/m_i^2$
χ	mass-weighted total spin of the binary, $\chi = (m_1\chi_1 + m_2\chi_2)/M$
$\langle h_1, h_2\rangle$	inner product between two waveforms, see (2.47)
$\mathcal{O}$	overlap, inner product maximized over time and phase shifts
$\mathscr{M}$	mismatch, $\mathscr{M} = 1 - \mathcal{O}$
FF	fitting factor, fully optimized inner product
$\mathscr{M}_{\rm FF}$	fully optimized mismatch, $\mathscr{M}_{\rm FF} = 1 - {\rm FF}$
S_n	noise spectral density of a detector
Λ	likelihood ratio
Γ_{ij}	Fisher information matrix

Table of Contents

Chapter 1

Introduction

Our current understanding of the weakest of all fundamental forces, *gravity*, is based on Einstein's theory of General Relativity. The interaction of space, time, matter and energy is described in a geometrical picture that not only explains why Newton's apple falls to the ground, it also predicts phenomena that go well beyond the classical perception of an attracting force. All experimental and observational tests of General Relativity were passed successfully so far, from the perihelion advance of Mercury, the time dilation of global-positioning satellites to the bending of light around massive astrophysical objects. One prediction, however, could not be directly detected so far: *gravitational waves* (GWs).

This will (hopefully) change in the near future. Kilometer-size detectors, based on the design of a Michelson laster interferometer, have been built to pick up tiny oscillations of spacetime itself [7–9, 19, 99, 127, 173, 174]. A network of these instruments, distributed all over the globe, is already in operation or in an upgrade phase to reach a sensitivity that should be good enough to detect several signals per year [4].

What are we looking, or rather "listening", for? Although every accelerated mass distorts the spacetime and, in principle, emits GWs, the effects are so inconceivably weak for any human or even planetary movements, that we have to aim for the most violent processes in the universe. One prominent candidate of a first detection is the inspiral and merger of the most compact objects that exist: *black holes* (BHs). If a binary forms and spirals inwards, the heavy masses move with a velocity close to the speed of light at their final encounter, which should produce a very energetic burst of gravitational radiation. This signal originates directly at the core of the process; it is not obscured on by stars, stellar medium or other obstacles along its way to earth, so detecting GWs will open an entirely new window to the universe, complementing what we can infer today from electromagnetic radiation and other observations.

Despite these gravitationally violent processes, the signals are still extremely weak when they arrive at the detector on earth, and it is a theoretically and computationally challenging problem to identify such weak signatures in the noise-dominated data of GW detectors. However, a theoretically predicted model of the waveforms we are looking for greatly aids the search. In fact, the most sensitive search strategies are based on a comparison of theoretical *waveform templates* with the data to assign a statistical confidence about how likely the signal in question is buried in the noise. In addition, the characteristics of the

system that emitted the GW are encoded in the signal, and to extract such information we first have to understand how different physical parameters affect the GW signature.

Unfortunately, modeling GWs from coalescing BHs is a difficult problem by itself. To elicit the corresponding signal from Einstein's equation, we have to solve a nonlinear system of partial differential equations, which cannot be done exactly. Therefore, we have to make use of the most accurate approximations, either of analytical origin within the post-Newtonian (PN) approach [38], or solve the full equations numerically. Both fields have advanced tremendously over the past years, and each can provide a reliable description of a different part of the entire signal. PN methods are based on expanding relevant quantities in terms of a small parameter, such as the relative velocity of the bodies as a fraction of the speed of light. The results thus become more inaccurate the closer the binary is to merger, which means that the last part of the inspiral, the merger and the "ringdown" to the final BH have to be modeled differently. Here, numerical relativity (NR) can provide reliable data, but performing the simulations in full generality is a very time consuming process. Hence, only relatively short NR waveform parts can be generated.

The subject of this thesis is the combination of both approaches to obtain a complete and accurate picture of the entire GW signal emitted by coalescing BHs. When our studies started, there were already first approaches to describe the complete waveform by a combination of analytical and numerical data [14, 15, 60, 61, 80, 81], but these were restricted to nonspinning systems, and only a few NR simulations were available at that time. The aim of the present work is therefore to elaborate on the construction of complete waveform models, extend their validity range, and, most importantly, develop a general framework to assess their reliability and gauge the physics that can actually be done with them.

After a general introduction to the relevant topics in Chapter 2, we devote Chapter 3 to the question of how well PN and NR results agree, and we develop strategies to match both waveform parts to a complete *hybrid waveform*. Our studies demonstrate that a robust matching is indeed possible, and apart from time-domain procedures that have been applied by several groups [15, 45, 46, 49, 102, 128], we introduce a novel alternative that is based in the Fourier domain. Advantages and disadvantages of these techniques are discussed, and for the first time we provide a detailed receipt how multiple harmonic modes of PN waveforms have to be set up in order to connect them to a given NR simulation of precessing binaries. Chapter 3 is concluded by a description of two "phenomenological models" for binaries with aligned spins that describe the entire waveform in a closed form. Particularly the Fourier-domain based model was greatly supported by the work presented in this thesis.

Chapter 4 goes beyond the question of simply constructing templates. Here we ask how useful current models actually are. What is the main weakness that needs to be improved? We develop an algorithm that allows us to evaluate the error and ambiguities of current hybrid waveforms even without having NR data at hand. We take care that our error assessment is as close as possible to the strategy actually employed in GW searches, so that we can make meaningful statements about the loss of information we have to expect by using current waveform models as templates in search algorithms.

A central question of the modeling community to prepare for the era of advanced detectors is how the limited computer resources should be spent most efficiently. One could either perform few very long simulations or explore the parameter space with more, but shorter runs. Here we address this question by evaluating the error of our complete waveform model as a function of the available length of the NR signal. Other authors have explored the same idea [45, 82, 128], but the idealistic requirements imposed on individual hybrids led to the conclusion that *much longer* NR simulations than currently feasible are needed in order to make complete waveform models accurate enough. We show that our efficient approach to estimate errors agrees with those results if we impose the same restrictions, but we extend the analysis to *waveform families* instead of individual waveforms and calculate the appropriate "fitting factor" and parameter uncertainties in that case.

The results we find are much more optimistic. We show that the parameters of the source can be inferred from the signal to an accuracy of $\sim 1\%$ for total mass and symmetric mass ratio and about 0.1 (absolute error) for the total spin magnitude, assuming a currently achievable length of NR simulations (~ 10 orbits before merger). This is in many relevant cases smaller or comparable to the statistical biases one has to accept in any case due to the presence of detector noise. The number of signals that may be lost due to an inexact model is less than 3% of the detectable events for most parts of the parameter space. Only models of systems with very high spin magnitudes and mass ratios $\gtrsim 4$ are still rather uncertain, but this is the regime where improvements in the analytical treatment is expected in the near future.

We conclude with a discussion of our results in Chapter 5, where we point out that the model errors we find are potentially good enough for the first detections and interpretation of signals whose amplitude is close to the detection threshold. In that sense, the prospects of being prepared for immediate astrophysical applications of GW detections are rather good, provided that our models are subsequently refined once higher PN corrections are determined and more NR simulations become available. A reliable method to address more fundamental questions, such as testing General Relativity or determining the nature of matter in neutron stars from GW observation, however, requires much more accurate models than those we can construct today.

The research for this doctoral thesis resulted already in several publications which are listed below.

[141] F. Ohme, M. Hannam, S. Husa, N. Ó Murchadha, *Stationary hyperboloidal slicings with evolved gauge conditions.* Class. Quant. Grav. **26** 175014 (2009)

[162] L. Santamaría, F. Ohme, P. Ajith, B. Brügmann, N. Dorband, M. Hannam, S. Husa, P. Mösta, D. Pollney, C. Reisswig, E. L. Robinson, J. Seiler, B. Krishnan, *Matching post-Newtonian and numerical relativity waveforms: systematic errors and a new phenomenological model for non-precessing black hole binaries.* Phys. Rev. **D82** 064016 (2010)

[104] M. Hannam, S. Husa, F. Ohme, D. Müller, B. Brügmann, *Simulations of black-hole binaries with unequal masses or nonprecessing spins: Accuracy, physical properties, and comparison with post-Newtonian results.* Phys. Rev. **D82** 124008 (2010)

[102] M. Hannam, S. Husa, F. Ohme, P. Ajith, *Length requirements for numerical-relativity waveforms.* Phys. Rev. **D82** 124052 (2010)

[16] P. Ajith, M. Hannam, S. Husa, Y. Chen, B. Brügmann, N. Dorband, D. Müller, F. Ohme, D. Pollney, C. Reisswig, L. Santamaría, J. Seiler, *Inspiral-merger-ringdown waveforms for black-hole binaries with non-precessing spins.* Phys. Rev. Lett. **106** 241101 (2011)

[140] F. Ohme, M. Hannam, S. Husa, *Reliability of complete gravitational waveform models for compact binary coalescences.* Phys. Rev. **D84** 064029 (2011)

[146] F. Pannarale, L. Rezzolla, F. Ohme, J. S. Read, *Will black hole-neutron star binary inspirals tell us about the neutron star equation of state?* Phys. Rev. **D84** 104017 (2011)

[139] F. Ohme, *Analytical meets numerical relativity – status of complete gravitational waveform models for binary black holes.* Class. Quant. Grav. **29** 124002 (2012)

[12] P. Ajith *et al.*, *The NINJA-2 catalog of hybrid post-Newtonian/numerical-relativity waveforms for non-precessing black-hole binaries.* Class. Quant. Grav. **29** 124001 (2012)

This thesis constitutes a summary, discussion and extension of only the results that are associated with GW models for BH binaries. The comparison of PN and NR data presented in Sec. 3.2 was published in [104] and my contribution was to prepare the different PN approximants (including the subtle discussion of spin effects) and analyze their agreement with NR data. The phenomenological waveform models [16, 162] presented in Secs. 3.5.1 and 3.5.2 were supported by my analysis of PN approximants, particularly in the frequency domain. The Fourier-domain PN/NR hybridization scheme introduced in Sec. 3.3.2 and the discussion based on it in Sec. 3.4 were partly published in [161, 162], and they represent my original contribution to this analysis. Studies about the required length of numerical simulations were started in [102], where I contributed to the error analysis of various hybridization procedures, presented here in Sec. 4.3, and the PN-induced error analysis for spinning systems. The refined study of PN errors, without NR data and also in terms of fully optimized fitting factors, was published in [140], and it is one of the main results presented in this thesis (see Secs. 4.4 and 4.5). As such, it was developed and carried out by myself.

Chapter 2

Foundations

2.1 A geometrical theory of gravity

More than 200 years after Isaac Newton explained *gravity* as a force that accelerates every body with nonzero mass through the attraction of another mass, Albert Einstein published a very different, geometrical theory of gravitation [85, 86]. According to it, the acceleration that causes bodies to move on a curved path is not a characteristic of the bodies themselves, but of the *spacetime* they move in. Masses warp this spacetime, so that an observer experiences the effect of matter as an attracting force. However, *General Relativity* goes beyond these empirically well-proven facts. It predicts, for example, that even massless light can be affected on its path from source to observer by the warped spacetime, and there are objects so heavy and compact, that nothing can escape their immediate vicinity. So far, General Relativity has passed all experimental tests, and both the bending of light and the existence of black holes (BHs) are established phenomena in our current view of the universe.

Mathematically, the spacetime is described by a differentiable four-dimensional manifold with a smooth metric $g_{\mu\nu}$ whose signature is $(-,+,+,+)$. The *line element* then reads

$$ds^2 = g_{\mu\nu}\, dx^\mu\, dx^\nu \,, \tag{2.1}$$

where we sum over all indices that appear twice (once as subscript, once as superscript). We can interpret (2.1) as an infinitesimal distance ds^2 that is the result of infinitesimal changes along the coordinates x^μ. The simplest example is the flat space, or *Minkowski space*, that reads in terms of the time coordinate t and Cartesian coordinates (x, y, z)

$$ds^2 = -dt^2 + dx^2 + dy^2 + dz^2 \,. \tag{2.2}$$

Note that we have adopted a unit system where the speed of light c and the gravitational constant G are set to unity, and we shall stick to this convention throughout this thesis.

In flat space, infinitesimal movements in one and then in another direction commute, but this is no longer true in curved spacetime. In fact, the *curvature* can be defined in terms of the *Riemann tensor* $R^\rho{}_{\sigma\mu\nu}$ by the difference of successively acting derivatives. It satisfies

$$\nabla_\mu \nabla_\nu V^\rho - \nabla_\nu \nabla_\mu V^\rho = R^\rho{}_{\sigma\mu\nu} V^\sigma \tag{2.3}$$

for every smooth vector field V^ρ. The operator ∇_μ is the *covariant derivative* (or Levi-Civita connection) which is uniquely defined as a linear, metric compatible and torsion-free connection. Using the *Christoffel symbols* $\Gamma^\sigma_{\mu\nu}$, is reads explicitly

$$\nabla_\mu V^\nu = \partial_\mu V^\nu + \Gamma^\nu_{\mu\sigma} V^\sigma \ , \qquad \text{with} \tag{2.4}$$

$$\Gamma^\nu_{\mu\sigma} = \frac{1}{2} g^{\nu\lambda} \left(\partial_\mu g_{\sigma\lambda} + \partial_\sigma g_{\mu\lambda} - \partial_\lambda g_{\mu\sigma} \right) \ . \tag{2.5}$$

With these definitions, the Riemann tensor can be written as [66, 134, 192]

$$R^\rho_{\ \sigma\mu\nu} = \partial_\mu \Gamma^\rho_{\ \nu\sigma} - \partial_\nu \Gamma^\rho_{\ \mu\sigma} + \Gamma^\rho_{\ \mu\lambda} \Gamma^\lambda_{\ \nu\sigma} - \Gamma^\rho_{\ \nu\lambda} \Gamma^\lambda_{\ \mu\sigma} \ , \tag{2.6}$$

and in combination with (2.5) we see that $R^\rho_{\ \sigma\mu\nu}$ is a function of the metric, its first and second derivatives.

To relate these geometrical quantities to gravity, we first have a look at the Newtonian case, which can be described as a second-order differential equation of the Newtonian potential Φ that is related to the mass density ρ via

$$\Delta \Phi = 4\pi\rho \ . \tag{2.7}$$

There is a similar construction in General Relativity where the mass density is represented by the energy momentum tensor $T_{\mu\nu}$ and the left-hand side is replaced by the Einstein tensor

$$G_{\mu\nu} = R_{\mu\nu} - \frac{1}{2} R \, g_{\mu\nu} \ . \tag{2.8}$$

Here we used the contractions of the Riemann tensor, $R_{\mu\nu} = R^\lambda_{\ \mu\lambda\nu}$ (Ricci tensor) and $R = R^\mu_\mu$ (Ricci scalar). Finally, the *Einstein equations* can be written in a compact form as

$$G_{\mu\nu} = 8\pi T_{\mu\nu} \ , \tag{2.9}$$

where the constant 8π was fixed to correctly recover the Newtonian limit. Just like Newton's description, (2.9) relates derivatives up to second order of "a field" (here the metric $g_{\mu\nu}$) to a mass distribution. However, the energy momentum tensor $T_{\mu\nu}$ generally is a function of $g_{\mu\nu}$ itself, and (2.9) is a coupled system of nonlinear differential equations.

Note that the trace of (2.9) yields $R = -8\pi T$, where $T = T_\mu^{\ \mu}$, which leads to the equivalent form of the Einstein equations

$$R_{\mu\nu} = 8\pi \left(T_{\mu\nu} - \frac{1}{2} T \, g_{\mu\nu} \right) \ . \tag{2.10}$$

From (2.10) we see that in the vacuum case, where $T_{\mu\nu} = 0 = T$, we have

$$R_{\mu\nu} = 0 \ . \tag{2.11}$$

In this thesis we shall employ different approaches to solve the vacuum Einstein equations approximately, either through analytical approximations or numerically. Let us,

however, conclude this section with an important *exact* solution of (2.11). The unique nontrivial spherical symmetric solution [37] reads

$$ds^2 = -\left(1 - \frac{2M}{R}\right) dT^2 + \left(1 - \frac{2M}{R}\right)^{-1} dR^2 + R^2\, d\Omega^2 \,, \tag{2.12}$$

where $d\Omega^2 = d\theta^2 + \sin^2\theta\, d\varphi^2$, and (R, θ, φ) can be interpreted as standard spherical coordinates. This solution was found by Karl Schwarzschild in 1916 [168] and it describes a one-parameter family of spacetimes that we today identify as isolated, nonspinning *black holes* (BHs) with mass M. The generalization to axially symmetric solutions – *spinning BHs* – was found later by Kerr [117]. They constitute the most compact objects in the universe as the entire mass is formally contained in the origin. There is strong observational evidence that BHs indeed exist (see, e.g., [159]), for instance in the center of our galaxy. In addition, other compact objects such as neutron stars (for an overview of observations, see [120]) are well approximated by the Kerr solution outside their dense matter core.

2.2 Gravitational waves

2.2.1 Weak field limit

Another exciting prediction of Einstein's theory of General Relativity will become the main subject of this thesis: *gravitational waves* (GWs). These are ripples in spacetime itself that propagate at the speed of light (which we set to unity). Their existence and properties can be derived from a weak-field approximation, and we shall briefly outline this derivation following closely the textbook by Schutz [167].

We assume the spacetime to be "almost flat", i.e., there exists a coordinate system where

$$g_{\mu\nu} = \eta_{\mu\nu} + h_{\mu\nu} \,, \qquad \text{with } |h_{\mu\nu}| \ll 1 \,. \tag{2.13}$$

We denoted the flat Minkowski metric (2.2) by $\eta_{\mu\nu}$ and $h_{\mu\nu}$ satisfies the properties of a tensor field on a flat background, or equivalently in the framework of Special Relativity. To maintain the form (2.13), we can only allow Lorentz transformations and small *gauge transformations* of the type

$$x^{\mu\prime} = x^\mu + \xi^\mu \,, \tag{2.14}$$

where ξ^μ are functions of the coordinates x^ν. Demanding that the coordinate transformations are small in the sense $|\partial_\mu \xi^\nu| \ll 1$, we find from (2.13) that $h_{\mu\nu}$ transforms to linear order in ξ^μ as

$$h_{\mu\nu} \to h_{\mu\nu} - \partial_\mu \xi^\nu - \partial_\nu \xi^\mu \,. \tag{2.15}$$

To expand the Einstein equations (2.9) to linear order in $h_{\mu\nu}$ we note that

$$R_{\rho\sigma\mu\nu} = \frac{1}{2}\left(\partial_\sigma\partial_\mu h_{\rho\nu} + \partial_\rho\partial_\nu h_{\sigma\mu} - \partial_\rho\partial_\mu h_{\sigma\nu} - \partial_\sigma\partial_\nu h_{\rho\mu}\right) \,, \tag{2.16}$$

$$R_{\sigma\nu} = R^{\lambda}{}_{\sigma\lambda\nu} = \frac{1}{2}\left(\partial_\sigma\partial^\lambda h_{\lambda\nu} + \partial_\nu\partial^\lambda h_{\lambda\sigma} - \partial^\lambda\partial_\lambda h_{\sigma\nu} - \partial_\sigma\partial_\nu h\right), \tag{2.17}$$

$$R = R^{\rho}{}_{\rho} = \partial^\rho\partial^\lambda h_{\rho\lambda} - \partial^\lambda\partial_\lambda h \tag{2.18}$$

(to linear order in $h_{\mu\nu}$), where $h = h^{\lambda}{}_{\lambda}$. These expressions can be simplified further by using the *trace reverse*

$$\bar{h}_{\mu\nu} = h_{\mu\nu} - \frac{1}{2}\eta_{\mu\nu}h \tag{2.19}$$

and imposing $\partial^\lambda\bar{h}_{\lambda\nu} = 0$. This condition, which is commonly referred to as the *Lorentz gauge*, can always be satisfied by an appropriate coordinate transformation (2.15). With these simplifications, we find that the Einstein equations read to first order

$$\Box\bar{h}_{\mu\nu} = \partial^\lambda\partial_\lambda\bar{h}_{\mu\nu} = -16\pi T_{\mu\nu}\ , \tag{2.20}$$

which is a simple wave equation for $\bar{h}_{\mu\nu}$ on a flat background. The general complex solutions reads

$$\bar{h}_{\mu\nu} = A_{\mu\nu}\, e^{i k_\lambda x^\lambda} \qquad \text{with}\ \ k^\lambda k_\lambda = 0\ . \tag{2.21}$$

To satisfy the gauge we have chosen, we also need $k^\lambda A_{\lambda\nu} = 0$, so the general solution are plane waves that travel along null vectors, i.e., with the speed of light.

The coordinate transformation that led to this result was not unique. In particular, any transformation (2.14) that fulfills $\Box\xi^\mu = 0$ maintains the Lorentz gauge, and we can exploit this remaining freedom to identify the independent components of $\bar{h}_{\mu\nu}$. In vacuum, we can impose without violating the Lorentz gauge $\bar{h} = 0$ (which makes the distinction between $h_{\mu\nu}$ and its trace reverse superfluous) as well as $h_{0i} = h_{00} = 0$ $(i = 1,2,3)$. If we further choose the direction of wave propagation along the z-axis, we find $h_{3\nu} = 0$. Hence, we are left with only two independent components (or *polarizations*) which are commonly denoted by h_+ and $h_\times$,

$$h_{\mu\nu} = \begin{pmatrix} 0 & 0 & 0 & 0 \\ 0 & h_+ & h_\times & 0 \\ 0 & h_\times & -h_+ & 0 \\ 0 & 0 & 0 & 0 \end{pmatrix}\ . \tag{2.22}$$

The set of gauge conditions we employed to obtain (2.22) is commonly referred to as the *transverse-traceless* (TT) gauge.

The effect of a GW on test masses can be seen by the deviation of their geodesics. Consider two free falling particles. In the local TT frame of one particle, the connection vector to the other particle be expressed by x^μ. The acceleration of x^μ is then given by

$$\frac{d^2x^\mu}{dt^2} = R^{\mu}{}_{00\lambda}\, x^\lambda\ . \tag{2.23}$$

With (2.16) we can express the Riemann tensor in terms of $h_{\mu\nu}$,

$$\frac{d^2x^\mu}{dt^2} = \frac{1}{2}\frac{d^2h_{\mu\lambda}}{dt^2}\, x^\lambda \tag{2.24}$$

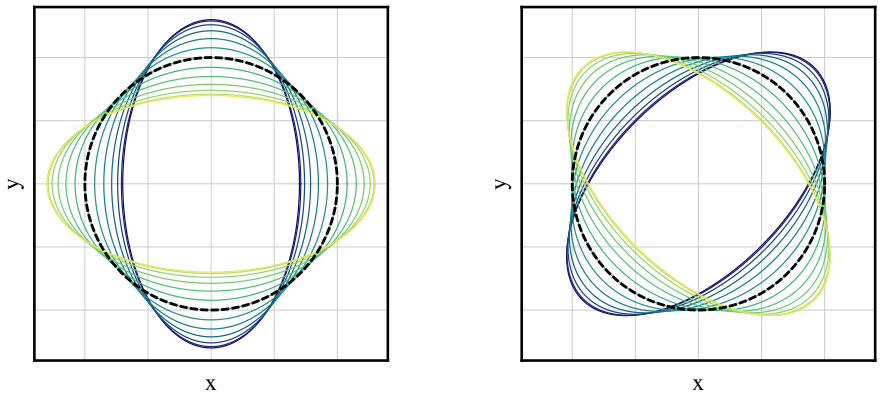

Figure 2.1: Effect of a GW traveling in z-direction on a ring of test particles. The left panel assumes a pure plus polarization, the right panel a cross polarization. The ring, initially at rest (dashed), is warped periodically (shown in different colors) with the frequency of the GW.

(we were free to lower the index μ, because $h_{\mu\nu}$ has only spatial nonvanishing components), from which we see that a passing GW acts like a force one the second body, provided we are in the inertial frame of the first free falling body. To leading order, we can solve (2.24) by

$$x^\mu(t) = \left(\delta^\mu_\lambda + \frac{1}{2}h_{\mu\lambda}(t)\right) x^\lambda_0 \,, \tag{2.25}$$

from which we can deduce a clear picture how the plus and cross polarizations affect free falling particles.

Imagine a ring of test bodies in the x-y-plane (we are still in the transverse-traceless gauge). In our derivation, the GW travels perpendicular to this ring in the z-direction, and now we further assume $h_\times = 0$. The remaining polarization h_+ is an oscillating function that periodically stretches and shrinks the distance between the particles in x-direction and opposite in y-direction. The cross polarization $h_\times$ has a similar effect, but rotated to the plus polarization by 45°. An illustration of these effects is provided by Fig. 2.1. It is this periodic change of the distance between test masses that builds the basis of measuring GWs with laser interferometers, as we shall explain in Sec. 2.3.1.

2.2.2 Generating gravitational waves

We have introduced GWs as weak perturbations of the metric on a flat background. According to Einstein's equations, they fulfill the wave equation (2.20), but how are these waves generated in the first place? We shall review the basic principles here, following the explanations in [65, 66, 167, 192].

The general solution of (2.20) can be written in terms of the retarded integral

$$h_{\mu\nu}(t, x^i) = 4 \int \frac{T_{\mu\nu}(t - |x^i - y^i|, y^i)}{|x^i - y^i|}\, d^3y \,, \tag{2.26}$$

where we have split four-dimensional vectors in their time and spatial part, $x^\mu = (t, x^i)$, and the integral is performed over the past light cone of the event (t, x^i). We now assume

that the source is far away from the observer and does not move too fast, so that $|x^i - y^i|$ can be approximated by the constant distance R. The Fourier transform of (2.26) with respect to the time reads then

$$\tilde{h}_{\mu\nu}(\omega, x^i) = \frac{4e^{i\omega R}}{R} \int \tilde{T}_{\mu\nu}(\omega, y^i)\, d^3y \ . \tag{2.27}$$

The energy-momentum tensor satisfies the conservation law $\partial_\mu T^{\mu\nu} = 0$, which translates in Fourier space into $-\partial_j \tilde{T}^{j\nu} = i\omega \tilde{T}^{0\nu}$. Integration by parts yields

$$\int \tilde{T}^{ij}(\omega, y^i)\, d^3y = -\int y^i\, \partial_k \tilde{T}^{kj}\, d^3y \ , \tag{2.28}$$

where the surface integral vanished because we assumed a localized source. Applying this manipulation twice, together with the conclusion from the conservation law and the symmetry of the energy momentum tensor finally yields

$$\tilde{h}_{jk}(\omega, x^i) = -2\omega^2 \frac{e^{i\omega R}}{R} \int y^j y^k\, \tilde{T}^{00}(\omega, y^i)\, d^3y \ , \qquad \text{or equivalently} \tag{2.29}$$

$$h_{jk}(t, x^i) = \frac{2}{R} \frac{\partial^2}{\partial t^2} \int y^j y^k\, T^{00}(t - r, y^i)\, d^3y \ . \tag{2.30}$$

The spatial components determine $h_{\mu\nu}$ entirely, as we assumed the Lorentz gauge which implies $-i\omega\tilde{h}^{0\nu} = \partial_j \tilde{h}^{j\nu}$.

The solution in form of Eq. (2.30) is instructive in several ways. First, notice that for our assumptions $T^{00} \approx \rho$, where ρ is the mass density. Hence, GWs are triggered by the second time derivative (acceleration) of the mass-density distribution. We further see form (2.30) that the radiation falls off inversely with the distance to the source; thus, astrophysically triggered GWs are indeed very weak when they reach the earth. Furthermore, the radiation is quadrupolar at leading order. This is a direct consequence of the conservation law for energy and momentum, which bans any mono- or dipolar gravitational radiation.

In the remainder of this thesis, we shall focus on orbiting binary BHs, so we use them as an example to illustrate (2.30). In the context here, we can treat them approximately as two point particles orbiting around each other. For circular orbits we find in the Keplerian case

$$v^2 = \frac{M}{r} \ , \qquad \omega_{\rm orb} = \sqrt{\frac{M}{r^3}} = \frac{v}{r} \ , \tag{2.31}$$

with v and r denoting the relative velocity and distance between the two bodies, respectively; M is their total mass ($M = m_A + m_B$), and $\omega_{\rm orb}$ is the orbital frequency. We put the two BHs in the x^1-x^2 plane, with their locations given in the center-of-mass frame by

$$x^i_A = \frac{M\eta r}{m_A} \big[\cos(\omega_{\rm orb} t), \sin(\omega_{\rm orb} t), 0\big] \ , \qquad x^i_B = -\frac{m_A}{m_B} x^i_A \ , \tag{2.32}$$

where we used $\eta = m_A m_B / M^2$ to denote the symmetric mass ratio. The mass distribution is now constructed from the corresponding δ-distributions, and in this particular form, it is

easy to solve the integral (2.30) explicitly. It reads

$$h_{jk} = \frac{4M\eta r^2\omega_{\rm orb}^2}{R}\begin{pmatrix} -\cos[2\omega_{\rm orb}(t-R)] & -\sin[2\omega_{\rm orb}(t-R)] & 0 \\ -\sin[2\omega_{\rm orb}(t-R)] & \cos[2\omega_{\rm orb}(t-R)] & 0 \\ 0 & 0 & 0 \end{pmatrix}, \tag{2.33}$$

and the "amplitude" can also be written through (2.31) as $4M\eta v^2/R$. This is a very useful result. We see that orbiting compact objects emit GWs at quadrupole order with a frequency that is twice their orbital frequency. Of course, to obtain the entire evolution of the binary, we have to include an estimate of the emitted energy, which will be the starting point of *post-Newtonian* approximants that we shall summarize in Sec. 2.4.

2.3 Detecting gravitational waves

2.3.1 Laser interferometers

Because a GW changes the proper distance between objects, its effect should in principle be measurable by a thoroughly designed experiment. There have been several attempts to do so, pioneered by Weber's [194] and subsequently developed bar detectors, that were designed such that a passing GW, if strong enough, would excite the bar's resonant frequency. Despite Weber's claim in 1969 [195, 196], however, no significant signals could be detected conclusively so far, mainly because the expected GW amplitudes $h \lesssim 10^{-21}$ are too weak for the sensitivity of the detectors.

The most promising effort today to detect these weak signals for the first time directly is a world-wide network of large-scale laser interferometers. Figure 2.2 shows their locations. The network consists of the 4 km-size detectors from the Laser Interferometer Gravitational-wave Observatory (LIGO) [7, 173, 174], VIRGO with 3 km arm length [8, 9], GEO 600 [99, 127] and TAMA [19]. The latest developments include an upgrade to Advanced LIGO [108], the construction of the Large-scale Cryogenic Gravitational-wave Telescope (LCGT) in Japan [187] and a possible commissioning of a LIGO detector in India (IndiGO).

The basis of these instruments is a Michelson interferometer, in which laser beams are sent in orthogonal directions. The principle layout is shown in Fig. 2.3. We have seen in Sec. 2.2 that a passing GW will stretch and shrink the proper distance between the end test masses, and the proper length of the arm, say in x-direction while a GW is traveling in z-direction (we are still in the TT gauge), is given by

$$L + \Delta L = \int_0^L \sqrt{g_{xx}}\, dx = \int_0^L \sqrt{1+h_+}\, dx \approx L\left(1 + \frac{h_+}{2}\right). \tag{2.34}$$

This approximation is only valid in the *long wavelength* regime, where the wavelength of the GW $\lambda \gg L$. In the cases we shall consider, however, this is always true, because the detectors turn out to be most sensitive around ~ 100 Hz, which corresponds to $\lambda \approx 3000$ km. Note that a rigorous derivation of the detector response does not just assume that the light beams measure the proper length of the detector arms, their paths and frequencies are affected by the distortions of spacetime themselves. The final result for the frequency shift

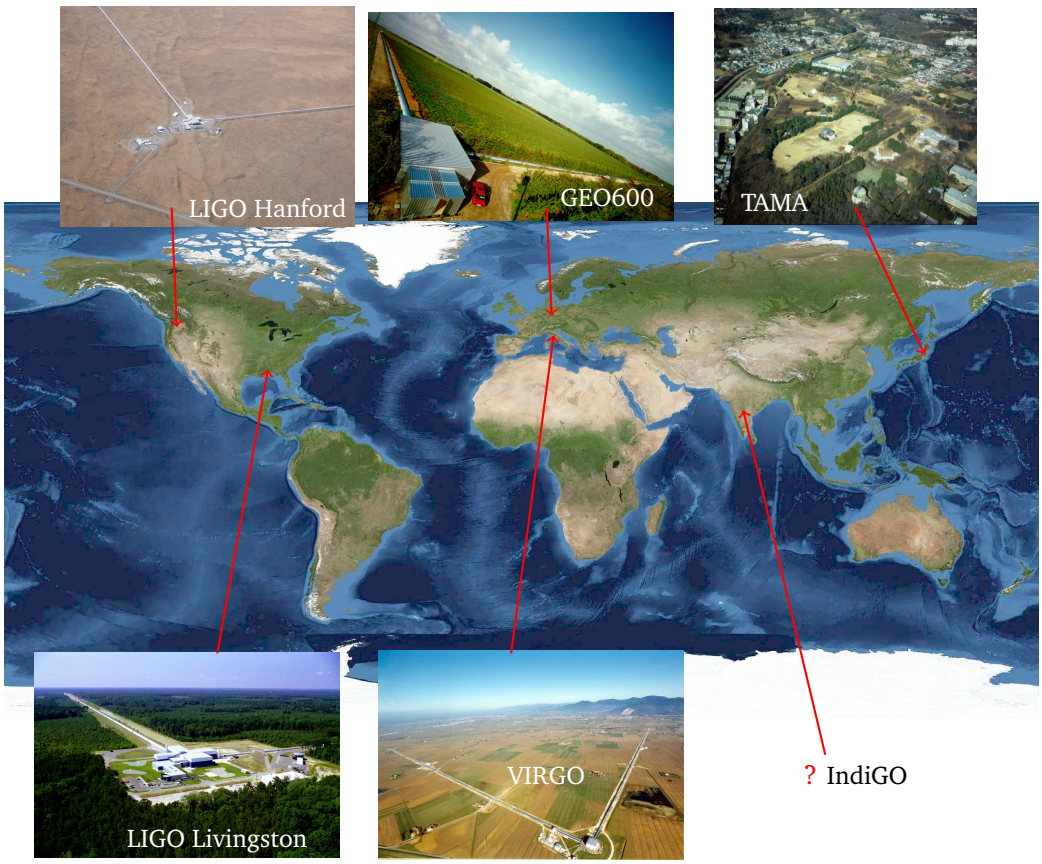

Figure 2.2: Network of large-scale laser interferometers.

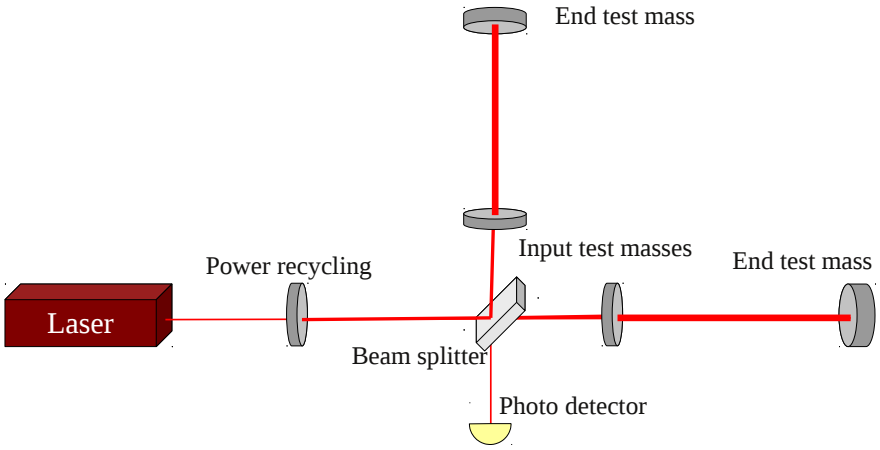

Figure 2.3: Basic layout of a GW laser interferometer. The laser power and sensitivity is enhanced by a power recycling mirror and Fabry-Pérot cavities between the input test masses and the end test masses. The phase difference (thereby length difference) of both arms is measured at the photo detector.

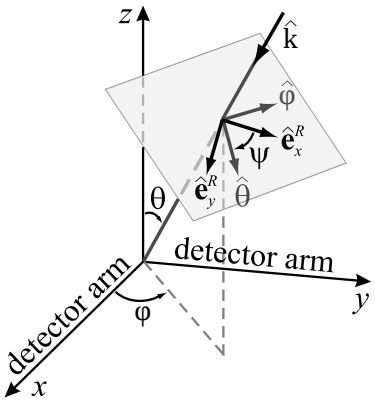

Figure 2.4: Angles between detector and source in the detector frame. The sky location is defined by (θ, φ), ψ is used to specify a reference frame orthogonal to the line of sight. The GW propagates along $\hat{k}$. Figure adapted from [54].

of the light that traveled along the spatial unit vector $\hat{\xi}^i$ is

$$\frac{\Delta\omega}{\omega} = \frac{1}{2}\,\frac{\hat{\xi}^i\hat{\xi}^j\,\Delta h_{ij}}{1-\hat{k}_j\hat{\xi}^j}\,, \tag{2.35}$$

where $\hat{k}_j$ is the propagation direction of the GW, and Δh_{ij} denotes the difference of the metric perturbation at the beginning and end point of the light travel.

We now consider the total effect at the beam splitter (see Fig. 2.3) caused by light rays that were sent in $\hat{x}^i$ and $\hat{y}^i$ direction, respectively, and reflected by the end mirrors. Again, we apply the long wavelength approximation, which enables us to simplify (2.35) by a Taylor expansion of Δh_{ij}. The final result reads

$$\frac{\Delta\dot{\Phi}}{\omega} = L\left(\hat{y}^i\hat{y}^j - \hat{x}^i\hat{x}^j\right)\dot{h}_{ij}\,, \tag{2.36}$$

where we have used the abbreviation $\Delta\dot{\Phi} = \Delta\partial\Phi/\partial t = \partial(\Delta\Phi)/\partial t$ to replace the frequency shift by the time derivative of the phase shift. Integrating (2.36) relates the phase difference at the beam splitter to the GW

$$\Delta\Phi = \frac{2\pi}{\lambda}L\left(\hat{y}^i\hat{y}^j - \hat{x}^i\hat{x}^j\right)h_{ij}\,, \tag{2.37}$$

just as we would have concluded from the mere change of the proper distance between the test masses.

The detector response $h_{\text{resp}} = \hat{x}^i\hat{x}^j h_{ij}$ can be expressed in terms of the angles (θ, φ, ψ) that define the source location with respect to the detector frame [54, 163],

$$\begin{aligned} h_{\text{resp}}(t) &= F_+(\theta,\varphi,\psi)\,h_+(t) + F_\times(\theta,\varphi,\psi)\,h_\times(t) \\ F_+(\theta,\varphi,\psi) &= \frac{1}{2}\left(1+\cos^2\theta\right)\cos 2\varphi\cos 2\psi - \cos\theta\sin 2\varphi\sin 2\psi \\ F_\times(\theta,\varphi,\psi) &= \frac{1}{2}\left(1+\cos^2\theta\right)\cos 2\varphi\sin 2\psi + \cos\theta\sin 2\varphi\cos 2\psi\,. \end{aligned} \tag{2.38}$$

For an illustration, see Fig. 2.4. Note that, for a compact binary on circular orbits, we found in (2.33) that $h_+(t) = h_0\cos\phi(t)$ and $h_\times(t) = h_0\sin\phi(t)$, which can be easily generalized to the case where the orbital plane is inclined to the plane perpendicular to the line of sight. Denoting this inclination angle by ι, we find

$$h_+ = \frac{h_0}{2}\left(1+\cos^2\iota\right)\cos\phi(t)\,, \qquad h_\times = h_0\cos\iota\sin\phi(t)\,. \tag{2.39}$$

The detector response (2.38) then can be reduced to the form

$$h_{\text{resp}} = A(\theta, \varphi, \psi, \iota)\, h_0 \cos\left[\phi(t) + \phi_0(\theta, \varphi, \psi, \iota)\right] \ , \tag{2.40}$$

where the time-independent geometrical quantities A and Φ_0 can easily be deduced from (2.38) and (2.39), see [163] for explicit expressions.

2.3.2 Detector noise sources

As we have just sketched, a laser interferometer can in principle measure the GW strain by a phase shift of two destructively interfering laser beams. However, the signal is still extremely weak. For a GW amplitude $h \sim 10^{-21}$, the length change $L\,h$ in a km-size detector is of the order of 10^{-18} m, and although the light is sent back and forth multiple times between the input and the end test masses (Fig. 2.3) to extend the light path, the typical length change will still be of the order of $\sim 10^{-16}$. Many other physical effects can cause such small vibrations which then could be mistaken as a GW signal, and we shall review some of those noise sources below. We closely follow the overviews in [112, 163].

Seismic noise are ground vibrations caused by the cultural and natural environment. The detector, particularly the mirrors, have to be carefully shielded against these vibrations, which is achieved by suspending the optical elements from pendulums that act as mechanical filters above their own resonance frequency.

Thermal noise describes the thermal vibrations of the mirrors and their suspensions. The LIGO detectors are operated at room temperature, so the confusion by thermal fluctuations has to be reduced by using materials with a very high quality factor Q, i.e., the resonant vibrations are confined to a small band width.

Shot noise originates from the statistical nature of detecting light quanta at the photo detector. The number of arriving photons fluctuates, and the variance of this random process can be reduced by increasing the power of the laser beam. As the output power of a laser is limited technologically, power recycling mirrors are introduced to increase the power in the cavity.

Radiation pressure noise is the conjugated quantum noise to shot noise. When the laser power increases, the confusion due to momentum transfer to the mirrors increases as well. As we are interested in measuring a classical quantity (the GW) with a quantum field (light), however, there is the opportunity to reduce the uncertainty in one part of the quantum field at the cost of increasing it in a for our purposes nonsignificant part. This "squeezed light" [5] has been tested already in GEO600 [188] and will be incorporated in the advanced detectors.

Gravity gradient noise is caused by fluctuations of the Newtonian gravitational field both from man-made sources and the natural environment (seismic waves, changes in the air density etc.). The detector cannot be shielded from this noise (apart from the choice of the location), and although it did not affect the initial detectors considerably, gravity gradient noise is expected to become the limiting factor at low frequency for more advanced detectors.

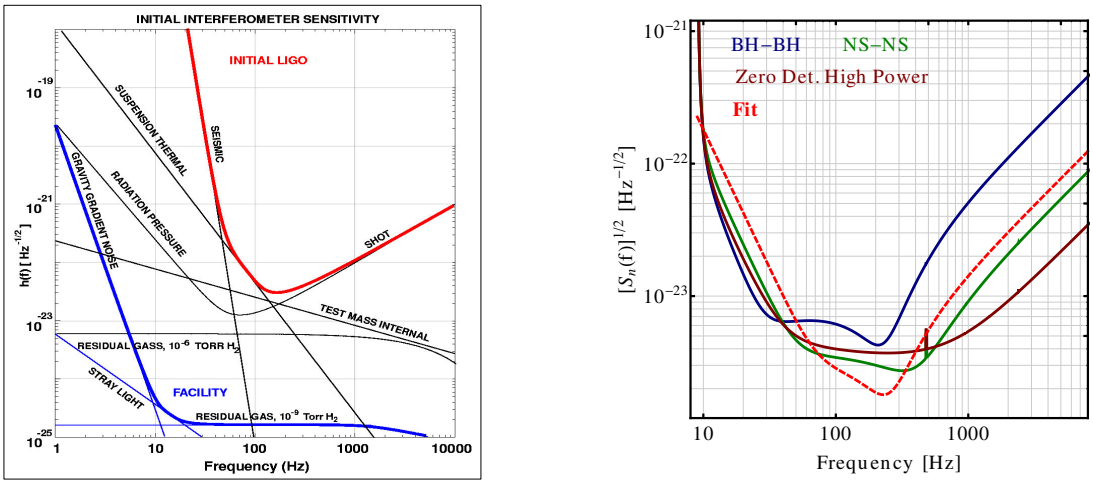

Figure 2.5: *Left panel:* Summary of typical noise sources in GW interferometers, here for initial LIGO. Figure adopted from [112]. *Right panel:* Anticipated noise curves of Advanced LIGO as detailed in [171] and the analytical formula from [15, 163]. "BH-BH" is a configuration optimized for detecting BH binaries with a total mass of $60M_\odot$, whereas "NS-NS" targets neutron star binaries with individual masses of $1.4M_\odot$. The "zero detuned, high power" configuration is the overall most sensitive setup.

There are many more sources of noise in the detectors and subtle details involved in dealing with them. The sum of all noise contributions defines the sensitivity of the interferometer, and the left panel of Fig. 2.5 provides a summary for the initial LIGO detector. Advanced LIGO will considerably improve upon this, and since one main motivation of the work presented in this thesis is to prepare for the advanced detector era, we shall in the following calculations assume a noise curve $S_n(f)$ for Advanced LIGO. Reference [171] provides anticipated shapes for several detector configurations, and we show some of them in the right panel of Fig. 2.5 together with an analytical fit that was made before the these data were available. This fit reads [15, 163]

$$S_n(f) = 10^{-49}\left(\hat{f}^{-4.14} - \frac{5}{\hat{f}^2} + 111\,\frac{1-\hat{f}^2+\hat{f}^4/2}{1+\hat{f}^2/2}\right), \tag{2.41}$$

with $\hat{f} = f/215\,\mathrm{Hz}$. We shall show in the next section, how this quantity enters the search for GWs in detector data. To be consistent with earlier work [15, 102, 104, 107, 162] we will mostly stick to the analytical fit (2.41) in our calculations, and although the numbers we shall present depend on this choice, the order of magnitude and conclusions based on relative changes of the computed quantity are fairly robust with respect the details of the noise curve. Furthermore, all of these predictions are idealized estimates of the detector performance, and working with real data involves additional difficulties that go beyond the ambiguity of our choice of $S_n(f)$ in theoretical studies.

2.3.3 Matched-filter search for compact binaries

As we have just outlined, the data stream $s(t)$ that is taken by the detector is corrupted by various noise sources, and the problem of actually detecting a GW signal in $s(t)$ essentially becomes a statement about the statistical significance of hypotheses. Particularly for signals

from inspiraling compact objects such as BHs or neutron stars, the theoretical knowledge of the GW signature can be used to test the hypothesis $\mathscr{H}_1$: the signal $h(\boldsymbol{\lambda})$ is buried in the noisy data stream, against the null hypothesis $\mathscr{H}_0$: there is no signal present. Here we introduced the vector $\boldsymbol{\lambda}$ to collect all parameters of the waveform model h.

Through different ways (see, e.g., [114]), one can argue that the optimal way to decide whether one should accept or reject $\mathscr{H}_1$ is to look at the *likelihood ratio*

$$\Lambda = \frac{P(\mathscr{H}_1|s)}{P(\mathscr{H}_0|s)} \,, \tag{2.42}$$

where $P(\mathscr{H}|s)$ is the probability that $\mathscr{H}$ is true given that the data s was measured. The *Neyman-Pearson* criterion is to accept $\mathscr{H}_1$ if Λ exceeds some pre-defined threshold. This threshold is based on fixing a tolerated *false alarm probability* (i.e., a detection is declared although no signal was present), and the Neyman-Pearson criterion ensures that the test has a maximal probability of detection (or minimal false dismissal probability).

Let us now write the data stream as a linear superposition of the noise $n(t)$ and, if present, a GW signal h_0,

$$s(t) = n(t) + h_0(t) \,. \tag{2.43}$$

Assuming n is *stationary Gaussian noise* with zero mean, we can find explicit expressions for the probability of a particular realization. Before we express the result in a convenient way, we have to introduce the *Fourier transform* of any function $x(t)$ as

$$\tilde{x}(f) = \int_{-\infty}^{\infty} x(t)\, e^{2\pi i t f}\, dt \,. \tag{2.44}$$

It turns out, that the *noise spectral density* $S_n(f)$ that we have already seen in Fig. 2.5 is related to the Fourier transform of the noise autocorrelation by

$$\overline{\tilde{n}(f)\, \tilde{n}^*(f')} = \frac{1}{2} S_n(|f|)\, \delta(f - f') \,, \tag{2.45}$$

where the overline indicates the expectation value, * denotes the complex conjugation and $\delta(f - f')$ is the δ-distribution. As outlined for instance in [88], expressing the probability of a particular Gaussian noise realization naturally leads to

$$\Lambda = \frac{e^{-\langle s-h(\boldsymbol{\lambda}), s-h(\boldsymbol{\lambda})\rangle/2}}{e^{-\langle s,s\rangle/2}} \tag{2.46}$$

with the inner product defined by

$$\langle s, h\rangle = 4\,\mathrm{Re} \int_0^{\infty} \frac{\tilde{s}(f)\, \tilde{h}^*(f)}{S_n(f)}\, df \,. \tag{2.47}$$

The results can be interpreted rather intuitively. The likelihood ratio (2.46) assesses whether $s - h(\boldsymbol{\lambda})$ or s alone are more likely realizations of stationary Gaussian noise with the specified spectrum. The inner product (2.47) can also be understood as an optimal linear filter of the data that maximizes the correlation with the GW signal if h is indeed

present in s [163]. The integrand is weighted with the sensitivity of the detector such that $\overline{\langle n,n\rangle} = 1$, as we can see from (2.45). (Note that the factor 4 in (2.47) comes from the definition of the one-sided noise spectral density and the integration over positive frequencies instead of the entire real axis.)

We shall extensively use the inner product (2.47) in this thesis to quantity the agreement of different waveforms. It is therefore beneficial to elaborate on its applications in data-analysis search strategies. Let us assume that the data indeed includes the GW signal h_0 as in (2.43). The logarithm of the likelihood ration (2.46) reads

$$\begin{aligned}\ln\Lambda &= -\frac{1}{2}\big\langle s-h(\boldsymbol{\lambda}), s-h(\boldsymbol{\lambda})\big\rangle + \big\langle s,s\big\rangle \\ &= \big\langle s,h(\boldsymbol{\lambda})\big\rangle - \frac{1}{2}\big\langle h(\boldsymbol{\lambda}),h(\boldsymbol{\lambda})\big\rangle \longrightarrow \big\langle h_0,h(\boldsymbol{\lambda})\big\rangle - \frac{1}{2}\big\langle h(\boldsymbol{\lambda}),h(\boldsymbol{\lambda})\big\rangle\ . \end{aligned} \tag{2.48}$$

We have simply used the linearity of the inner product and the arrow indicates the transition to the expectation value, where all inner products of noise-independent quantities with n vanish.

According to the Neyman-Pearson criterion, we should set a threshold for Λ, or equivalently for $\ln\Lambda$ to decide whether $h(\boldsymbol{\lambda})$ is a possible candidate of a real GW signal. To understand the influence of h onto this detection claim, let us split the freedom in our template signal into its norm $\|h\| = \sqrt{\langle h,h\rangle}$ and the normalized waveform $\hat{h} = h/\|h\|$. It is easy to show that (2.48) is maximized if $\|h\| = \langle h_0,\hat{h}\rangle$. Inserting this into (2.48) yields

$$\max_{\|h\|}\ln\Lambda = \frac{1}{2}\left(\|h_0\|\big\langle\hat{h}_0,\hat{h}\big\rangle\right)^2\ . \tag{2.49}$$

We interpret (2.49) in the following way. The signal h_0 can only be detected, if $\ln\Lambda$ is large enough for *any* $h(\boldsymbol{\lambda})$ in our template bank, and assuming at least an optimal norm of the template led to (2.49). The value of this expression has two contributions: the *optimal signal-to-noise ratio* (SNR) $\rho = \|h_0\|$ and the normalized inner product, or *match*, between template and signal,

$$m[h_0,h(\boldsymbol{\lambda})] = \big\langle\hat{h}_0,\hat{h}(\boldsymbol{\lambda})\big\rangle = \frac{\big\langle h_0,h(\boldsymbol{\lambda})\big\rangle}{\|h_0\|\|h(\boldsymbol{\lambda})\|}, \qquad (-1\le m\le 1)\ . \tag{2.50}$$

No matter how bad the match is (unless it is exactly zero), if the signal is loud enough, i.e., $\|h_0\|$ is large enough, then we will detect it. However, very loud events are expected to occur extremely rarely with the current sensitivities of ground-based detectors, and the success of these instruments crucially depends on the ability to detect as many signals as possible, particularly close to the detection threshold (which is commonly given as $\rho\approx 8$). Therefore, good waveform models that resemble the true GW signals with a very high match are invaluable, and it is this understanding that forms the basic motivation for this thesis.

Let us introduce some more, closely related quantities. The *effectualness* of a template bank can be quantified by the best match over the entire family of waveform models. This fully optimized match is called the *fitting factor*, and it reads

$$\mathrm{FF} = \max_{\boldsymbol{\lambda}}\frac{\big\langle h_0,h(\boldsymbol{\lambda})\big\rangle}{\|h_0\|\|h(\boldsymbol{\lambda})\|}\ . \tag{2.51}$$

A fitting factor of unity is the ideal case, where the signal h_0 can be extracted from the data without any loss in SNR. For any FF < 1, (2.49) tells us that signals have to have an optimal SNR that is greater than the detection threshold by a factor of $1/\mathrm{FF}$ to still be detected. Thus, the deviation of the fitting factor from unity is a quantitative measure of how many signals are missed due to a not perfectly matching template bank. More specifically, we have seen in Sec. 2.2.2 that the GW amplitude, and with it the SNR, depends on $1/\text{distance}$. If the effectively detectable distance is reduced by a factor x, then the volume is reduced by x^3, and, assuming uniformly distributed sources, the number of detectable sources decreases similarly by a factor of x^3. With this in mind, we can interpret the fitting factor schematically as

$$\mathrm{FF} = \sqrt[3]{\frac{\text{detected signals}}{\text{ideally detectable signals}}}\,, \tag{2.52}$$

where we understand the denominator as the number of signals that could be detected with an exact waveform model. A commonly used criterion is to accept a maximal loss of 10% of the signals, which demands a fitting factor not less than $\sqrt[3]{0.9} \approx 0.965$.

Having an effectual template bank does not ensure that the parameters of the source are extracted accurately. Again, we have two effects that may spoil the *parameter estimation* accuracy. First, even if the waveform templates are perfect and there is indeed a set of parameters with $h(\boldsymbol{\lambda}_0) = h_0$, the presence of noise can confuse the estimate, and the 'best-fitting' parameters $\bar{\boldsymbol{\lambda}}$ that maximize (2.51) not necessarily coincide with $\boldsymbol{\lambda}_0$. The typical *bias* $\bar{\boldsymbol{\lambda}} - \boldsymbol{\lambda}_0$ can be estimated in the high SNR regime within the *Fisher-matrix* approach. We simplify refer to [190] and Sec. 4.6 for more details, and give the final result here:

$$\left(\bar{\lambda}^i - \lambda_0^i\right)_{\text{stat.}} = \sqrt{\Gamma^{-1}_{ii}} \qquad \text{with } \Gamma_{ij} = \left\langle \frac{\partial h}{\partial \lambda^i}(\boldsymbol{\lambda}_0), \frac{\partial h}{\partial \lambda^j}(\boldsymbol{\lambda}_0) \right\rangle\,. \tag{2.53}$$

The inner product of the first derivatives is called the Fisher-information matrix Γ_{ij}, and its inverse provides the statistical parameter biases on the diagonal, as well as the correlation between the parameters in the other components.

The *systematic biases*, on the other hand, are due to the fact that the template waveforms generally do not represent the real signal h_0 perfectly, and deviations in the waveform model lead to a misinterpretation of the parameters. Under the same assumptions as before, i.e., to linear order, these errors can be estimated by [69, 90]

$$\left(\bar{\lambda}^i - \lambda_0^i\right)_{\text{sys.}} = (\Gamma^{-1}[\bar{\boldsymbol{\lambda}}])^{ij} \left\langle \frac{\partial h}{\partial \lambda^j}(\bar{\boldsymbol{\lambda}}), \delta h \right\rangle\,, \tag{2.54}$$

where δh accounts for the difference between the template models and the true waveform. The total parameter error is simply the sum of statistical and systematic bias.

Note that Γ_{ij} scales quadratically with the SNR, so the statistical bias (2.53) drops linearly with increasing SNR of the signal. In contrast, the model-induced systematic bias (2.54) is independent of the SNR, and for sufficiently strong signals, these will be the dominant source of error. A sufficient (but not necessary) condition, that the systematic errors are smaller than the statistical errors is that the waveform difference δh is below the

noise level. Thus, if

$$\|\delta h\| < 1 \tag{2.55}$$

the difference between target and model signal is *indistinguishable* by the detector [125]. Recently [82], it was argued that the model-induced uncertainty should be reduced even below this level to

$$\|\delta h\| < \epsilon^2 \,, \tag{2.56}$$

with $\epsilon \lesssim 1/2$. Often, demanding $\mathrm{FF} > \mathrm{FF}_{\mathrm{min}}$ (for suitably high $\mathrm{FF}_{\mathrm{min}}$) is associated with the effectualness of a waveform family for detection, whereas if (2.55) or (2.56) are satisfied, the templates are sometimes referred to as *faithful*. Here, however, we want to understand faithfulness as having a sufficiently small systematic bias, as it was originally introduced in [73].

While the strategy we presented here is optimal for stationary Gaussian noise, we have to keep in mind that real detector data mostly do not fulfill this assumption, and glitches are an additional source of confusion that has to be excluded by other techniques, such as a set of vetoes, χ^2-tests and sophisticated estimates of the background noise. See [17] for a detailed discussion of the algorithm employed by the LIGO Scientific Collaboration [183].

2.3.4 Implementation of the overlap

As the inner product is the main tool in this thesis to make quantitative statements about the quality of waveform models, we devote this short section to lay out explicitly how we calculate variants of it efficiently.

One simplification we always employ is to leave the specification of a particular sky location and the construction of the detector response (2.38) aside and only consider h_+ and $h_\times$. We can do so, because given the GW polarizations for a particular binary system, we can always construct the detector response for arbitrary sky locations with (2.38). Our goal to produce accurate waveform templates is therefore independent of the orientation and position of the source and detector.

In addition, note that the inner product (2.47) is most conveniently formulated in terms of the Fourier-domain representations of h_+ and $h_\times$, and since they are real-valued functions of the time, their Fourier transforms satisfy $\tilde{h}_{+/\times}(-f) = \tilde{h}^*_{+/\times}(f)$. Thus, the nonnegative frequencies alone define the waveform polarizations. We can manifestly confine the information to only those frequencies by dealing with a particular complex combination of h_+ and $h_\times$,

$$h = h_+ - i\, h_\times \,. \tag{2.57}$$

Often, we shall refer to h simply as the GW signal. We have learnt in Sec. 2.2.2 that the signal of a binary-BH system is characterized by $h_+ = A\cos\phi$ and $h_\times = A\sin\phi$, where both A and ϕ may be time-dependent functions. When we now expand these expressions into the complex form

$$h_+ = \frac{A}{2}\left(e^{i\phi} + e^{-i\phi}\right) \,, \qquad\qquad h_\times = -i\frac{A}{2}\left(e^{i\phi} - e^{-i\phi}\right) \tag{2.58}$$

$$\Rightarrow \quad h = A\, e^{-i\phi} \,, \tag{2.59}$$

we find that the Fourier spectrum of h consists of only "half" of the spectrum of both h_+ and $h_\times$. We do not lose information, however, as we can reconstruct the time-domain polarizations simply through (2.57), and their Fourier transforms are given by

$$\tilde{h}_+(f) = \frac{\tilde{h}(f) + \tilde{h}^*(-f)}{2} \,, \qquad\qquad \tilde{h}_\times(f) = \frac{\tilde{h}^*(-f) - \tilde{h}(f)}{2i} \,. \tag{2.60}$$

Considering h instead of individual polarizations has another advantage when calculating the inner product of two such combinations h_1 and h_2. In most applications, we are not interested in a particular time or phase scale of the waveform, i.e., signals that are equal except for an overall shift in time or phase are considered the same. The natural way to compare them is therefore the inner product, maximized over time and phase shifts, and this quantity is commonly called the *overlap*

$$\mathcal{O}(h_1, h_2) = \max_{t_0, \phi_0} \frac{4}{\|h_1\| \|h_2\|} \,\mathrm{Re} \int_0^\infty \frac{\tilde{h}_1(f)\, \tilde{h}_2^*(f)}{S_n(f)}\, e^{i(2\pi t_0 f + \phi_0)}\, df \,. \tag{2.61}$$

We have explicitly written out the effect of a relative time and phase shift in (2.61), and we can now perform the maximization simply in two steps.

1. For any value of t_0, the phase shift that maximizes the real part of the integral is the one that rotates the complex number on the real axis. Thus, maximizing with respect to ϕ_0 is equivalent to taking the magnitude of the complex number.
2. The remaining freedom in t_0 can be expressed by the inverse Fourier transform $\mathscr{F}^{-1}$, so that (2.61) becomes

$$\mathcal{O}(h_1, h_2) = \frac{4}{\|h_1\| \|h_2\|} \max_{t_0} \left| \mathscr{F}^{-1} \left[\frac{\tilde{h}_1 \tilde{h}_2^*}{S_n} \right] (t_0) \right| \,. \tag{2.62}$$

This is a computationally very useful interpretation, as there are very fast algorithms to calculate the inverse Fourier transform numerically for large arrays of possible time shifts.

Let us conclude this section with some comments on the numerical fast Fourier transform (FFT). Although this is a very well understood and vastly applied technique, it is useful to recall some properties of the discretization in order to avoid spending computer resources unnecessarily on too fine grids while increasing the resolution might be essential in other regimes. Consider the example of a numerically calculated GW h of a coalescing BH binary. As we shall show later in this thesis, the Fourier spectrum is dropped by several orders of magnitude for frequencies above $Mf \approx 0.2$. If the signal actually had a compact support in the frequency domain in $f \in [-f_N, f_N]$ (f_N is called the Nyquist frequency), we could represent it *exactly* through a sinc-interpolation of discrete points sampled at

$$\Delta t = \frac{1}{2 f_N} \,. \tag{2.63}$$

However, this also implies that the time-domain signal cannot have compact support (see, e.g., [98]). Here we usually deal with simulated signals of finite length that, conversely,

cannot have a compact support in the Fourier domain, so the above statement is not applicable exactly. If we sample the data nevertheless according to (2.63), frequencies $|f| > f_N$ are *aliased* into the interval $[-f_N, f_N]$. If their contribution, however, is small, we may still accept the discrete Fourier transform as an accurate representation of the signal. For our example of a typical signal from a BH binary, we could approximate $Mf_N \approx 0.2$ which leads to time steps of $\Delta t/M = 2.5$.

This result might be surprising as, for instance, numerical codes need a much higher timing accuracy to predict the GW signal correctly. One should, however, keep in mind that the *post processing* of the waveforms often requires much less data points. Indeed, we can check that the Fourier transform of a typical numerical waveform, sampled for example at $\Delta t/M = 0.144$ differs from the FFT of the same waveform with a 15 times sparser sampling only by a relative factor of $< 0.2\%$, which is much less than the numerical error of the original waveform. One source of confusion sometimes stems from the calculation of the overlap (2.61), which often requires a very fine sampling of the inverse FFT (see for instance [12]). However, we can achieve the required accuracy either by sampling the original time-domain waveforms accordingly dense, which can be very time consuming in large parameter studies; or we calculate $\tilde{h}$ efficiently with a lower sampling rate and then *interpolate* later by simply adding a long null stream to the FFT. This interpolation is fast and very accurate as long as we approximately fulfill the above discussed condition that the spectrum of $\tilde{h}$ is confined to the properly calculated frequency range.

2.4 Post-Newtonian waveform models for coalescing compact binaries

After a detailed motivation why we need good models of the gravitational radiation emitted by astrophysically relevant systems, we shall now outline how such models can be obtained. The focus lies on signals from *coalescing binary BHs* as they constitute one of the most promising sources of a first direct detection of GWs. In addition, the analytical treatment that we shall present in this section generally applies to *compact objects* including neutron stars (without, however, taking tidal effects into account that have also been calculated [78, 79, 89, 111, 191]).

2.4.1 Energy and flux

Let us start with the compact binary on a circular orbit that we calculated at the end of Sec. 2.2.2. We have seen that the signal satisfies the form

$$h(t) = \frac{4M\eta v^2}{R}\, e^{-i(2\omega_{\rm orb}t+\phi_0)}\,, \tag{2.64}$$

where v is the velocity, M is the total mass of the system, η is the symmetric mass ratio, R is the distance between source and observer and $\omega_{\rm orb}$ is the orbital angular frequency. The Newtonian energy of this circular movement is given by

$$E = -\frac{M\eta}{2}\, v^2\,. \tag{2.65}$$

Of course, locally defining an energy is difficult in General Relativity, because it has to be extracted from the curved spacetime itself, and there is no unambiguous way to separate it from some "background" metric. Here, however, we introduced the GW as a small perturbation of the Minkowski spacetime, and pursuing this strategy, we can construct an equivalent of the GW's energy-momentum tensor from second-order terms in $h_{\mu\nu}$ [66, 167, 192]. This also enables us to define the *flux* of energy that is radiated away from the source through GWs. Averaged over all directions and extracted at infinite distance from the source, it reads [147]

$$\frac{dE}{dt} = -\mathscr{L} \tag{2.66}$$
$$\text{with} \quad \mathscr{L} = \frac{1}{5}\overline{\frac{d^3Q^{jk}}{dt^3}\frac{d^3Q_{jk}}{dt^3}} \quad \text{and} \quad Q_{jk}(t) = \int \rho(t,x^i)\left(x_j x_k - \frac{1}{3}\delta_{jk}x^l x_l\right) d^3x \ .$$

Here, $\mathscr{L}$ abbreviates the total *luminosity*, ρ is the mass distribution and δ_{ij} is the Kronecker symbol. For our example of two point particles on a circular orbit, we find

$$\mathscr{L} = \frac{32\eta^2}{5}\,v^{10} \ . \tag{2.67}$$

The *post-Newtonian* (PN) approximation provides an elaborate extension of these quantities by expanding the metric and derived quantities in terms of the small parameter v/c [38] (note that we use units with $c = 1$, so v itself can be interpreted as the expansion parameter). We shall collect the explicit expressions below, restricting ourselves to the systems we study in detail throughout this thesis: BH binaries with spins aligned to the orbital angular momentum $\boldsymbol{L}$. Although this does not capture the entire parameter space (we do not consider precessing spins except in Sec. 3.4.4), modeling aligned spins is the natural extension of nonspinning models, and recent studies [10, 16] indicate that the inclusion of this dominant spin effect already allows for the detection of a large fraction of generic systems.

The binary systems we consider are defined by the masses of the BHs, denoted by m_i, and the individual spins $\boldsymbol{S}_i$ $(i = 1, 2)$. In agreement with previously used definitions, let us summarize the notation we employ:

$$\begin{aligned} M &= m_1 + m_2 \ , & \eta &= \frac{m_1 m_2}{M^2} \ , \\ \delta &= \frac{m_1 - m_2}{M} \ , & \chi_i &= \frac{\boldsymbol{S}_i \cdot \boldsymbol{L}}{\|\boldsymbol{L}\| m_i^2} \\ \chi_s &= \frac{\chi_1 + \chi_2}{2} & \chi_a &= \frac{\chi_1 - \chi_2}{2} \ . \end{aligned} \tag{2.68}$$

The energy is currently determined up to 3PN order, i.e., the expansion is carried out up to v^6-corrections above the leading order. The form we show here is derived for quasi-circular orbits, and the explicit expressions can be found for instance in [38, 41, 53, 76] and references therein. We closely follow the presentation of [13]. Leading-order and next-to-leading order spin-orbit effects [20, 39, 118] are included as well as spin-spin effects that appear at relative 2PN order [70, 118, 133, 148]; note that the square terms in

the individual spins are valid only for BHs (and not, e.g., for neutron stars) as discussed in [53, 70, 148]. The energy reads

$$\begin{aligned} E(v) = -\frac{M\eta v^2}{2}\Bigg\{1 - v^2\left(\frac{3}{4}+\frac{\eta}{12}\right) + v^3\left[\frac{8\,\delta\chi_a}{3} + \left(\frac{8}{3}-\frac{4\eta}{3}\right)\chi_s\right] \\ + v^4\left[\frac{19\eta}{8} - 2\delta\chi_a\chi_s - \frac{\eta^2}{24} + (4\eta-1)\chi_a^2 - \chi_s^2 - \frac{27}{8}\right] \\ + v^5\left[\chi_a\left(8\,\delta - \frac{31\delta\eta}{9}\right) + \left(\frac{2\eta^2}{9} - \frac{121\eta}{9} + 8\right)\chi_s\right] \\ - v^6\left[\frac{35\eta^3}{5184} + \frac{155\eta^2}{96} - \left(\frac{34445}{576} - \frac{205\pi^2}{96}\right)\eta + \frac{675}{64}\right]\Bigg\}\,. \end{aligned} \tag{2.69}$$

The flux is determined up to 3.5PN order, and in addition to the spin effects listed above we add a 2.5PN correction that is due to the energy flow into the BHs, as calculated in [18]. The final result reads

$$\begin{aligned} \mathscr{L} = \frac{32}{5}\,\eta^2\,v^{10}\Bigg\{1 - v^2\left(\frac{1247}{336}+\frac{35}{12}\eta\right) + v^3\left[4\pi - \frac{11\delta\chi_a}{4} + \left(3\eta - \frac{11}{4}\right)\chi_s\right] \\ + v^4\left[\frac{33\delta\chi_a\chi_s}{8} + \frac{65\eta^2}{18} + \left(\frac{33}{16} - 8\eta\right)\chi_a^2 + \left(\frac{33}{16} - \frac{\eta}{4}\right)\chi_s^2 + \frac{9271\eta}{504} - \frac{44711}{9072}\right] \\ + v^5\Bigg[\left(\frac{701\delta\eta}{36} - \frac{59\delta}{16}\right)\chi_a + \left(\frac{227\eta}{9} - \frac{157\eta^2}{9} - \frac{59}{16}\right)\chi_s - \frac{583\pi\eta}{24} - \frac{8191\pi}{672} \\ - \frac{1-3\eta}{4}\,\chi_s\left(1+3\chi_s^2+9\chi_a^2\right) - \frac{1-\eta}{4}\,\delta\chi_a\left(1+3\chi_a^2+9\chi_s^2\right)\Bigg] \\ + v^6\Bigg[-\frac{1712}{105}\ln(4v) - \frac{1712\gamma}{105} - \frac{775\eta^3}{324} - \frac{94403\eta^2}{3024} + \left(\frac{41\pi^2}{48} - \frac{134543}{7776}\right)\eta \\ + \frac{16\pi^2}{3} + \frac{6643739519}{69854400}\Bigg] + v^7\left[\frac{193385\pi\eta^2}{3024} + \frac{214745\pi\eta}{1728} - \frac{16285\pi}{504}\right]\Bigg\}\,, \end{aligned} \tag{2.70}$$

where $\gamma \approx 0.5772$ is the Euler constant.

With these expressions for energy and flux, we can construct the inspiral phase of the GW by assuming that the energy changes slowly due to outgoing radiation. Several slightly different methods to obtain the phase evolution are discussed in the next sections.

2.4.2 Time-domain PN approximants

Starting from the energy-balance law (2.66) we can solve for the time evolution of the expansion parameter $v(t)$, assuming that the system evolves as an adiabatic sequence of quasi-circular orbits with instantaneous energy (2.69) and flux (2.70). A simple application of the chain rule yields

$$\frac{dE}{dt} = \frac{dE}{dv}\,\frac{dv}{dt} \overset{(2.66)}{=} -\mathscr{L}(v)$$

$$\Rightarrow \quad \frac{dv}{dt} = -\frac{\mathscr{L}(v)}{dE(v)/dv} \,. \tag{2.71}$$

The phase evolution of the binary is given by the integral of the orbital frequency $\omega_{\rm orb}$

$$\phi_{\rm orb} = \int \omega_{\rm orb}\, dt \,, \qquad\qquad M\omega_{\rm orb} = v^3 \,. \tag{2.72}$$

There are various ways to solve these equations, and each strategy defines a particular PN approximant. The *TaylorT1* approximant, for example, is obtained by numerically integrating (2.71) and (2.72) in consideration of (2.70) and the derivative of (2.69).

We can also construct the inverse of (2.71) and re-expand $(dE/dv)/\mathscr{L}$ in terms of v to 3.5PN order. This has the advantage that we can now analytically integrate $t(v)$, and the resulting *TaylorT2* approximant reads

$$\begin{aligned}
t(v) = t_0 - \frac{5M}{256\eta\, v^8}\Bigg\{ & 1 + v^2\left[\frac{11\eta}{3} + \frac{743}{252}\right] + v^3\left[-\frac{32\pi}{5} + \frac{226\delta\chi_a}{15} + \left(\frac{226}{15} - \frac{152\eta}{15}\right)\chi_s\right] \\
& + v^4\left[\frac{3058673}{508032} + \frac{5429\eta}{504} + \frac{617\eta^2}{72} - \frac{81}{4}\delta\chi_a\chi_s - \left(\frac{81}{8} - \frac{\eta}{2}\right)\chi_s^2 - \left(\frac{81}{8} - 40\eta\right)\chi_a^2\right] \\
& + v^5\left[-\frac{7729\pi}{252} - \frac{13\pi\eta}{3} + \left(\frac{147101}{756} - \frac{4906\eta}{27} - \frac{68\eta^2}{3}\right)\chi_s + \left(\frac{147101}{756} + \frac{26\eta}{3}\right)\delta\chi_a \right. \\
& \left. \quad + (6-6\eta)\delta\chi_s^2\chi_a + (6-18\eta)\chi_s\chi_a^2 + (2-6\eta)\chi_s^3 + (2-2\eta)\delta\chi_a^3\right] \\
& + v^6\left[\frac{6848\gamma}{105} - \frac{10052469856691}{23471078400} + \frac{128\pi^2}{3} + \left(\frac{3147553127}{3048192} - \frac{451\pi^2}{12}\right)\eta - \frac{15211\eta^2}{1728}\right. \\
& \quad + \frac{25565\eta^3}{1296} + \frac{6848\ln(4v)}{105} - \left(\frac{584\pi}{3} - \frac{448\pi\eta}{3}\right)\chi_s - \frac{584\pi\delta\,\chi_a}{3} \\
& \quad + \left(\frac{6845}{672} - \frac{43427\eta}{168} + \frac{245\eta^2}{3}\right)\chi_s^2 + \left(\frac{6845}{672} - \frac{1541\eta}{12} + \frac{964\eta^2}{3}\right)\chi_a^2 \\
& \quad \left. + \left(\frac{6845}{336} - \frac{2077\eta}{6}\right)\delta\,\chi_s\chi_a\right] + v^7\left[-\frac{15419335\pi}{127008} - \frac{75703\pi\eta}{756} + \frac{14809\pi\eta^2}{378}\right. \\
& \quad + \left(\frac{4074790483}{1524096} + \frac{30187\eta}{112} - \frac{115739\eta^2}{216}\right)\delta\,\chi_a \\
& \quad + \left(\frac{4074790483}{1524096} - \frac{869712071\eta}{381024} - \frac{2237903\eta^2}{1512} + \frac{14341\eta^3}{54}\right)\chi_s \\
& \quad + (228\pi - 16\pi\eta)\,\chi_s^2 + (228\pi - 896\pi\eta)\,\chi_a^2 + 456\pi\delta\,\chi_s\chi_a - \\
& \quad \left(\frac{3237}{14} - \frac{14929\eta}{84} + \frac{362\eta^2}{3}\right)\chi_s^3 - \left(\frac{3237}{14} - \frac{87455\eta}{84} + 34\eta^2\right)\delta\chi_a^3 \\
& \quad \left. - \left(\frac{9711}{14} - \frac{39625\eta}{84} + 102\eta^2\right)\delta\,\chi_s^2\chi_a - \left(\frac{9711}{14} - \frac{267527\eta}{84} + \frac{3574\eta^2}{3}\right)\chi_s\chi_a^2\right]\Bigg\} \,.
\end{aligned} \tag{2.73}$$

Note that the formal re-expansion also yields contributions to higher orders than those in (2.73). However, since 4PN and higher terms in flux and energy are not fully determined, the expressions one could compute are incomplete. The same applies to spin contributions at relative orders higher than 2.5PN. However, we decided to keep those incomplete contributions, and we shall discuss implications of that in Sec. 3.2.

The TaylorT2 approximant is completed by calculating the phase in a similar way. We

use

$$\frac{d\phi_{\rm orb}}{dv} = \frac{v^3}{M}\frac{dt}{dv} \tag{2.74}$$

and expand the right-hand side. The analytical integration yields

$$\begin{aligned}
\phi_{\rm orb}(v) = \phi_0^{\rm orb} - \frac{1}{32\eta v^5}\Bigg\{ & 1 + v^2\left[\frac{3715}{1008} + \frac{55\eta}{12}\right] + v^3\left[-10\pi + \frac{565\delta\chi_a}{24} + \left(\frac{565}{24} - \frac{95\eta}{6}\right)\chi_s\right] \\
& + v^4\left[\frac{15293365}{1016064} + \frac{27145\eta}{1008} + \frac{3085\eta^2}{144} - \frac{405}{8}\delta\,\chi_a\chi_s - \left(\frac{405}{16} - \frac{5\eta}{4}\right)\chi_s^2 - \left(\frac{405}{16} - 100\eta\right)\chi_a^2\right] \\
& + v^5\ln v\left[\frac{38645\pi}{672} - \frac{65\pi\eta}{8} - \left(\frac{735505}{2016} - \frac{12265\eta}{36} - \frac{85\eta^2}{2}\right)\chi_s - \left(\frac{735505}{2016} + \frac{65\eta}{4}\right)\delta\chi_a\right. \\
& \left. - \left(\frac{45}{4} - \frac{45\eta}{4}\right)\delta\chi_s^2\chi_a - \left(\frac{45}{4} - \frac{135\eta}{4}\right)\chi_s\chi_a^2 - \left(\frac{15}{4} - \frac{45\eta}{4}\right)\chi_s^3 - \left(\frac{15}{4} - \frac{15\eta}{4}\right)\delta\chi_a^3\right] \\
& + v^6\left[\frac{12348611926451}{18776862720} - \frac{1712\gamma}{21} - \frac{160\pi^2}{3} - \left(\frac{15737765635}{12192768} - \frac{2255\pi^2}{48}\right)\eta + \frac{76055\eta^2}{6912}\right. \\
& - \frac{127825\eta^3}{5184} - \frac{1712\ln(4v)}{21} + \left(\frac{730\pi}{3} - \frac{560\pi\eta}{3}\right)\chi_s - \left(\frac{34225}{2688} - \frac{217135\eta}{672} + \frac{1225\eta^2}{12}\right)\chi_s^2 \\
& \left. + \frac{730\pi\delta\chi_a}{3} - \left(\frac{34225}{2688} - \frac{7705\eta}{48} + \frac{1205\eta^2}{3}\right)\chi_a^2 - \left(\frac{34225}{1344} - \frac{10385\eta}{24}\right)\delta\,\chi_s\chi_a\right] \\
& + v^7\left[\frac{77096675\pi}{2032128} + \frac{378515\pi\eta}{12096} - \frac{74045\pi\eta^2}{6048} - \left(\frac{20373952415}{24385536} + \frac{150935\eta}{1792} - \frac{578695\eta^2}{3456}\right)\delta\chi_a\right. \\
& - \left(\frac{20373952415}{24385536} - \frac{4348560355\eta}{6096384} - \frac{11189515\eta^2}{24192} + \frac{71705\eta^3}{864}\right)\chi_s - \left(\frac{285\pi}{4} - 5\pi\eta\right)\chi_s^2 \\
& - \left(\frac{285\pi}{4} - 280\pi\eta\right)\chi_a^2 - \frac{285\pi}{2}\delta\,\chi_s\chi_a + \left(\frac{16185}{224} - \frac{74645\eta}{1344} + \frac{905\eta^2}{24}\right)\chi_s^3 \\
& + \left(\frac{16185}{224} - \frac{437275\eta}{1344} + \frac{85\eta^2}{8}\right)\delta\chi_a^3 + \left(\frac{48555}{224} - \frac{198125\eta}{1344} + \frac{255\eta^2}{8}\right)\delta\,\chi_s^2\chi_a \\
& \left. + \left(\frac{48555}{224} - \frac{1337635\eta}{1344} + \frac{8935\eta^2}{24}\right)\chi_s\chi_a^2\right]\Bigg\}.
\end{aligned} \tag{2.75}$$

Both $t(v)$ and $\phi_{\rm orb}(v)$ together define $\phi_{\rm orb}(t)$ implicitly.

The *TaylorT3* approximant is derived from the TaylorT2 expressions by inverting the Taylor series $t(v)$ analytically and plugging $v(t)$ into (2.75). The final result can be written as an closed-form Taylor expansion $\phi_{\rm orb}(t)$. Since we never employ this approximant in this thesis, we omit the explicit expressions here and refer to the literature [48, 58].

The *TaylorT4* approximant goes back to the energy-balance law (2.66) and re-expands the right-hand side in terms of v. The resulting differential equation is truncated at the appropriate PN order (3.5PN), and it reads

$$\begin{aligned}
\frac{dv}{dt} = \frac{32\eta}{5M}v^9\Bigg\{ & 1 - v^2\left[\frac{11\eta}{4} + \frac{743}{336}\right] + v^3\left[4\pi - \frac{113\delta\chi_a}{12} + \left(\frac{19\eta}{3} - \frac{113}{12}\right)\chi_s\right] \\
& + v^4\left[\frac{81\delta\chi_a\chi_s}{8} + \frac{59\eta^2}{18} + \left(\frac{81}{16} - 20\eta\right)\chi_a^2 + \left(\frac{81}{16} - \frac{\eta}{4}\right)\chi_s^2 + \frac{13661\eta}{2016} + \frac{34103}{18144}\right] \\
& + v^5\left[\left(\frac{3\eta}{4} - \frac{3}{4}\right)\delta\chi_a^3 + \left(\frac{9\eta}{4} - \frac{9}{4}\right)\delta\chi_a\chi_s^2 + \left(\frac{1165\eta}{24} - \frac{31571}{1008}\right)\delta\chi_a - \frac{189\pi\eta}{8} - \frac{4159\pi}{672}\right. \\
& \left. + \left(\frac{27\eta\chi_a^2}{4} - \frac{9\chi_a^2}{4} - \frac{79\eta^2}{3} + \frac{5791\eta}{63} - \frac{31571}{1008}\right)\chi_s + \left(\frac{9\eta}{4} - \frac{3}{4}\right)\chi_s^3\right]
\end{aligned} \tag{2.76}$$

$$
\begin{aligned}
&+\nu^6\left[\frac{16447322263}{139708800}+\frac{16\pi^2}{3}-\frac{1712\gamma}{105}-\frac{5605\eta^3}{2592}+\frac{541\eta^2}{896}+\left(\frac{451\pi^2}{48}-\frac{56198689}{217728}\right)\eta\right.\\
&-\frac{1712\ln(4v)}{105}+\left(\frac{1517\eta^2}{72}-\frac{23441\eta}{288}+\frac{128495}{2016}\right)\chi_s^2+\left(\frac{565\delta^2}{9}+\frac{89\eta^2}{3}-\frac{2435\eta}{224}+\frac{215}{224}\right)\chi_a^2\\
&\left.+\left(\frac{128495\delta}{1008}-\frac{12733\delta\eta}{144}\right)\chi_a\chi_s+\left(\frac{40\pi\eta}{3}-\frac{80\pi}{3}\right)\chi_s-\frac{80\pi\delta\chi_a}{3}\right]\\
&+\nu^7\left[\frac{91495\pi\eta^2}{1512}+\frac{358675\pi\eta}{6048}-\frac{4415\pi}{4032}-\left(\frac{11\eta^2}{24}-\frac{979\eta}{24}+\frac{505}{8}\right)\chi_s^3\right.\\
&+\left(\frac{\delta\eta^2}{8}+\frac{742\delta\eta}{3}-\frac{505\delta}{8}\right)\chi_a^3+\left(\frac{3\eta^2}{8}+\frac{917\eta}{12}-\frac{1515}{8}\right)\delta\chi_a\chi_s^2+12\pi\chi_s^2\\
&+\left(\frac{7007\eta}{24}-124\delta^2-\frac{3397\eta^2}{24}+-\frac{523}{8}\right)\chi_s\chi_a^2+(12\pi-48\pi\eta)\,\chi_a^2\\
&+\left(\frac{2045\eta^3}{216}-\frac{398017\eta^2}{2016}+\frac{10772921\eta}{54432}-\frac{2529407}{27216}\right)\chi_s+24\pi\delta\chi_a\chi_s\\
&\left.\left.+\left(\frac{845827\delta\eta}{6048}-\frac{41551\delta\eta^2}{864}-\frac{2529407\delta}{27216}\right)\chi_a\right]\right\}.
\end{aligned}
$$

The equations (2.76) and (2.72) are then integrated numerically.

2.4.3 PN strain and spherical harmonics

Having calculated $\phi_{\rm orb}(t)$ and $v(t)$ with any PN approximant, we can express the corresponding quadrupole GW strain as

$$h(t)=A(t)\,e^{-i2\phi_{\rm orb}(t)}\,, \tag{2.77}$$

where the amplitude $A(t)$ is given, to lowest order, by $A(t)=4M\eta v^2(t)/R$, see (2.33). Higher-order corrections to (2.77) have been calculated in [24, 42], and with the connection to numerical waveforms in mind, we shall use the decomposition of these expansions in terms of *spin-weighted spherical harmonics*.

Specifically, we introduce basis functions on the sphere ${}_sY^{\ell m}$ that depend on the standard spherical coordinates (θ,φ). These spherical harmonics with spin weight s are defined as [93]

$${}_{-s}Y^{\ell m}(\theta,\varphi)=(-1)^s\sqrt{\frac{2\ell+1}{4\pi}}d^{\ell}_{ms}(\theta)\,e^{im\varphi}\,, \tag{2.78}$$

where d^{ℓ}_{ms} is the Wigner matrix. The GW can now be expanded in terms of these spherical harmonics (with spin weight -2), i.e.,

$$h(t;\theta,\varphi)=\sum_{\ell=2}^{\infty}\sum_{m=-\ell}^{\ell}h^{\ell m}(t)\,{}_{-2}Y^{\ell m}(\theta,\varphi)\,. \tag{2.79}$$

The quantity $h(t;\theta,\varphi)$ is very similar to the detector response (2.38), only that here it is still a combination of h_+ and $h_\times$ as the real and imaginary part, respectively. Let us illustrate this explicitly. At leading order, we find

$$h(t;\theta,\varphi)=h^{22}(t)\,{}_{-2}Y^{22}(\theta,\varphi)+h^{2-2}(t)\,{}_{-2}Y^{2-2}(\theta,\varphi) \tag{2.80}$$

with $h^{22} = A^{22}\exp(-2i\phi_{\rm orb})$, $h^{2-2} = (h^{22})^*$ and

$$ {}_{-2}Y^{22} = \sqrt{\frac{5}{64\pi}}\,(1+\cos\theta)^2\; e^{2i\varphi} \;, \quad {}_{-2}Y^{2-2} = \sqrt{\frac{5}{64\pi}}\,(1-\cos\theta)^2\; e^{-2i\varphi} \;. \tag{2.81} $$

Combing the expressions above we can expand (2.80) to

$$ h(t;\theta,\varphi) = \underbrace{A^{22}\sqrt{\frac{5}{4\pi}}\frac{\left(1+\cos^2\theta\right)}{2}\cos(2\phi_{\rm orb}-2\varphi)}_{\simeq F_+(\theta,\varphi,0)\,h_+(t)} \underbrace{-iA^{22}\sqrt{\frac{5}{4\pi}}\cos\theta\sin(2\phi_{\rm orb}-2\varphi)}_{\simeq F_\times(\theta,\varphi,0)\,h_\times(t)} , $$

which is nothing but the complex equivalent of (2.38). By comparing to (2.77) we also find the leading-order amplitude

$$ A^{22} = \sqrt{\frac{64\pi}{5}}\,\frac{M\eta v^2}{R} \;. \tag{2.82} $$

Incorporating higher PN expansion orders extends the amplitude A^{22} to a Taylor series in v, but we also find a more complex angular dependency of the full waveform due to nonvanishing $h^{\ell m}$ beyond the leading-order contributions. Their general form (neglecting precession) satisfies

$$ h^{\ell m}(t) = A^{\ell m}(t)\, e^{-im\phi_{\rm orb}(t)} \;. \tag{2.83} $$

Explicit expressions for $A^{\ell m}$ can be found in [42] up to 3PN order, and spin contributions up to 2PN order are provided in [24]. For completeness, let us only give the dominant mode here:

$$ \begin{aligned} A^{22} = \sqrt{\frac{64\pi}{5}}\,\frac{M\eta v^2}{R}\Bigg\{ & 1 + v^2\left[\frac{55}{42}\eta - \frac{107}{42}\right] + v^3\left[2\pi - \frac{4}{3}\chi + \frac{2\eta}{3}(\chi_1+\chi_2)\right] \\ & - v^4\left[\frac{2173}{1512} + \eta\left(\frac{1069}{216} + 2\chi_1\,\chi_2\right) - \frac{2047}{1512}\eta^2\right] - v^5\left[\frac{107\pi}{21} - \eta\left(\frac{34\pi}{21} - 24i\right)\right] \\ & + v^6\left[\frac{27027409}{646800} - \frac{856\gamma}{105} + \frac{428i\pi}{105} + \frac{2\pi^2}{3} + \eta\left(\frac{41\pi^2}{96} - \frac{278185}{33264}\right) - \frac{20261\eta^2}{2772}\right. \\ & \left. + \frac{114635\eta^3}{99792} - \frac{856}{105}\ln(4v)\right]\Bigg\} \;. \end{aligned} \tag{2.84} $$

Following [162] we used $\chi = (\chi_1 m_1 + \chi_2 m_2)/M$ in the equation above.

2.4.4 Frequency-domain PN approximant

Apart from the time-domain approximants, we can use the assumption of "stationarity" that we employed to construct a series of circular orbits also to find a closed-form solution in the frequency domain. The resulting approximant is commonly referred to as *TaylorF2* [25, 72, 74]. It can be derived within the *stationary phase approximation*, and we shall outline the important steps below.

We assume a slowly varying amplitude, $\dot{A}^{\ell m}/A^{\ell m} \ll m\dot{\phi}_{\rm orb}$, and expand the phase around a fixed point in time t_f,

$$ \phi_{\rm orb}(t) \approx \phi_{\rm orb}(t_f) + \dot{\phi}_{\rm orb}(t_f)\,(t-t_f) + \frac{\ddot{\phi}_{\rm orb}(t_f)}{2}(t-t_f)^2 \tag{2.85} $$

$$\Rightarrow\ \tilde{h}^{\ell m}(f) = \int_{-\infty}^{\infty} h^{\ell m}(t)\, e^{2\pi i f t}\, dt = \int_{-\infty}^{\infty} e^{\ln A^{\ell m} + i(2\pi f t - m\phi_{\rm orb})}\, dt \tag{2.86}$$
$$\approx \int_{-\infty}^{\infty} e^{\ln A^{\ell m} + i[2\pi f t_f - m\phi_{\rm orb}(t_f)]} e^{i[2\pi f - m\dot{\phi}_{\rm orb}(t_f)](t-t_f)}\, e^{-i(t-t_f)^2 m\ddot{\phi}_{\rm orb}(t_f)/2}\, dt\ .$$

Under our assumptions, variations in $A^{\ell m}$ can be neglected, so the first factor in the integrand is not time-dependent. The second exponential term vanishes, because we now specify the time we expand around by

$$m\dot{\phi}_{\rm orb}(t_f) = 2\pi f\ . \tag{2.87}$$

Expressed in words, we expand around the time when the phase derivative of the time-domain GW mode equals the actual Fourier frequency. This is one origin of sometimes referring to the derivative of the time-domain phase simply as the "frequency".

The remaining integral in (2.86) can be solved analytically

$$\int_{-\infty}^{\infty} e^{-i(t-t_f)^2 m\ddot{\phi}_{\rm orb}(t_f)/2}\, dt = \sqrt{\frac{2\pi}{m\ddot{\phi}_{\rm orb}(t_f)}} e^{-i\pi/4}\ . \tag{2.88}$$

Collecting all terms finally yields

$$\tilde{h}^{\ell m}(f) = A^{\ell m}(t_f)\sqrt{\frac{2\pi}{m\ddot{\phi}_{\rm orb}(t_f)}}\, e^{i[2\pi f t_f - m\phi_{\rm orb}(t_f) - \pi/4]}\ , \tag{2.89}$$

which is evaluated using the TaylorT2 expressions for time (2.73) and phase (2.75). This is trivial, as they are given as functions of v, and we have

$$v(t_f) = [M\dot{\phi}_{\rm orb}(t_f)]^{1/3} = \left(\frac{2\pi M f}{m}\right)^{1/3}\ . \tag{2.90}$$

As for the other approximants, let us conclude this section with the explicit expression of the TaylorF2 phase. Distinct from the time-domain versions, however, different spherical harmonic modes do not simply differ in their phases by the factor m, and we only provide the dominant mode here. It reads

$$\begin{aligned}
\tilde{\phi}^{\ell 2}(v) = {}& \frac{2t_0}{M}v^3 - 2\phi_0^{\rm orb} - \frac{\pi}{4} + \frac{3}{128\eta\, v^5}\left\{1 + v^2\left[\frac{3715}{756} + \frac{55\eta}{9}\right] - v^3\left[16\pi - \left(\frac{113}{3} - \frac{76\eta}{3}\right)\chi_s - \frac{113\delta\chi_a}{3}\right]\right.\\
& + v^4\left[\frac{15293365}{508032} + \frac{27145\eta}{504} + \frac{3085\eta^2}{72} - \left(\frac{405}{8} - \frac{5\eta}{2}\right)\chi_s^2 - \left(\frac{405}{8} - 200\eta\right)\chi_a^2 - \frac{405}{4}\delta\,\chi_s\chi_a\right]\\
& + v^5(1+3\ln v)\left[\frac{38645\pi}{756} - \frac{65\pi\eta}{9} - \left(\frac{735505}{2268} - \frac{24530\eta}{81} - \frac{340\eta^2}{9}\right)\chi_s - \left(\frac{735505}{2268} + \frac{130\eta}{9}\right)\delta\chi_a\right.\\
& \left. - (10-10\eta)\delta\,\chi_s^2\chi_a - (10-30\eta)\chi_s\chi_a^2 - \left(\frac{10}{3} - 10\eta\right)\chi_s^3 - \left(\frac{10}{3} - \frac{10\eta}{3}\right)\delta\chi_a^3\right]\\
& + v^6\left[\frac{11583231236531}{4694215680} - \frac{6848\gamma}{21} - \frac{640\pi^2}{3} - \left(\frac{15737765635}{3048192} - \frac{2255\pi^2}{12}\right)\eta + \frac{76055\eta^2}{1728} - \frac{127825\eta^3}{1296}\right.\\
& - \frac{6848\ln(4v)}{21} + \left(\frac{2920\pi}{3} - \frac{2240\pi\eta}{3}\right)\chi_s + \frac{2920\pi}{3}\delta\chi_a - \left(\frac{34225}{672} - \frac{217135\eta}{168} + \frac{1225\eta^2}{3}\right)\chi_s^2\\
& \left.\left. - \left(\frac{34225}{672} - \frac{7705\eta}{12} + \frac{4820\eta^2}{3}\right)\chi_a^2 - \left(\frac{34225}{336} - \frac{10385\eta}{6}\right)\delta\,\chi_s\chi_a\right]\right\}
\end{aligned} \tag{2.91}$$

$$
\begin{aligned}
&+\nu^7\left[\frac{77096675\pi}{254016}+\frac{378515\pi\eta}{1512}-\frac{74045\pi\eta^2}{756}-\left(\frac{20373952415}{3048192}+\frac{150935\eta}{224}-\frac{578695\eta^2}{432}\right)\delta\chi_a\right.\\
&-\left(\frac{20373952415}{3048192}-\frac{4348560355\eta}{762048}-\frac{11189515\eta^2}{3024}+\frac{71705\eta^3}{108}\right)\chi_s-(570\pi-40\pi\eta)\chi_s^2\\
&-(570\pi-2240\pi\eta)\chi_a^2-1140\pi\delta\,\chi_s\chi_a+\left(\frac{16185}{28}-\frac{74645\eta}{168}+\frac{905\eta^2}{3}\right)\chi_s^3\\
&+\left(\frac{16185}{28}-\frac{437275\eta}{168}+85\eta^2\right)\delta\chi_a^3+\left(\frac{48555}{28}-\frac{198125\eta}{168}+255\eta^2\right)\delta\,\chi_s^2\chi_a\\
&\left.+\left(\frac{48555}{28}-\frac{1337635\eta}{168}+\frac{8935\eta^2}{3}\right)\chi_s\chi_a^2\right]\Bigg\}\,,
\end{aligned}
$$

where v has to be replaced according to (2.90) by $v=(\pi Mf)^{1/3}$.

2.4.5 Precessing systems

We have provided a detailed collection of the equations we employed to perform the parameter study later presented in this thesis. These are, however, restricted to nonprecessing systems, and we briefly outline the missing pieces here that are needed for the general description of arbitrary spin configurations. We closely follow the collection of expressions recently provided by Ajith [10].

The spin-dependent contributions to the PN energy and flux were actually derived in a more general form than given in (2.69) and (2.70). In particular, they contain scalar products of the 3-dimensional spin vectors $\boldsymbol{S}_i$ $(i=1,2)$ and the Newtonian angular momentum $\boldsymbol{L}_N$. The latter is perpendicular to the constantly changing orbital plane, and we usually refer only to the normalized vector $\hat{\boldsymbol{L}}_N$. With these more general terms, we could simply re-derive all time-domain approximants, but we omit those lengthy expressions here.

The three vectors $\{\boldsymbol{S}_1,\boldsymbol{S}_2,\hat{\boldsymbol{L}}_N\}$ are only constant in the nonprecessing case, generally they change their directions continuously (the spin magnitudes are constants, however). An additional set of equations has to be introduced that governs these dynamics, and the most recent PN expansions read [39, 54]

$$
\frac{d\boldsymbol{S}_i}{dt}=\boldsymbol{\Omega}_i\times\boldsymbol{S}_i\,,\qquad i=1,2\,, \tag{2.92}
$$

$$
\begin{aligned}
\text{where}\quad \boldsymbol{\Omega}_1=\frac{\nu^5}{M}\left\{\left(\frac{3}{4}+\frac{\eta}{2}-\frac{3\delta}{4}\right)\hat{\boldsymbol{L}}_N-\frac{\nu}{2M^2}\left[3\left(\boldsymbol{S}_2+\frac{m_2}{m_1}\boldsymbol{S}_1\right)\cdot\hat{\boldsymbol{L}}_N\,\hat{\boldsymbol{L}}_N-\boldsymbol{S}_2\right]\right.\\
\left.+\nu^2\left(\frac{9}{16}+\frac{5\eta}{4}-\frac{\eta^2}{24}-\frac{9\delta}{16}+\frac{5\delta\eta}{8}\right)\hat{\boldsymbol{L}}_N\right\}\,,
\end{aligned} \tag{2.93}
$$

and $\boldsymbol{\Omega}_2$ is obtained by exchanging the indices $1\longleftrightarrow 2$ in $\boldsymbol{S}_i$ and m_i in (2.93). Finally, the set of equations for precessing adiabatic PN approximants is completed by the evolution of $\hat{\boldsymbol{L}}_N$,

$$
\frac{M^2\eta}{\nu}\left[1+\left(\frac{3}{2}+\frac{\eta}{6}\right)\nu^2\right]\frac{d\hat{\boldsymbol{L}}_N}{dt}=-\frac{d}{dt}(\boldsymbol{S}_1+\boldsymbol{S}_2)\,. \tag{2.94}
$$

All equations have to be solved simultaneously in order to obtain $v(t)$, $\boldsymbol{S}_1(t)$, $\boldsymbol{S}_2(t)$ and $\hat{\boldsymbol{L}}_N(t)$.

Having solved the coupled system of differential equations, calculating the emitted GW signal is also more complicated than the nonprecessing case. We have to account for the motion of the orbital plane, which leads to a modulation of the GW strain. The corresponding corrections for arbitrary inclination angles have been calculated by Arun *et al.* [24], and we can simply plug the phase evolution and the coordinates of all relevant vectors into those equations. Note in particular that the equivalent of the orbital phase that enters the waveform modes $\sim e^{-im\Phi}$ has an additional term that originates from the precession of $\boldsymbol{L}_N$. It reads

$$\Phi(t) = \int \left(\omega_{\rm orb} - \frac{d\alpha}{dt}\cos\iota\right) dt \ , \tag{2.95}$$

where α and ι are the spherical coordinates of $\boldsymbol{L}_N$, i.e., the angles measured from the x- and z-axis, respectively.

2.4.6 Other inspiral descriptions

Our overview of PN waveform approximants is not meant to be complete, we merely wanted to collect the equations we shall use to calculate the analytically modeled inspiral as part of our "complete" models. For a more detailed overview of various analytical inspiral descriptions, we refer to [58].

Let us at least mention some other approaches that originated in PN calculations. The *TaylorEt* approximant [94, 181] is motivated by the fact that the standard approximants are based on assuming exact circular orbits, whereas TaylorEt employs a truncated expansion along "PN-accurate" circular orbits. However, it is very close in spirit to the TaylorT*n* approximants, except that the expansion parameter is the energy instead of the velocity. Different studies have shown that, compared to other approaches, TaylorEt does not exhibit the same agreement with different PN approximants or numerically generated data [43, 58, 95].

A very successful and sophisticated transformation of the standard Taylor-expanded PN results is the *effective-one-body* (EOB) formalism [56, 57, 73, 75]. It relies on mapping the two-body problem to an effective one-body Hamiltonian with appropriate energy levels. Re-expanding and re-summing various quantities that enter the EOB metric are aimed at improving the convergence properties also closer to the merger of the two compact objects. Most prominently, recent studies extended the PN-derived EOB description of the inspiral by introducing additional parameters that were determined by comparison with independent, numerical simulations of the very late inspiral, merger and ringdown [60, 61, 77, 80, 81, 144, 145, 180, 201]. We shall briefly return to this in Sec 3.5.3. This thesis is concerned with a similar in spirit, but on a technical level alternative approach to the construction of full waveforms.

A third technique we shall briefly mention here are effective-field-theory calculations of moving particles in curved spacetime. These have been very successful in calculating PN spin contributions through an approach entirely different from standard PN expansions. See, e.g., [151, 152].

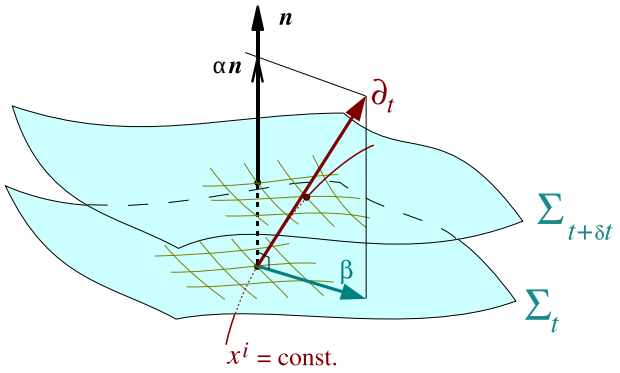

Figure 2.6: Illustration of the spacetime foliation employed by NR. Proceeding from one time slice Σ_t to the the next $\Sigma_{t+\delta t}$, points of fixed spatial coordinates x^i move along the vector field ∂_t. The direction can be split into the contribution perpendicular to the slice ($= \alpha \boldsymbol{n}$, where $\boldsymbol{n}$ is the unit normal vector) and another parallel to the slice ($= \beta^i$); α and β^i are called lapse and shift, respectively. Figure adapted from [96].

2.5 Numerical relativity

The analytical waveform models we presented in Sec. 2.4 are very convenient because they are formulated as ordinary differential equations that are fast to solve with standard numerical techniques. In some cases (e.g., TaylorF2) the GW signal is even given in a closed form. However, all PN models have an obvious limitation: they are analytical *approximations* of solutions to the Einstein equations and their range of validity is restricted to small relative velocities and weak gravity. To solve the entire problem, we have to deal with the full equations at some point, and the only way to solve the system in full generality is by integrating it numerically.

The field of *numerical relativity* (NR) contributes to various research areas, from mathematical relativity over BH science to astrophysics. In our context, it is invaluable to simulate the last stages a coalescing BH binary undergoes and to predict the GW signal of the late inspiral, merger and ringdown. It is beyond the scope of this introduction to review the history and developments of NR comprehensively. We merely summarize selected aspects of numerically treating the Einstein equations in vacuum and refer to [67, 100, 110, 131, 177] for recent overviews of the field.

To recast the Einstein equations (2.9) into an evolution system that can be integrated forward in time, the 4-dimensional spacetime is split into 3-dimensional hypersurfaces Σ_t that are characterized by an induced metric γ_{ij}. The coordinates are defined by two additional gauge quantities: the lapse α that specifies how much time elapses from one hypersurface to the next along the normal n^μ, and the shift vector β^i that fixes the corresponding spatial coordinates. Figure 2.6 illustrates the setup.

This "3+1" split of the spacetime allows for a separation of the Einstein equations into two constraint and two evolution equations, known as the *ADM equations* due to by Arnowitt, Deser and Misner [21]. In the form introduced by York [199] they read

$$R + K^2 - K_{ij}K^{ij} = 16\pi\rho \ , \tag{2.96}$$

$$D_k K^k_i - D_i K = 8\pi j_i \ , \tag{2.97}$$

$$\partial_t \gamma_{ij} = -2\alpha K_{ij} + D_i\beta_j + D_j\beta_i \ , \tag{2.98}$$

$$(\partial_t - \mathscr{L}_\beta)K_{ij} = -D_iD_j\alpha + \alpha(R_{ij} - 2K_{ik}K^k_j + KK_{ij}) - 8\pi\alpha\left(S_{ij} - \frac{1}{2}\gamma_{ij}(S-\rho)\right). \tag{2.99}$$

Therein, D_i is the covariant derivative induced in the 3-dimensional hypersurfaces, $K_{\mu\nu} =$

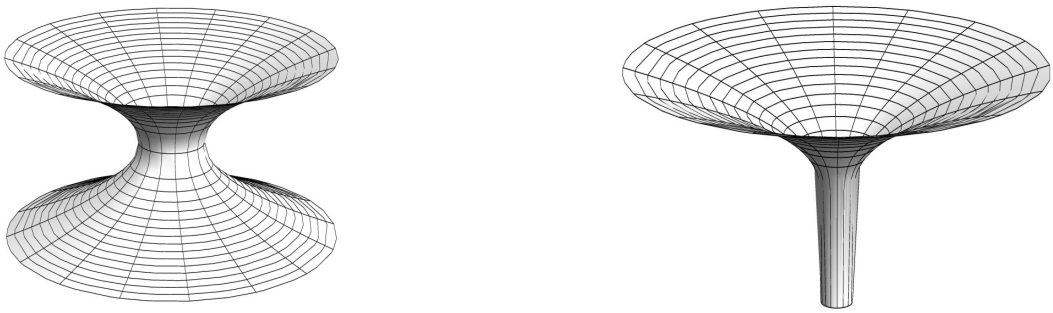

Figure 2.7: Representation of a single BH in a moving-puncture simulation. The embedding diagrams show the wormhole topology (left panel) of the initial time slice that quickly evolves to the stationary trumpet representation (right panel). (Published in [103])

$-\nabla_\mu n_\nu - n_\mu n^\rho \nabla_\rho n_\nu$ is the extrinsic curvature, $K = K_\mu{}^\mu$ is its trace, R_{ij} is the Ricci tensor, $\mathscr{L}_\beta$ is the Lie derivative along β^i, and the energy density ρ, the momentum density j_i and S_{ij} are projections of the energy-momentum tensor. The latter vanish in the vacuum case that we consider here. Note that the Hamiltonian constraint (2.96) and the momentum constraint (2.97) are elliptic equations that have to be fulfilled on every time slice, whereas (2.98) and (2.99) are evolution equations for the spatial metric and the extrinsic curvature. We see that the second-order Einstein equations have been transformed to a first-order-in-time system, just as a standard wave equation can be reduced to first order by introducing the first time-derivate as an independent variable. Here, the extrinsic curvature is related to the time-derivative of the spatial metric γ_{ij} in (2.98).

The ADM equations are numerically unstable, and most of todays codes use the Baumgarte-Shapiro-Shibata-Nakamura (BSSN) reformulation [32, 170] which evolves similar quantities, but rescaled by a conformal factor ψ. However, the system of equations is not complete unless the lapse and the shift are specified by a set of gauge conditions. They ensure that the singularities of the simulated BHs do not interfere with the numerical integration, and a very successful approach is the *moving puncture* gauge. Therein, the initial slice represents each BH by a wormhole geometry with one end compactified at a single point: the "puncture". The extrinsic curvature is deduced from the initial parameters for momentum and spin [200], and the corresponding conformal factor can be constructed following [50]. However, assuming conformal flatness (i.e., the initial metric equals flat space scaled with a conformal factor) introduces additional radiation in the simulation, the *junk radiation*, which quickly leaves the system once the simulation has started to evolve. In addition, the moving puncture gauge then drives the BH representation to a "trumpet" topology [103, 105]. See Fig. 2.7 for an illustration. Once these gauge artifacts have passed, the punctures freely move through the numerical grid according to the physical motion of the BHs, and multiple levels of spatial resolution are adapted to this movement.

An alternative approach to moving-puncture simulations is the generalized harmonic formulation where the coordinates fulfill the condition $\Box x^\mu = H^\mu$ with some specific source function H^μ [91, 154]. Furthermore, instead of avoiding the singularity of BHs automatically through some appropriate gauge choice, one can leave out a portion inside the event horizon from the computational domain [185]. The technique, called "excision",

should not effect the physical properties of the system as no information can travel out of the excluded region. However, care has to be taken that the system remains numerically stable, and finding appropriate boundary conditions is far from trivial.

With both methods just outlined a breakthrough was achieved in 2005 [31, 62, 153], and stable NR simulations of a few orbits plus merger and ringdown to a final Kerr black hole have become a standard tool to consistently predict the last stages of a binary BH coalescence [107]. The exploration of the whole parameter space, however, has just begun and, for instance, long simulations of systems with mass-ratios higher than $q = m_2/m_1 \sim 5$ are still exceptionally time-consuming. Nevertheless, the waveforms that can be extracted from the available NR simulations provide valuable hints on how to complete our understanding of the emitted GW signal, and Chapter 3 in this thesis is devoted to the combination of analytical and numerical results.

Before, let us briefly review how the GW signal is commonly extracted in NR simulations. Instead of measuring some small perturbation on a flat background, a less ambiguous way to calculate the outgoing transverse gravitational radiation is provided by the Newman-Penrose scalar Ψ_4 [137], which is a component of the Weyl tensor in a particular complex tetrad. In NR, it is a convenient object to extract the GW content, because it is related to strain by two time derivatives

$$\Psi_4 = \frac{\partial^2 h}{\partial t^2} = \frac{\partial^2}{\partial t^2}\left(h_+ - i\,h_\times\right) \ . \tag{2.100}$$

To obtain h, one has to integrate Ψ_4 twice, which can lead to unphysical drifts in h. As detailed in the study by Reisswig and Pollney [157], these amplified errors in the numerical GW strain are not only due to undetermined integration constants (which can be removed by a linear fit) but also originate in the small numerical error of Ψ_4 whose amplitude is enlarged by the integrations.

There are several procedures to reduce the error in Ψ_4 and h. Similar to the treatment of the GW strain in PN, Ψ_4 is commonly decomposed into spin-weighted spherical harmonics, see Sec. 2.4.3. The calculation of the individual modes $\Psi_4^{\ell m}$ involves integrals over a sphere of constant extraction radius $r_{\rm ex}$, and this integration smooths out some numerical noise that is otherwise present at fixed points in the coordinate system. Gauge ambiguities that are introduced by the integration over a fixed coordinate radius can be minimized by extracting the GW signal at several extraction radii and extrapolate the results to infinity. With recent developments, it also became possible to measure the signal directly at null infinity via Cauchy-characteristic extraction [28, 156].

One very elegant way to perform the time integrations in order to get h out of a relatively clean Ψ_4 is to first transfer it to the Fourier domain. Here, integrations become simple divisions [as can readily be verified from the definition of the Fourier transform (2.44)], and we find

$$\tilde{h}(f) = -\frac{\tilde{\Psi}_4(f)}{(2\pi f)^2} \ . \tag{2.101}$$

The problem we are faced with now is that the numerically generated signal is of finite length, and discretely Fourier-transforming it leads to other artifacts. These can in turn be

reduced by filtering the signal appropriately, and [157] suggests multiplying $\tilde{\Psi}_4$ with f/f_0 (for $f < f_0$) in every integration step. The parameter f_0 is the lowest physically relevant frequency in the signal, so these filter methods rely on a localized physical content of the GW signal some distance away from the origin. However, for the systems we study here, this assumption is well justified by the fact that the orbital frequencies solely define the range of relevant f, and any numerical simulation will start at some finite frequency that then increases over the course of the inspiral. This may change, however, for strongly precessing systems where multiple frequencies are present, and further studies are needed to find the best integration method for these systems.

Chapter 3

Combining analytical and numerical waveform data

3.1 Motivation to connect complementary waveform pieces

The world-wide effort to directly detect *gravitational waves* (GWs) for the first time is an ambitious project that unites the expertise from various fields in experimental and theoretical physics. A network of instruments, containing the Laser Interferometer Gravitational-wave Observatory (LIGO) [7, 173, 174], VIRGO [8, 9] and GEO600 [99, 127], will soon reach a sensitivity where the signatures of coalescing compact binaries are expected to be seen above the noise level of the detectors a few times to hundreds of times per year [4]. In the case of binaries that consist of black holes (BHs) and/or neutron stars, the correct interpretation of the GW signals crucially depends on the quality of theoretically predicted *template waveforms* that have to be used to identify the physical properties of the source.

Here we focus on waveform families of *binary BHs* as they constitute one of the most promising sources of a first direct detection of GWs. Their modeling typically combines two very different approximation procedures. One describes the early inspiral of both objects through an asymptotic expansion in terms of the relative velocity v/c, where c is the speed of light. As long as this quotient is small, the resulting post-Newtonian (PN) equations are an adequate representation of the dynamical evolution of the binary [38]. Because of the simple form of PN approximants that provide the GW signal in terms of differential equations or, in some cases, even in a closed form, they have long been the favorite tool for data-analysis applications.

However, as the two BHs orbit around each other, they lose energy through the emission of GWs, and their distance shrinks along with an increase in velocity. Consequently, PN predictions become more and more inaccurate the closer the binary gets to merger. One coarse, yet commonly used limit of how far one may trust standard PN approximants is the last stable circular orbit of a test particle around a Schwarzschild black hole. The velocity at this point is $v_{\rm LSO} = 1/\sqrt{6}$ (recall that we use units where $c = 1$) which leads to a dominant GW frequency of

$$f_{\rm LSO} = \frac{v_{\rm LSO}^3}{M\pi} = \frac{1}{M\pi 6^{3/2}} \approx \frac{0.022}{M} \,. \tag{3.1}$$

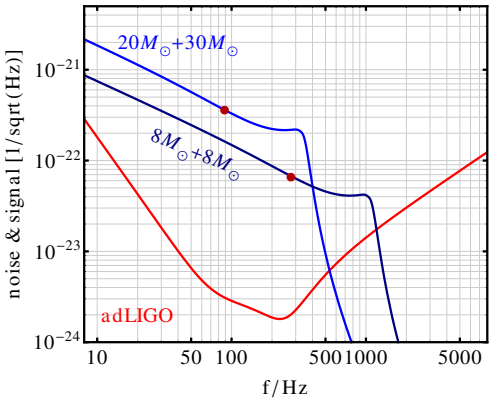

Figure 3.1: The sky-averaged GW strains $\tilde{h}(f)\sqrt{f}$ of two nonspinning binary-BH systems with masses as indicated. The assumed distance from the source is 100Mpc. The red curve shows the analytical fit of the Advanced LIGO noise curve, $\sqrt{S_n(f)}$, as given in [16]. Red dots indicate $f_{\rm LSO}$, given in (3.1), which constitutes a coarse estimate of how far PN templates alone could be used in a GW search.

Beyond this point, standard PN formulations alone do not give a reliable prediction of the GW signal, which becomes particularly problematic for heavier binary systems (i.e., with higher values of the total mass M) where frequencies above $f_{\rm LSO}$ may well be in the sensitive region of the detector. Fig. 3.1 illustrates this issue for two examples of binary systems in the Advanced LIGO detector band. Different analytical modifications are known that try to enhance the convergence of the PN series, even close to merger, and one of the most successful methods is the *effective-one-body* (EOB) approach [56, 57, 73, 75].

Without further information, however, all these analytical schemes break down at some point prior to the merger of both BHs, and a second approach has to be used to model the dynamics from the late inspiral through the merger: *numerical relativity* (NR). In NR, the full Einstein equations are usually solved discretely on a finite grid that is adapted to the movement of the two bodies, and the resolution in space and time is chosen fine enough to obtain a converging result. The GW content is extracted at finite radii and then extrapolated to infinity, or it is directly extracted at null infinity via Cauchy-characteristic extraction [28, 156]. For current overviews of the field see for example [67, 100, 110, 131, 177].

Both numerical and analytical approaches have their limitations. The PN-based formulations are, by construction, not valid throughout the entire coalescence process; NR relies on computationally very expensive simulations that become increasingly challenging (and time-consuming) with larger initial separations, higher spin magnitudes of the BHs and higher mass-ratios $q = m_1/m_2$ (m_i are the masses of the individual BHs and we use the convention $m_1 \geq m_2$). Thus, to build models of the complete inspiral, merger and ringdown signal, one has to combine information from both analytical and numerical approximations. See Fig. 3.2 for an illustration of the dominant harmonic mode of a nonspinning binary.

These "complete" waveforms are indispensable to perfect current search strategies. They constitute our best and most complete approximation of the real signals that we are trying to detect, which makes them ideal target waveforms in a simulated search to test existing analysis algorithms. The Numerical INJection Analysis (NINJA) project [12, 27] is dedicated to that question. The other important application of complete waveforms is to derive an analytical model from them which leads to an improved template bank in the search. The improvement manifests itself, e.g., in a wider detection range and a more accurate extraction of the physical information encoded in the signals. Ongoing searches

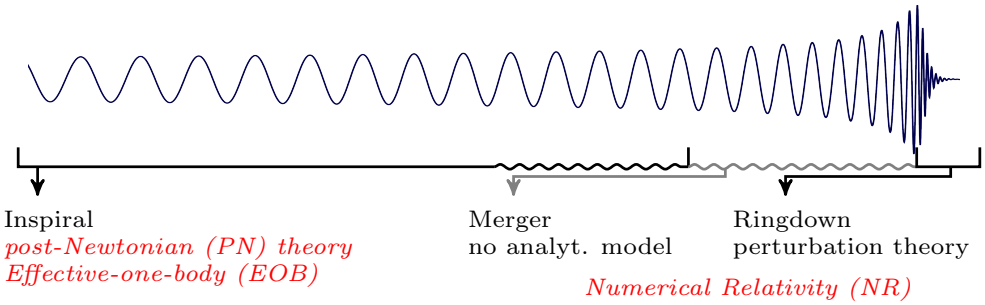

Figure 3.2: The dominant spherical harmonic mode of the GW signal of two coalescing (nonspinning) BHs as a function of time. The different approximation schemes and their range of validity are indicated. Wavy lines illustrate the regime close to merger where analytical methods have to be bridged by NR.

with such templates in LIGO data are summarized for instance in [6].

This chapter describes the methodology to combine PN and NR data into individual *hybrid waveforms*. We shall first analyze the agreement of analytical and numerical results and then provide detailed information on how to smoothly connect the two waveform parts. We conclude with a discussion of waveform families that can be derived from a set of complete hybrids. Most results presented here are already published in [16, 104, 139, 162].

3.2 Comparison of PN and NR waveforms

In the late inspiral regime, a few orbits before merger, both PN and NR predict the GW signal of a coalescing BH binary. This shall become our starting point to connect both descriptions. An important question that has to be answered first is whether both approaches give a *consistent* picture of the late inspiral dynamics. If they would not agree well, either PN or NR or both descriptions cannot be trusted, and we cannot proceed with building a complete waveform model on this basis. Furthermore, it will become clear later in this chapter that a reasonable matching of two complementary waveform parts requires an overlapping region where both approaches yield the same data, at least to some extent.

3.2.1 NR and PN setups

The numerical data we use here are described in detail in [104] and we recall the basic parameters of the simulations in Table 3.1. We separate them into two series of simulations:

- Equal-mass binaries where each BH has the same spin aligned with the orbital angular momentum $\boldsymbol{L}$. The spin magnitudes are characterized by $\chi_i = \boldsymbol{S}_i \cdot \boldsymbol{L}/(m_i^2|\boldsymbol{L}|)$, and χ_i ranges from -0.85 to 0.85.
- Nonspinning binaries with mass ratio q ranging from 1 to 4.

The GW content was extracted in terms of the Newman-Penrose scalar $\Psi_4 = d^2h/dt^2$ at $r_{\rm ex} = 90M$ in each case. We can see that every simulation covers at least 10 GW cycles of the dominant $\ell = 2$, $m = 2$ mode, where we define the number of cycles simply by the

q	χ_i	$D_{\rm ini}/M$	e	$M\omega_{\rm ini}$	$N_{\rm GW}$	$t_{\rm peak}/M$	$M\omega_{\rm RD}$	M_f/M	a_f/M_f
1	-0.85	13.0	0.0025	0.040	16	1868	0.457	0.969	0.412
1	-0.75	13.0	0.0016	0.0395	17	2036	0.466	0.968	0.446
1	-0.50	12.5	0.0029	0.042	18	2065	0.490	0.965	0.531
1	-0.25	12.0	0.0025	0.044	18.5	1955	0.519	0.959	0.609
1	0	12.0	0.0018	0.044	19	1939	0.553	0.951	0.686
1	0.25	12.0	0.0061	0.043	21.5	2129	0.595	0.942	0.760
1	0.50	11.0	0.0061	0.049	20	1739	0.650	0.936	0.832
1	0.75	10.0	0.0060	0.055	19	1432	0.728	0.921	0.898
1	0.85	10.0	0.0050	0.055	20	1492	0.770	0.895	0.915
2	0	10.0	0.0023	0.058	12.5	1069	0.522	0.962	0.623
3	0	10.0	0.0016	0.058	14.5	1240	0.489	0.972	0.540
4	0	10.0	0.0026	0.057	16	1396	0.467	0.978	0.471

Table 3.1: Summary of the configurations simulated. The table indicates the initial coordinate separation $D_{\rm ini}$ of the punctures and the eccentricity e of the resulting coordinate motion. The initial GW frequency is $M\omega_{\rm ini}$, and the ringdown frequency of the final merged black hole is $M\omega_{\rm RD}$. The simulation includes $N_{\rm GW}$ cycles before the peak of the GW amplitude, which occurs at $t_{\rm peak}$. The final black hole has mass M_f and spin a_f.

phase evolution up to the maximum modulus of the GW, divided by 2π. These ten GW cycles will be the range where we compare to analytical approximations.

The PN approximations we consider were given explicitly in Sec. 2.4, but let us recall the basic derivations here to highlight an important subtlety. The starting points of all standard PN approximants are the energy E and the GW flux (or luminosity) $\mathscr{L}$ of a BH binary on quasi-circular orbits. Both quantities are given in the PN framework as expansions in v/c, up to $(v/c)^7$ (3.5PN order), where v is the relative velocity and c the speed of light. We work in units where $c=1$, so v is our expansion parameter and it is related to the orbital phase $\phi_{\rm orb}$ via

$$v = (M\omega_{\rm orb})^{1/3} , \qquad \frac{d\phi_{\rm orb}}{dt} = \omega_{\rm orb} . \tag{3.2}$$

The energy-balance law $dE/dt = -\mathscr{L}$ can be transformed to an evolution equation for v,

$$\frac{dv}{dt} = -\frac{\mathscr{L}}{dE/dv} \tag{3.3}$$

which in turn leads to the ℓm-mode of the gravitational wave strain

$$h^{\ell m}(t) = A^{\ell m}(t)\, e^{-im\phi_{\rm orb}(t)} . \tag{3.4}$$

The amplitudes $A^{\ell m}$ are given as expansions in v to 3PN order in the non-spinning case [42] and up to 2PN order in spinning contributions [24]. When we compare to the NR Ψ_4 in this section, we calculate the second time-derivative of the PN strain numerically.

As we have introduced in Sec. 2.4.2, a direct (numerical) integration of (3.3) and (3.2) is referred to as the *TaylorT1* approximant. If instead the right-hand side of Eq. (3.3) is re-expanded as a Taylor series in v before integrating, the resulting approximant is called *TaylorT4*. This re-expansion is truncated at the same order as the energy and flux (i.e., 3.5PN); all higher powers in v are incomplete and therefore neglected.

If we apply the same strategy to the spin contributions that enter at 1.5PN (leading order spin-orbit coupling), 2PN (spin-spin) and 2.5PN order (next-to-leading order spin-orbit), we should neglect all spin-dependent terms in the re-expansion of (3.3) that appear at 3PN and 3.5PN order. We denote the resulting approximant that was used for instance in [101] as *TaylorT4 (truncated)*. If we instead disregard the distinction of spinning and non-spinning terms and use the "full" re-expansion up to 3.5 PN order, thereby keeping incomplete spin contributions at 3 and 3.5PN order, we denote the resulting approximant simply as *TaylorT4*.

3.2.2 Phase comparison

We now compare the PN and NR phase (denoted by ϕ), each defined as the argument of the complex scalar Ψ_4, respectively. Our procedure is to consider the phase for the N GW cycles up to the matching frequency $M\omega_m = 0.1$. We line up the PN and NR phase functions so that they agree when $d\phi/dt = \omega(t) = \omega_m$, and relabel this event as $t = 0$. We then calculate the phase disagreement as it accumulates over N cycles back in time. Note that although our comparison is over a fixed number of GW cycles, it is *not* over a fixed frequency range, due to the different frequency evolution in each configuration. In the same way, the comparison is also over different lengths of time between different configurations. However, we have found that the qualitative behavior of the comparison results does not depend on whether we compare over a fixed range of cycles, frequency, or time.

One way to quantify the disagreement is simply through the phase difference $\Delta\phi(t) = \phi_{\rm PN}(t) - \phi_{\rm NR}(t)$, and previous studies [101, 106] quoted $\Delta\phi(t_N)$ as the accumulated phase difference, where t_N is the time N cycles prior to the point where $\omega = \omega_m$. This procedure gives consistent results, but we may worry in general that $\Delta\phi(t)$ is not a monotonic function, and so a more robust procedure is to consider instead

$$\overline{\Delta\phi}(t_N) = \frac{1}{\sqrt{-t_N}} \left[\int_{t_N}^{0} \Big(\phi_{\rm NR}(t) - \phi_{\rm PN}(t) \Big)^2 dt \right]^{1/2} . \tag{3.5}$$

This gives us a measure of the average rate of increase of the phase disagreement. A similar procedure was also used in [49], although in that study the alignment of the waveforms was adjusted to minimize $\overline{\Delta\phi}$. An elegant alternative measure of the accumulated phase disagreement is given in Eq. (3.15) of [130]. We instead wish to evaluate how well the PN phase evolution agrees with the fully general relativistic NR results. For comparison with previous results in the literature, we will also show the results of a direct calculation of $\phi_{\rm PN}(t) - \phi_{\rm NR}(t)$.

Fig. 3.3 shows the disagreement between the PN and NR phase for the equal-mass configurations with non-precessing spins over $N = 10$ GW cycles. Three PN approximants are used: TaylorT1, TaylorT4, and TaylorT4-truncated, as described in the previous section.

We see that in both calculations of the accumulated phase disagreement, TaylorT1 is the most robust. It performs best in the nonspinning case (which is to be expected, since the nonspinning contributions are known to higher PN order than the spinning contributions),

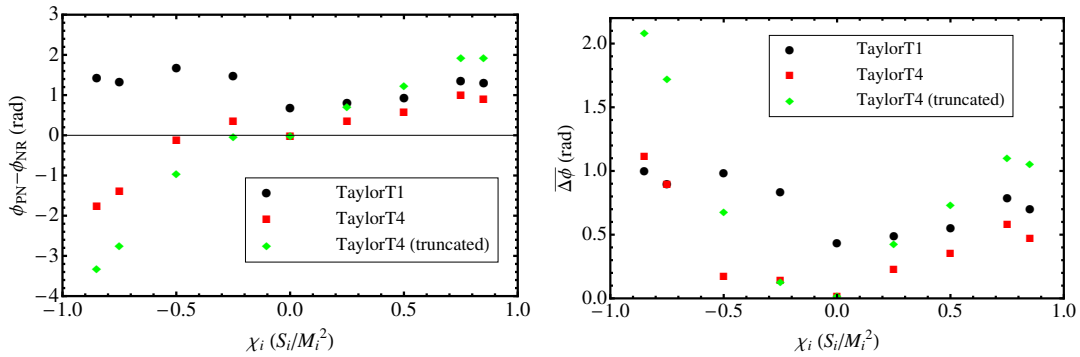

Figure 3.3: Phase disagreement between NR and PN results for three choices of PN approximant, for configurations that consist of equal-mass binaries with equal spins oriented parallel or anti-parallel to the orbital angular momentum. The first panel shows the accumulated phase disagreement for the ten GW cycles up to $M\omega_m = 0.1$. The second panel shows the integrated square of the phase disagreement, Eq. (3.5).

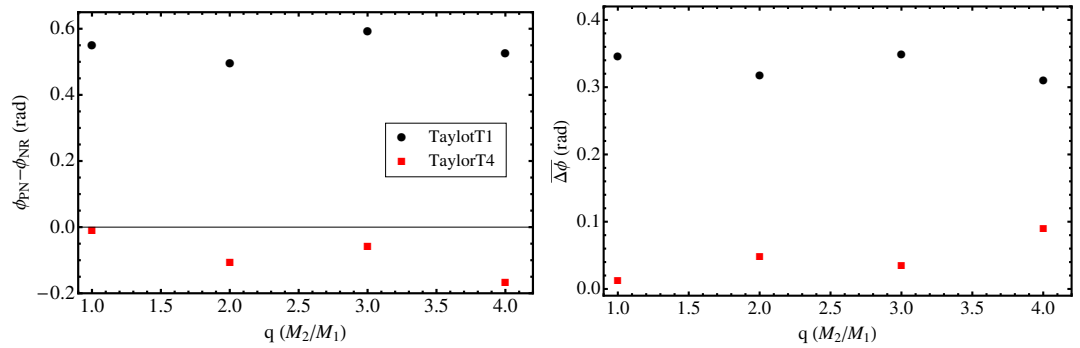

Figure 3.4: Phase disagreement between NR and PN results for two choices of PN approximant, for configurations that consist of nonspinning black holes of unequal mass, with mass ratio q.

and for all spinning cases the accumulated phase disagreement is between 1.0 and 2.0 rad, while the square-averaged phase disagreement is between 0.5 and 1.0 rad. We see also that TaylorT4-truncated performs worse as the spin is increased, and for large anti-aligned spins performs very poorly. The full TaylorT4 approximant performs better for most spin values, although it is again poor for large anti-aligned spins.

Fig. 3.4 shows a similar plot, but this time for the unequal-mass nonspinning configurations. The $q = 2$ simulations consist of less than ten cycles before $M\omega = 0.1$, so we consider only $N = 8$ cycles in the phase comparison. In this case we see that TaylorT4 continues to perform well for unequal-mass configurations. We expect that at higher mass ratios the performance of all PN approximants will deteriorate, but up to $q = 4$ this deterioration cannot be clearly measured; the performance of TaylorT1 and TaylorT4 shows some variation with mass ratio, but this is not monotonic.

We note that the numerical phase error caused by finite numerical resolutions can be measured in a similar way, i.e., by aligning the finite-resolution data to Richardson-extrapolated data at $M\omega = 0.1$. The accumulated phase error over 10 NR orbits back in time is then 0.1 rad and less for all simulations, which leads us to the conclusion that the PN disagreement shown in Figs. 3.3 and 3.4 is not considerably spoiled by numerical errors. More details on the assessment of the numerical error can be found in [104].

From our phase comparison analysis, we conclude that the TaylorT1 approximant is most robust over the entire subset of the BH-binary parameter space that we have studied. The TaylorT4 approximant performs well for all nonspinning cases. The performance of TaylorT4 for spinning cases varies greatly between our two choices of treatment of the higher-order spin contributions, but for both choices shows poor agreement for large anti-aligned spins. We caution, however, that the performance of the approximants over a relatively small number of numerical cycles does not tell us how well they perform before at lower frequencies, and we will discuss this point at great length in Chapter 4.

3.2.3 Amplitude comparison

We now compare the PN prediction for the inspiral wave amplitude with numerical results, for the $(\ell = 2, m = 2)$ mode. It was found before in [106] that in the equal-mass nonspinning case the quadrupole PN amplitude was larger than the full general relativistic amplitude during inspiral by about 7%. It was later shown in [48] that the amplitude agreement could be improved to within 2% if corrections up to 3PN order were used. For equal-mass binaries with aligned spins, it was then reported in [101] that the quadrupole PN amplitude disagreement rose to about 12% in highly spinning cases.

Here we extend these previous analyses of the quadrupole amplitude to anti-aligned and unequal-mass cases. We also compare with the PN amplitude that results from using all currently known amplitude corrections (up to 3PN order nonspinning [42, 119] and up to 2PN order spinning contributions [24, 197]). We have taken care when combining results for amplitude functions from different sources in the literature, in particular regarding different conventions for the choice of relative phase factors. In our implementation we now follow the convention of [24], which differs from that of [42], from which we originally took our nonspinning amplitude contributions. We have checked for consistency with the amplitude of the $\ell = |m| = 2$ modes as given in [34], and we have compared with an independent code as part of the NINJA project [1]. In addition, we have also checked that inconsistent choices of the relative phase factors (e.g., caused by misprints in the literature) significantly increase the deviation of the NR and PN amplitudes; the correct choices lead to the best agreement with results from full general relativity.

An unambiguous time-domain analysis of the amplitude is difficult, because the apparent amplitude difference between PN and NR is in fact a combination of both the amplitude *and* phase disagreement – if the amplitude were measured with no error by the code, but two waveforms are out of phase, they will appear to have a non-zero amplitude error when compared in the time domain. This point was discussed in some detail in [106], where they used a parametrization of the NR amplitude in terms of GW phase to reduce the effects of dephasing on the amplitude analysis. This works well if the phase error as a function of GW frequency is small, but this will not always be true. We expect (from the PN and perturbation theories) that the GW amplitude is a function of the GW frequency, and so the ideal method to measure the amplitude accuracy would be to reparametrize the amplitude as a function of GW frequency.

This procedure also presents problems: the GW frequency from NR is a numerically noisy function during the early and late parts of the simulation; it is certainly not the

smooth monotonically increasing function that we expect it to be on physical grounds. We can partially circumvent this difficulty by producing a smooth analytic fit of the frequency function, and considering the GW phase and amplitude as parametrized by that function. The smoothing process may itself introduce numerical artifacts, and either mask or exaggerate the PN-NR differences. But in general it is sufficient to allow us to calculate reasonably clean PN-NR deviations.

Our method for modeling the NR GW frequency is as follows, based on an earlier version that was used (for equal-mass, nonspinning waveforms) in the work for the Samurai project [107]. For the inspiral, we start with the analytic TaylorT3 approximant for the frequency, as given in [55]. We neglect the highest-order (3.5PN) nonspinning term and replace it by a free parameter that will be fit to our data. In addition, following [55], we do not specify the value of the spin, but also treat it as a free parameter – remember that our goal is to produce a clean analytic fit to the frequency, and we are not interested in whether all of the parameters have their usual physical interpretation. The modified TaylorT3 frequency function is then

$$\begin{aligned}\Omega_{\rm PN}(\tau) = \frac{1}{4}\tau^{-3/8}\Bigg\{1 &+ \left(\frac{743}{2688}+\frac{11}{32}\eta\right)\tau^{-1/4} - \frac{3}{10}\pi\tau^{-3/8} \\ &+ \left(\frac{47}{40}\frac{S}{M^2}+\frac{15}{32}\frac{\delta M}{M}\frac{\Sigma}{M^2}\right)\tau^{-3/8} + \left(\frac{1855099}{14450688}+\frac{56975}{258048}\eta+\frac{371}{2048}\eta^2\right)\tau^{-1/2} \\ &+ \left(-\frac{7729}{21504}+\frac{13}{256}\eta\right)\pi\tau^{-5/8} + \Bigg[\left(\frac{101653}{32256}+\frac{733}{896}\eta\right)\frac{S}{M^2} \\ &+ \left(\frac{7453}{7168}+\frac{347}{896}\eta\right)\frac{\delta M}{M}\frac{\Sigma}{M^2}\Bigg]\tau^{-5/8} + \Bigg[-\frac{720817631400877}{288412611379200}+\frac{53}{200}\pi^2+\frac{107}{280}\gamma \\ &- \frac{107}{2240}\ln\left(\frac{\tau}{256}\right)+\left(\frac{25302017977}{4161798144}-\frac{451}{2048}\pi^2\right)\eta-\frac{30913}{1835008}\eta^2 \\ &+ \frac{235925}{1769472}\eta^3\Bigg]\tau^{-3/4} + a\tau^{-7/8}\Bigg\},\end{aligned} \tag{3.6}$$

where $\eta = m_1 m_2/M^2$ is the symmetric mass ratio, $S = S_1 + S_2$ is the total spin parallel to the orbital angular momentum, $\Sigma = M(S_2/m_2 - S_1/m_1)$, $\delta M = m_1 - m_2$ and γ is the Euler constant. In the cases we consider here, the spins are nonzero only in the equal-mass case, and the spins are always equal to each other, so the $(\delta M\,\Sigma)$ terms do not contribute. The function τ is usually given by $\tau = \eta(t_c - t)/(5M)$, and t_c is interpreted as the "time of coalescence" in standard PN theory, although a more appropriate term would be "time of divergence".

In order to produce a formula that can be fit through our data, we redefine τ as

$$\tau^2 = \frac{\eta^2(t_c - t)^2}{25M^2} + d^2, \tag{3.7}$$

where both t_c and d are free parameters that are fit to the data. This modification of τ prevents $\Omega_{\rm PN}$ from diverging at $t = t_c$. In the form that we have written it, $\Omega_{\rm PN}$ is now symmetric about $t = t_c$, which is certainly not physically realistic, but beyond this point we can make a smooth transition to a different function, which models the ringdown [104].

For completeness, let us mention that that the model of the ringdown phase is a

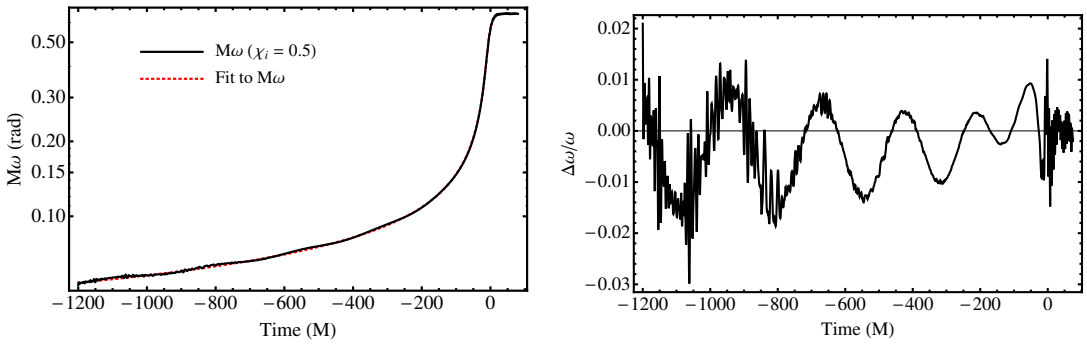

Figure 3.5: Analytic fit to the GW frequency for the $\chi_i = 0.5$ case. The right panel shows the fractional difference between the fit and numerical data. For this configuration, the error in the fit is dominated by the residual eccentricity in the simulation.

modified ansatz suggested in [30], and we write the full frequency as

$$\Omega(t) = \Omega_{\rm PN}(\tau) + \left[\Omega_f - \Omega_{\rm PN}(\tau)\right] \left(\frac{1+\tanh[\ln\sqrt{\kappa} - (t-t_0)/b]}{2}\right)^{\kappa}. \tag{3.8}$$

The constants $\{t_c, t_0, S, \kappa, a, b, \Omega_f\}$ are parameters that are determined to produce the best fit to the numerical data. The constant Ω_f corresponds to a fit of the ringdown frequency, but the other parameters have no clear physical interpretation. (Even the "spin" parameter S really amounts to no more than a modification of the 1.5PN and 2.5PN terms in the description of the inspiral frequency.)

Fig. 3.5 shows a typical frequency fit, in this case for $\chi_i = 0.5$. We see that the dominant error in the fit is due to the residual eccentricity in this simulation; the aligned-spin cases are based on quasi-circular parameters and have the highest eccentricity of all the cases we studied. The procedure does not work quite so well in cases with high spin; the frequency evolution is not captured so well during the early inspiral, or in the $200M$ before the peak GW amplitude. The fitting formula (3.6) could be modified to address this, and indeed the model of the transition to ringdown (3.8) has since been improved by the authors of [30]. These issues, and the masking of eccentricity effects, mean that this frequency fit is far from ideal, and cannot be used for a convergence study of the amplitude. However, it is adequate for the purpose of providing a rough estimate of the amplitude disagreement between NR and PN.

Another issue we had to deal with is that the NR amplitude shows variations with numerical extraction radius that are comparable to the level of disagreement with the PN predictions. However, the error in the amplitude seems to fall off as $1/r_{\rm ex}^2$ (see [106] for a discussion of this effect), and allows us to perform an accurate extrapolation to $r_{\rm ex} \to \infty$. Having obtained the accurate amplitude of $r_{\rm ex}\Psi_4$, we then express the amplitude as a function of frequency, which allows us to easily compare with the PN amplitude, which is always expressed as a function of frequency. Note that for this comparison we perform a frequency fit to our data during only the inspiral, which allows us to much more accurately capture the amplitude evolution.

Fig. 3.6 shows the average disagreement between the PN and NR amplitudes over the 10 cycles up to $M\omega = 0.1$, for the equal-mass spinning cases. The results using both

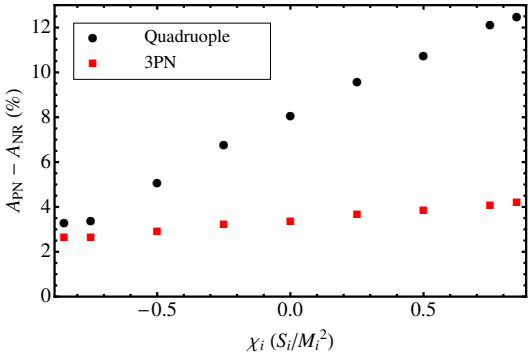

Figure 3.6: Average amplitude disagreement between PN and NR results, over the last ten cycles up to $M\omega = 0.1$. The quadrupole PN amplitude error is only about 3% for large anti-aligned spins, but rises to around 13% for large aligned spins. When the amplitude corrections are included up to 3PN-order, the PN amplitude error is only 3-4% for all spin values.

the quadrupole and 3PN order amplitudes are shown. As seen in [101] the quadrupole amplitude disagreement rises to just over 12% for the highly spinning cases. The increase in disagreement is approximately linear with respect to the spin, and we predict that the maximum disagreement for extreme-spin black holes would be around 14%. For large anti-parallel spins, the quadrupole amplitude performs much better, and drops to around 3% for $\chi_i = -0.85$.

When PN amplitude contributions up to 3PN (nonspinning)/2PN (spinning) order are used, the agreement with NR results is much better. In the nonspinning case it is 3%, consistent with the results in [48]. (Note that the uncertainty in the extrapolated NR amplitude is around 1%.) The variation with spin is small, rising to only 4% in the high-spin hang-up cases, and falling to 2.5% in the high-spin anti-hang-up cases. We find similar results for the unequal-mass cases, where the average disagreement is around 3%.

3.2.4 Conclusions from this study

From the study of the disagreement between analytical approximations and numerical late-inspiral data, we can draw important conclusions that already indicate the issues we have to address in the construction of complete signals. These are in detail:

- Analytical and numerical predictions of the GW reasonably agree in the portion of the inspiral that is captured by both approaches.
- Although a good agreement in this short part of the final waveform is desirable and useful for an unambiguous matching of analytical and numerical data, it is no guarantee that the long complete waveform accurately represents the true signal, or that the PN approximant that agrees best in the *late inspiral* is also the favorite description of the *entire inspiral*.
- The "amount of disagreement" highly depends on
  1. which specific PN approximant is used, and
  2. how PN and NR data are *aligned* with each other.
- Given that there is no perfect agreement between PN and NR, we cannot expect *any* complete waveform to truly represent the final waveform predicted by General Relativity. However, there will be a way to estimate both the best way to combine PN and NR waveforms and the uncertainty that is introduced in this process.

In the light of these conclusions we understand that it is hard to conclusively define *a priori* the optimal combination of an analytical approximation with NR data. In fact, it will be of major importance to explore the variety of possible combinations and deduce from it an estimate of the uncertainty inherited in the waveform model from the individual ingredients. Chapter 4 is devoted to that question. Now we shall turn to the actual construction of hybrid PN+NR waveforms and examine a few different hybridization strategies.

3.3 Constructing hybrid waveforms

3.3.1 Time-domain variants

In the following, we shall consider the GW strain as predicted by a PN approximant, $h_{\rm PN}$, and its complement calculated by NR, $h_{\rm NR}$. Each h is understood as a complex function of time that combines the $+$ and $\times$ polarization,

$$h(t) = h_+(t) - i\,h_\times(t) = A(t)\,e^{i\phi(t)}\,. \tag{3.9}$$

We are not concerned with the specific detector output, which would involve additional geometrical functions of the sky position [see (2.38)]. In addition, h is commonly decomposed into spherical harmonics with spin weight -2, and we will implicitly refer to the dominant mode with $\ell = 2$, $m = 2$ if not stated otherwise.

Let us start with the simplest case. Although h is generally a function of all parameters of the BH binary, we assume that all of them are fixed, except for a free translation in phase and time. Specifically, we assume a given total mass, mass ratio and spins of the system; the "initial" time and phase, often also reformulated as time and phase "at coalescence" are unspecified. We denote the latter as t_0 and ϕ_0. The problem of *aligning* and *matching* $h_{\rm PN}$ and $h_{\rm NR}$ now essentially becomes a problem of finding the, in some sense, *optimal* values for t_0 and ϕ_0. (Note that the final waveform will still be characterized by a free time and phase translation, so a PN-NR matching procedure actually determines the *relative* time and phase shift, $t_0^{\rm PN} - t_0^{\rm NR}$ and $\phi_0^{\rm PN} - \phi_0^{\rm NR}$, respectively. For brevity, we will refer to these differences simply as t_0 and ϕ_0.)

How do we aligned the two waveform parts? We have seen in Sec. 3.2 that neither the PN/NR phases nor the amplitudes agree perfectly, so we would not expect that imposing

$$h_{\rm PN}(t_m) = h_{\rm NR}(t_m) \tag{3.10}$$

at a single "matching" time t_m leads to a robust procedure. Also note that the phase shift only affects ϕ, whereas the time shift affects both phase and amplitude,

$$\phi(t) \mapsto \phi(t - t_0) + \phi_0\,, \qquad A(t) \mapsto A(t - t_0)\,. \tag{3.11}$$

Since (3.10) implies $A_{\rm PN}(t_m) = A_{\rm NR}(t_m)$, we see that matching the complex waveforms at a single point defines t_0 solely through the amplitudes and ϕ_0 follows from preserving continuity.

The more important quantity both from the data-analysis perspective and from the analytical modeling is, however, the phase of the GW and its derivative, which we casually

call the frequency

$$\omega(t) = \left| \frac{d\phi(t)}{dt} \right| \tag{3.12}$$

(not to be confused with the frequency in Fourier space). The variables t_0 and ϕ_0 can also be solely determined through ϕ and ω, as $\omega(t)$ does not depend on ϕ_0 and we can determine t_0 by demanding $\omega_{\rm PN}(t_m) = \omega_{\rm NR}(t_m)$. The relative phase shift then follows through $\phi_{\rm PN}(t_m) = \phi_{\rm NR}(t_m)$. The obvious drawback of this method is that the amplitudes are not required to agree at t_m or anywhere else.

These *point-matching* procedures introduce one additional free parameter: the matching time t_m. Its choice, however, is guided rather strongly by considerations about the quality of the PN and NR data at different points in time. PN approximants are expected to become more and more inaccurate with later times (the expansion parameter is a monotonically increasing function of time). In NR, on the other hand, junk radiation caused by imperfect initial data has to leave the systems first before a relatively clean GW signal can be extracted. This is the regime where t_m should lie, as early as the NR data permits. One has to keep in mind, however, that $\phi_{\rm NR}$ and $\omega_{\rm NR}$ are noise functions and slightly different choices of t_m may lead to considerably different hybrids.

The reduce the impact of numerical noise, it is beneficial to calculate t_0 and ϕ_0 not at a single point but determine them over an entire *interval* (t_1, t_2). The relative time and phase shift can then be found by a minimization of, e.g.,

$$\int_{t_1}^{t_2} \left[X_{\rm PN}(t; t_0, \phi_0) - X_{\rm NR}(t) \right]^2 dt \ , \tag{3.13}$$

where X could be the GW strain or phase or any other suitable function. Ajith *et al.* [14, 15] introduced this alignment procedure for $X \equiv h$ and originally included an additional scaling factor of the NR amplitude. Since the PN amplitude description advanced since then and the agreement with NR is now much better (recall Fig. 3.6), we refrain from using an additional scaling factor and preserve all quantities as they come out of the respective approach.

This *interval-matching* strategy introduces two additional parameters, t_1 and t_2, and their choices are not as obvious as in the case of only one parameter t_m. In fact, the considerations for t_m apply to t_1 as well, but it is not clear how long the interval should be. It should certainly be long enough so that numerical errors average out to some extent, and the more pronounced the frequency evolution is from t_1 to t_2 the more accurate one can fix t_0. On the other hand, when t_2 becomes larger, we extend the interval towards the region where standard PN approximants become more unreliable. A compromise has to be found, and we shall look at this question in more detail in the case of a frequency-domain matching procedure. Let us just point out that time-domain hybridization methods, as the ones described here, were analyzed by MacDonald, Nissanke and Pfeiffer [128], and they suggest that the matching interval should at least cover a 10% frequency increase from t_1 to t_2.

Illustrations of matching PN and NR data either at a single point or over an interval are provided in Figs. 3.7 and 3.8, respectively (the lower panels are inspired by similar plots in

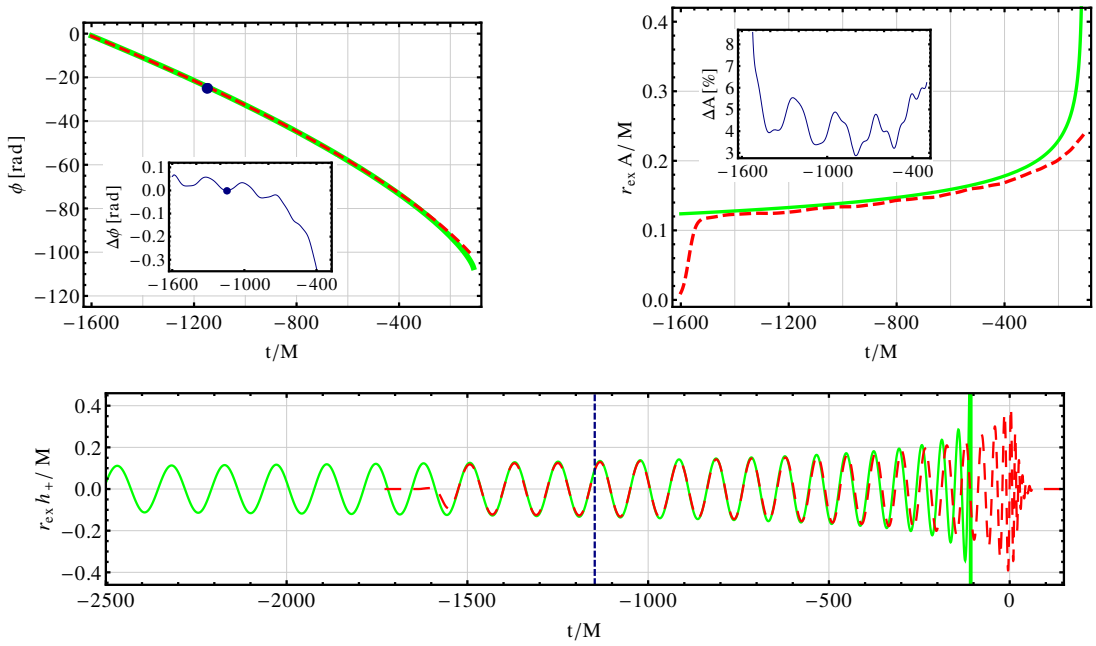

Figure 3.7: Time-domain matching of the TaylorT1 PN inspiral (green) to BAM NR data (red dashed) for an equal-mass binary system with aligned spins of magnitude $\chi_i = 0.5$. We show the phase ϕ and the amplitude A of the GW h as well as its real part $\mathrm{Re}\, h = h_+$. The matching is performed at a single point (marked in blue), demanding a continuously differentiable phase transition. Here we chose $M\omega(t_m) = 0.055$.

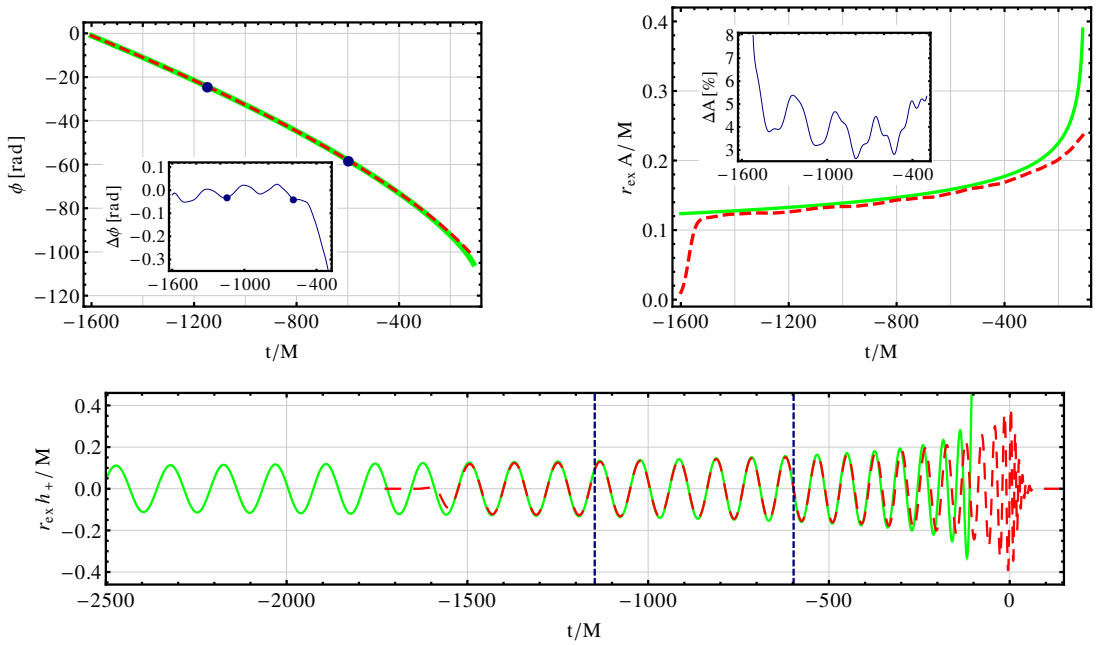

Figure 3.8: The same configuration as in Fig. 3.7, only here the matching is performed over an entire interval where the square difference of the phases is minimized. We employed the interval (t_1, t_2) defined by $M\omega(t_1) = 0.055$ and $M\omega(t_2) = 0.07$.

the literature [12, 14, 15]). The data we show correspond to an equal-mass binary with two spinning black holes, where each spin is aligned to the orbital angular momentum and has a dimensionless magnitude of $\chi_i = 0.5$ ($i = 1, 2$). The point-matching procedure (Fig. 3.7) was carried out to ensure continuity in frequency and phase, and we chose t_m by $M\omega(t_m) = 0.055$. The matching interval in Fig. 3.8 uses the same moment of time for t_1, and t_2 was chosen to satisfy $M\omega(t_m) = 0.07$. The integral (3.13) we minimize is simply the phase difference, i.e., $X = \phi$ therein. We see that both approaches hardly differ in the way they align the two signal parts. However, they do lead to slightly different numbers, and for completeness we note that the optimal relative time shifts that were found differ by $7.6M$, the phase shifts disagree by 0.45 rad. What effect such ambiguities have to the entire waveform and how relevant this is in data-analysis applications will be discussed in detail in Chapter 4.

After aligning $h_{\rm PN}$ and $h_{\rm NR}$, we now have to express the full waveform as some combination of the two parts. In principle, this is a separate step in the hybridization process, but there is often a natural way to do it suggested by the alignment procedure. For instance, if (3.10) is satisfied we could simply define the full waveform as a piecewise combination of $h_{\rm PN}(t)$ for $t \leq t_m$ and $h_{\rm NR}(t)$ for $t > t_m$. This would ensure a continuous function. Performing the point matching only in terms of the phase and frequency (as in Fig. 3.7), we obtain a piecewise function that has a continuously differentiable phase but most likely a discontinuity at t_m in the amplitude. An interesting option to cure this problem is to define the transition from PN to NR separately for phase and amplitude, i.e.,

$$h(t) = A(t)\, e^{i\,\phi(t)} \quad \text{with} \qquad \phi(t) = \begin{cases} \phi_{\rm PN}(t), & t \leq t_m \\ \phi_{\rm NR}(t), & t > t_m \end{cases}$$
$$\text{and} \qquad A(t) = \begin{cases} A_{\rm PN}(t), & t \leq t_m^A \\ A_{\rm NR}(t), & t > t_m^A \end{cases}, \tag{3.14}$$

where $t_m \neq t_m^A$ is allowed, and a reasonable way to define t_m^A is to demand a continuous transition in the amplitude as well. The existence of such a point in time is of course not guaranteed when the alignment is only based on the phase (again, see Fig. 3.7), but then one could perform a smooth transition from one amplitude to the other to maintain differentiability.

Evidently, it can become very useful (even necessary) to carry out the transition from the PN to the NR part of the waveform over an interval, instead of at a single point. This usually follows the pattern

$$X(t) = X_{\rm PN}(t)\,[1 - \mathscr{T}(t)] + \mathscr{T}(t)\, X_{\rm NR}(t)\,, \tag{3.15}$$

where X denotes some quantity related to the GW signal (like strain, phase or amplitude) and $\mathscr{T}$ is a taper function that smoothly goes from zero to unity, either on a compact interval [(t_1, t_2) would be a natural choice in that case] or over the entire real axis. Usually, $\mathscr{T}$ is a function of additional free parameters that model its steepness. Examples are a simple linear increase as used in [14, 15], a tanh-function [162], the Planck taper [129] or properly adjusted cosines [128].

To conclude, a good way to represent the final hybrid waveform in our examples, Figs. 3.7 and 3.8, would be to use (3.14) only for the phase. The "matching" or "transition"

time t_m is given trivially in the point-matching case, but it has to be determined separately by a root-finding algorithm when the phase differences are minimized over an interval. However, a least-square fit of the phase ensures that there is indeed a suitable $t_m \in (t_1, t_2)$. The amplitudes in our example, on the other hand, cannot be matched smoothly at a single point. We need to employ a blending function to connect them, which could have the form

$$A(t) = \begin{cases} A_{\rm PN}(t), & t < t_1 \\ A_{\rm PN}(t)\,(t_2 - t)/(t_2 - t_1) + A_{\rm NR}(t)\,(t - t_1)/(t_2 - t_1), & t_1 \leq t \leq t_2 \\ A_{\rm NR}(t), & t > t_2\,. \end{cases} \tag{3.16}$$

The parameters t_1 and t_2 could actually be the boundaries of the fitting interval, although in principle they can be defined independently of that.

3.3.2 Frequency-domain matching

An interesting variation of the hybridization methods we have just discussed is to match PN and NR data in the Fourier domain instead of the time domain. This approach is inspired by three observations. (1) The final complete waveform should resemble its original ingredients as accurate as possible, but in what sense do we define this agreement? In the end, we aim at using the waveforms in data-analysis applications, which suggests to use the appropriate inner product defined in this context (see Sec. 2.3.3). This naturally leads us to the conclusion that, if PN data accurately predicts the signals of low-mass binaries and NR is the right description for sufficiently high masses, a complete waveform should necessarily resemble the two parts correctly *in the Fourier domain*. (2) We use analytical approximations that rely on expansions in terms of the velocity v, and it would be useful to represent the waveforms in terms of this or directly related quantities. Consistent with the adiabatic evolution that we assume from the outset, we can relate v to the orbital frequency $\omega_{\rm orb}$ and the dominant GW frequency $f_{\rm GW}$ by

$$v = (M\omega_{\rm orb})^{1/3} = (M\pi f_{\rm GW})^{1/3}. \tag{3.17}$$

Thus, $\tilde{h}(f)$ (we drop the subscript "GW" again, as it is clear what f refers to in this context) is also a useful representation from a purely theoretical point of view. (3) The numerical data is usually not extracted in terms of h, but rather as its first or second derivative. Integrating in time adds a source of error to the result, but if we perform the integration in the frequency domain, it becomes a simple division by $2\pi i f$. In that sense, hybridizing h or, e.g., the Newman-Penrose scalar $\Psi_4 = \ddot{h}$ makes no difference in the Fourier domain. In addition to that, numerical data always contains noise which shows up on top of the signal we want to measure. In the Fourier domain, however, we can identify a local region that contains the *physical information* we are interested in. By dropping the rest, we can hope to reduce the numerical error (we practically apply a filter), which is not so simple in the time domain where the entire data set contains physical information.

There is also an important caveat. Connecting two signal parts in time or frequency domain is generally *not commutable*, as the Fourier transform is a global transformation. In other words, we have to check explicitly that the late inspiral and merger signal does

not significantly affect the frequency range of the early inspiral and vice versa. We shall comment on this while we describe the construction process in detail below, and again in Sec. 3.4.4. Note, however, that this issue potentially limits the applicability of a Fourier-domain matching to waveforms with clearly separable frequency content, and precessing spins might not allow for this.

We shall now focus on the majority of waveforms we have access to, which are non-precessing, and describe the construction process in analogy to time-domain algorithms. Let $\tilde{h}(f)$ be the Fourier-domain representation of $h(t)$, defined by

$$\tilde{h}(f) = \tilde{A}(f)\, e^{i\,\tilde{\phi}(f)} = \int_{-\infty}^{\infty} h(t)\, e^{2\pi i f t}\, dt\ . \tag{3.18}$$

Note that we use the convention with a positive sign in the exponent in order to put the support of the $\ell = 2$, $m = 2$ mode of the GW to positive frequencies. The principle strategy to produce a hybrid waveform $\tilde{h}$ from $\tilde{h}_{\rm PN}$ and $\tilde{h}_{\rm NR}$ follows very closely the receipt detailed for time-domain hybrids, with only a few distinctions.

Preparing the data requires slightly more effort. We use the direct output from the NR simulation, which in our case is always the Newman-Penrose scalar Ψ_4, and Fourier transform it discretely by a standard FFT algorithm. Thereby, we found it useful to apply a window function that smoothly suppresses the NR waveform at the beginning of the data stream and, although less essential, after the ringdown signal has dropped significantly in amplitude. This way, we ensure that the Fourier spectrum is only minimally affected by the finite length of the NR signal and by numerical artifacts, such as the early burst of junk radiation. Following the suggestion of McKechan, Robinson and Sathyaprakash [129] we use a form of the *Planck taper* function

$$\mathcal{T}(t; t_1, t_2) = \begin{cases} 0, & t \le t_1 \\ \left[\exp\left(\frac{t_2 - t_1}{t - t_1} + \frac{t_2 - t_1}{t - t_2}\right) + 1\right]^{-1}, & t_1 < t < t_2 \\ 1, & t > t_2 \end{cases} \tag{3.19}$$

to taper the data before Fourier transforming. The other modification that becomes very useful is to *interpolate* the frequency-domain data simply by adding a long null stream to the original Ψ_4 data. This does not add *physical information*, but it leads to a higher resolution of the discrete Fourier spectrum, which in turn can become useful, e.g., when unfolding the phase of the signal.

The NR GW strain is finally calculated by means of

$$\tilde{h}_{\rm NR}(f) = -\frac{\tilde{\Psi}_4^{\rm NR}(f)}{(2\pi f)^2}\ , \tag{3.20}$$

and we are free to dismiss the $f = 0$ contribution, because the physical information is confined to a region with exclusively positive or negative frequencies, some distance away from the origin.

The PN data can be prepared in a similar manner if it has to be calculated in the time domain first. Here, however, we want to fully exploit the advantage of working in the frequency domain and assuming an adiabatic evolution by employing the *TaylorF2*

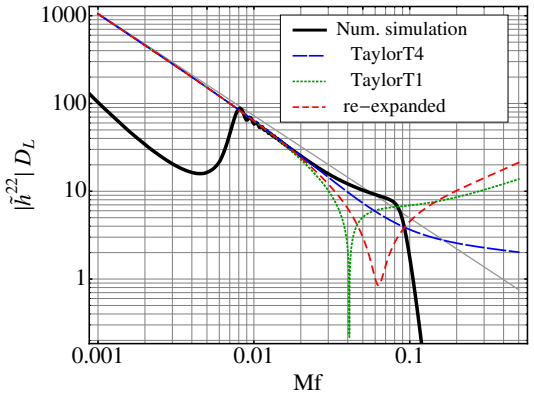

Figure 3.9: Different variants of constructing the PN Fourier amplitude in the stationary-phase approximation for the equal-mass, nonspinning case. The labels explain how $(2\pi/|\ddot{\phi}|)^{1/2}$ is treated in (3.22). The thick curve shows data obtained by a numerical simulation with the BAM code [52] which begins at $Mf \approx 0.008$. The straight gray line illustrates the restricted PN amplitude, $r_{\rm ex}\tilde{A}/M^2 = |\tilde{h}^{22}|D_L = \pi\sqrt{2\eta/3}(\pi Mf)^{-7/6}$.

approximant. This is based on the stationary-phase approximation and yields the GW signal in a closed form directly in the Fourier domain (see Sec. 2.4.4 and [72, 74]). The phase satisfies the form

$$\tilde{\phi}_{\rm PN}(f\,;t_0,\phi_0) = \tilde{\phi}_{\rm F2}(f) + 2\pi f\,t_0 + \phi_0\ , \tag{3.21}$$

where $\phi_{\rm F2}$ is the PN expansion in powers of f, Eq. (2.91), and t_0 and ϕ_0 represent the free time and phase shift of the waveform.

In contrast to that, the amplitude does not depend at all on either t_0 or ϕ_0. We still have to make a choice here, because in the stationary-phase approximation, $\tilde{A}$ can be related to the time-domain quantities of the GW, A and ϕ, by

$$\tilde{A}(f) = A(t_f)\sqrt{\frac{2\pi}{\left|\ddot{\phi}(t_f)\right|}} \qquad \text{with} \quad \left|\dot{\phi}(t_f)\right| = 2\pi f\ . \tag{3.22}$$

There are many ways to express $|\ddot{\phi}| = \dot{\omega}$ in PN theory, notably each PN approximant finds a slightly different treatment of the frequency evolution. Especially convenient are those approximants that provide $\dot{\omega} = 2\dot{\omega}_{\rm orb}$ analytically in terms of $\omega_{\rm orb} = \pi f$ itself, and we could simply insert the appropriate expressions of, e.g., the TaylorT1 or TaylorT4 approximant [cf. (2.71) and (2.76)] into (3.22). A different way to treat (3.22) is to re-expand $1/\sqrt{|\ddot{\phi}|}$ in terms of v, which can be related to f through (3.17), and explicit expressions can be found for instance in [24]. Here we simply use whatever choice follows most closely the NR prediction of the amplitude, and in Fig. 3.9 we illustrate that this is the TaylorT4 variant of $\tilde{A}_{\rm PN}$. The same choice was employed, e.g., in [155].

Having prepared both $\tilde{h}_{\rm NR}$ and $\tilde{h}_{\rm PN}$, we can now proceed with matching them. We have already described different possibilities of doing so in Sec. 3.3.1, and many of those time-domain procedures can easily be adapted to the Fourier domain. Let us highlight once more, however, that in the Fourier space, only the phase is affected by linear phase and time translations of the waveform. Thus, it is natural to base the matching procedure on aligning $\tilde{\phi}_{\rm PN}(f\,;t_0,\phi_0)$ and $\tilde{\phi}_{\rm NR}(f)$. As an interval matching is more robust to numerical artifacts, we choose to define t_0 and ϕ_0 by the values that minimize the square-difference of the PN and the NR phase, see (3.13) with $X = \tilde{\phi}$ and the integration runs from f_1 to f_2 over f instead of t.

When we apply this strategy to the nonprecessing NR waveforms we have access to, we find that it works as good as the time-domain procedures with some additional features. We

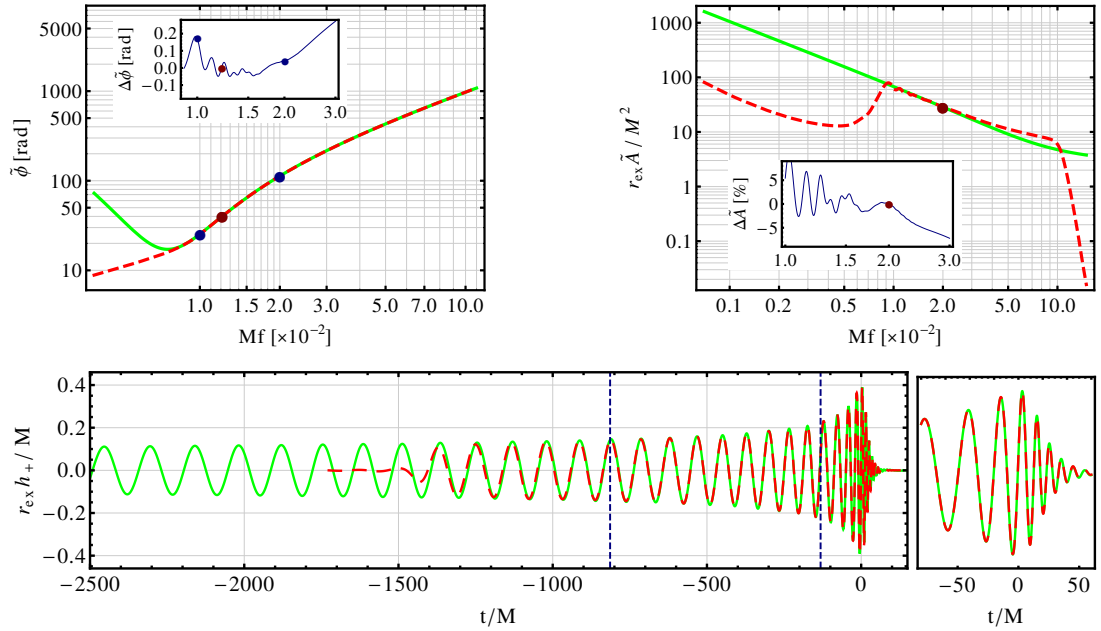

Figure 3.10: The same configuration as in Figs. 3.7 and 3.8, but here the matching is performed in the frequency domain. The upper panel show PN (green solid) and NR (red dashed) data, the lower panel compares the NR data with the full hybrid, transformed to the time domain. PN and NR waveforms are aligned by minimizing the square of the phase difference in the interval $Mf \in (0.01, 0.02) \Rightarrow M\omega \in (0.063, 0.126)$ (illustrated as blue dots/vertical dashed lines). The complete hybrid is a piecewise function with transition points for phase and amplitude at $Mf_m = 0.012$, $Mf_m^A = 0.020$, respectively (indicated by red dots).

shall explain them by an illustration in Fig. 3.10, which is the frequency-domain equivalent of Fig. 3.8. Compared to our earlier choice, where we defined the matching interval in terms of the "frequencies" $Md\phi/dt \in (0.055, 0.07)$, we now had to use higher frequencies $2\pi Mf \in (0.063, 0.126)$ for the matching interval in Fourier space in order to avoid the corruption by edge effects of the numerical Fourier transform. Note, however, that this is just an illustrative comparison (also used in the lower panel of Fig. 3.10 to transform the matching interval to the time domain) and generally, $d\phi/dt$ and the Fourier variable $2\pi f$ are *not* exactly the same. One should also keep in mind that the TaylorF2 approximant does not diverge "close to the merger" in the Fourier space, which results in a more flexible frequency range for the fitting procedure. A more detailed discussion of the length of the matching interval in the Fourier space will follow in Sec. 3.4.1.

Another useful difference between a time and a frequency-domain hybridization is that in the latter case we find that the PN/NR amplitude differences often oscillate around zero. Thus, we can not only perform the transition from PN to NR at a single point in phase but also in amplitude, i.e., we can fully apply the frequency-domain equivalent of (3.14). In our example, Fig. 3.10, we picked a relatively low transition frequency for the phase ($Mf_m = 0.012 \Leftrightarrow M\omega_m = 0.075$) but a high frequency for the amplitude ($Mf_m^A = 0.020 \Leftrightarrow M\omega_m^A = 0.126$). The latter could have been chosen smaller, too, but this would only mean to include unphysical oscillations of the NR data in the hybrid.

Finally, we have obtained a piecewise description of the entire IMR waveform in the

Fourier domain, which perfectly resembles our PN approximant at low frequencies and the FFT of the NR data at high frequencies. As we have pointed out at the beginning of this section, we have to make sure that this "stitching" procedure in the frequency space does not introduced severe artifacts in the time domain. (Note that the inverse should hold for time-domain matching procedures as well, although this is often not explicitly considered.) We can check this now by performing an inverse Fourier transform of a portion of our hybrid, and compare this data to its original time-domain ingredients. Since we have not used a time-domain PN approximant in our example here, we can only reasonably compare to the NR data, which are transformed from Ψ_4 to h via the Fourier domain as well, see (3.20), Sec. 2.5 and [157]. The agreement between the full hybrid waveform and the NR data is striking, as shown in the lower panel of Fig. 3.10. In fact, we find a maximal phase disagreement between the hybrid and $h_{\rm NR}$ of 0.1 rad during the last 7 orbits (14 GW cycles) and through merger and ringdown. The amplitudes agree within 3% in this range, and within 1% from 5 orbits before merger on. These numbers are comparable to the numerical errors reported in [104], and they are below the uncertainties we inevitably have due to the disagreement between numerical and analytical approximations, cf. Figs. 3.3, 3.6 and 3.8. This is a strong reassurance that the assumptions underlying our frequency-domain approach are valid in the region where we combine both waveform parts.

To conclude, we have presented various strategies of matching PN and NR data to a complete hybrid signal. Over the last years, such algorithms became more and more standard tools of the waveform modeling community, and they will remain essential pieces in future studies of GW-search capabilities [12]. Time-domain hybridization procedures are used most commonly today [15, 45, 46, 49, 102, 128], but in the course of this dissertation, we introduced the Fourier-domain hybridization as a complementary alternative with many useful applications [140, 162]. We shall in depth analyze various aspects of these methods in the remainder of this thesis, and often the results will be conveniently obtained in either the time or frequency domain, but they are generalizable to the overall hybridization issue.

3.4 Further aspects of matching PN and NR data

3.4.1 Matching interval

One crucial freedom of the matching procedures we presented above is the point or interval where the PN and the NR part of the waveform are aligned. Through choosing it we define the relative time (t_0) and phase shift (ϕ_0) between both signal segments, and this has an effect not only in the small region where both waveform descriptions overlap, but on the entire GW. In contrast, the actual transition from PN to NR *after* the alignment can also be accomplished in many different ways, but this ambiguity only affects the direct transition region which is a small portion of the entire signal.

Here we shall consider the frequency-domain hybridization procedure introduced in Sec. 3.3.2 and address the question of how a "good" matching interval (f_1, f_2) can be defined quantitatively. Recall that in this interval, we minimize the square difference

between the PN and NR phase, i.e., we calculate

$$\min_{t_0,\phi_0} \int_{f_1}^{f_2} \left[\tilde{\phi}_{\rm PN}(f\,;t_0,\phi_0) - \tilde{\phi}_{\rm NR}(f)\right]^2 df \tag{3.23}$$

together with the values of t_0 and ϕ_0 that achieve this best phase agreement. So far, we motivated the choices of f_1 and f_2 only vaguely by the quality of the waveform data. The matching should be performed in a relatively low frequency regime, because PN approximants are expected to become progressively less accurate descriptions towards higher frequencies. On the other hand, NR data restricts the accessible range to frequencies close to the merger, and we should use an interval that is not (or hardly) spoiled by junk radiation, edge effects etc. These considerations already severely limit the range of possible choices for f_1 and f_2.

Within this reasonable range, one still finds that different matching intervals lead to slightly different best-fit values of t_0 and ϕ_0. In addition to that, one should keep in mind that even for a fixed matching interval, small deviations in t_0 could be compensated by a phase shift ϕ_0, and the difference (3.23) might be nearly as small as the minimum for a nonoptimal relative waveform shift. In short, the alignment is an ambiguous process, and we can indeed use this ambiguity to quantify the goodness of our matching window. Our idea is to analyze the 1-σ parameter uncertainties of the fit (3.23), which we denote by Δt_0 and $\Delta\phi_0$, respectively. The matching interval that yields the smallest errors and therefore allows the most accurate determination of t_0 and ϕ_0 shall become our favorite choice.

Before we present an example, let us elaborate on the concept of parameter uncertainties in a discrete least-square fit, which shows many similarities to the maximum likelihood estimation (Sec. 2.3.3) and the Fisher-matrix approach. Assume that the function $\zeta(x,\boldsymbol{\lambda})$ is fitted through the data $d(x_k)$ to determine the parameters $\boldsymbol{\lambda} = (\lambda_1, \lambda_2, \ldots)$ by minimizing

$$\sum_k \left[d(x_k) - \zeta(x_k,\boldsymbol{\lambda})\right]^2 . \tag{3.24}$$

We further assume that the data is a superposition of ζ with a fixed set of parameters $\hat{\boldsymbol{\lambda}}$ and stationary Gaussian noise with zero mean and variance σ^2,

$$d(x_k) = \zeta(x_k,\hat{\boldsymbol{\lambda}}) + n(x_k)\,, \qquad p(n) \propto e^{-n^2/(2\sigma^2)}\,. \tag{3.25}$$

In the proximity of the best-fit $\boldsymbol{\lambda} = \bar{\boldsymbol{\lambda}}$ we now approximate (3.24) by a Taylor expansion to second order in $\boldsymbol{\lambda}$ (note that the first derivatives vanish because we expand around the parameters that minimize the sum),

$$\begin{aligned}\sum_k \left[d(x_k) - \zeta(x_k,\boldsymbol{\lambda})\right]^2 \approx \sum_k \left[d(x_k) - \zeta(x_k,\bar{\boldsymbol{\lambda}})\right]^2 \\ + \Delta\lambda^i\Delta\lambda^j \sum_k \left([\zeta(x_k,\bar{\boldsymbol{\lambda}}) - d(x_k)] \frac{\partial^2\zeta}{\partial\lambda^i\partial\lambda^j} + \frac{\partial\zeta}{\partial\lambda^i}\frac{\partial\zeta}{\partial\lambda^j}\right).\end{aligned} \tag{3.26}$$

The 1-σ parameter errors are now those where the sum differs by σ^2 (i.e., the noise level) from the best fit. This takes into account that the best-fit parameters do not necessarily

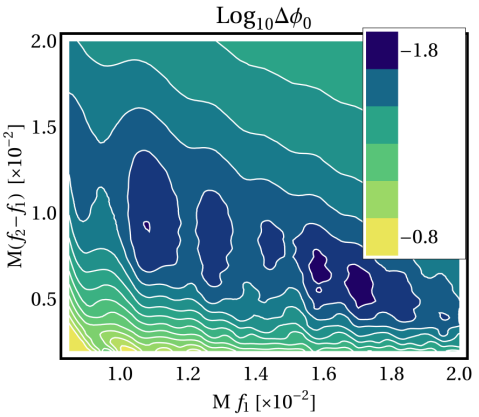

Figure 3.11: A contour plot of the fitting error $\Delta\phi_0$ that is obtained in a least-square fit of the numerical and the PN phase in the interval (f_1, f_2). The waveform comes from a nonspinning binary with mass ratio 2; the NR data is calculated with the `Llama` code, and we employ the TaylorF2 PN approximant.

coincide with $\hat{\boldsymbol{\lambda}}$, because the noise can confuse the estimate. In practice, one would first estimate σ through the mean residual (3.24) itself, then calculate the second-order contribution in (3.26) and inverse this matrix. The square-roots of the diagonal elements, multiplied by σ, yield the desired parameter uncertainties. We use the built-in functions of MATHEMATICA [198] to obtain the parameter errors directly from the least-square-fit routine.

Of course, in our case we align the PN phase to the NR phase, and the disagreement originates from a *systematic* discrepancy between both descriptions, rather than Gaussian noise. The concept of 1-σ errors is still useful to quantify the ambiguity of the fitting process. It takes into account how well both phases agree in the fitting interval, because the smaller the square difference is, the smaller are the estimated variance σ and thus the errors of t_0 and ϕ_0. Also, by considering these errors we quantify how much the phase actually depends on the fitted parameters in the considered interval, which is a formal way of expressing the need that $\tilde{\phi}_{\rm PN}$ has to be sufficiently sensitive to time and phase shifts in (f_1, f_2) to allow for a good fit. The last caveat we should mention is that the numbers for Δt_0 and $\Delta\phi_0$ are resolution-dependent. They roughly scale with $1/\sqrt{N}$, where N denotes the number of discrete points used to evaluate (3.23). In principle, we can increase the resolution in the Fourier space almost arbitrarily, which would lead to smaller and smaller fitting errors. However, the conclusions we are going to draw from this study are based on relative comparisons of the parameter errors, and those are independent of the resolution.

After this theoretical preface, let us now analyze a concrete example. We consider a nonspinning binary with mass ratio $q = 2$. The numerical data was calculated by the `Llama` code [150] and details about this simulation can be found, e.g., in [162]. After Fourier transforming the data, we find that it is reasonably clean for GW frequencies $Mf \gtrsim 0.01$ (similar to Fig. 3.10), but instead of choosing a fitting interval "by eye", we now perform the phase fitting for multiple intervals (f_1, f_2) and analyze the corresponding 1-σ fitting errors. As before, we use the TaylorF2 approximant as the PN model.

Figure 3.11 shows the result of $\Delta\phi_0$ as a function of the lower boundary and the length of the fitting interval (for completeness: we used a resolution of the NR data in frequency space of $M\Delta f = 3.125 \times 10^{-5}$). We discussed before that the parameter uncertainty should increase with a decreasing number of data points to fit, and indeed we see that very short fitting intervals are not a good choice. However, when the interval becomes too long, it

reaches into a frequency regime where PN and NR differ considerably, which leads to an increased σ estimate and larger parameter errors as well. Similarly, if we start at too low frequencies, where our NR waveform does not describe the physical signal correctly, we find that the fitting errors are also large. It is the power of this approach to balance all these considerations automatically.

There are clearly multiple best-fit islands in Fig. 3.11 but we see that the optimal interval choice turns out to be a long frequency width starting at low frequencies, or a relatively short interval starting closer to the merger. Regarding the increasing error PN most likely introduces towards higher frequencies, we prefer using an early and long matching interval. In Fig. 3.11 we find the optimal choice to be $Mf \in (0.0108, 0.0203)$. The result is similar if we analyze the uncertainty of the time shift t_0. In principle, one should repeat this analysis for every waveform one wishes to hybridize, although similar data (in particular, if similar frequency ranges are covered by NR) lead to similar results, and a generalization to a set of waveforms should be possible. However, different PN approximants have different divergence properties, particularly in the time domain, and with this method we have proposed a quantitative way to find an optimal matching interval in all of these cases.

3.4.2 Physical parameters in PN and NR

One implicit assumption we have made so far is that the *intrinsic, physical parameters* of the PN and NR waveform are the same. This is certainly a reasonable assumption as we want to model an exsisting physical scenario that is merely described by two different approaches. However, we shall dedicate this section to a brief discussion of the level of confidence we should have in this perception. More detailed explanations can be found for instance in [162].

Analytical and numerical approximations are not independent from each other, mostly because the initial data for NR is constructed with guidance from PN approximations [59, 113, 116, 186, 193]. There are, however, fundamental differences how each approach simulates the desired system. The PN framework models BHs as point particles, whereas NR defines them by their apparent horizons and either excites the spacetime inside the horizons [153, 172, 176] or the singularities are tracked in an adapted coordinate representation [31, 62, 103, 105]. Consequently, the definitions of masses and spins differ between the two frameworks, and although the point-particle approximation is often a very useful representation of the system, there may be systematic deviations from measures that are defined on the apparent horizon (which is itself a gauge dependent quantity [138]).

As long as we are dealing with just the numerical or PN waveforms by themselves, these small effects in the definitions of mass and spin are not important for most applications. In fact, we can treat them as just convenient parameterizations of the waveform without worrying about their detailed physical interpretation. However, when we wish to compare the results from frameworks as different as PN and NR this may no longer work. Depending on the details of the matching procedure, systematic differences between the various definitions might need to be taken into account, or at the very least they should be quantified. Note that even a small variation in the intrinsic parameter of, say, the inspiral

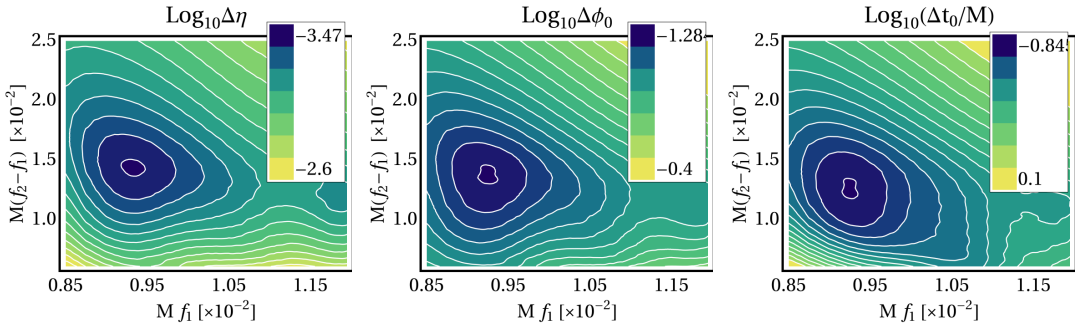

Figure 3.12: Contour plots of the fitting errors obtained in a Fourier-domain PN/NR matching procedure. The data are the same as used for Fig. 3.11, only here, a variation of the symmetric mass ratio η is also taken into account.

part can translate to a considerably different entire waveform over possibly hundreds of cycles in the detector band.

In the absence of a thorough theoretical understanding of the disagreement in physical parameters originating from distinct definitions in PN and NR, one alternative approach would be to simply dismiss the nominal values of the parameters in one framework and determine them through a fit of the waveform (just as we always vary the time and phase scale). As we have access to a discrete number of NR waveforms but a continuous analytical description of the inspiral, we consider the fitting of the PN parameters to given NR data. This, of course, risks being spoiled by the inaccurate PN description of the late inspiral, but we shall nevertheless explore the idea here.

The NR waveform we use for our example is the `Llama` waveform of mass ratio 2 that we used already in Sec. 3.4.1. We keep the total mass and spins in both PN and NR at the same values, respectively, and add only one additional degree of freedom to the phase fit: the variation of the symmetric mass ratio η. We may be worried that this entails already so much flexibility of the PN phase that it can basically match any section of the NR waveform, each with different values of (η, t_0, ϕ_0). When we repeat the 1-σ error analysis of the parameters that was introduced in the previous section, however, we find that we actually gain more structure in the plane of possible fitting intervals. Specifically, Fig. 3.12 illustrates that we now find a uniquely localized optimal fitting interval that is roughly common for all parameters. We can unambiguously conclude that the NR data in our example permits a sensible PN comparison starting at $Mf_1 \approx 0.0093$, and the fitting interval should not extend further than $Mf_2 \approx 0.023$. Note that the latter is remarkably close to the frequency of the last stable circular orbit (3.1), which is a commonly used point indicating how far PN can be trusted. At this optimal choice of the fitting interval, bearing in mind that we use an NR resolution of $M\Delta f = 3.125 \times 10^{-5}$, we see that we can fit η, ϕ_0 and t_0 to better than 10^{-3}, 0.06 and $0.15M$, respectively.

Apart from the errors, the actual best-fit value of η is also of great interest. Fig. 3.13 shows this value as a function of the start frequency of the matching interval. In addition, the color bar indicates the width of the interval. We see that there is indeed a large variation in the value of the symmetric mass ratio that leads to the best phase agreement between PN and NR. Very short matching intervals yield a monotonically decreasing η with increasing

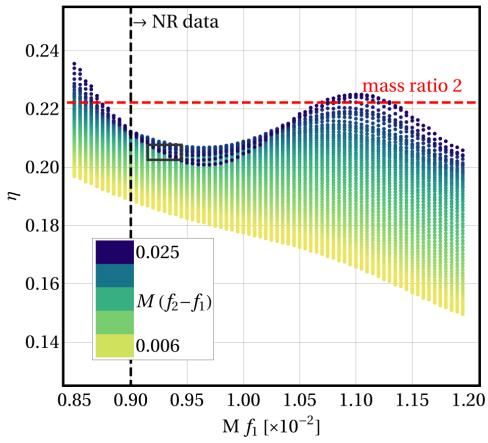

Figure 3.13: Best-fit value of η as a function of the start frequency f_1 of the matching interval for the waveform which corresponds nominally to a mass ratio of 2, i.e., $\eta_{\rm NR} = 2/9 = 0.222\ldots$; this is shown by a horizontal dashed line. The vertical dashed line at $Mf_1 = 0.009$ is the start frequency of the NR waveform. A rectangle highlights the region of minimal fitting errors from Fig. 3.12. We see that the best determined values of η are clearly less than $\eta_{\rm NR}$.

frequencies, very long intervals show an oscillating behavior. The most trustworthy values are those that are reasonably robust to small changes of the matching interval and which are accurately determined in the respective range (f_1, f_2) (as determined in Fig. 3.12). Consequently, if we had to define the PN parameter η from a phase-fitting study like Fig. 3.13, we should look at moderately long matching intervals that start shortly after the NR data becomes reliable. In our example, we find $\eta \approx 0.205$ which is 8% less than the nominal NR value for a mass ratio 2.

For completeness, let us note that we repeated the same exercise with a variable relative total mass while keeping the mass ratio fixed. The total mass M itself is a trivial scale factor and does not have to be specified, but we can, by convention, keep the NR total mass $M_{\rm NR}$ as the overall scale and fit the (relative) mass of the PN waveform. The results we find for the parameter errors are very similar in structure to Fig. 3.12, and the best-fit value obtained with the optimal fitting interval was $M_{\rm PN}/M_{\rm NR} \approx 0.97$. When we accept this difference in the total mass and then employ another least-square fit of the PN phase, now with a variable η, we find that the best-fit value differs from the nominal symmetric mass ratio of a 2:1-binary only by 0.3%. One could take this as an indication that a multiple fitting indeed allows for a consistent determination of the relative differences in physical parameters, but we caution that systematic uncertainties, e.g., coming from the truncated PN series and their representation in different approximants, most likely exceed the uncertainties in the physical parameters that originate from different definitions in the NR and PN frameworks.

Therefore, further studies are necessary to estimate the order of magnitude one has to consider for possible deviations in physical parameters between PN and NR. The discussion in this section merely introduced these additional sources of errors that may become significant in future constructions of complete waveform models. For the remainder of this thesis, however, we shall always assume the same values for the total mass, mass ratio and spins both in PN and NR.

3.4.3 Higher modes

So far we always employed two important simplifications: (1) The GW can be decomposed into spin-weighted spherical harmonics, and we have only considered the dominant $\ell = 2$, $m = 2$ mode. (2) We only assumed BHs that have spins parallel to the orbital angular momentum, which reduces the significant dynamical processes to the evolution of the orbital frequency. No precession effects were present. In the following two sections, we shall briefly comment on generalizations of the hybridization methods presented before, so that both simplifications can successively be dropped.

Let us start with the simpler issue: the inclusion of *higher spherical harmonic modes*. Advances in numerical techniques and improved wave-extraction algorithms allow for an accurate determination of higher modes in NR data, in the best cases up to $\ell = 8$ [150]. On the PN side, the phase scales trivially with m through $\phi^{\ell m}_{\rm PN}(t) = -m\phi_{\rm orb}(t)$. In addition, Blanchet *et al.* [42] provide explicit expansions of the amplitudes for every mode $A^{\ell m}_{\rm PN}(t)$ up to 3PN order (spin-dependent terms up to 2PN order are given in [24]), which gives us access to spherically decomposed PN waveforms $h^{\ell m}_{\rm PN}$ up to $\ell = 8$ as well.

The procedures we have introduced in Sec. 3.3 can now be applied individually to every mode of the GW. With the most dominant waveform modes hybridized that way, one can proceed with reconstructing a more accurate detector response that is an orientation- and location-dependent sum of the individual modes of the GW. Note, however, that matching the individual waveform modes cannot be done entirely independent of each other, because both in PN and NR the evolution of the modes is coupled to each other, and we should not break this correlation by allowing arbitrary time and phase shifts for individual modes.

We discuss the practical implications of this restriction for the case of our novel frequency-domain matching here. The example NR data we shall use to illustrate our results are again obtained from the `Llama` simulation of a nonspinning binary with mass ratio 2. The TaylorF2 PN approximant has to be generalized to different modes by calculating the amplitudes via (3.22) for every mode,

$$\tilde{A}^{\ell m}_{\rm PN} = A^{\ell m}_{\rm PN}(t_f)\sqrt{\frac{2\pi}{m\ddot{\phi}_{\rm orb}(t_f)}} \qquad \text{with } \; m\dot{\phi}_{\rm orb}(t_f) = 2\pi f \; . \tag{3.27}$$

Similarly, the Fourier-domain phase is m-dependent through

$$\tilde{\phi}^{\ell m}_{\rm PN} = 2\pi f\, t_f - m\phi_{\rm orb}(t_f) - \frac{\pi}{4} = 2\pi f\, t_0 + \phi^{\ell m}_0 - \frac{\pi}{4} + \tilde{\phi}^{\ell m}_{\rm F2}(f)\,, \tag{3.28}$$

where we have to express t_f and $\phi_{\rm orb}(t_f)$ as functions of the frequency f by using the respective *TaylorT2* expressions, see e.g., [49, 58] and Sec. 2.4.2. Note that the final result contains the mode-specific PN Taylor expansion $\tilde{\phi}^{\ell m}_{\rm F2}$ and the free parameters t_0 and $\phi^{\ell m}_0$, where only the latter actually changes with changing m (it is, however, ℓ-independent).

Our procedure of a consistent PN/NR matching in Fourier space is now as follows. We determine the free relative time and phase shift by a least-square fit of the phases of the dominant $\ell = 2$, $m = 2$ mode. The parameters of all other modes are then uniquely defined by the best-fit values we found for the dominant mode. In particular, the time shift t_0 is the same for all modes, and the phase shift satisfies

$$\phi^{\ell m}_0 = \frac{m}{2}\phi^{22}_0 + \phi^{\ell m}_{\rm amp}\,. \tag{3.29}$$

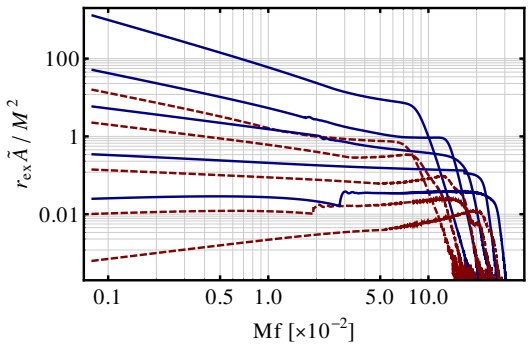

Figure 3.14: Fourier-domain hybrid-waveform amplitudes for various spherical harmonic modes, all belonging to a nonspinning system with mass ratio 2. The blue solid lines show the $m = \ell$ modes for $\ell = 2,3,4,5,6$ (from top to bottom). The red dashed lines illustrate the corresponding $m = \ell - 1$ modes.

The second term in (3.29) becomes necessary by our treatment of the PN amplitude. We conveniently use

$$\tilde{h}^{\ell m}_{\rm PN}(f) = \left|\tilde{A}^{\ell m}_{\rm PN}(f)\right| \; e^{i\,\tilde{\phi}^{\ell m}_{\rm PN}(f)} \,, \tag{3.30}$$

although in general the PN amplitude is a complex expansion. However, we can recast it into its modulus and a phase correction, and since frequency-dependent contributions to this additional phase are formally of higher order (the appropriate expansion of the tan function shows that they enter at relative 5PN order for the dominant mode) we can neglect them [3]. The remaining constant phase term $\phi^{\ell m}_{\rm amp}$ is an integer multiple of $\pi/2$, depending on the leading factor of the corresponding PN amplitude in [42], which is either ± 1 or $\pm i$.

In Figs. 3.14 and 3.15 we present the results for our example of a nonspinning binary with mass ratio 2. The Fourier-domain amplitudes of the hybrid are constructed with no freedom in the alignment, and we deliberately stick to our method of switching from PN to NR at a single frequency in order to visualize the (dis)agreement we find for the amplitudes without smoothing it away with a blending function. As we can see in Fig. 3.14, a number of modes match almost perfectly, whereas others disagree considerably [in particular, $(\ell, m) = (6,6),(5,5),(5,4)$]. The disagreement of higher modes is not unexpected, considering the fact that their amplitudes are determined to lower relative order (i.e., the expansion contains fewer contributions). Consequently, our sanity check of transforming the hybrid back into the time domain and comparing to the original NR data only works satisfactory with the strongest modes, $m = \ell$ and $m = \ell - 1$ with $\ell \leq 4$. These are shown in Fig. 3.15 and we add for completeness that the phase disagreement for all displayed modes is less than 0.1 rad (less than 0.05 rad for the most part); the amplitude differences are below 5% for $\ell = 2$ and $(\ell, m) = (3,3)$, they reach up to 10% for all $\ell = 4$ modes and are even above 10% during the inspiral for the $(3,2)$ mode. We see that the quality of the higher modes of complete GWs is mainly limited by the available PN expansion, but generalizing hybridization procedures to the most important subleading modes with currently established techniques should pose no major difficulties, as we have just demonstrated.

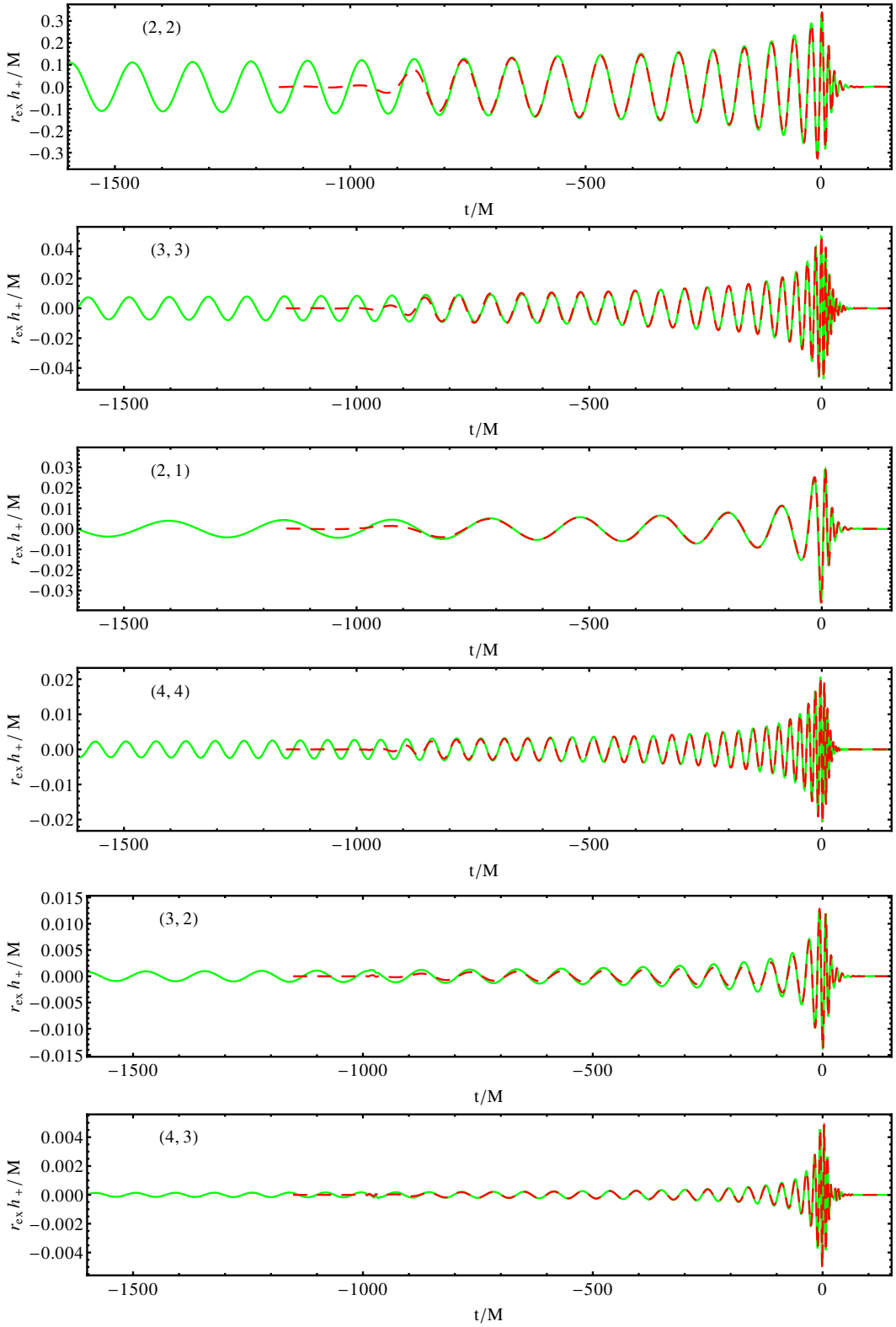

Figure 3.15: The leading contributions of the GW decomposed into spin-weighted spherical harmonics. The `Llama` NR data of the nonspinning binary with mass ratio 2 are shown as red dashed lines. The green solid curves are obtained from the TaylorF2 Fourier-domain hybrid. The numbers in brackets specify the (ℓ, m) mode.

3.4.4 Precession

A slightly more involved issue is the construction of *complete waveforms for precessing binaries*. Compared to the simpler case of BHs with spins aligned to the orbital angular momentum, precession dynamics have to be described by a lot more quantities that evolve in time. Apart from the phase within the orbital plane, one has to track the movement of the plane itself as well as the evolution of each spin vector [20, 68, 118]. This makes the construction of complete waveform models more involved, and accurate and robust approaches that merge analytical and numerical results into a simple description are still missing. Here, however, we are concerned with the construction of individual hybrid waveforms. We employ the time-domain *TaylorT4* approximant for arbitrary spins (sometimes dubbed "Spin-Taylor"), that is still based on the adiabatic evolution of quasi-circular orbits, but now we have to solve a system of coupled differential equations for the orbital frequency $\omega_{\rm orb}$ (measured in the orbital plane), the spin vectors $\boldsymbol{S}_1$ and $\boldsymbol{S}_2$ as well as the Newtonian angular momentum $\boldsymbol{L}_N$. For a collection of explicit equations, see Sec. 2.4.5 and [10, 24, 39].

Integrating these equations can be performed reasonably fast, and we use MATHEMATICA [198] routines to accurately calculate the time evolution of all above mentioned quantities. Given an NR simulation of a precessing binary, however, one difficulty is to find the appropriate PN initial data. The spins and the orbital plane constantly change their orientation, and it is not clear a priori which PN initial conditions evolve to the same setup as assumed by NR. One could of course approach the problem the other way around, namely start with some PN initial data, evolve the system up to a smaller separation and let the NR code 'take over' by feeding in the appropriate quantities from the end of the PN evolution. This idea was explored already by Campanelli *et al.* [63], who found that although the results from PN and NR agree reasonably in the early inspiral, they quickly differ considerably with progressing simulation time. The cause of this disagreement is manifold. Apart from the fact that a truncated PN series will always deteriorate close to the merger, the disagreement potentially stems from the different frameworks used in PN and NR to define physical quantities (see Sec. 3.4.2), and in particular from the transition from Bowen-York initial data [44, 50] to the actually modeled system in the NR simulation.

Here we explore an alternative approach that is close to our treatment of nonprecessing binaries. We already discussed the idea of determining both the relative waveform shift *and* physical parameters by a fit of NR data. We shall do something similar now for precessing binaries by extracting "initial parameters" from NR data and plugging those into a PN system of equations that is integrated backwards and forwards in time. All parameters that are time-independent will be assumed to be the same in PN and NR, i.e., the total mass, the mass ratio and the magnitudes of the spins are *not determined* by any fit, but simply defined with the same values in the respective frameworks. The initial directions of the unit vectors $\hat{\boldsymbol{S}}_1$, $\hat{\boldsymbol{S}}_2$ and $\hat{\boldsymbol{L}}_N$, however, are read off the NR simulation at a fixed time during the inspiral. Measuring the spins in NR typically employs the formalism of quasilocal horizons [26], and determining the spin direction is a coordinate-dependent process [64, 115]. When combining PN and NR descriptions for precessing binaries, however, we are anyway forced to relate different coordinate systems with each other, and if the BHs are still far

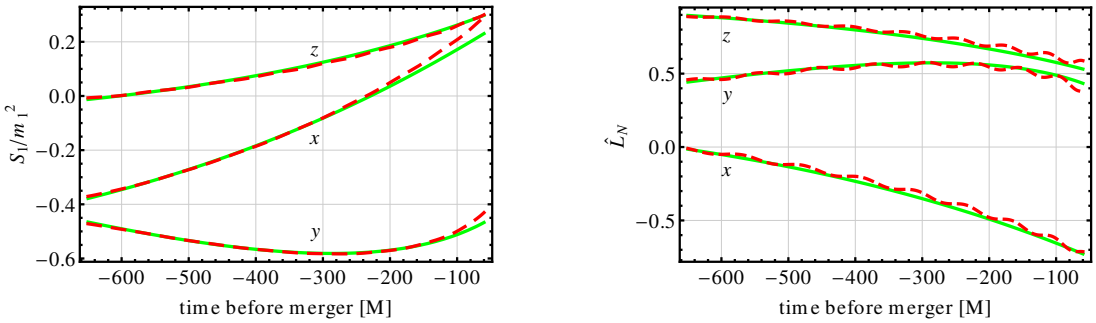

Figure 3.16: Evolution of the spin $\boldsymbol{S}_1$ and the Newtonian orbital angular $\hat{\boldsymbol{L}}_N = \boldsymbol{L}_N/|\boldsymbol{L}_N|$ as measured from NR (red dashed curves) and calculated from the TaylorT4 approximant (green solid lines). The PN results are obtained by extracting the initial data from NR, here at $t = -531M$, and the initial orbital frequency is obtained by a least-square fit of $\boldsymbol{S}_1$, here in the range $t/M \in (-531, -181)$. The simulated binary system has a mass ratio of 4, with $\chi_1 = 0.6$, the smaller BH is not spinning and the angle between $\boldsymbol{L}_N$ and $\boldsymbol{S}_1$ is $\approx 110.7°$.

enough separated in the simulation, we can hope to sensibly identify the NR measures with the PN parameters, in due consideration of the appropriate spin supplementary condition in PN that entails constant spin magnitudes [87, 118]. The direction of the Newtonian orbital angular momentum is estimated simply through the motion of the punctures and the vector product of the separation and the relative velocity. Again, this is a coordinate-dependent measure, but we merely extract from the NR simulation that the modeled system is (approximately) characterized at some instant by the measured $\hat{\boldsymbol{S}}_1$, $\hat{\boldsymbol{S}}_2$ and $\hat{\boldsymbol{L}}_N$.

To complete the set of initial parameters we need to specify the corresponding instantaneous orbital frequency. We could deduce this from the orbital motion of the punctures as well, but as $\omega_{\rm orb}$ is the most crucial quantity entering the GW signal, we find that better results are achieved if $\omega_{\rm orb}$ is determined by a fit. Ideally, we would base this fit on a quantity directly related to the GW (such as its phase), but since the transformation from $\{\hat{\boldsymbol{L}}_N(t), \boldsymbol{S}_1(t), \boldsymbol{S}_2(t), \omega_{\rm orb}(t)\}$ to $h_{\rm PN}(t)$ is again a nontrivial process that introduces further coordinate ambiguities, we decided to separate the integration of the PN evolution from the calculation of the GW. Consequently, our fit of the initial $\omega_{\rm orb}$ is based on the evolution of a physical quantity, and we found it convenient to fit the spin of the heavier BH for a few hundred M of evolution time. In summary, we picked an early time $t_{\rm ini}$ in the NR simulation, extracted $\hat{\boldsymbol{L}}_N(t_{\rm ini})$, $\hat{\boldsymbol{S}}_1(t_{\rm ini})$ and $\hat{\boldsymbol{S}}_2(t_{\rm ini})$ and additionally calculated the value of $\omega_{\rm orb}(t_{\rm ini})$ that yields the smallest difference

$$\int_{t_{\rm ini}}^{t_{\rm end}} \left|\hat{\boldsymbol{S}}_1^{\rm NR}(t) - \hat{\boldsymbol{S}}_1^{\rm PN}[t; \omega_{\rm orb}(t_{\rm ini})]\right|^2 . \tag{3.31}$$

With all initial conditions defined, we can proceed with integrating the orbital frequency within the instantaneous orbital plane (we use the TaylorT4 approximant) and the three vectors $\boldsymbol{S}_1(t)$, $\boldsymbol{S}_2(t)$ and $\hat{\boldsymbol{L}}_N(t)$ by employing the evolution equations (2.92) and (2.94). In Fig. 3.16 we demonstrate the efficacy of our approach for a highly precessing binary with mass ratio 4. The NR simulation was performed at the Albert Einstein Institute in Golm with the `Llama` code. With our way of defining the PN initial data, we obtain a PN system that resembles the NR data very well. The small oscillations of the NR $\hat{\boldsymbol{L}}_N$ that are visible in the right panel of Fig. 3.16 might be due to some residual eccentricity in the

simulation, coordinate effects of the puncture motion or indeed physical affects that are not captured by the adiabatic PN model. Since the effects on the waveform, however, are small, we neglect these oscillations for now and continue with our introduction of the basic strategy to build precessing hybrids.

Even with assuming that we have modeled the same system analytically and numerically, we cannot immediately combine the two waveform parts due to various complications. Firstly, there is another initial parameter, the initial phase, which does not enter the waveform simply as $e^{i\phi_0}$ (this is just the lowest order effect); there are higher order amplitude corrections that depend on ϕ_0 [24]. Knowing them analytically, however, we can still fit for an optimal ϕ_0 between the PN and NR part of the waveform. Secondly, although finding the initial parameters also relates the time between the PN and NR evolution, there is the problem that the physical quantities affect the PN waveform *immediately* whereas if we consider a waveform extracted at some finite radius in NR, there is a time lag between the spin evolution and the observed GW. As already discussed in [63], this time lag approximately corresponds to the travel time between source and observer, but gauge effects will spoil this relation, and we shall determine both ϕ_0 and t_0 by an additional least-square fit of the GW phase, just as in the nonprecessing case.

Another issue we should to take into account when matching the PN and NR waveforms are possible rigid rotations between the respective coordinate frames. These rotations do not affect the evolution of $\omega_{\rm orb}$, $\boldsymbol{L}_N$ and the spins, but they can considerably alter the spherical harmonic modes of the GW [93]. See also the recent discussions of an optimal choice of the coordinate frame [47, 142, 143, 166]. Here we use the explicit expressions provided in the appendix of [24] to translate the integrated PN quantities into $h^{\ell m}_{\rm PN}(t)$, which include up to 2PN spin-dependent amplitude corrections. As before, we employ a PN phase with 3.5PN nonspinning/2.5PN spinning corrections and incomplete spin terms up to 3.5PN order. The amplitude expressions were derived in a particular coordinate system proposed by Finn and Chernoff [88] which is characterized by the initial total angular momentum $\boldsymbol{J}_0 \approx \boldsymbol{L}_N(t_i) + \boldsymbol{S}_1(t_i) + \boldsymbol{S}_2(t_i)$ pointing along the z-axis. We can specifically change into this frame after the PN integration by picking an early time ($t_i \approx -10^9 M$ before the merger), calculating $\boldsymbol{J}_0$ at this instant and rotating the entire system such that $\boldsymbol{J}_0$ points along the z-axis. The spherical harmonic modes we obtain in this rotated system are denoted by $h'_{\ell m}$, and we rotate back to the original NR frame by [24, 63, 93, 166]

$$h_{\ell m} = \sum_{m'=-\ell}^{\ell} D^{\ell}_{m'm}(0, \theta_J, -\phi_J)\, h'_{\ell m'} = \sum_{m'=-\ell}^{\ell} d^{\ell}_{m'm}(\theta_J)\, e^{-im'\phi_J}\, h'_{\ell m'} \,. \tag{3.32}$$

Here, θ_J and ϕ_J are the spherical coordinates of $\boldsymbol{J}_0$ about which we rotated the system initially; D and d are Wigner matrices (in the sign convention adopted by MATHEMATICA). We checked that these twice rotated waveform modes reasonably agree with those obtained by directly plugging the unrotated PN quantities into the formulas given by Arun *et al.* [24], provided that the integration constant ϕ_0 is modified accordingly.

With this, we have almost completed our preparation of the PN inspiral. Since the numerical waveform data is provided in terms of the Newman-Penrose scalar $\Psi_4 = \ddot{h}$ in our case, we decided to hybridize Ψ_4 instead of h. We could also try to transform Ψ_4 to h first, but although Reisswig and Pollney [157] suggest that a frequency-domain integration

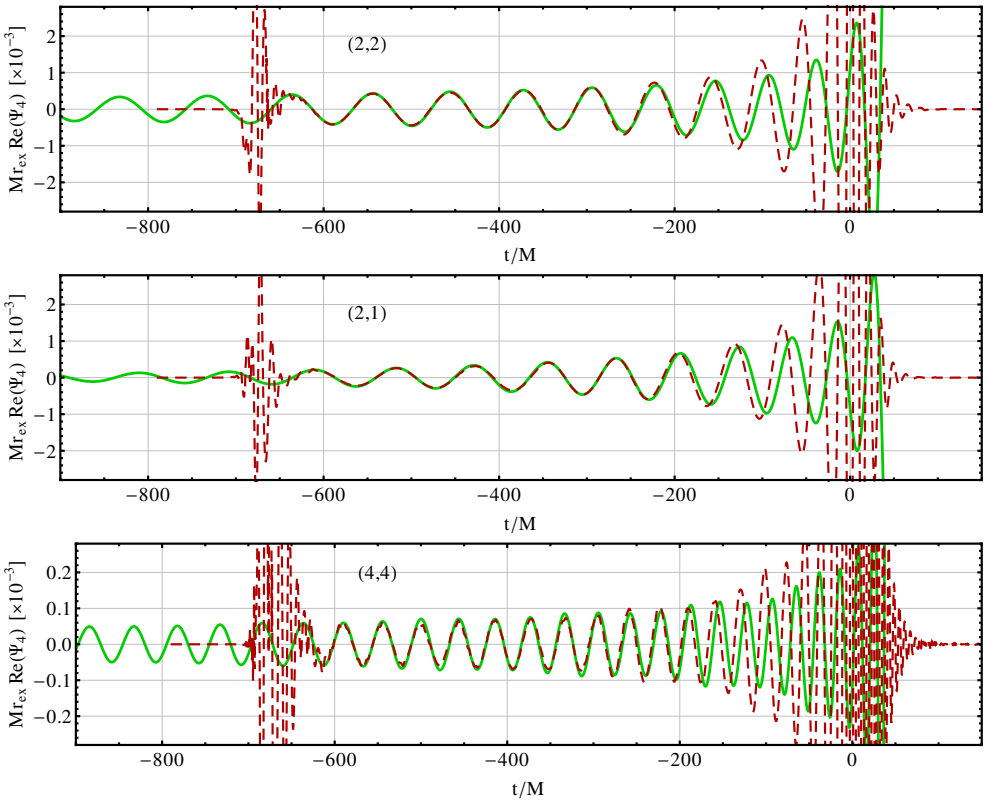

Figure 3.17: Hybrid spherical harmonics (in terms of $\Psi_4 = \ddot{h}$) for the precessing system described in Fig. 3.16. The PN (green) and NR (red dashed) waveform parts are aligned by a least-square fit of the $\ell = 2$, $m = 2$ phase within $t/M \in (-531, -261)$. The coordinate frame is defined by the NR simulation.

potentially works for precessing waveforms as well, we are cautious not to remove *physical information* from the waveform by filtering out lower frequencies. For the same reason, we do not hybridize in the Fourier domain but match the $\ell = 2$, $m = 2$ modes of Ψ_4^{NR} and d^2h_{PN}/dt^2 in the time domain. The results for the example introduced in Fig. 3.16 are shown in Fig. 3.17. Note that the burst of radiation in NR shortly after $t = -700M$ is the already mentioned junk radiation that stems from imperfect initial data. Again, we can clearly see how aligning one mode automatically aligns all the other modes properly. In addition, the (almost arbitrary) NR coordinate frame in which we represent the Ψ_4 hybrids here exhibits large contributions in the $\ell = 2$, $m = \pm 1$ and even $m = 0$ modes. For a use in data-analysis applications, it is crucial to express the GW signal with its multiple harmonics in this case, or find an appropriate coordinate frame that is tailored such that one dominant mode carries the bulk of radiated energy [47, 142, 143, 166].

For completeness, we mention that the modes shown in Fig. 3.17 exhibit a phase disagreement between PN and NR of $|\Delta\phi| < 0.1\,\mathrm{rad}$ for $\ell = 2$ and $|\Delta\phi| < 0.2\,\mathrm{rad}$ for $(\ell, m) = (4, 4)$ in the matching interval. The amplitudes differ by less than 5% for the $\ell = 2$ modes, up to 20% for $\ell = 4$ and to even more than 50% for $\ell = 3$ (although $|\Delta\phi| < 0.1\,\mathrm{rad}$ holds here as well). We suggest that the main cause for these large discrepancies are only few known spin-dependent PN amplitude corrections. We can check that our hybridization procedure did not introduce additional artifacts by transforming the Ψ_4 hybrid back to

h. Now we can employ the frequency-domain integration (3.20) because we can extend the data to almost arbitrarily low frequencies. A meaningful way to confirm that this transformation is allowed is to compare the original PN solution $h_{\rm PN}$ to the hybrid $h_{\rm hyb}$ that was constructed in terms of Ψ_4, and we find for our example

$$\left| \frac{h^{22}_{\rm PN}(t) - h^{22}_{\rm hyb}(t)}{h^{22}_{\rm hyb}(t)} \right| < 1\% \tag{3.33}$$

for all t less than the matching region. Note that is is not a pure statement about the amplitude accuracy, it also ensures that the phases agree very accurately over *thousands of M* in evolution time. We find similar values for all other modes.

3.5 Complete waveform models

In the previous sections we discussed strategies for connecting any given NR waveform with an appropriate analytical inspiral model. The resulting hybrid describes the entire inspiral-merger-ringdown signal of one particular BH-binary system with given parameters. These waveform data are very useful as *state-of-the-art target signals* that could be used, e.g., in a simulated search to test existing search algorithms and entire pipelines. The NINJA project [1] explores this idea, first only with NR data [27] and currently also with complete hybrids [12].

In this section, we shall present another very important application of hybrid waveforms: they can build the basis of an entire *family of template signals* that can be used in GW searches for unknown signals from coalescing binaries. The main difficulty we have to address here is the interpolation from a discrete set of complete waveforms to an analytical model that allows arbitrary physical parameters, at least in a certain range. Discussing all details of this interpolation procedure would be out of the scope of this thesis, and it would exhibit some conceptual repetitions of what we have explained for hybrid waveforms already. Instead, we shall summarize the most important results here and refer to the literature for more details.

3.5.1 Time-domain hybrids – Fourier-domain phenomenological model

One very successful approach to build complete *phenomenological models* was promoted by Ajith *et al.* The first version of that model [14, 15] ("Phenom*A*") employed the TaylorT1 approximant with restricted (Newtonian) amplitude as the inspiral description and matched it in the time domain to NR data from `BAM` [52] and `CCATIE` [149]. Only the dominant modes ($\ell = 2$, $m = \pm 2$) of nonspinning binaries with mass ratio $q \leq 4$ were considered.

The successive and most recent model by Ajith *et al.* [16] ("Phenom*B*") is improved by the inclusion of 3PN nonspinning [42] and 2PN spinning [24] corrections to the PN amplitude. In addition to the nonspinning configurations, spins aligned to the orbital angular momentum are considered. NR waveforms are obtained from `BAM`, `CCATIE` and `Llama` [150], although the latter are used solely for testing purposes. Only the `BAM` waveforms actually contribute to the construction of the model. These in total 24 simulations cover the parameter space in the following series:

1. equal-mass binaries with equal, nonprecessing spins $\chi_i = \pm\{0.25, 0.5, 0.75, 0.85\}$, described in [101, 104],
2. nonprecessing, equal-spin binaries with $q = \{2, 2.5, 3\}$ and $\chi_i = \{\pm 0.5, 0.75\}$,
3. nonspinning binaries with $q = \{1, 1.5, 2, 2.5, 3, 3.5, 4\}$.

After constructing TaylorT1 hybrids in the time domain (by minimizing the waveform differences over an interval) with each of those NR waveforms, Ajith *et al.* [16] proceed by Fourier transforming this set of hybrids. Every complete waveform in its frequency representation is then fitted by a phenomenological model which is inspired by the TaylorF2 approximant, but instead of fixing all expansion coefficients by PN theory, they are determined by a least-square fit. The amplitude is described by a piecewise function that bridges the PN inspiral and the quasi-normal ringdown with a purely empirical middle part.

The final model developed in [16] reads[1]

$$\begin{aligned}
&\tilde{h}(f) = \tilde{A}(f)\, e^{i\,\Psi(f)}\,, \qquad \text{with} \\
&\tilde{A}(f) = C f_1^{-7/6} \begin{cases} f'^{-7/6} \left(1 + \sum_{i=2}^{3} \alpha_i\, v^i\right) & \text{if } f < f_1 \\ w_m\, f'^{-2/3} \left(1 + \sum_{i=1}^{2} \epsilon_i\, v^i\right) & \text{if } f_1 \le f < f_2 \\ w_r\, \mathscr{L}(f, f_2, \sigma) & \text{if } f_2 \le f < f_3, \end{cases} \\
&\Psi(f) = 2\pi f\, t_0 + \phi_0 + \frac{3}{128\,\eta\, v^5} \left(1 + \sum_{k=2}^{7} v^k\, \psi_k\right)\,,
\end{aligned} \tag{3.34}$$

where $f' = f/f_1$, $v = (\pi M f)^{1/3}$, $\epsilon_1 = 1.4547\,\chi - 1.8897$, $\epsilon_2 = -1.8153\,\chi + 1.6557$ (estimated from hybrid waveforms), C is a numerical constant whose value depends on the sky-location, orientation and the masses, $\alpha_2 = -323/224 + 451\,\eta/168$ and $\alpha_3 = (27/8 - 11\,\eta/6)\chi$ are the PN corrections to the Fourier domain amplitude [24]. In addition, the Lorentzian function $\mathscr{L}$ is defined by

$$\mathscr{L}(f, f_2, \sigma) = \frac{1}{2\pi}\, \frac{\sigma}{(f - f_2)^2 + \sigma^2/4}\,, \tag{3.35}$$

and $w_{m,r}$ are normalization constants to ensure continuity of $\tilde{A}(f)$.

The independent physical parameters of the model are ϕ_0 and t_0 (that correspond to the global phase and time shift of the signal), the symmetric mass ratio

$$\eta = \frac{m_2\, m_2}{(m_1 + m_2)^2} \tag{3.36}$$

and a *mass-weighted total spin*

$$\chi = \frac{m_1 \chi_1 + m_2 \chi_2}{m_1 + m_2}, \qquad \text{where } \chi_i = \frac{\boldsymbol{S}_i \cdot \hat{\boldsymbol{L}}}{m_i^2} \tag{3.37}$$

(m_i are the individual masses). The reduction of the number of independent spin parameters from two (χ_1, χ_2) to only one (χ) is motivated by the observation that the dominant

[1] Note that, depending on the definition of the Fourier transform, the phase of $\tilde{h}$ can have a different sign. In this thesis, we consistently use the definition that puts the support of the $\ell = 2$, $m = 2$ mode to positive frequencies. We therefore differ in the sign from the original publication [16].

	$x^{(10)}$	$x^{(11)}$	$x^{(12)}$	$x^{(20)}$	$x^{(21)}$	$x^{(30)}$
ψ_2	-920.9	492.1	135	6742	-1053	-1.34×10^4
ψ_3	1.702×10^4	-9566	-2182	-1.214×10^5	2.075×10^4	2.386×10^5
ψ_4	-1.254×10^5	7.507×10^4	1.338×10^4	8.735×10^5	-1.657×10^5	-1.694×10^6
ψ_6	-8.898×10^5	6.31×10^5	5.068×10^4	5.981×10^6	-1.415×10^6	-1.128×10^7
ψ_7	8.696×10^5	-6.71×10^5	-3.008×10^4	-5.838×10^6	1.514×10^6	1.089×10^7
	$y^{(10)}$	$y^{(11)}$	$y^{(12)}$	$y^{(20)}$	$y^{(21)}$	$y^{(30)}$
f_1	0.6437	0.827	-0.2706	-0.05822	-3.935	-7.092
f_2	0.1469	-0.1228	-0.02609	-0.0249	0.1701	2.325
σ	-0.4098	-0.03523	0.1008	1.829	-0.02017	-2.87
f_3	-0.1331	-0.08172	0.1451	-0.2714	0.1279	4.922

Table 3.2: Phenomenological parameters of the Ajith *et al.* model [16]. The left column specifies the auxiliary parameters entering (3.34), and the coefficients define their value as a function of the physical parameters η and χ; see (3.38) and (3.39).

spin effects in PN are governed by χ, and this almost degenerate relation was also observed in NR equal-mass waveforms [158].

All remaining parameters are determined by least-square fits of the hybrids, and the fitting range is adjusted so that systems are best modeled whose merger and ringdown actually fall into the Advanced LIGO frequency band. Of course, introducing an arbitrary (yet as small as possible) number of parameters to fit a relatively small number of hybrids is not difficult. In the next step, however, these auxiliary parameters have to be mapped smoothly to the physical parameters (notably symmetric mass ratio and spin) in order to allow for an interpolation in the parameter space. With guidance from PN, [16] defines

$$\psi_k = \psi_k^0 + \sum_{i=1}^{3}\sum_{j=0}^{N} x_k^{(ij)} \eta^i \chi^j, \tag{3.38}$$

$$\pi M \mu_k = \mu_k^0 + \sum_{i=1}^{3}\sum_{j=0}^{N} y_k^{(ij)} \eta^i \chi^j \,, \tag{3.39}$$

where $N = \min(3-i, 2)$ and $\mu_k = \{f_1, f_2, \sigma, f_3\}$. To allow for a reasonable extrapolation, particularly towards higher mass ratios, results from the test-mass limit ($\eta \to 0$) are also included in the fit. The final coefficients $x_k^{(ij)}$ and $y_k^{(ij)}$ are provided in Table 3.2.

As a confirmation that these multiple fits do not lead to an inaccurate description of the original waveforms, we can calculate the *fitting factor* (i.e., the normalized inner product optimized over all parameters of the model, see Sec. 2.3.3) between the set of construction hybrids and the final model. As reported in [16], the values of the fitting factor are always above 0.98 for total masses between $10M_\odot$ and $400M_\odot$. Equally important, hybrids in different points of the parameter space that were *not in the construction set* are detected with almost the same efficiency. We shall discuss the accuracy of this and other waveform families in more detail in Chapter 4.

3.5.2 Alternative Fourier-domain phenomenological model

Another phenomenological model was introduced by Santamaría *et al.* [162] ("PhenomC") as an alternative description of binaries with aligned spins. The construction of this model is in some aspects similar to the previously discussed approach, but there are distinct features we shall highlight below.

The same NR waveforms that were used by Ajith *et al.* [16] are also used here for constructing hybrids, but [162] decides to to employ the Fourier-domain hybridization with the TaylorF2 approximant that was detailed in Sec. 3.3.2. The set of hybrids is then again fitted in the frequency domain to a phenomenological model. Here, however, the model directly incorporates the known PN inspiral. The idea promoted in [162] is to use the analytical descriptions of the inspiral and the ringdown without modifications in their respective validity range and smoothly bridge them by a phenomenological middle part.

The complete *phase* $\tilde{\phi}(f) = \arg\tilde{h}(f)$ (again, only of the dominant mode) reads

$$\tilde{\phi}(f) = \tilde{\phi}^{22}_{\mathrm{F2}}(f)\,\mathcal{T}^{-}_{f_1}(f) + \psi(f)\,\mathcal{T}^{+}_{f_1}(f)\,\mathcal{T}^{-}_{f_2}(f) + \tilde{\phi}^{22}_{\mathrm{RD}}\,\mathcal{T}^{+}_{f_2}(f)\,, \tag{3.40}$$

where $\tilde{\phi}^{22}_{\mathrm{F2}}$ is the TaylorF2 phase-expansion given in the appendix of [162].[2] The blending function is defined as

$$\mathcal{T}^{\pm}_{f_0}(f) = \frac{1}{2}\left[1 \pm \tanh\left(\frac{4(f-f_0)}{d}\right)\right]\,, \tag{3.41}$$

where $d = 0.005/M$ was found experimentally as the optimal value. The transition frequencies f_1 and f_2 roughly correspond to the points where our NR simulations start and where the merger happens, respectively, and the best match between the phenomenological model and the hybrids was obtained with $f_1 = 0.9 f_{\mathrm{RD}}$ and $f_2 = f_{\mathrm{RD}}$. The ringdown frequency f_{RD}, in turn, is determined by an analytical fit provided in [36],

$$f_{\mathrm{RD}}(a,M) = \frac{1}{2\pi M}\left[k_1 + k_2(1-a)^{k_3}\right], \quad k_i = \{1.5251, -1.1568, 0.1292\}\,. \tag{3.42}$$

Here, aM^2 is the spin magnitude of the final black hole, and we employ another fitting formula from the literature that maps the spin parameter χ (3.37) and the symmetric mass ratio η (3.36) of the binary to a [160],

$$\begin{aligned} a &= \left|\chi + k_1\eta\chi^2 + k_2\eta^2\chi + k_3\eta\chi + 2\sqrt{3}\eta + k_4\eta^2 + k_5\eta^3\right|, \\ k_i &= \{-0.129, -0.384, -2.686, -3.454, 2.353\}\,. \end{aligned} \tag{3.43}$$

Finally, $\tilde{\phi}^{22}_{\mathrm{RD}}$ is simply the Fourier transform of a damped sinusoidal oscillation (to leading order), which motivates the linear ansatz

$$\tilde{\phi}^{22}_{\mathrm{RD}}(f) = \beta_1 + \beta_2 f\,. \tag{3.44}$$

[2] The TaylorF2 phase-expansion given in [162] misses one self-spin term at 2PN order that was derived in [133], see also the comment in [13]. Since the phenomenological fit is defined with respect to the expressions in [162], however, one has to retain them in the model, even if the actual PN contributions are updated in the literature. In that sense, also $\tilde{\phi}^{22}_{\mathrm{F2}}$ is part of a "phenomenological" description in (3.40) [3].

The β_i parameters are not fitted, but obtained from the pre-merger ansatz by taking the value and slope of ψ at the transition point $f_2 = f_{\rm RD}$. The only phenomenological part in (3.40) is this pre-merger phase ψ that we write in a PN-inspired form as

$$\psi(f) = \frac{1}{\eta}\left[\alpha_1 (Mf)^{-5/3} + \alpha_2 (Mf)^{-1} + \alpha_3 (Mf)^{-1/3} + \alpha_4 + \alpha_5 (Mf)^{2/3} + \alpha_6 Mf\right] . \quad (3.45)$$

All coefficients α_k are determined by least-square fits of the hybrid phases between f_1 and f_2.

The phenomenological *amplitude* $|\tilde{h}(f)| = \tilde{A}(f)\, M^2/R$ (R is the distance from the source) does not need a purely phenomenological middle piece. Instead we can write it as

$$\tilde{A}(f) = \tilde{A}_{\rm ePN}(f)\, \mathcal{T}^-_{f_0}(f) + \tilde{A}_{\rm RD}(f)\, \mathcal{T}^+_{f_0}(f) . \quad (3.46)$$

The transition function is defined in (3.41) and we now employ $d = 0.015/M$ and $f_0 = 0.98 f_{\rm RD}$. The first amplitude part is an extended PN description

$$\tilde{A}_{\rm ePN}(f) = \left|\tilde{A}_{\rm PN}(f)\right| + \gamma_1 (Mf)^{5/6} , \quad (3.47)$$

where $\tilde{A}_{\rm PN}(f)$ is the stationary-phase PN amplitude in its TaylorT4 version (see Fig. 3.6), and the formally next undetermined contribution in a re-expansion is added with the fitting parameter γ_1. The amplitude of the ringdown can be motivated by perturbation theory [182] that yields $h^{22}_{\rm RD}(t) \propto \exp(-\pi f_{\rm RD} t/Q - 2\pi i\, f_{\rm RD} t)$. Our ansatz in the Fourier domain is therefore[3]

$$\tilde{A}_{\rm RD}(f) = \delta_1 \mathcal{L}(f, f_{\rm RD}, \delta_2 f_{\rm RD}/Q)\, f^{-7/6} \quad (3.48)$$

with the Lorentzian

$$\mathcal{L}(f, f_0, \sigma) = \frac{\sigma^2}{(f - f_0)^2 + \sigma^2/4} . \quad (3.49)$$

The factor $f^{-7/6}$ in (3.48) is introduced to correct the Lorentzian at high frequencies, since the hybrid data shows a faster falloff, and δ_1 accounts for the overall amplitude scale of the ringdown. In principle, the phenomenological parameter δ_2 should not be necessary because the width of the Lorentzian for the ringdown should be given by the quality factor Q, which is predicted by [36]

$$Q(a) = q_1 + q_2 (1 - a)^{q_3}, \qquad q_i = \{0.7000, 1.4187, -0.4990\} . \quad (3.50)$$

However, recall that here we estimate the final spin from the initial configuration using the fit given in [160]; δ_2 accounts for the errors in this fit and other ambiguities in our construction.

In total, we have introduced nine phenomenological parameters that have to be defined by a map from the physical parameters of the binary, and [162] finds

$$\Lambda_k = \sum_{i+j\in\{1,2\}} \zeta_k^{(ij)} \eta^i \chi^j , \quad (3.51)$$

with the coefficients provided in Table 3.3.

Λ_k	$\zeta^{(01)}$	$\zeta^{(02)}$	$\zeta^{(11)}$	$\zeta^{(10)}$	$\zeta^{(20)}$
α_1	-2.417×10^{-3}	-1.093×10^{-3}	-1.917×10^{-2}	7.267×10^{-2}	-2.504×10^{-1}
α_2	5.962×10^{-1}	-5.6×10^{-2}	1.52×10^{-1}	-2.97	1.312×10^{1}
α_3	-3.283×10^{1}	8.859	2.931×10^{1}	7.954×10^{1}	-4.349×10^{2}
α_4	1.619×10^{2}	-4.702×10^{1}	-1.751×10^{2}	-3.225×10^{2}	1.587×10^{3}
α_5	-6.32×10^{2}	2.463×10^{2}	1.048×10^{3}	3.355×10^{2}	-5.115×10^{3}
α_6	-4.809×10^{1}	-3.643×10^{2}	-5.215×10^{2}	1.87×10^{3}	7.354×10^{2}
γ_1	4.149	-4.07	-8.752×10^{1}	-4.897×10^{1}	6.665×10^{2}
δ_1	-5.472×10^{-2}	2.094×10^{-2}	3.554×10^{-1}	1.151×10^{-1}	9.64×10^{-1}
δ_2	-1.235	3.423×10^{-1}	6.062	5.949	-1.069×10^{1}

Table 3.3: Phenomenological parameters of the Santamaría *et al.* model [162]. The left column specifies the auxiliary parameters entering (3.45), (3.47) and (3.48). The coefficients define their value as a function of the physical parameters η and χ; see (3.51).

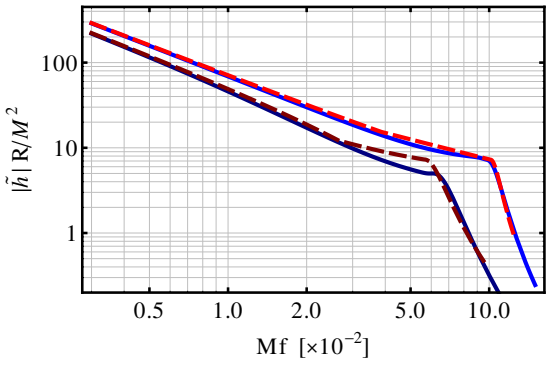

Figure 3.18: The phenomenological amplitudes (normalized by the distance R and total mass M) described in Secs. 3.5.1 (red dashed) and 3.5.2 (blue solid). The chosen parameters of the binaries are $q=1$, $\chi=0.6$ (upper curves) and $q=4$, $\chi=-0.6$ (lower, darker curves), respectively.

Santamaría *et al.* [162] prove that their model is effectual in detecting the waveforms it was constructed from and also in detecting other signals that were not in the construction set. In that sense, both phenomenological models summarized here achieve the same goal. However, they are *not identical*. Fig. 3.18 illustrates that there are small differences, which should not surprise us, given that both approaches start with a different set of target hybrids (with distinct matching procedures and PN approximants), they employ different phenomenological descriptions that are eventually fitted in slightly different frequency intervals. The uncertainty caused by this ambiguous modeling has to be quantified, but instead of proceeding with a detailed comparison of both models, we shall address the questions of reliability of waveform models from a broader perspective in Chapter 4.

3.5.3 Other complete waveform models

For completeness, let us mention other models that provide an analytical description of the complete GW signal. One very successful approach that has already undergone several iterations is to incorporate additional information from NR in a refined effective-one-body (EOB) [56, 57, 73, 75] formalism. Depending on the number of available NR waveforms as well as the modifications introduced to the EOB description, various versions of such *EOBNR*

[3] In (3.48) we correct a typo in the literature where the last argument of $\mathscr{L}$ misses $f_{\rm RD}$.

models have been developed [60, 61, 77, 80, 81, 144, 145, 180, 201]. It is beyond the scope of this thesis to repeat the technical details of the EOB formalism and its extensions. For the sake of comparison to other approaches, however, we shall summarize the general strategy towards complete IMR EOBNR models below.

The main additions that allow for the description of the entire GW signal are (a) a generalization of the EOB formalism which introduces free parameters to be calibrated by NR simulations and (b) attaching a series of damped sinusoidal oscillations (quasinormal modes) representing the final stage of the BH ringdown (see, e.g., [35]). The proposed variants of EOBNR mainly differ in the way the original EOB description is modified and which free parameters are introduced. Two of the most recent versions by Damour and Nagar [77] and Pan *et al.* [144] extend the standard EOB form through the following steps:

- Two unknown parameters representing the 4PN- and 5PN-order contributions are added to the radial potential [commonly referred to as $A(u)$] that enters the Hamiltonian. As for many quantities in the EOB framework, using *Padé* resummation [73] proves to be superior to the Taylor-expanded form (which is, however, not always true, see the discussion about a generalization to spinning BHs [145] and also [135]).

- The radiation-reaction force and the waveform modes are written in a resummed, factorized manner [71]. Additional coefficients are introduced in the waveform, accounting for further, undetermined PN contributions and next-to-quasi-circular corrections.

- A sum of quasi-normal modes is attached to the inspiral-plunge EOBNR waveform over a certain time interval around the peak of the waveform mode.

The impact of NR on the above strategy is manifold. Some parameters (like the EOB-dynamical parameters introduced into the radial potential) are directly determined through minimizing the phase difference between the analytical and numerical GW. Other parameters are derived from independent (i.e., not EOB-related) fits of the numerical data, such as predictions of the final spin of the remnant BH or the maximum of the modulus of the GW. Note, however, that for a direct comparison (and thereby calibration), analytical and numerical waveforms have to be *aligned*, i.e., a relative shift in time and phase has to be fixed by some minimization procedure. We found the same need in all construction algorithms for complete GW signals.

In short, the characteristics of EOBNR constructions are that a well-adapted analytical description is extended and *informed* by NR data, so that finally a time-domain description based on a set of differential equations provides the entire inspiral to plunge signal that is completed by attaching the ringdown waveform.

It should be noted that, although the procedure of combining PN and NR data in a first step and analytically modeling them in a second step is clearly divided only in the phenomenological constructions, they are not entirely different from the EOBNR approach. If the inspiral model used in the hybrid would be EOB and an extended EOB description is chosen as the “phenomenological model”, then we would recover the EOBNR construction. Likewise, if the EOBNR construction would calibrate its model against a

complete hybrid signal instead of pure NR data, it would be conceptually no different from phenomenological constructions (which does not imply that one construction cannot be superior to the other). The important question ultimately is how *flexible* and *accurate* each individual strategy (with all its detailed distinctions) can predict the unknown real GW signal. We shall touch this question in Chapter 4.

Finally, let us mention another phenomenological family that was constructed by Sturani *et al.* [178, 179] as a first step to model waveforms of precessing binaries. In this approach, a Taylor-expanded time-domain approximant (TaylorT4) is extended and finally fitted to NR data. Just like EOBNR (although less sophisticated), the resulting model is given in form of time-domain differential equations with quasinormal ringdown modes attached.

3.5.4 Physical range of waveform models

Understanding the concepts underlying the construction of complete waveform models is mainly interesting when we want to to compare various approaches, deduce why they lead to slightly different waveforms and, most importantly, assess the quality of individual families. Before we turn to that question, however, we summarize the facts that are interesting for the actual usage of the waveforms in data-analysis applications. In particular, before applying the model to a set of physical parameters, one should have a clear perception of *where in the parameter space* these models have been constructed. Although this range does not necessarily coincide with the range of parameters the model can be used with, it nevertheless is a good indication where it can be trusted most.

The waveform models that have been introduced in the previous sections are tailored to model binary BHs with comparable masses inspiralling on quasi-circular orbits. There are successful efforts to exploit the synergy of analytical methods and NR also for other scenarios, like the extreme mass-ratio regime [201, 202] or binary neutron star coalescences [29, 80]. Here we focus on binary BHs in the comparable-mass regime only, as they are the most promising sources for the upcoming generation of ground-based GW detectors whose detection and interpretation may require information both from PN and NR.

In Table 3.4 we provide an overview of selected, recent models for this regime. Apart from an alias (partially adopted from the LIGO-Virgo collaboration [183, 184]) we indicate the inspiral model which is either based on the EOB approach or derived from Taylor-expanded PN quantities. The NR codes that contributed to the construction of the given models are the Spectral Einstein Code (`SpEC` [164, 175]), `BAM` [52] and `MayaKranc` [189], where the few `SpEC` waveforms are notably long and accurate, the `BAM` simulations provide the largest diversity in parameter space with moderately long waveforms, and the data calculated with `MayaKranc` are the only precessing simulations used to calibrate analytical models to date.

Other distinctive features of the models listed in Table 3.4 are for example as follows:

- PhenomB/C are closed-form frequency-domain representations of the GW; EOBNR and PhenSpin provide the signal in terms of time-domain differential equations.
- EOBNR models can readily be extended beyond the dominant spherical harmonic

Alias	Ref.	Inspiral	NR code	Calibration range	Calibrated parameters
EOBNR	[77]	EOB	SpEC, BAM	$q \leq 4$ & $q \to 0$ no spins	2 dynamical from $q = 1$ + fits from $q \in \{1, 2, 4\}$
EOBNR	[144]	EOB	SpEC	$q \leq 6$ & $q \to 0$ no spins	2 dyn.+4 waveform par. 5 modes from 5 NR runs
Phenom*B*	[16]	T1	BAM	$q \leq 4$ & $q \to 0$ aligned spins	6 phase, 4 amplitude from 24 NR simulations
Phenom*C*	[162]	F2	BAM	$q \leq 4$ aligned spins	6 phase, 3 amplitude from 24 NR simulations
PhenSpin	[178]	T4	MayaKranc	$q = 1, \chi_i = 0.6$ precession	2 phase param. 24 NR sim.+4 Phenom*B*

Table 3.4: A selection of recent complete waveform models for BH binaries with comparable masses on quasi-spherical orbits. We summarize the reference where the model was described, the approximate inspiral waveforms and NR codes that were employed, the parameter range in which each model was calibrated (q is the mass ratio) and the number of parameters and NR simulations used to build the model.

of the GW, whereas the phenomenological models and PhenSpin solely provide the signal in terms of the $\ell = 2, m = \pm 2$ spin-weighted spherical harmonic modes.

- The PhenSpin model is a first attempt to model generic precessing spin configurations, but it is so far only calibrated to equal-mass systems and dimensionless spin magnitudes of 0.6. All other models in Table 3.4 are only applicable to nonspinning systems or systems where the spin of each BH is aligned (or antialigned) with the total orbital angular momentum.

In the aligned-spin case, both phenomenological waveform families reduce the two spin parameters to one "total" spin (3.37). As recently shown by Ajith [10], this degeneracy in the spin parameters can be further optimized, and it will be an important goal for future models to describe as many physical effects as possible with the smallest possible number of parameters. In the nonspinning case, all waveforms presented here are parametrized in terms of the *physical* parameters total mass and symmetric mass ratio (plus initial time and phase) but it may be useful both from the modeling and the search point of view to refrain from this parametrization strategy once all additional spin dynamics are included. Note that very recently, an EOBNR prototype was proposed that includes aligned-spin configurations [145, 180], but this first exploratory study only employed two equal-mass simulations (performed with SpEC) with equal spins $\chi_1 = \chi_2 \approx \pm 0.44$.

Apart from the listed facts, there are many more procedures involved in checking the validity of proposed models. Most importantly, it has been shown to some extent that the models mentioned here all agree to reasonable accuracy with the waveforms they were derived from, but also with waveforms that were *not* in the construction set. Thus, with an increasing number of available numerical simulations, all these models can not only be extended and refined, they can also be cross-checked extensively until, ideally, one can confidently interpolate over the entire parameter space independent of the set of waveforms actually used to calibrate the model.

Chapter 4

Reliability of hybrid waveforms

4.1 Basic approach to quantify errors

4.1.1 Motivation

This chapter is devoted to the question of how confident we can be with a final hybrid PN+NR waveform. After all, we demonstrated in Chapter 3 that one can find a smooth connection between the two parts of a (supposedly common) GW signal, but the use of this waveform in actual analysis algorithms of GW interferometers requires a much deeper error analysis with a quantitative understanding of the uncertainty introduced in the modeling process. Most results presented here have been published in [139, 140].

Let us recapitulate the choices that had to be made along the way outlined in Chapter 3.

- Which PN formulation should be employed?
- What *physical parameters* in PN and NR are consistent with the other framework?
- Which NR resolution, extraction formalism etc. is sufficient?
- How long do the NR waveforms have to be?
- What is the appropriate way to match analytical and numerical data?

When constructing a complete waveform, each of these questions has to be answered and different choices lead to slightly different results. The important conclusion we shall draw from this is that none of the complete IMR waveforms is based on an unambiguous construction, and the spread of possible results that different reasonable choices yield is a measure of the uncertainty within the modeling process.

The following sections are devoted to quantifying the different sources of uncertainty. One after another, we shall vary an ingredient of the waveform construction slightly (i.e., we will compare slightly different choices) while keeping the others unchanged. The basic mathematical scheme for this comparison is introduced in Sec. 4.1.2 and it is then subsequently applied to errors in the NR regime, hybridization errors and finally errors coming from the PN part of the signal. The latter will turn out to dominate the error budget by far, and we shall refine the error estimate to allow for realistic accuracy requirements that are meaningful for GW data-analysis applications.

4.1.2 Defining an error measure

Particular for the PN inspiral part of the signal, we lack a well-defined notion of error. Hence, we shall quantify the waveform uncertainty in the following sense. Let

$$h = h_+ - i\,h_\times \tag{4.1}$$

be the complex GW strain that combines the plus and cross polarization of the GW as the real and imaginary part, respectively. (We omit the superscript $\ell = 2$, $m = 2$ here, but we implicitly refer to this particular dominant mode, if not stated otherwise.) It is subject to several errors, and we account for these errors here simply by the fact that one could have taken slightly different ingredients $h_{\rm PN}$ and $h_{\rm NR}$ for the same physical scenario. These could be different post-Newtonian approximants and numerical data from different codes or different resolutions. Denoting the different waveform models by h_1 and h_2, we calculate the mismatch

$$\mathscr{M} = 1 - \mathscr{O}(h_1, h_2) = 1 - \max_{\phi_0, t_0} \frac{\langle h_1, h_2\rangle}{\|h_1\|\,\|h_2\|} \tag{4.2}$$

$$= 1 - \max_{\phi_0, t_0} \left[4\,\mathrm{Re} \int_{f_1}^{f_2} \frac{\tilde{h}_1(f)\tilde{h}_2^*(f)}{S_n(f)} \frac{df}{\|h_1\|\|h_2\|} \right], \tag{4.3}$$

where ϕ_0 and t_0 are relative phase and time shifts between the waveforms and $\|h\|^2 = \langle h, h\rangle$. S_n is the noise spectral density of the assumed detector, * indicates the complex conjugation and (f_1, f_2) is a suitable integration range. $\mathscr{O}$ is called the overlap (or match) of the two waveforms. In the following, we will consistently use $f_1 = 20$Hz and S_n is given by the analytic fit of the design sensitivity of Advanced LIGO [15]. The upper integration bound f_2 is given by our waveform model, and we use $f_2 = 0.15/M$, although the results do not depend sensitively on this value (M is the total mass of the binary).

We use this formulation to quantify the agreement of h_1 and h_2, because it is directly adopted from the matched-filter detection strategy, as we have outlined in Sec. 2.3.3. Broadly speaking, the mismatch indicates here how "close" h_1 and h_2 are. Smaller values for $\mathscr{M}$ represent smaller errors in the waveform model, given that h_1 and h_2 are approximations of the same signal. Direct conclusions can be drawn from calculating the mismatch. If $\mathscr{M}$ is less than some threshold, we regard the final hybrid as *accurate enough* for the purpose in question. If, for example, up to $x = 10\%$ of the detectable signals may be missed due to a mismatch of real and modeled waveform, we can allow this mismatch to be at most $\mathscr{M} = 1 - \sqrt[3]{1-x} \approx 3.5\%$, disregarding the addition from a discrete template spacing. If we account for the latter, one may decrease the accepted mismatch in the waveform modeling to 1.5% (see a similar discussion in [102]) or even 0.5% as suggested in [125].

A generally more stringent requirement is that the uncertainty we have in the modeling is *indistinguishable* by the detector. Such a statement is obviously dependent on how "loud" the signal is in the detector. As discussed in [125] and further detailed in [82, 123] we can write the indistinguishability criterion as

$$\|h_1 - h_2\|^2 < \epsilon^2\,, \tag{4.4}$$

where the waveforms are optimally aligned in the sense of (4.3) and ϵ parametrizes the effective noise-increase due to model uncertainties. The minimal requirement for h_1 and

h_2 to be indistinguishable is $\epsilon = 1$, although [82] argues that $\epsilon \sim 1/2$ and probably less are more reasonable thresholds. Manipulating (4.4) under the assumption of equal norms[1], $\|h_1\| = \|h_2\| = \|h\|$, leads to the equivalent inequality (see a similar calculation in [132])

$$\begin{aligned} \|h_1 - h_2\|^2 = \langle h_1 - h_2, h_1 - h_2\rangle &= \|h_1\|^2 + \|h_2\|^2 - 2\langle h_1, h_2\rangle \\ &\approx \|h\|^2\Big[2 - 2\mathcal{O}(h_1, h_2)\Big] = 2\|h\|^2\mathscr{M} \end{aligned} \tag{4.5}$$

$$\Rightarrow \ (4.4) \iff \mathscr{M} < \frac{1}{2\rho_{\rm eff}^2}\,, \tag{4.6}$$

where $\rho_{\rm eff} = \|h\|/\epsilon$ is the effective SNR of the signal.

When we later calculate $\mathscr{M}$ as a measure of the error in hybrid waveforms, we can set various thresholds based on $\mathscr{M} < \mathscr{M}_{\rm max}$ or Eq. (4.6) to evaluate the reliability of current models. Defining a threshold for $\mathscr{M}$ is commonly associated with the problem of signal detection whereas the criterion (4.6) is often used to quantify the performance in estimating parameters of an unknown signal. However, the quantities as we have introduced them here miss additional optimizations that are performed in actual searches and we shall elaborate on the implications of that below. Let us just point out here that the mismatch in the form of Eq. (4.3) (i.e., without further optimizations over physical parameters) assesses the quality of a single waveform, but not of a *waveform family*.

4.2 Errors in the NR regime

We start quantifying the uncertainties in hybrid waveforms by analyzing the NR contribution. Quantifying errors is an important and very natural process for numerical integrations, and the uncertainty of NR waveforms is usually given in terms of phase and amplitude errors. Through some additional assumptions, these can be related to quantities like the mismatch (4.3) [123–125], but we shall directly calculate $\mathscr{M}$ here and show phase and amplitude errors only for illustrative purposes.

The examples we choose are two nonspinning configurations with mass ratios 1 and 2. NR data were obtained for each case with the `Llama` code [150] and Table 4.1 summarizes the information that is relevant for a hybridization of these data with PN inspiral waveforms. The simulations were performed at different resolutions to verify the convergence of the code. The lower-resolution runs we consider here employed a finest grid spacing of $0.025M$ ($q = 1$) and $0.02M$ ($q = 2$) and the high-resolution grid spacing was $0.02M$ ($q = 1$) and $0.016M$ ($q = 2$), respectively. Since we aim at matching the NR waveforms in the frequency domain to a frequency-domain PN approximant, we first Fourier transform the NR GW signal and then use Richard extrapolation (assuming 8th order convergence for the phase and 4th order for the amplitude) to obtain an estimate of the "exact" data in the frequency domain.

The differences of the data sets obtained at different resolutions are first illustrated in terms of phase and amplitude errors, see Fig. 4.1. We show the shape of each function and

[1] Instead of equal norms, we may also consider $\|h_2\|/\|h_1\| = 1 + \delta$, which leads at linear order in δ the following approximation: $\|h_1 - h_2\|^2 \approx 2\|h_1\|\|h_2\|\mathscr{M}$.

q	$D_{\rm ini}\,[M]$	$r_{\rm ex}\,[M]$	$M\omega_{\rm ini}$ (GW)	GW cycles	length $[M]$
1	11	∞	0.05	15.6	1350
2	10	500	0.05	12.7	920

Table 4.1: `Llama` simulations of coalescing binary BHs with mass ratio 1 and 2. We provide the initial separation $D_{\rm ini}$ of both BHs, the extraction radius of the GW (Cauchy-characteristic extraction was used in the equal-mass case [156]), the earliest "usable" GW frequency $\omega_{\rm ini}$ (3.12), the number of GW cycles before merger and the length (after removing the junk radiation) of the simulation. All GW-related quantities refer to the $\ell = 2, m = 2$ mode. These waveforms have been submitted to the NINJA project [27].

the difference

$$\Delta\zeta = \zeta_{\text{low res.}} - \zeta_{\text{high res.}} \tag{4.7}$$

(where ζ denotes either phase or amplitude, both in the time and frequency domain). In the time domain, we only compare the high with the low resolution data, whereas in the frequency domain, we also include the Richardson-extrapolated data. As any practical use of the waveforms (e.g., in a search algorithm or hybridization scheme) possibly employs a free global time and phase translation, we exploited this freedom as well through a minimization of the phase difference over an interval in time or frequency, respectively. The results presented in Fig. 4.1 depend on this choice, and we performed the least-square fits over $t/M \in (-1235, 112)$ ($q = 1$), $t/M \in (-770, -72)$ ($q = 2$) and $Mf \in (0.02, 0.09)$ for both cases.

Particularly due to this freedom of aligning the waveforms, phase and amplitude comparisons are ambiguous and it is hard to find a well-defined notion of *the error*, see a detailed discussion in [104]. There are still some conclusions we can draw from Fig. 4.1. First, the numbers obtained in the time and the frequency domain can differ considerably, and a specific accuracy goal (e.g., a phase error of at most X rad) does not mean very much if the alignment procedure and the domain are not prescribed (see also the discussion about the waveform length in [126]). Note that we show the originally extracted Newman-Penrose scalar Ψ_4 (see Sec. 2.5) in the time domain, but the strain h in the frequency domain. However, due to our conversion from Ψ_4 to h (2.101), the errors shown for $\tilde{h}$ are the same as for $\tilde{\Psi}_4$. The other observation we can clearly make from a relative comparison of the errors shown in Fig. 4.1 is that the $q = 2$ case exhibits larger errors than the $q = 1$ case, and we anticipate these to originate from the generally more demanding treatment of two BHs with unequal masses, but also from the extraction of the GW signal which is done only in the $q = 1$ simulation by Cauchy-characteristic extraction [156], recall Table 4.1.

Having illustrated the discrepancies between different resolutions of the same integration, we shall now turn to the computation of the mismatch between the resulting waveforms. We are interested in the effect of finite-resolution errors on the entire hybrid waveform, hence we hybridize each NR waveform with the appropriate TaylorF2 inspiral (see Sec. 3.3.2), matched over $Mf \in (0.01, 0.02)$. We then calculate $\mathscr{M}$ between the Richardson-extrapolated version and a finite-resolution variant of the full waveform. Our result is shown in Fig. 4.2, from which we conclude that current state-of-the-art techniques used for the equal-mass waveforms lead to errors in the hybrid waveform that are negligible.

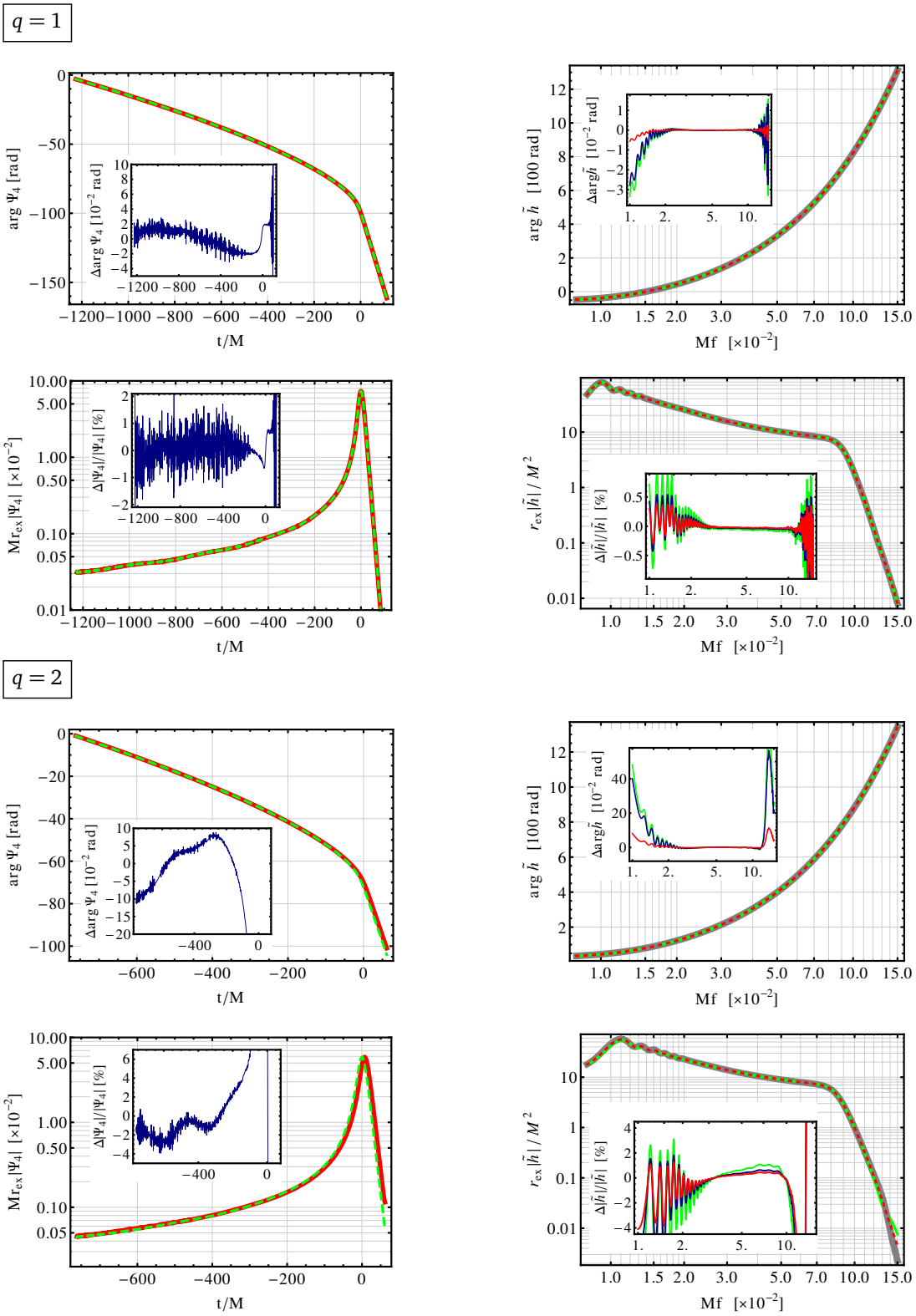

Figure 4.1: The two NR simulations summarized in Table 4.1 performed with different resolutions. The left column presents the amplitude and phase in the time domain, the right column shows the equivalent quantities in the frequency domain. The low-resolution data (and its difference to the Richardson extrapolation) is shown in green, the high-resolution data is drawn in red. The blue lines show the difference between low and high resolution, the gray lines in the Fourier domain are the Richardson-extrapolated data.

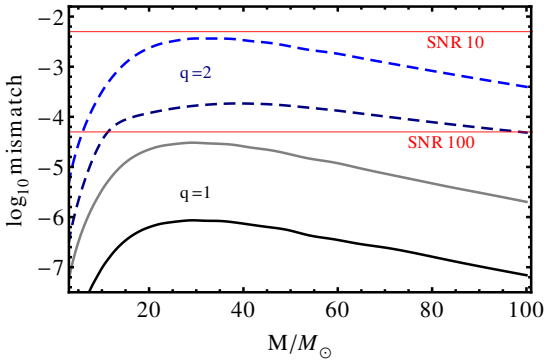

Figure 4.2: The mismatch (4.3) of hybrid waveforms that employ NR data with different resolutions. The curves compare Richardson-extrapolated data with high-resolution and low-resolution runs, respectively (from bottom to top). The lower solid lines belong to $q = 1$ simulations, the blue dashed lines are for $q = 2$. Horizontal red lines show the threshold of indistinguishability according to (4.6).

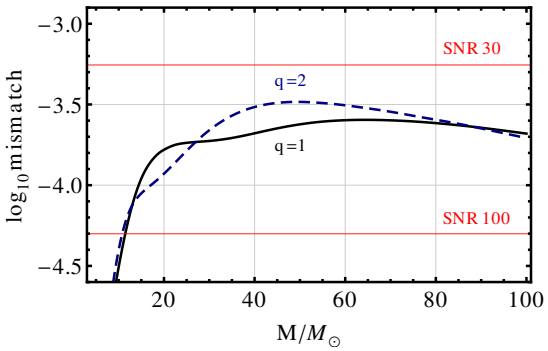

Figure 4.3: The mismatch (4.3) of hybrid waveforms that employ NR data from either the `Llama` or the `BAM` code. The black solid line illustrates the equal-mass case, the blue dashed curve compares simulations of a binary with mass ratio $q = 2$. Horizontal red lines show the threshold of indistinguishability according to (4.6).

Even the low-resolution data cause a mismatch error indistinguishable for events as loud as effective SNR 100. In agreement with the time-domain behavior, Fig. 4.1, the $q = 2$ simulations exhibit larger discrepancies, which serve as a conservative estimate of the NR resolution error. The high-resolution run we would use to construct waveform templates, however, leads to mismatches that are still not greater than 1.9×10^{-4}, which is below the noise confusion up to SNRs of 50.

Similar plots have been published in [128, 162] for partly different numerical simulations, but with comparable numbers. In addition, the joint efforts of the "Samurai" project [107] proved the consistency of NR waveforms by comparing numerical simulations of equal-mass, nonspinning binaries from five different NR codes. No completion of the waveforms with PN inspiral signals was considered as the focus laid primarily on the NR data and their errors. Therefore, the mismatches reported in [107] are restricted to high frequencies, thus high masses of the system (total mass $> 180M_\odot$), and values of $\mathscr{M} < 10^{-3}$ are found.

In the future, such consistency checks have to be repeated in different parts of the parameter space to ensure that the relatively small errors found so far can be assumed generally. As we have access to numerical simulations from two different codes, `Llama` and `BAM` [52], we can conclude our estimates here by calculating the mismatch of hybrids with NR data from these different codes. This does not only quantify the effect of finite resolutions, but takes into account a mixture of various additional features of the codes, such as the grid setup, the gauge, the wave extraction formalism and many other details. The result we present in Fig. 4.3 is very satisfactory. Although the disagreement between different codes is greater than the finite-resolution error of the respective "best" run (highest resolution for `BAM` and Richardson extrapolation for `Llama`), we still find that the

additional ambiguities do not cause deviations of the waveform that would considerably affect the search for GW signals with low and moderate SNR.[2] Of course, in the rare occasion of an extremely loud event, one would have to investigate the accuracy of the waveform templates further and maybe consider performing dedicated, highly accurate NR simulations for that case. For the most urgent goal of preparing full waveform templates for "every-day use" in Advanced LIGO, however, current NR simulations are good enough to be incorporated in hybrid waveforms.

4.3 Hybridization errors

The next source of uncertainty we shall discuss in this section is related to the fact that there are different strategies to combine two parts of supposedly the same waveform into one signal. As we have shown in Sec. 3.2, one is forced to overlap analytical and numerical results in the late merger regime (as early as the NR simulation permits), so one cannot expect that they agree perfectly, and there is some ambiguity about the way an "optimal alignment" of both waveform parts is defined. Most common in the construction process is to decompose the GW h into phase ϕ and amplitude A by $h = Ae^{i\phi}$. The alignment of the inspiral and NR parts is then carried out by minimizing a phase difference, either over an entire interval or at discrete points, utilizing the frequency $\omega = d\phi/dt$ as well.

A detailed analysis of various aspects involved in such procedures was already discussed in Sec. 3.4 and also published in [128, 162]. For example, we calculated in our example of a frequency-domain matching that the relative time shift between both waveform parts can be determined, in the best case, up to an uncertainty of $\Delta t_0/M \approx 0.15$ (Fig. 3.12) [162]. Ref. [128] complements this statement by estimating that $\Delta t_0/M \lesssim 1$ is required for an accurate matching with $\mathscr{M} < 2\times 10^{-4}$. In addition, the recommended matching interval is formulated in terms of the frequency evolution $\omega_1 \to \omega_2$ within this interval, and [128] suggest $(\omega_2 - \omega_1)/\omega_m \gtrsim 0.1$ (where ω_m is the transition frequency from PN to NR).

We shall pursue a direct comparison of various hybridization procedures here and express their differences again in terms of the mismatch. We consider three hybridization strategies, each connecting a nonspinning equal-mass simulation performed with BAM with the corresponding TaylorT4 PN approximant.

Time-domain matching 1: After choosing a matching frequency ω_m, the relative time shift t_0 between NR and PN waveform is determined by enforcing

$$\frac{d\phi_{\rm NR}}{dt}(t_m) = \omega_{\rm NR}(t_m) = \omega_m = \omega_{\rm PN}(t_m + t_0) = \frac{d\phi_{\rm PN}}{dt}(t_m + t_0)\,. \tag{4.8}$$

The waveforms are then matched at the moment in time where the frequency reaches ω_m, and the relative phase shift is obtained by demanding continuity in the phase,

$$\phi_{\rm NR}(t_m) = \phi_{\rm PN}(t_m + t_0) + \phi_0\,. \tag{4.9}$$

As a result, the transition from the PN phase to its NR complement is carried out at a single point. A similar transition is also realized for the amplitude, but there is no

[2] Note that a similar plot was published in [162]. Fig. 4.3 is an updated version of this previous analysis. We now find smaller errors due to an improved post-processing of the waveforms.

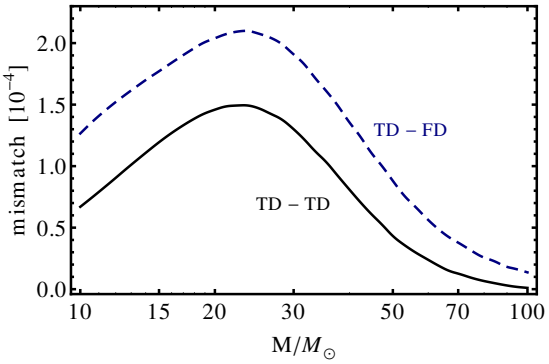

Figure 4.4: The mismatch (4.3) of hybrid waveforms for nonspinning, equal-mass BHs. The difference that is measured here originates solely from different hybridization procedures, where the solid black line indicates the mismatch between two time-domain methods, and the blue dashed curve is a comparison between a frequency-domain matching and the time-domain method 1 (see text).

freedom left to align the waveforms. Instead, we simply search for the point in time where the PN and NR amplitudes agree and match them there. Note that we chose to hybridize the Newman-Penrose scalar Ψ_4 instead of the strain h, and the latter was calculated afterwards in the frequency domain by dividing $\tilde{\Psi}_4$ by $-(2\pi f)^2$.

Time-domain matching 2: A different time-domain matching procedure was used in [14, 15], and we adapt it here for Ψ_4. The specific method is to choose again a matching frequency, ω_m, and to then locate the time in both the PN and NR waveforms when that frequency is reached. We then combine the two waveforms over a $200M$-long window, aligning the waveforms such that the quantity

$$\Delta\Psi = \int_{t_1}^{t_2} \left|\Psi_{4,\mathrm{NR}}(t) - a\, e^{i\phi_0}\, \Psi_{4,\mathrm{PN}}(t+t_0)\right|^2 dt \tag{4.10}$$

is minimized, where t_1 and t_2 are respectively $100M$ before and after the time t_m at which the NR waveform reaches ω_m, a is a scale factor, t_0 and ϕ_0 are time and phase offsets. The hybrid is constructed by making a linear transition between $\Psi_{4,\mathrm{PN}}$ and $\Psi_{4,\mathrm{NR}}$ over the matching window.

Frequency-domain matching: The third hybridization method to compare is a variant of the frequency-domain matching described in Sec. 3.3.2 and [162]. We produce an FFT of the time-domain TaylorT4 approximant and an FFT of the numerical Ψ_4 data. The phase of the frequency-domain PN and NR signals is then matched in the interval $\omega \in (\omega_1, \omega_2)$, and the points where the Fourier-domain phases and amplitudes agree, respectively, are taken as the transition frequencies from PN to NR.

For the results we show in Fig. 4.4 (which is an updated version of Fig. 1 in [102]) we used a matching frequency of $M\omega_m = 0.07$ for the time-domain procedures and a matching interval of $M\omega \in (0.0566, 0.113)$ in the Fourier domain, which lead to a phase matching frequency $M\omega_m = 0.068$.

We see that the maximum mismatch is about 0.015% between the two time-domain hybrids[3] and 0.02% between the time-domain and frequency-domain hybrids. Clearly the error due purely to the hybridization procedure is, like the mismatch error of the numerical

[3]The numbers we present here are slightly less than the published ones in [102], because a more efficient mismatch routine now allows for a more accurate minimization with respect to the time shift.

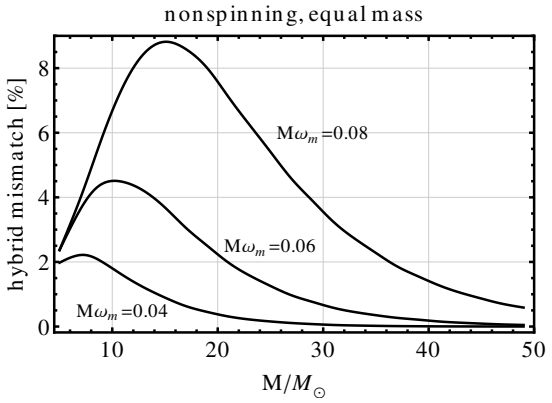

Figure 4.5: The mismatch (4.3) of hybrid waveforms for nonspinning, equal-mass BHs, each employing the same NR data, but the inspiral in obtained either with the TaylorT1 or TaylorT4 approximant. The matching frequency between NR and PN is indicated next to each curve.

waveforms, negligible. If we consider the indistinguishability criterion (4.6), then these hybrids would be indistinguishable for SNRs of $\rho_{\text{eff}} < 50$. However, let us point out that these results are calculated in the equal-mass, nonspinning case with and the TaylorT4 approximant that accidentally agrees extremely well with later merger NR data.

We further note that the difference between hybrids constructed with ostensibly the same numerical waveforms and PN approximants may have larger differences than those shown here. For example, if we compare either of the hybrids we have just described, with hybrids constructed using the integrated wave strain, as in [14, 15], then the mismatch can be as high as 0.8%. This is due not to the hybridization process, but to artifacts introduced in the time-domain integration of Ψ_4 to h. For a more detailed discussion of this integration see Sec. 2.5 and [157].

4.4 Uncertainty of the inspiral waveform – NR length requirements

So far, we applied the strategy outlined in Sec. 4.1.2 to estimate the uncertainty in the NR part of the waveform and the hybridization process. Both error sources turned out to be tolerable. Now we consider the long PN inspiral part of the hybrid waveform, where it is particularly difficult to find a well-defined notion of error. As a practical criterion, we shall compare different PN approximants, all consistently constructed to highest available PN order and completed with common NR data. The result is that the mismatch of such hybrids is *orders of magnitude* greater than what we calculated so far.

As an example, Fig. 4.5 shows the mismatch of hybrid waveforms that were constructed with the NR waveform of a SpEC equal-mass, nonspinning simulation [2, 165], but with inspiral waveforms either from the TaylorT1 or TaylorT4 approximant. The matching frequencies are chosen as $M\omega_m = 2\pi M f_m \in \{0.04, 0.06, 0.08\}$, and the stitching procedure is carried out in the Fourier domain as explained in Sec. 3.3.2 and [162]. The mismatch errors we obtain are of the order of a few percent, whereas those from Figs. 4.2 to 4.4 are a factor of 100 or more smaller.

Having realized that the dominant source of error in the full waveform is the PN part, particularly at high frequencies not yet covered by NR, one simple solution to reduce its

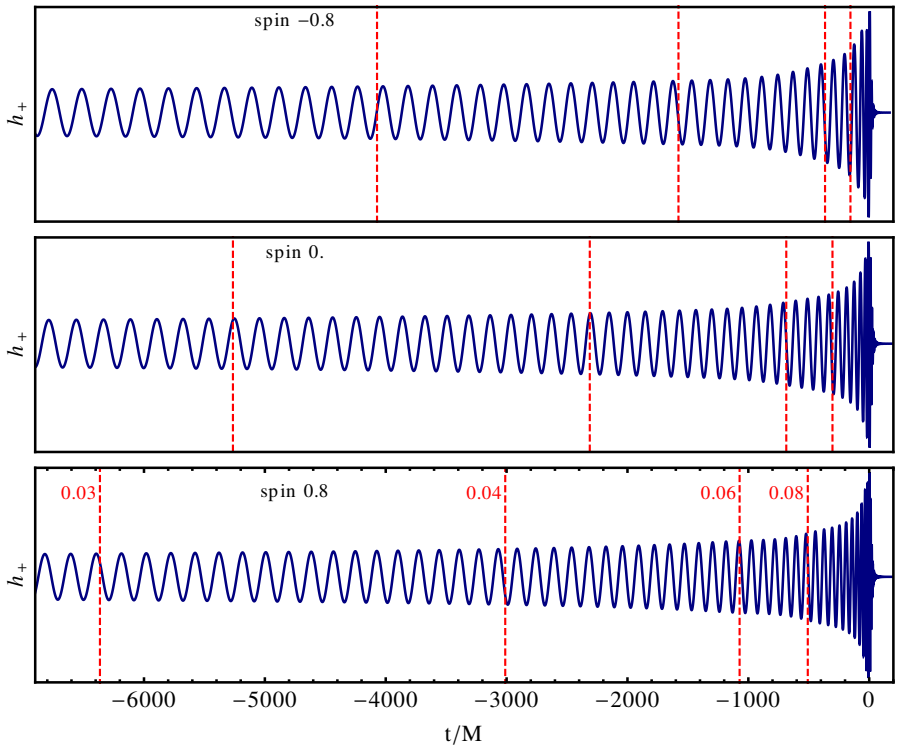

Figure 4.6: Full IMR waveforms (constructed from the phenomenological model [162]) for equal-mass BHs with spins aligned to the orbital angular momentum and dimensionless spin parameter −0.8, 0 or 0.8 (from top to bottom). The vertical lines show the moment in time when a particular instantaneous frequency $M\omega = Md\phi/dt$ is reached. The indicated frequencies are the same for each case; the time when they are reached differs, however, due the highly spin-dependent frequency evolution.

influence is to employ longer NR signals and use accordingly smaller matching frequencies. This effect is also illustrated in Fig. 4.5. Indeed, reducing ω_m does reduce the mismatch error everywhere (i.e., for all values of the total mass), but the computational costs are immense. If we would require a mismatch not greater than, say, 1.5%, then not even $M\omega_m = 0.04$ would be good enough in the nonspinning case, and the situation is most likely worse for spinning and unequal-mass systems.

To demonstrate what such matching frequencies mean in terms of simulation length, Fig. 4.6 illustrates how many GW cycles of the $\ell = 2$, $m = 2$ mode are required to reach a certain frequency. Evidently, NR waveform length requirements depend not only on the desired $M\omega_m$ but also on the physical parameters to be modeled. A system with BHs that highly spin parallel to the orbital angular momentum is characterized by a decelerated frequency evolution of the binary. Thus, a particular matching frequency means more orbits to be simulated numerically than in the nonspinning or the anti-aligned spin case.

With these issues in mind, it is very important to carefully estimate the PN-induced error of hybrid waveforms throughout the parameter space. This will not only complete the error assessment of full waveforms, it will also lead to very important conclusions about how long NR waveforms actually have to be to allow a meaningful combination with PN data. This is a major input to be provided by the waveform modeling community, otherwise the limited computational resources are in danger to be spent inefficiently.

We shall address these issues in the following sections, starting with deeper insights into the structure and the calculation of the mismatch $\mathscr{M}$. The results of our first parameter study will be that far more NR orbits are required than currently possible to reduce the mismatch to an acceptable level. Calculating $\mathscr{M}$ in the form of (4.3), however, only allows for limited conclusions due to the following restriction: the efficacy of a model in a search is determined by the best match between the true waveform and *any waveform* in the search model. This best match (called the fitting factor, see Sec. 2.3.3) should be calculated not only by comparing two candidates but by maximizing the match over all of the physical parameters of the model. With access to hybrids from discrete points in the parameter space, we are only able to maximize the match over the total mass of the binary, which should lead to (possibly very) conservative estimate of waveform length requirements. Only an enhanced error estimate based on the generalization of (mis)matches to fitting factors will lead to data-analysis relevant statements about the accuracy of *waveform families*, and we shall introduce the appropriate concept in Sec. 4.5.

4.4.1 Refined mismatch calculations

To simplify our calculations, recall that the full hybrid is is constructed from a PN description $h_{\rm PN}$ and the NR part $h_{\rm NR}$. We assume that the transition from $h_{\rm PN}$ to $h_{\rm NR}$ is enforced at a single frequency

$$\tilde{h}(f) = \begin{cases} \tilde{h}_{\rm PN}(f)\,, & \text{for } f \leq f_m \\ \tilde{h}_{\rm NR}(f)\,, & \text{for } f > f_m \end{cases}\,, \tag{4.11}$$

where $\tilde{h}$ denotes the Fourier transform of h and f_m is the matching frequency. Such a procedure can be employed in a direct Fourier-domain construction of the hybrid [162], but it is also approximately true for time-domain hybrid constructions (see the detailed description in Sec. 3.3). In the latter case, the transition is carried out at a time t_m, where the instantaneous frequency is $\omega(t_m) = \frac{d\arg h}{dt} = 2\pi f_m$. Then, for (4.11) to be true, we have to assume that

1. the transition frequency in the Fourier domain is equal to the instantaneous matching frequency calculated in the time domain;
2. the signal at times $t < t_m$ only significantly affects the Fourier domain for $f < f_m$ and $t > t_m$ correspondingly determines the wave for $f > f_m$.

These assumptions are not trivial since the Fourier integral is a "global" transformation. However, it was shown that assuming such a stationarity is reasonable in a regime where both PN and NR are valid [162]. In addition, we just showed in Sec. 4.3 that time- and frequency-domain construction methods lead to very similar results.

To gain some insights on the structure of Eq. (4.3) and simplify the mismatch in the case where only the PN-inspiral parts of the waveforms differ, we further assume:

3. Following our earlier findings and [107, 162] we regard the error on the NR side as small, negligible compared to the uncertainties PN introduces up to currently practical matching frequencies.

4. Independent of the PN approximant that is used, the norm of the waveforms are to high accuracy the same (i.e., only the phase is affected). This is reasonable to take as a good approximation, because the amplitude description in PN is usually formulated as a function of the orbital frequency [24, 34, 42] (which we again identify with the content on the Fourier side as well) and the mismatch is much more sensitive to phase differences than to amplitude discrepancies.

Let us now consider a binary BH system with fixed physical parameters. Our error measurement assumes the construction of two hybrid waveforms that differ in the PN part only. Their overlap reads

$$\begin{aligned}\mathcal{O}(h_1,h_2) &= 1-\mathcal{M}(h_1,h_2)\\ &= \max_{\phi_0,t_0}\left[4\,\mathrm{Re}\int_{f_1}^{f_2}\frac{|A_1A_2|}{S_n}e^{i(\phi_1-\phi_2)}\,e^{i(2\pi f\,t_0+\phi_0)}\frac{df}{\|h_1\|\|h_2\|}\right],\end{aligned} \tag{4.12}$$

where $A_i=|\tilde{h}_i|$ and $\phi_i=\arg\tilde{h}_i$. The effect of a time and phase shift of one waveform with respect to the other is explicitly written out in the second exponential term.

Assuming two PN models (PN1 and PN2) combined with the same NR waveform we trivially obtain the phase difference

$$\phi_1-\phi_2=\begin{cases}\phi_{\mathrm{PN1}}-\phi_{\mathrm{PN2}} & ,f<f_m\\ 0 & ,f\geq f_m\,.\end{cases} \tag{4.13}$$

Note that (4.13) is only true for one particular alignment of the two waveforms, any other relative shift in time or phase leads to an additional dephasing, also beyond f_m. Since we have separated this effect explicitly in (4.12), we are, however, free to write $\phi_1-\phi_2$ as in (4.13). The open question is the functional form of the PN phase-difference (or simply the PN phase error) in the case where the NR part of h_1 and h_2 are perfectly aligned. Here we have to apply an actual matching procedure, although we can use any preferred method *without* having NR data at hand. The key property of (4.13) we are exploiting is that only PN-PN differences are taken into account, and a direct PN-NR comparison is not necessary. The only input we need from NR simulations is the amplitude $|\tilde{h}|=A_1=A_2$ for $f>f_m$. A good estimate for that can be taken from phenomenological models, such as the ones introduced in Sec. 3.5 and [16, 162], where the Fourier-domain amplitude is approximated by a closed-form analytic description. A similar approach was recently suggested by Boyle [45] who realized that it is sufficient to combine PN approximants with *ersatz* NR data which he takes from the EOBNR model [56, 57, 61, 145]. We independently derive an algorithm here that is based on the same perceptions but highlights that no NR phase information *at all* is needed.

The final global time and phase shift used in (4.12) to maximize the overlap is simply a (phase shifted) inverse Fourier transform of the remaining integrand. Its maximal real part is obtained by choosing ϕ_0 (for any t_0) such that the generally complex number lies on the real axis.

Based on that, our final algorithm for estimating hybrid mismatch errors caused by the uncertainty in the PN model is the following:

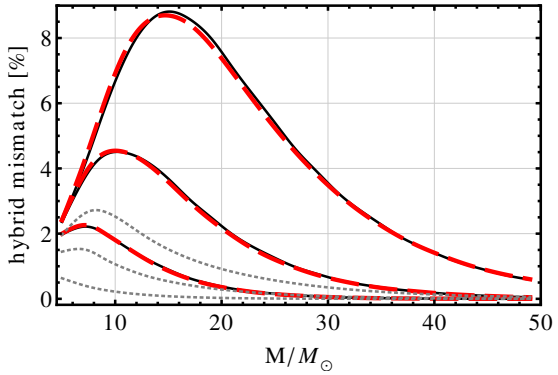

Figure 4.7: Hybrid mismatches in the equal-mass, nonspinning case. Black solid lines are mismatches of actual TaylorT1/T4+NR hybrids, whereas the red dashed lines are our estimates obtained without directly using any NR data (NR amplitude taken from a phenomenological model). The gray dotted lines describe the PN mismatch contribution derived in (4.14) that does not include a possible dephasing of the NR part. The matching frequencies for each set are from bottom to top $M\omega_m = 0.04, 0.06, 0.08$.

1. Calculate the two PN waveforms expressing the uncertainty to be quantified.
2. Apply the matching procedure such that one PN approximant is matched to the other at f_m (as if it were the NR waveform).
3. Fourier transform the aligned PN waveforms and keep the data for $f \in [f_1, f_m]$.
4. Complete the waveforms in the Fourier domain by using an existing expression for the amplitude in the range $f \geq f_m$, e.g., from phenomenological models [16, 162] or from a short NR simulation. Set the phase in this regime to 0 (or any other function, but equal for both $\tilde{h}_1$ and $\tilde{h}_2$).
5. Calculate the overlap of $\tilde{h}_1$ and $\tilde{h}_2$ by maximizing the magnitude of the inverse Fourier transformation.

To test the efficacy of our approach, we return to the nonspinning, equal-mass example of Fig. 4.5 and superimpose the results of our simplified calculation. The agreement illustrated in Fig. 4.7 is excellent in all cases. As expected by the relatively small effect of the amplitude on the mismatch calculation, our method proves to be fairly robust with respect to the chosen amplitude description in the NR regime. In fact, the dashed lines in Fig. 4.7 use the phenomenological model detailed by Santamaría *et al.* in [162] but there is no noticeable difference when we use the model presented by Ajith *et al.* in [16].

4.4.2 Mismatch contributions

The method presented above can readily be applied to estimate the inspiral uncertainty of hybrids with the caveats mentioned in the introduction to Sec. 4.4, and we shall do so in Sec. 4.4.3. For now, however, let us manipulate the mismatch (4.3) further to separate the various contributions to it. We make this important aside to point out that, although only the PN contribution is considered as ambiguous here, its influence on the final waveform error is twofold: directly through the (power-weighted) PN mismatch and in terms of an additional dephasing, also of the "exact" high-frequency part.

We can see these two effects separately through the following instructive lower bound on $\mathscr{M}$ which is obtained under the list of assumptions detailed in Sec. 4.4.1.

$$\mathscr{M} = 1 - \frac{4}{\|h\|^2} \max_{\phi_0, t_0} \left[\mathrm{Re} \int_{f_1}^{f_m} \frac{\tilde{h}_1 \tilde{h}_2^*}{S_n} df + \int_{f_m}^{f_2} \frac{|\tilde{h}|^2}{S_n} df \right]$$

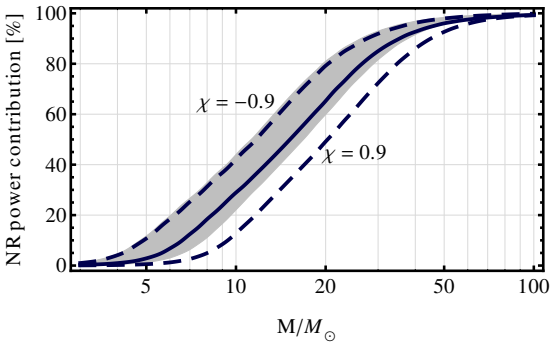

Figure 4.8: Power contribution of an NR waveform containing 10 orbits before merger to the complete signal. The solid line indicates a non-spinning binary with mass ratio $q = 4$, the dashed lines are the corresponding binaries with spins (anti)aligned to the orbital angular momentum. For comparison, the area enclosed by $q = 2, \chi = \pm 0.9$ systems is included in gray.

$$\geq 1 - \max_{\phi_0, t_0} \frac{\langle h_1, h_2 \rangle}{\|h\|^2_{(f_1,f_m)}} \frac{\|h\|^2_{(f_1,f_m)}}{\|h\|^2} - \frac{\|h\|^2_{(f_m,f_2)}}{\|h\|^2}$$
$$= \frac{\|h\|^2_{(f_1,f_m)}}{\|h\|^2} \mathscr{M}_{\rm PN} \,. \tag{4.14}$$

Here we introduced the notation $\|h\|^2_{(a,b)}$ to specify the integration range. $\mathscr{M}_{\rm PN}$ is the mismatch of the PN part only, restricted to $f < f_m$. In the first line of (4.14) we use the fact that the amplitudes agree (in fact, we do not require pointwise agreement, only the norm is assumed to be the same) and that $h_1 = h_2$ for $f > f_m$. The second line is a lower estimate because the maximization was originally carried out by shifting the entire waveforms relative to each other, whereas now we allow the maximization over the PN part alone. The final step involves the obvious relation $\|h\|^2 = \|h\|^2_{(f_1,f_2)} = \|h\|^2_{(f_1,f_m)} + \|h\|^2_{(f_m,f_2)}$.

The interpretation of (4.14) is straightforward: the mismatch of hybrids is determined by the uncertainty of PN [restricted to the frequency range (f_1, f_m)] multiplied by the fraction of power that is coming from the PN part of the wave signal. This fundamental error, independent of the actual PN/NR fitting, is directly inherited from the differences of standard PN approximants and any PN/NR matching cannot be better than the result of (4.14). Put differently, the maximally achievable reduction of the PN mismatch error is given by the relative power contributed by the NR waveform. In Fig. 4.8, we show $\|h\|^2_{(f_m,f_2)}/\|h\|^2$, where f_m is chosen such that 10 NR orbits before merger are assumed for each set of physical parameters (data obtained through the phenomenological model [162]). In agreement with our previous discussion (see, e.g., Figs. 4.6 and 4.7) we see that modeling antialigned spins and large total masses requires a smaller number of NR orbits than large aligned spins (hangup case) and smaller masses.

In view of the simple form of (4.14), one might be tempted to conclude that analyzing the overlaps or fitting factors (or whatever strategy is appropriate) of different PN approximants directly leads to conclusions of how reliable the hybrid is for a particular choice of f_m. When we compare, however, the mismatch of actual hybrid waveforms with the estimate (4.14) we find that the latter is considerably less than $\mathscr{M}$. An illustration of that is included in Fig. 4.7, where we show the lower bound (4.14) in comparison with the actual (and accurately estimated) mismatches.

Why is the hybrid disagreement that much greater than what is expected from PN in the given frequency range? The reason can be identified from the derivation of (4.14), where we effectively allow an optimal alignment (for each M) of both PN models while

independently keeping the NR part *perfectly aligned*. In a true hybrid mismatch calculation, one the other hand, a time and/or phase shift always affects the *entire PN+NR hybrid*, and an optimal alignment of one part leads to a dephasing of the other. This effect is not caused by an erroneous matching, but an illustration of the fact that the optimal choice of t_0 and ϕ_0 in the sense of Eq. (4.3) is mass (frequency)-dependent for the PN models we consider.

Finally, by considering the obvious generalization of (4.14),

$$\mathscr{M} \geq \frac{\|h\|^2_{(f_1,f_m)}}{\|h\|^2}\,\mathscr{M}_{\rm PN} + \frac{\|h\|^2_{(f_m,f_2)}}{\|h\|^2}\,\mathscr{M}_{\rm NR}\,, \tag{4.15}$$

we can identify the three main contributions to the hybrid uncertainty: The PN and NR error, each weighted by the power they contribute to the signal, and the misalignment caused by the fact that in the hybridization procedure the PN wave is aligned at high frequency which is potentially different from the optimal alignment for lower frequencies. The procedure introduced in Sec. 4.4.1 automatically takes the dominant PN error and possible misalignments (also of the NR part) into account.

4.4.3 PN errors, part I (mismatches)

Now that we have established an algorithm to predict mismatches of full waveforms with an ambiguous inspiral part, we can exploit the computationally cheap procedure and calculate $\mathscr{M}$ for many different physical scenarios. Our aim is to show how "reliable" the final combination of PN and NR waveforms is in different points of the parameter space, assuming that the physical parameters are fixed from the outset.

First, let us highlight again that ideally, we are interested in the mismatch of the approximate waveform model to the true one. Since we cannot calculate the latter (which would also make the whole discussion pointless), we estimate the PN uncertainty by calculating the mismatch between different approximants. This can certainly be no more than a rough estimate since we are not aware of any principle that would guide us to which approximants at which PN order should be compared in order to obtain a well-defined notion of the PN error.

To still reach some understanding of the uncertainty in currently used high-order PN models we present the anticipated hybrid mismatches when the approximants TaylorT1, TaylorT4 and TaylorF2 are used. Recall that TaylorT1 and T4 are solutions of ordinary differential equations in the time domain describing the adiabatic inspiral of the BBH on quasicircular orbits, whereas TaylorF2 is a frequency-domain description based on the stationary phase approximation. Details on these approximants can be found in Sec. 2.4.2 as well as, e.g., in [48, 58] and references therein. Throughout this thesis, we always employ the highest currently determined PN order, i.e., 3.5PN accurate phasing with spin contributions up to 2.5PN (and incomplete terms at higher order) and the 3PN amplitude expansion [42] including up to 2PN spinning corrections [24].

As in the construction of phenomenological models, we restrict the parameter space to black holes with comparable masses and spins aligned or antialigned with the orbital angular momentum of the binary $\boldsymbol{L}$ (with its unit vector denoted by $\hat{\boldsymbol{L}}$). Then, each spin

can be parameterized by just one dimensionless quantity,

$$\chi_i = \frac{\boldsymbol{S_i} \cdot \hat{\boldsymbol{L}}}{m_i^2}\,, \quad i = 1, 2, \tag{4.16}$$

where m_i and $\boldsymbol{S}_i$ are mass and spin of the individual black hole, respectively. By exploiting a degeneracy in the spins, as observed in [158, 189], the parameter space can be further reduced, and we only use the mass-weighted total spin

$$\chi = \chi_1\, m_1/M + \chi_2\, m_2/M \tag{4.17}$$

and the symmetric mass-ratio

$$\eta = \frac{m_1 m_2}{M^2} \tag{4.18}$$

to label the different physical setups. (In fact, in the following analyses, each point with fixed χ is represented by $\chi_1 = \chi_2 = \chi$.)

To assess how the accuracy of currently feasible hybrid waveforms varies in the parameter space, we apply the algorithm outlined in Sec. 4.4.1 for different mass-ratios ranging from equal masses to 4:1, with spin magnitudes from -0.9 to 0.9 in each case. For every pair (η, χ) one obtains mass-dependent mismatches in the form of Fig. 4.7 that generally increase with increasing matching frequency $M\omega_m$.

Several plots illustrating this behavior can already be found in the literature. Contour plots of the mismatch as a function of mass and matching frequency are the main result of Boyle [45], and we obtain similar results by continuously varying $M\omega_m$, e.g., in Fig. 4.7. Taking the maximum mismatch with respect to the total mass instead (i.e., only considering the peaks in Fig. 4.7), Fig. 4 by Damour, Nagar and Trias in [82] shows the inaccuracy of TaylorF2 hybrids compared to EOBNR as a function of the matching frequency. Figure 11 by MacDonald, Nissanke and Pfeiffer in [128] presents a similar study with Taylor approximants and actual NR data. Given some slightly different choices in our approaches (especially lower cutoff frequency and detector noise curve) the results we obtain are fully consistent with the numbers presented in the articles mentioned.

Generally, the conclusions [45, 82, 128] draw are sobering regarding GW detections and parameter estimation. The mismatches found are too high, current numerical relativity waveforms are *by far* too short and hybrids are consequently too inaccurate. In the following, we illustrate the basis of these statements and expand the existing knowledge by exploring the parameter space. To reduce the dimensionality of the problem, we calculate the maximum of the mismatch with respect to the total mass and fix $M\omega_m = 0.06$ (which corresponds to approximately 10 GW cycles before the maximum of $|h(t)|$ in the equal-mass case, see Fig. 4.6).

In Fig. 4.9 we show contour plots that compare either TaylorT1 with TaylorT4 hybrids or TaylorT1 with TaylorF2 hybrids. The matching frequency is fixed at $M\omega_m = 0.06$. Certainly, we could include many more variants of PN approximants (including different versions of EOBNR), but we find it sufficient to present some general conclusions that become already clear from the examples chosen here. As reported before [82, 102] we see that deviating from equal-mass cases, the disagreement generally becomes larger. This effect

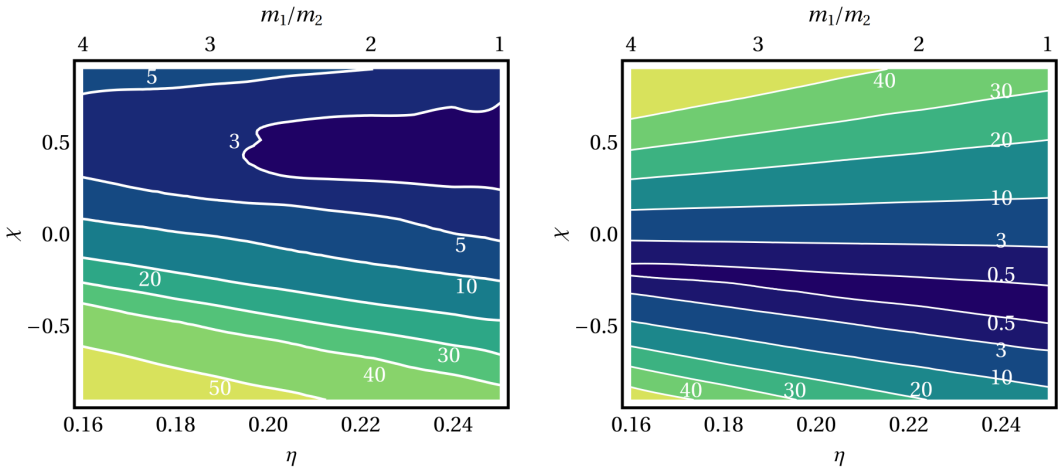

Figure 4.9: Contour plots of the mismatch (in %) between different fictitious hybrids, as a function of the symmetric mass-ratio η and equal aligned spins with dimensionless magnitude χ. *Left panel:* PN part either defined by the TaylorT1 or TaylorT4 approximant. *Right panel:* Comparison of TaylorT1 and TaylorF2 in the PN part.

is even more pronounced when increasing spin magnitudes are considered. Heuristically we can understand the worse performance for increasing spins by the simple fact that spin contributions are only included up to 2.5PN order, whereas nonspinning terms are known up to relative 3.5PN order. Surprisingly, the 'island' or 'band' of minimal mismatch does not occur strictly around vanishing spin magnitudes, indicating that different approximants can *by chance* agree extremely well in some portions of the parameter space. For completeness, let us report that the TaylorT4/TaylorF2 mismatch yields a pattern similar to the right panel of Fig. 4.9 but with minimal values moved to weakly positive spins.

The conclusions suggested by Fig. 4.9 and results from previous work [45, 128, 162] are indeed disappointing. If the mismatches caused by different PN approximants actually represent a reasonable estimate for the uncertainty in currently practical hybrid waveforms, then values up to $\mathscr{M} \approx 50\%$ are certainly unacceptable. Reducing the matching frequency, thereby demanding longer NR waveforms, does reduce the mismatch everywhere, but it leads to unrealistic requirements in many portions of the parameter space.

To illustrate this, Table 4.2 addresses two important questions by analyzing the TaylorT1/TaylorF2 hybrid mismatches in selected points in the parameter space. First, what is the required matching frequency if a desired accuracy has to be fulfilled? Note that due to our algorithm we overcome the restriction of currently available NR waveform lengths that the authors in [128, 162] were facing. We also do not rely on assuming a particularly promising "candidate waveform" to act as a long NR waveform as was done in [45, 102]. In fact, phase information above $M\omega_m$ is not required and does not enter the result; we can simply apply our algorithm to arbitrarily small matching frequencies. For each set of parameters we take the maximal mismatch with respect to the total mass M (which we, however, restrict to $M \geq 5M_\odot$ for computational reasons) and thus obtain the monotonically increasing function $\max_M \mathscr{M}(M\omega_m)$. By demanding either $\mathscr{M} < 3\%$ as the most relaxed requirement or the more stringent case of indistinguishable differences for effective SNRs of at most 20 [see (4.6)] we obtain the values given in Table 4.2. In

q	χ	$M\omega_m[\times 10^{-2}]$		$M_{\rm min}/M_\odot$ ($M\omega_m = 0.06$)	
		$\mathscr{M} < 3\%$	$\rho_{\rm eff} < 20$	$\mathscr{M} < 3\%$	$\rho_{\rm eff} < 20$
1	0.0	3.93 *(23)*	1.15 *(212)*	15	40
2	0.2	2.40 *(68)*	0.99 *(313)*	25	49
3	0.5	1.70 *(155)*	0.84 *(499)*	33	57
4	0.8	1.38 *(268)*	0.75 *(730)*	38	61

Table 4.2: Faithfulness of hybrid waveforms based on a TaylorT1/TaylorF2 comparison for selected physical parameters. The required matching frequency is reported if either a 3% maximal mismatch $\mathscr{M}$ can be tolerated or if the error should be indistinguishable for SNRs less than 20, see (4.6). The parentheses indicate the number of GW cycles to the maximum of $|h(t)|$. The two right columns assume $M\omega_m = 0.06$ and give the minimal mass, where the waveforms are accurate enough in the sense described above.

parentheses we also give the number of GW cycles from $d\phi_{\rm GW}/dt = \omega_m$ to the maximum of $|h(t)|$ as predicted by the phenomenological waveform model [162].

It is unlikely that the typical length of "long" numerical waveforms will change by an order of magnitude before the advent of Advanced LIGO, and so a more practical question is: given a currently achievable NR waveform length, in which mass-range is the PN+NR hybrid accurate enough? As an example we assume again a matching frequency of $M\omega_m = 0.06$ and show on the right-hand side of Table 4.2 the minimal masses the hybrid is accurate for in the sense detailed above. For comparison, the pure NR part occupies the entire frequency band down to 20Hz for masses $M \geq 97M_\odot$. Note that, distinct from [82], we do not consider errors *above* $M\omega_m$ here, since we have shown that the errors of *hybrid waveforms* are dominated by an ambiguous PN part. Additional effects have to be taken into account when possibly fitted closed-form waveform models are considered. Therefore, our values for $M_{\rm min}$ are less than the corresponding results in [82] that are based on the comparison of EOBNR and the phenomenological model of [16].

The obvious message from Table 4.2 is that *in general* extremely long NR simulations would be needed to overcome the intrinsic uncertainty in standard PN formulations for given physical parameters. For NR waveforms containing so many cycles our assumption that their intrinsic error can be neglected is possibly no longer valid, which would lead to even higher modeling errors. Anyway, the numbers presented are only an "order of magnitude" estimate in this most conservative approach. The reader should always keep in mind that our notion of error is based on comparing different, at highest available order consistent PN descriptions and especially concrete statements for particular points in parameter space may be spoiled by an (un)fortunate choice of approximants (see a similar discussion in [102]). More importantly, as we shall show in the next section, fixing the physical parameters of the waveforms from the outset greatly overestimates the uncertainty for signal detection.

4.5 PN errors, part II (fitting factors)

4.5.1 Estimating fitting factors for hybrid waveforms

The accuracy assessment presented in Sec. 4.4 only allows for very limited conclusions about the actual utility of hybrid waveforms in various applications. Apart from the restrictions coming from our limited understanding of the PN error there is also an important fact we have neglected so far: in astrophysically relevant applications the knowledge of physical parameters like total mass, mass ratio and spin is never *exact*. If a set of hybrid waveforms constitutes a *waveform family* which is used to extract information from an unknown signal, then the standard matched-filter procedures rely on varying (and maximizing with respect to) such parameters. The accuracy of the predicted "best-fit" parameters is once again limited by the detector noise and the modeling error and even if the latter exceeds the first, one may still argue that a tolerated bias does not significantly reduce the scientific output from GW detections.

In this section we shall therefore consider combinations of NR data with a particular PN approximant as the ingredients of an entire manifold of waveforms, parametrized by an absolute time and phase scale (t_0 and ϕ_0) as well as the physical parameters introduced before: M (total mass), η [symmetric mass-ratio (4.18)] and χ [spin combination (4.17)]. The efficiency of detecting a signal defined by t_0, ϕ_0, M, η and χ is properly quantified through the fitting factor

$$\mathrm{FF} = \max_{M',\eta',\chi'} \mathcal{O}\Big[h_1(M',\eta',\chi'), h_2(M,\eta,\chi)\Big]. \tag{4.19}$$

Note that the maximization with respect to t_0 and ϕ_0 is already included in the definition of the overlap $\mathcal{O}$, see (4.12).

The accuracy threshold for detection we quoted before is indeed defined including this additional maximization, i.e., in terms of

$$\mathcal{M}_{\mathrm{FF}} = 1 - \mathrm{FF}\ . \tag{4.20}$$

If a waveform family $\{h_1\}$ satisfies $\mathcal{M}_{\mathrm{FF}}(h_1, h_2) < \mathcal{M}_{\max}$ (with sufficiently small $\mathcal{M}_{\max}$) then it is said to be *effectual* in the detection of the target signal h_2 [73]. The results in Sec. 4.4.3 are only a lower bound on this effectualness.

The accuracy requirements for parameter estimation are naturally more demanding than those for detection. In the recent literature [82, 125, 128, 162] the *faithfulness* of waveforms was usually defined by the criterion (4.4) (without optimization with respect to physical parameters), thereby demanding that the maximal information can be extracted from the data without being restricted by the model itself. Here, however, we want to understand faithfulness in the original sense introduced in [73] that is based on the difference of the target waveform parameter λ with the recovered model parameter $\bar{\lambda}$ for which (4.19) is maximal. If this bias $\Delta\lambda = \bar{\lambda} - \lambda$ is small enough, we can still accept the waveform model family as sufficiently accurate, even for parameter estimation. Therefore, by analyzing $\mathcal{M}_{\mathrm{FF}}$ and the corresponding parameters we can sensibly make analogous conclusions as before, but based on the actual optimization strategy that is employed in current template-based GW searches.

Because of the additional freedom of varying physical parameters we now have to calculate the *ambiguity function*

$$\mathscr{A}(\boldsymbol{\lambda}', \boldsymbol{\lambda}) = \mathscr{O}\left[h_1(\boldsymbol{\lambda}'), h_2(\boldsymbol{\lambda})\right] \tag{4.21}$$

between hybrids constructed from the same set of NR waveforms but members of different PN approximants. It depends on the parameters of the waveforms, $\boldsymbol{\lambda}'$ and $\boldsymbol{\lambda}$, as well as the waveform models themselves.

Since the phase difference above $M\omega_m$ in the overlap integral (4.12) does not vanish generally for $\boldsymbol{\lambda}' \neq \boldsymbol{\lambda}$, we have to slightly modify the algorithm presented in Sec. 4.4.1. In particular, we now need an estimate of how small changes in physical parameters affect the phase difference in the assumed NR regime. (The PN regime is affected as well, but there is no qualitative difference to the PN comparison incorporated before.) One possible strategy to quantify phase changes along variable physical parameters is to perform a number of numerical simulations and interpolate between the data obtained. Depending on the density of samples in the η and χ directions (the scaling with M is given trivially by a single simulation), such a procedure can be very time- and resource-consuming. However, the phenomenological fittings performed in [14–16, 162] (and also described in Sec. 3.5) have utilized exactly this type of interpolation, and we conveniently use the result of [162] here because the fitting there is localized to frequencies close to and in the NR regime.

Finally, to ensure the proper relative alignment, our algorithm to calculate $\mathscr{A}$ for arbitrary (in practice small) variations in all parameters is to match different PN approximants to a phenomenological waveform (phase and amplitude) that is used above $M\omega_m$ resulting in a hybrid $\tilde{h}(f; M, \eta, \chi, t_0, \phi_0)$.

Let us highlight that although we are now building PN+phenomenological hybrids our analysis is not assessing how accurate individual waveforms describe the entire coalescence process. Note for instance that we could have introduced this hybridization concept already in the previous section, but, as we have shown, the phase above the matching frequency did not enter the overlap calculation. Similarly now, we use the phenomenological phase description merely to model the M-, η- and χ-dependence at higher frequencies. Figure 4.10 illustrates what kind of information we are using by plotting slices of the ambiguity function of the phenomenological model with itself for the case $\eta = 0.2$ (mass-ratio ≈ 2.6), $\chi = 0.3$ and $M/M_\odot \in \{10, 50, 100\}$. In Sec. 4.4 we only exploited $\mathscr{A} = 1$ for $\boldsymbol{\lambda}' = \boldsymbol{\lambda}$ whereas now we need an estimate of the shape of $\mathscr{A}$ also for $\boldsymbol{\lambda}' \neq \boldsymbol{\lambda}$ (although for small $|\boldsymbol{\lambda}' - \boldsymbol{\lambda}|$).

We can make two immediate observations from Fig. 4.10. Especially for small masses we see that relatively small changes in, for instance, symmetric mass-ratio or total mass (the other parameters are kept constant, respectively) modify the waveform considerably, so that the high mismatches for equal parameters (reported, e.g., in Figs. 4.7 and 4.9) could potentially be reduced drastically by only small variations in the physical parameters of one model waveform. Although the formal criterion (4.4) for faithfulness (or better indistinguishability) failed, the fitting factor could still be extremely close to unity with a minimal bias in the parameters. The second interesting observation from Fig. 4.10 is that the width around the maximum of the ambiguity function increases towards higher masses so that a comparison of two waveforms is increasingly insensitive to parameter changes at higher frequencies. This in turn endorses our assumption that the fitting factors and biases

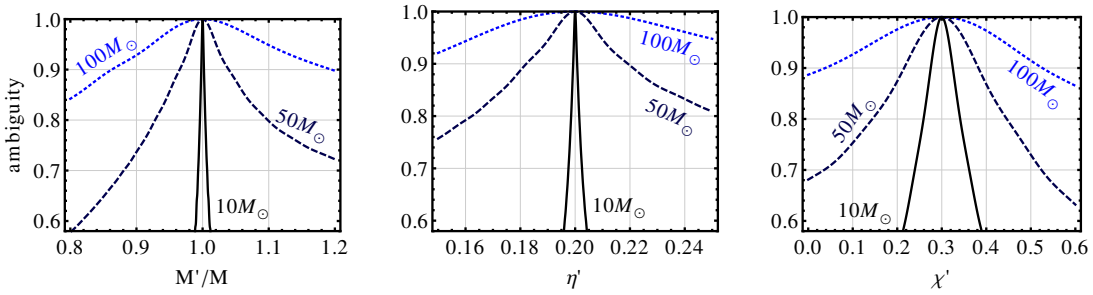

Figure 4.10: The ambiguity function (4.21) between two phenomenological waveforms [162], where h_2 is fixed with $\eta = 0.2$, $\chi = 0.3$ and the total mass as indicated in the plots. The parameters of h_1 are varied individually while the others are kept constant at the values of h_2, respectively.

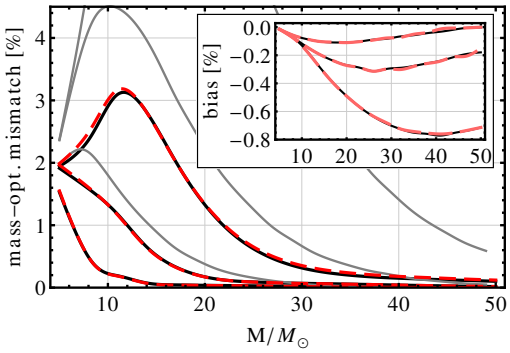

Figure 4.11: The mass-optimized mismatch between equal-mass, nonspinning TaylorT1/TaylorT4+NR hybrids (black solid lines) compared to our NR-free estimate (dashed lines). The matching frequencies are $M\omega_m \in \{0.04, 0.06, 0.08\}$ from bottom to top. The gray lines show the results of nonoptimized mismatches for comparison, see also Fig. 4.7. The inset illustrates the relative bias in the total mass (matching frequencies in reverse order).

we shall calculate are dominated by PN effects (and not the choice of data above $M\omega_m$) for small masses, where the accuracy requirements turned out to be hardest to satisfy.

4.5.2 Comparison with previous results

Before exploring fitting factors across the parameter space, let us present two examples that illustrate the general conclusions we shall draw in this section. We first come back to the canonical equal-mass, nonspinning case and the TaylorT1/TaylorT4 comparison that was employed before (see Fig. 4.7 and [102]). To test the validity of our approach we again compare our estimate to hybrids constructed with actual NR data (matched at $M\omega_m \in \{0.04, 0.06, 0.08\}$, respectively). Because of the unavailability of NR data with arbitrary η and χ, we for now only optimize with respect to the total mass M. Note that the results shown in Fig. 4.11 fully agree with the analysis of Hannam *et al.* [102] (see Fig. 6 therein). They not only confirm that our combination of PN and phenomenological data accurately predicts the disagreement of the "true" PN+NR hybrids, one can also observe the striking improvement when the additional maximization with respect to M is taken into account. The peak mismatch without optimization was approximately 8.8%, 4.5% or 2.2%, depending on $M\omega_m$. With mass optimization we instead find $\mathscr{M}_{\mathrm{FF}} < 3.2\%$, 2.0% and 1.5%, respectively. The relative bias in the total mass, $(\bar{M} - M)/M$, is always less than 0.8% and the earlier the matching is performed the smaller the bias becomes.

A subsequent question that has not been answered so far is to what extent further optimizations, say along the symmetric mass-ratio and the spin(s) of the model system, improve the agreement between the waveform families even more. Full fitting factor

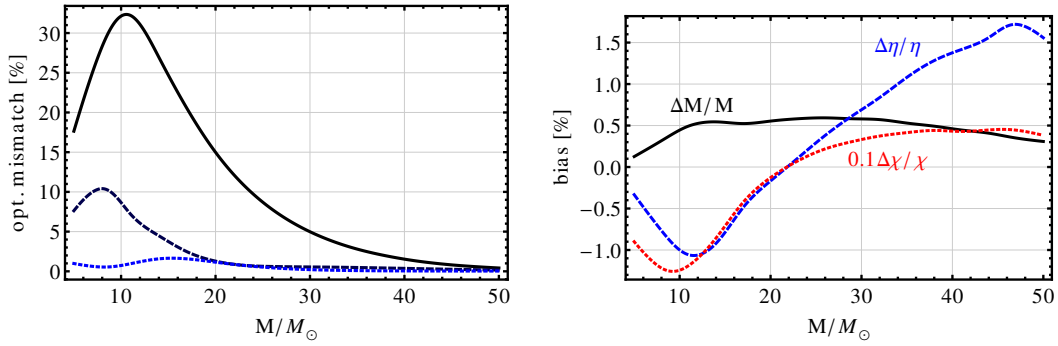

Figure 4.12: Mismatch between TaylorT1- and TaylorF2-based waveforms for mass ratio 4:1, $\chi = 0.5$ and matching frequency $M\omega_m = 0.06$ (left panel). The mismatch is not optimized (top solid line), mass-optimized (dashed line) or optimized with respect to all physical parameters of the TaylorF2-based model (lowest dotted line). The bias in the parameters are provided on the right panel.

calculations are commonly used to compare waveform models (see, e.g., [58, 82]), but they have not been employed in the context of hybrid waveforms and studies of the required length of numerical waveforms. Reference [102] only applied a crude estimation of the effect an additional mass-ratio optimization has, and concluded that a (total) mass-optimization alone serves as a sufficient assessment of the full fitting factor. We now find that this conclusion was incorrect. We illustrate the effect of further optimizations through the comparison of TaylorT1- and TaylorF2-based waveforms (matched at $M\omega_m = 0.06$) in Fig. 4.12. The TaylorT1 target signal is fixed as a system with mass-ratio 4:1 and spin $\chi = 0.5$, a point in parameter space that clearly fails all accuracy requirements when looking at Fig. 4.9. By maximizing with respect to M, however, the maximal mismatch drops from 32.2% to 10.4%. Varying all three considered physical parameters finally yields a curve with $\mathscr{M}_{\rm FF} \approx 1.6\%$ at maximum, making the TaylorF2-based family accurate enough for detection. The relative bias in the parameters are less than 1% for M, of the order of 1% for η and $\lesssim 10\%$ for χ.

Note that a faithfulness analysis, as in Sec. 4.4 and [45, 128], would conclude that NR waveforms with many hundreds of cycles are necessary to produce hybrids (and consequently waveform models) that are sufficient for parameter estimation purposes. Here we see that waveforms that we might at first sight regard as far too inaccurate, in fact may yield relatively small parameter biases when embedded in a waveform family.

After this insightful study of a selected example, let us extend our analysis to a set of target waveforms, distributed in parameter space. The optimization algorithm with respect to physical parameters is computationally more challenging than maximizing the inner product with respect to t_0 and ϕ_0 only. For each set of test parameters (η, χ) we have to construct a new waveform. Since TaylorF2 is an analytical closed-form PN description that is fast to evaluate and our matching to the phenomenological model is performed directly in Fourier space [162] we only consider TaylorF2 hybrids as test waveforms h_1. For the fixed target waveforms h_2 we chose to employ the TaylorT1 approximant, because it was shown in Sec. 3.2 and [104] that its (dis)agreement to premerger NR data is most robust over the considered parameter space and [45] noted that a maximal uncertainty estimate involves comparing to TaylorT1 inspirals.

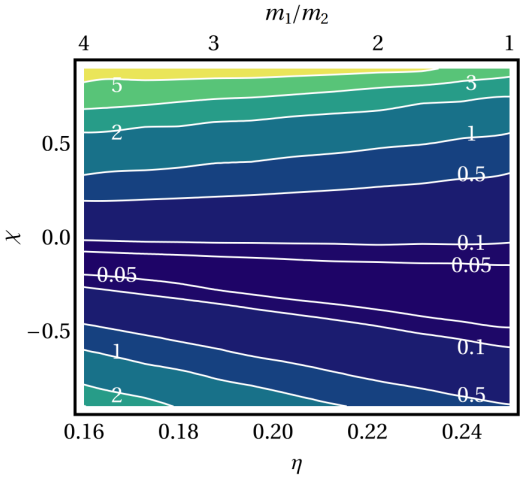

Figure 4.13: The maximum of the optimized mismatch (in %) for hybrids constructed either with TaylorT1 (target signal) or TaylorF2 (template signal) and a matching frequency of $M\omega_m = 0.06$.

Starting with equal parameters $\boldsymbol{\lambda}' = \boldsymbol{\lambda}$, we search for the nearest local maximum of the overlap $\mathcal{O}(h_1, h_2)$ by varying $\boldsymbol{\lambda}'$ along the gradient of the overlap. Thus, we ensure a quickly converging improvement after a relatively small number of iterations. The results we present, however, do not take into account the entire distribution of the ambiguity function and are still only a lower bound on the fitting factor. Given the tremendous decrease in mismatch for relatively small changes in physical parameters we argue nevertheless that this local extremum should serve as a reasonable estimate of the error one has to assume in terms of the fitting factor.

We repeat the exploration of the parameter space with a study similar to the one presented in Fig. 4.9. The matching frequency is again fixed at $M\omega_m = 0.06$ and we calculate $\mathscr{M}_{\text{FF}}$, Eq. (4.20), for masses $5M_\odot \leq M \leq 20M_\odot$. We checked that the mismatch decreases towards the boundaries of this interval, so that the enclosed maximum can indeed be regarded as the global extremum. After performing this maximization of the mismatch with respect to M for fixed (η, χ), we present our results as a contour plot in Fig. 4.13. The structure is very similar to the pattern of the nonoptimized mismatch, cf. the right panel of Fig. 4.9. The obvious difference is, however, that calculating the detection-relevant quantity $\mathscr{M}_{\text{FF}}$ instead of the diagonal mismatch $1 - \mathscr{A}(\boldsymbol{\lambda}, \boldsymbol{\lambda})$ results in numbers that are ~ 10 times less than what was considered before as error estimates.

This allows for very different conclusions: Even a moderate matching frequency like the one considered here leads to hybrids that are accurate enough for detection in a large portion of the parameter space. Simulating NR waveforms with few (< 10) orbits should hence be good enough for many applications considering systems with moderate spins and mass-ratios. Although this is a very broad statement, it is clearly distinct from previous analyses [45, 82, 128] that concluded *much longer* NR waveforms are needed to sensibly connect them to standard PN approximants.

Of course, Fig. 4.13 only shows the optimal agreement between the two considered waveform families and one might fear that the difference between simulated and recovered parameters is large in some parts of the parameter space. However, as anticipated by Fig. 4.12, the bias in total mass and symmetric mass-ratio are small, approximately $\pm 1\%$ and $\pm 1.5\%$ at most, respectively. The spin parameter χ is uncertain by $-0.15 \leq \Delta\chi \leq 0.05$.

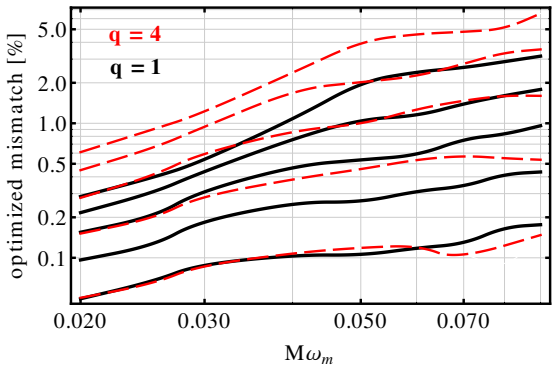

Figure 4.14: The fully optimized mismatch $\mathscr{M}_{\rm FF}$ as a function of the matching frequency $M\omega_m$ for equal-mass systems (solid lines) and mass-ratio 4:1 (dashed lines). The considered spins in each case are $\chi \in \{0, 0.2, 0.4, 0.6, 0.8\}$ from bottom to top.

A deeper analysis of these biases is beyond the scope of this paper and results are likely more model-dependent than the general conclusions we present here.

For completeness, we note that for increasing values of the simulated spin, $\Delta\eta$ and $\Delta\chi$ generally decrease from positive to negative values, ΔM increases at the same time. This correlation is expected from the form of the PN expansion, where modifications of M can be compensated at lowest order by changing η inversely. Studies of PN approximants in [58] show similar tendencies, although the biases reported there are considerably higher due to the absence of a common NR part at high frequencies. The same holds for the comparison of complete models (including uncertainties in the NR regime) [82]. The modeling biases we find should be compared to statistical errors of full waveform families. In the case of the nonspinning phenomenological model [15] a Fisher matrix study as well as Monte-Carlo simulations were presented in [11], and the uncertainties found for Advanced LIGO and signals of SNR 10 are $\Delta M/M \lesssim 3\%$ and $\Delta\eta/\eta \lesssim 8\%$ ($M < 100M_\odot$). These values are of the same order of magnitude as our results, and we take this as an indication that modeling errors do not vastly dominate the parameter estimation uncertainty. However, a deeper study of Fisher-matrix estimates in Sec. 4.6 shall rank the modeling errors properly.

4.5.3 Model accuracy for spinning systems

These new results constitute much brighter prospects for currently feasible NR simulations than the conclusions drawn in Sec. 4.4 and [45, 82, 102, 128]. In certain parts of the parameter space, however, the mismatch error presented in Fig. 4.13 is still too high, particularly if one keeps in mind that gaining sensitivity of GW detectors is extremely difficult on the hardware side and theoretical considerations should reduce this sensitivity as little as possible [82]. Therefore, $\mathscr{M}_{\rm FF} > 3\%$ for highly spinning systems should be improved by considering lower matching frequencies. Equally important is the question of whether numerical simulations for systems with moderate spins and mass ratios can be considerably shorter than $M\omega_m = 0.06$ which we assumed so far.

In Fig. 4.14 we analyze the dependence of the mismatch error by showing the maximum of $\mathscr{M}_{\rm FF}$ as a function of $M\omega_m$. We consider equal masses and mass-ratio 4:1 with spins $\chi \in \{0, 0.2, 0.4, 0.6, 0.8\}$ in each case. Note that we do not include negative values of χ here, because the fact that the mismatch error for $\chi < 0$ is smaller and not monotonic in χ (see Fig. 4.13) is likely an artifact of our choice of PN approximants (recall the obvious differences in Fig. 4.9). As expected, Fig. 4.14 illustrates that reducing the matching

orbits	equal-mass	mass-ratio 4:1
5	*1.5%:* $-0.76 < \chi < 0.60$	*3.0%:* $-0.95 < \chi < 0.55$
	0.5%: $-0.37 < \chi < 0.31$	*1.5%:* $-0.52 < \chi < 0.39$
10	*1.5%:* $-1.00 \leq \chi < 0.70$	*3.0%:* $-1.00 \leq \chi < 0.68$
	0.5%: $-0.45 < \chi < 0.39$	*1.5%:* $-0.56 < \chi < 0.48$
20	*0.5%:* $-0.97 < \chi < 0.57$	*3.0%:* $-1.00 \leq \chi < 0.79$
	0.2%: $-0.28 < \chi < 0.22$	*1.5%:* $-0.92 < \chi < 0.55$

Table 4.3: Range in spin parameter χ where a given accuracy requirement ($\mathscr{M}_{\rm FF} < 3\%, 1.5\%, 0.5\%$ or 0.2%) is fulfilled. Each row specifies the assumed number of orbits before merger for the NR waveform (= number of GW cycles divided by 2).

frequency, e.g., from $M\omega_m = 0.08$ to $M\omega_m = 0.02$, leads to an improvement in mismatch by a factor of 2 to 10, depending on the spin.

Larger values of the spin generally yield larger mismatches which in turn leads to stronger requirements for $M\omega_m$, assuming a given accuracy goal. This is unfortunate because the orbital hangup configuration of positive aligned spins decelerates the frequency evolution in the inspiral of the binary, demanding even longer simulations for a given frequency range.

As such extremely long NR waveforms may not be available in the near future (including the Advanced LIGO era), we continue with a slightly different application of our results: How reliable is a set of complete waveforms constructed with standard PN approximants and NR simulations covering 5 (10, 20) orbits before merger (i.e., 10, 20 or 40 GW cycles prior to the maximum of $|h(t)|$)? To quantify these uncertainties we have to combine an estimate of the minimal matching frequency allowed by such NR waveforms with the resulting mismatch error from Fig. 4.14. We calculate the first from the inverse Fourier transform of the phenomenological model [162] and the time derivative of the phase, $M\omega_m \approx |d \arg h(t_n)/dt|$, where $|\arg(t_n)| = |\arg h(t_{\rm max})| - n\,2\pi$ ($n = 10, 20, 40$, respectively), and $t_{\rm max}$ is the time of the maximum amplitude $|h|$. This spin- and η-dependent value is then taken into the results presented with Fig. 4.14 to estimate $\mathscr{M}_{\rm FF}$ for each configuration. Note that we use a more pessimistic error estimate for antialigned spins ($\chi < 0$) by assuming the mismatches of $|\chi|$ due to the reasons discussed above.

One kind of possible conclusion one can then draw is summarized in Table 4.3 for equal masses and mass-ratio 4:1. Given an accuracy goal (which we take as either 3%, 1.5%, 0.5% or 0.2%) we provide the range of spins in which hybrids with the specified number of NR orbits fulfill this goal. Note that the asymmetry in the spin parameter is only caused by the different matching frequencies waveforms with constant length permit. Again, we can very clearly see that even relatively short waveform are good enough for detection. In fact, mismatches of 0.5% are below the noise level for SNR 10, and differences of 0.2% are indistinguishable for SNR $\lesssim 16$ according to (4.6). However, one can also see from Table 4.3 that doubling the number of orbits does not enlarge the accuracy range dramatically in many cases, although such simulations would take far more computer power and time.

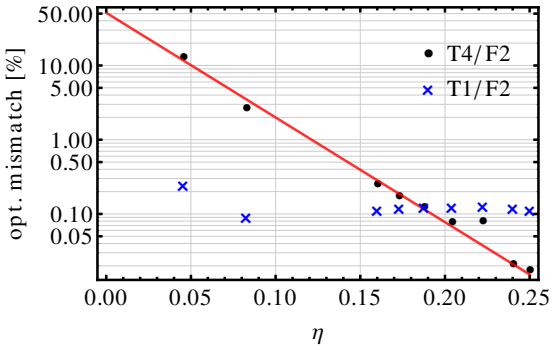

Figure 4.15: The fully optimized mismatch of nonspinning target signals employing either the TaylorT1 or TaylorT4 approximant with model waveforms constructed with TaylorF2 inspirals. The assumed matching frequency is always $M\omega_m = 0.06$. The bias in parameters is $|\Delta M|/M \lesssim 0.6\%$ (0.16%), $|\Delta\eta|/\eta \lesssim 1.0\%$ (0.3%), $|\Delta\chi| < 0.04$ (0.017), where the values in brackets indicate the restriction to $q \leq 4$.

4.5.4 Nonspinning unequal-mass systems

So far, we refrained from explicitly calculating mismatches for mass-ratios $>$ 4:1 here because our underlying phenomenological model was only calibrated to numerical simulations with mass-ratios $\leq$ 4:1. Pushing the model beyond these values would add another uncertainty in addition to the way we estimate PN errors already, and more elaborate studies (possible including different models such as [16] and variants of EOBNR) are needed to reach sound conclusions.

Nevertheless, numerical simulations of higher mass ratios are potentially interesting, and we shall try to estimate their reliability on the basis of our (extrapolated) knowledge here. We restrict this study, however, to nonspinning target signals. These are the systems where we do not expect the PN errors to drop significantly on the timescale of Advanced LIGO (in contrast to spinning binaries, where higher-order PN terms may well be calculated in the next few years). We find that the agreement between TaylorT1- and TaylorF2-based hybrids is exceptionally good along $\chi = 0$ (see Figs. 4.13 and 4.15). In contrast, the TaylorT4/TaylorF2 uncertainty increases towards higher mass-ratios (smaller values of η) as we would expect from the form of the PN expansion. Therefore, we shall conservatively base our statements on comparing TaylorT4 and F2 approximants in this section.

To illustrate our argument, we plot in Fig. 4.15 the maximum of the fully optimized (i.e., with respect to M, η and χ) mismatches between TaylorF2 and either TaylorT1 or TaylorT4 hybrids, all matched to fictitious NR data at $M\omega_m = 0.06$. The fixed target parameters are chosen as $\chi = 0$ with the mass ratio q varying from 1 to 4 in steps of 0.5 as well as $q = 10$ and $q = 20$. While the comparison with TaylorT1 yields weakly η-dependent mismatches below 0.3%, TaylorT4 target signals exhibit a steeply increasing divergence from the model signals towards higher mass ratios. Its approximately exponential behavior is well described by the following fitting formula

$$\log_{10} \mathscr{M}_{\mathrm{FF}} \approx -0.29 - 14.1\eta \tag{4.22}$$

which is included as a straight line in Fig. 4.15. A conservative estimate of the general model uncertainty would be the maximum of both data series for each η, i.e., (4.22) for small η and roughly constant $\mathscr{M}_{\mathrm{FF}} \approx 0.12\%$ for $\eta > 0.1866$ ($q < 3$).

Evidently, a matching frequency of $M\omega_m = 0.06$ is only good enough for $\eta > 0.081$ ($q < 10.2$) if a mismatch of at most 3% is tolerated. Again, reducing the matching frequency helps to increase the accuracy of the final waveform, and we systematically analyze how

orbits	mass ratio		$q = 20$
5	*3.0%:*	$q < 8.9$	$\max_M \mathscr{M}_{\rm FF} \approx 15\%$ $(19M_\odot)$
	1.5%:	$q < 6.8$	$21M_\odot : 12\%$, $63M_\odot : 0.3\%$
10	*3.0%:*	$q < 11.4$	$\max_M \mathscr{M}_{\rm FF} \approx 8.2\%$ $(13M_\odot)$
	1.5%:	$q < 8.6$	$21M_\odot : 3.0\%$, $63M_\odot : 1.6 \times 10^{-5}$
20	*3.0%:*	$q < 14.8$	$\max_M \mathscr{M}_{\rm FF} \approx 5.7\%$ $(11M_\odot)$
	1.5%:	$q < 10.7$	$21M_\odot : 0.8\%$, $63M_\odot : 6.4 \times 10^{-6}$

Table 4.4: Accuracy of nonspinning hybrid waveforms, based on combining PN TaylorT4 or TaylorF2 data with NR waveforms of specified length (defined by the number of orbits before merge = number of GW cycles divided by 2). *Left column:* Range in mass-ratio where a given accuracy requirement ($\max_M \mathscr{M}_{\rm FF} < 3\%$ or 1.5%) is fulfilled. *Right column:* Mismatch error for $q = 20$, both at maximum of all masses (location indicated in parentheses) and at astrophysically motivated minimal values of the total mass (see text).

useful numerical simulations of 5, 10 or 20 orbits before merger are in the nonspinning unequal-mass regime. For that, we calculate $\max_M \mathscr{M}_{\rm FF}$ as a function of the matching frequency and the symmetric mass ratio, similar to what was done for Fig. 4.14. The matching frequency is then converted to orbits before merger as explained in the previous section.

In Table 4.4 we present our results in analogy to Table 4.3, where we provided the range of the spin parameter χ in which the waveform model meets certain accuracy requirements. Now we complement the picture by restricting ourselves to the nonspinning case; our error estimates are based on optimized TaylorT4/TaylorF2 hybrid mismatches, and we present the accuracy range in terms of the mass ratio. Note that, although only five orbits of NR data before merger are sufficient for detection for most of today's standard simulations ($q \lesssim 6$), even the computationally very challenging goal of 20 orbits before merger is not enough to reliably model mass ratios as high as 15 or more for arbitrary total masses of the binary.

It should be pointed out, however, that we report the worst disagreement between the considered hybrids in the left column of Table 4.4, i.e., we demand that the assumed accuracy requirement is satisfied for *all* values of the total mass. As discussed in [45] already, one should rather understand the mismatch error and the accuracy requirement as functions of the total mass. After all, binaries with larger total mass have higher SNR in the detector (for constant distance of the source). More important for us here is that some of the considered astrophysical scenarios may not even exist or be extremely unlikely, and if the modeling error exceeds accuracy thresholds in these regions, we do not have to bother.

We illustrate this argument with a concrete example: The (fictitious) waveform of a binary with mass-ratio 20:1 exhibits the largest uncertainty at total masses less than $20M_\odot$, depending on the matching frequency (the values for NR simulations covering 5, 10 or 20 orbits before merger are given in parenthesis in the right column of Table 4.4). If we only consider *black holes* as objects in the binary and follow observational [92] and theoretical [33] evidence that their individual masses are $> 3M_\odot$, then the lowest total mass to consider in our error analysis is instead $63M_\odot$. With our idealized assumptions, this is a regime where the mismatch drops monotonically with increasing total mass (due to the dominating amount of exact high-frequency data), and the maximal uncertainty

at $63M_\odot$ proves to be more than sufficient for detection purposes, even with only a few NR orbits; see Table 4.4. In this sense, modeling higher mass-ratios is more accurate than comparable masses, as [45] noted already for diagonal (nonoptimized) mismatches.

One the other hand, one could argue that the smaller object in the 20:1-binary could also be a neutron star. If the companion is a much heavier black hole, tidal effects are extremely weak [146] and the plunge is hardly affected from finite size effects of the neutron star [169]. Thus, we may hope to accurately capture these systems with a binary-BH template family as well, and smaller total masses have to be considered. According to [97], (proto)neutron stars are expected to have masses $> 1M_\odot$, which is in agreement with current observations (see [120] for an overview). Assuming the lower bound of $1M_\odot$ for the mass of a single compact object, we consequently have to consider total masses down to $21M_\odot$ (for $q = 20$) which leads to higher modeling uncertainties in the waveform. However, as Table 4.4 shows, 10 NR orbits before merger would be virtually good enough for detection purposes, 20 orbits already yield a mismatch of only 0.8% at $21M_\odot$. Hence, even the theoretically and numerically difficult unequal-mass regime may well be modeled with only a few NR orbits, given the astrophysical expected properties of such systems.

Of course, these astrophysical limitations are highly uncertain, and the conservative error analyses are the ones presented in Table 4.3 and the left column of Table 4.4. However, given that caveat, we conclude that currently feasible numerical simulations are potentially good enough to model in combination with PN approximants an important fraction of the parameter space.

4.6 Fisher-matrix estimates

4.6.1 Relation to previously used error measures

The issues we have addressed particularly in Sec. 4.5 can be summarized in the following way: Given two waveform families $h_1(\boldsymbol{\lambda})$ and $h_2(\boldsymbol{\lambda})$, where $\boldsymbol{\lambda}$ is the vector of parameters characterizing the waveforms, we have estimated how different the waveforms are if they were constructed from slightly different ingredients. These uncertainties were quantified by either the distance $\|h_1(\boldsymbol{\lambda}) - h_2(\boldsymbol{\lambda})\|^2$ or equivalently the mismatch $\mathscr{M}\left[h_1(\boldsymbol{\lambda}), h_2(\boldsymbol{\lambda})\right]$. The conclusion that the PN errors heavily dominate the error budget was put into perspective by considering fully optimized mismatches $\min_{\boldsymbol{\lambda}'} \mathscr{M}\left[h_1(\boldsymbol{\lambda}), h_2(\boldsymbol{\lambda}')\right]$ that lead to considerably smaller differences of the waveform families at the cost of an additional uncertainty in the parameters, denoted by $\Delta\boldsymbol{\lambda}$.

How do we interpret such parameter ambiguities? In the case of waveform errors, we had the well-defined criteria (4.4) and (4.6) that told us if a particular model uncertainty is below the noise level so that we do not have to worry about it. The equivalent question to ask for the accuracy of the model parameters is how their determination is corrupted by the presence of noise, and how these noise-induced uncertainties compare to the model-induced errors we found in Secs. 4.5.3 and 4.5.4.

To answer these questions in detail, we would need to employ proper parameter-estimation algorithms and run GW searches with many realizations of the noise and various

injected sources. This is beyond the scope of this thesis, and we shall instead restrict ourselves to semi-analytical estimates within the Fisher-matrix formalism. This approach gives a trustworthy estimate of the ability to determine physical parameters only for loud enough signals, i.e., if the SNR is high enough, or if the waveform depends linearly on its parameters, which is clearly not the case for the waveforms we consider. Nevertheless, the order of magnitude we shall find in this approach will give us valuable hints on how to range noise-induced and model-induced parameter biases.

Let us first re-derive some well-known results to give a coherent picture of the error measures we use here. We denote the measured signal stream by s and assume it consists of some noise realization n and the signal $h(\boldsymbol{\lambda})$,

$$s = n + h(\boldsymbol{\lambda}) \,. \tag{4.23}$$

We assume the search to be conducted with an ideal waveform family $h(\boldsymbol{\lambda}')$ that includes the true signal at $\boldsymbol{\lambda}' = \boldsymbol{\lambda}$. The likelihood ratio reads

$$\Lambda = \frac{p\big(s|h(\boldsymbol{\lambda}')\big)}{p(s|0)} = \frac{e^{-\langle s-h(\boldsymbol{\lambda}'),s-h(\boldsymbol{\lambda}')\rangle/2}}{e^{-\langle s,s\rangle/2}} \,, \tag{4.24}$$

$$\ln\Lambda = -\frac{1}{2}\big\langle s-h(\boldsymbol{\lambda}'),s-h(\boldsymbol{\lambda}')\big\rangle + \frac{1}{2}\langle s,s\rangle \tag{4.25}$$

$$= \big\langle s,h(\boldsymbol{\lambda}')\big\rangle - \frac{1}{2}\|h(\boldsymbol{\lambda}')\|^2 \,. \tag{4.26}$$

With (4.23) we trivially find

$$\big\langle s,h(\boldsymbol{\lambda}')\big\rangle = \big\langle h(\boldsymbol{\lambda}),h(\boldsymbol{\lambda}')\big\rangle + \big\langle n,h(\boldsymbol{\lambda}')\big\rangle \,, \tag{4.27}$$

which shows immediately the impact a particular noise realization n has on the likelihood ratio. Since n has zero mean, however, the ensemble mean $\overline{\langle n,h(\boldsymbol{\lambda}')\rangle}$ over many noise realizations vanishes as well, and we find the statistical expectation value of the inner product $\langle s,h(\boldsymbol{\lambda}')\rangle$ to coincide with the expectation value of $\langle h(\boldsymbol{\lambda}),h(\boldsymbol{\lambda}')\rangle$. (For the sake of readability, we shall omit the overline and understand the inner products in the following as their ensemble means.)

A simple way to see how the Fisher matrix Γ_{ij} is related to the likelihood ratio is to expand $h(\boldsymbol{\lambda}')$ in terms of $\Delta\boldsymbol{\lambda} = (\boldsymbol{\lambda}' - \boldsymbol{\lambda})$:

$$\ln\Lambda = \big\langle h(\boldsymbol{\lambda}),h(\boldsymbol{\lambda}')\big\rangle - \frac{1}{2}\|h(\boldsymbol{\lambda}')\|^2 \tag{4.28}$$

$$\approx \big\langle h(\boldsymbol{\lambda}),h(\boldsymbol{\lambda})\big\rangle + \big\langle h(\boldsymbol{\lambda}),\partial_i h(\boldsymbol{\lambda})\big\rangle\Delta\lambda^i - \frac{1}{2}\|h(\boldsymbol{\lambda}')\|^2 \tag{4.29}$$

where we understand

$$\partial_i h(\boldsymbol{\lambda}) = \left.\frac{\partial h(\boldsymbol{\lambda}')}{\partial\lambda'^i}\right|_{\boldsymbol{\lambda}'=\boldsymbol{\lambda}} \,. \tag{4.30}$$

Expanding the last term of (4.29) in a similar way yields

$$\begin{aligned}\|h(\boldsymbol{\lambda}')\|^2 &= \big\langle h(\boldsymbol{\lambda}) + \Delta\lambda^i\partial_i h(\boldsymbol{\lambda}) + \ldots, h(\boldsymbol{\lambda}) + \Delta\lambda^j\partial_j h(\boldsymbol{\lambda}) + \ldots\big\rangle \\ &\approx \|h(\boldsymbol{\lambda})\|^2 + 2\big\langle h(\boldsymbol{\lambda}),\partial_i h(\boldsymbol{\lambda})\big\rangle\Delta\lambda^i + \underbrace{\big\langle\partial_i h(\boldsymbol{\lambda}),\partial_j h(\boldsymbol{\lambda})\big\rangle}_{=\Gamma_{ij}}\Delta\lambda^i\Delta\lambda^j \,.\end{aligned} \tag{4.31}$$

Finally, by inserting (4.31) in (4.29) we find that the second terms cancel each other, and we are left with

$$\ln\Lambda \approx \frac{1}{2}\left(\|h(\boldsymbol{\lambda})\|^2 - \Gamma_{ij}\,\Delta\lambda^i\Delta\lambda^j\right)\,, \tag{4.32}$$

which corresponds to a Gaussian likelihood ratio centered around $\Delta\boldsymbol{\lambda} = 0 \iff \boldsymbol{\lambda}' = \boldsymbol{\lambda}$. The often used "1-$\sigma$" deviation is satisfied along the $n-1$ dimensional ellipse (n is the dimension of $\boldsymbol{\lambda}$) where the likelihood is dropped by a factor of $\sqrt{e}$, hence

$$\ln\Lambda\Big|_{1\text{-}\sigma} = \frac{\|h(\boldsymbol{\lambda})\|^2}{2} - \frac{1}{2} \quad\Rightarrow\quad \Gamma_{ij}\,\Delta\lambda^i\Delta\lambda^j = 1\,. \tag{4.33}$$

The 1-σ error in the parameters can be read off the correlation matrix Γ^{-1}_{ij} simply through

$$\Delta\lambda^i = \sqrt{\Gamma^{-1}_{ii}}\,. \tag{4.34}$$

Another interesting aspect of (4.33) is that it is related to the indistinguishability criterion introduced in Eq. (4.4). In fact, one way to derive this criterion is based on the conclusions we shall present in the following. From the definition of Λ (4.25) we find that it can be rewritten as

$$\ln\Lambda = -\frac{1}{2}\big\langle n + h(\boldsymbol{\lambda}) - h(\boldsymbol{\lambda}'), n + h(\boldsymbol{\lambda}) - h(\boldsymbol{\lambda}')\big\rangle + \frac{1}{2}\big\langle n + h(\boldsymbol{\lambda}), n + h(\boldsymbol{\lambda})\big\rangle \tag{4.35}$$

$$= -\frac{1}{2}\|h(\boldsymbol{\lambda}) - h(\boldsymbol{\lambda}')\|^2 + \big\langle n, h(\boldsymbol{\lambda}')\big\rangle + \frac{1}{2}\|h(\boldsymbol{\lambda})\|^2\,, \tag{4.36}$$

which, again, can be reduced in the ensemble mean over many noise realizations to

$$\ln\Lambda = \frac{1}{2}\left(\|h(\boldsymbol{\lambda})\|^2 - \|h(\boldsymbol{\lambda}) - h(\boldsymbol{\lambda}')\|^2\right)\,. \tag{4.37}$$

By comparing (4.37) with (4.32) we find

$$\Gamma_{ij}\Delta\lambda^i\Delta\lambda^j = \|h(\boldsymbol{\lambda}) - h(\boldsymbol{\lambda}')\|^2\,, \tag{4.38}$$

hence the 1-σ requirement (4.33) becomes equivalent to

$$(4.33) \quad\Leftrightarrow\quad \|h(\boldsymbol{\lambda}) - h(\boldsymbol{\lambda}')\|^2 = 1\,. \tag{4.39}$$

In other words: the difference in $\boldsymbol{\lambda}$ that barely makes the waveforms distinguishable is an estimate of how well the parameters can be measured in the presence of noise. This is very intuitive, as we can only tell the difference in parameters if the waveforms can be distinguished from another. With that interpretation in mind, we should be able to easily relate our modeling errors and biases to Fisher matrix estimates.

4.6.2 Results for full binary-black-hole waveforms

In this section, we shall apply the equations derived in the previous section to full waveforms of coalescing BBHs. We are not concerned with a new calculation of the ambiguity of the waveform model here. On the contrary, we neglect these *systematic errors* for a moment

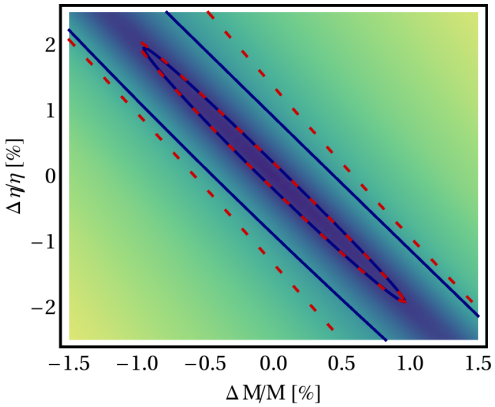

Figure 4.16: Comparison of mismatches and Fisher-matrix approach for a nonspinning $q = 3$, $20M_\odot$ binary. The blue lines are the mismatch contours of the 1-σ threshold for SNR 10 (inner ellipse) and for $\mathscr{M} = 10\%$, the dashed red lines show the corresponding Fisher-matrix estimates. The background color code illustrates the value of the mismatch between 34% (yellow) and 0 (violet).

and only determine the *statistical errors* caused by fact that different physical scenarios may display differences in their GW signals that are too weak to be detected above the noise level. We are therefore free to work with one GW model only, and we chose again the phenomenological model by Santamaría *et al.* [162] introduced in Sec. 3.5.2.

First, let us do a sanity check that the results derived before are applicable in our case. From (4.28), (4.32) and (4.38), and additionally assuming $\|h(\boldsymbol{\lambda})\| = \|h(\boldsymbol{\lambda}')\| = \rho$, we conclude

$$\mathscr{M}\left[h(\boldsymbol{\lambda}), h(\boldsymbol{\lambda}')\right] \approx \frac{\Gamma_{ij}\Delta\lambda^i\Delta\lambda^j}{2\rho^2} \,. \tag{4.40}$$

The two main assumptions that lead to this result are

1. we consider the ensemble mean over many noise realizations, and
2. $h(\boldsymbol{\lambda}')$ can be represented by its first-order Taylor expansion in the differences of the parameters.

While the first is always assumed implicitly throughout this thesis (we never deal with a particular noise realization), we can check the second assumption by calculation both sides of (4.40) independently. As an example, we consider the subfamily of nonspinning waveforms and chose for $\boldsymbol{\lambda}$ the parameters $M = 20M_\odot$, $\eta = 0.1875$ ($q = 3$), $t_0 = 0 = \phi_0$. The results do not depend on the particular values of t_0 and ϕ_0; it is, however, crucial to take their variation into account.

We now calculate the 4-dimensional Fisher matrix for SNR 10, although the final comparison we aim at is independent of the SNR due to the scaling in (4.40). The mismatches we obtain are optimized with respect to t_0 and ϕ_0, so we have to take the minimum with respect to Δt_0 and $\Delta\phi_0$ in the quadratic form $\Gamma_{ij}\Delta\lambda^i\Delta\lambda^j$, too. We do this simply through a numerical root-finding algorithm and then overlay the results with mismatches obtained with our standard overlap routine. As we see in Fig. 4.16, the first-order expansion accurately predicts the error ellipses around the true value, if the parameter deviations are not too large. In particular, the 1-σ (or distinguishability) threshold for SNR 10, $\mathscr{M} = 1/(2\times 10^2) = 0.5\%$, is well represented in the Fisher-matrix approach, whereas the disagreement between $\mathscr{M}$ and $\Gamma_{ij}\Delta\lambda^i\Delta\lambda^j$ can become much more pronounced for considerably higher values of the mismatch. As we are only interested in the 1-σ errors of the parameters here (for SNR ≥ 10), we conclude that in our case the Fisher-matrix errors (4.34) are a meaningful measure of the statistical uncertainty in the determination

q	χ	$\frac{M}{M_\odot}$	$\frac{\Delta M_n}{M}$ [%]	$\frac{\Delta M_m}{M}$ [%]	$\frac{\Delta \eta_n}{\eta}$ [%]	$\frac{\Delta \eta_m}{\eta}$ [%]	$\Delta\chi_n$	$\Delta\chi_m$
1	0.0	10	2.97	0.14	4.95	-0.34	0.039	-0.026
1	0.0	20	2.71	0.24	5.05	-0.10	0.033	-0.004
1	0.0	50	4.19	0.13	5.57	0.01	0.097	0.000
1	0.5	10	2.58	0.31	4.32	-0.78	0.022	-0.072
1	0.5	20	2.31	0.60	4.33	-0.21	0.033	-0.009
1	0.5	50	3.84	0.33	5.20	0.01	0.078	0.000
1	0.8	10	2.77	0.51	4.69	-1.14	0.022	-0.099
1	0.8	20	3.22	0.82	5.88	0.00	0.041	0.000
1	0.8	50	4.00	0.40	5.48	1.57	0.064	0.031
4	0.0	10	2.03	0.09	3.27	-0.17	0.031	-0.011
4	0.0	20	2.89	0.15	4.34	-0.05	0.057	-0.002
4	0.0	50	3.33	0.10	7.24	0.04	0.056	0.000
4	0.5	10	1.95	0.46	3.16	-1.02	0.018	-0.062
4	0.5	20	2.79	0.56	4.17	-0.17	0.041	-0.006
4	0.5	50	3.26	0.31	6.63	1.73	0.049	0.021
4	0.8	10	2.11	0.65	3.44	-1.29	0.012	-0.077
4	0.8	20	3.11	0.78	4.70	-0.06	0.029	-0.002
4	0.8	50	3.80	0.37	5.81	2.82	0.047	0.030

Table 4.5: The noise-induced parameter errors $\Delta\lambda_n$ at SNR 10 in comparison with the model-induced parameter uncertainties $\Delta\lambda_m$ (where λ is total mass M, symmetric mass-ratio η or spin χ, successively). The first three columns indicate the considered binary system.

of physical parameters.

We thus proceed with comparing the noise-related uncertainties, which from now on we denote by $\Delta\boldsymbol{\lambda}_n$, with the model-induced uncertainties $\Delta\boldsymbol{\lambda}_m$. The latter are taken from the calculations we detailed in Sec. 4.5. In particular, we compare TaylorF2 hybrids with TaylorT1 target signals, each family matched to fictitious NR data at $M\omega_m = 0.06$ (cf. Fig. 4.13). The deviation of the search parameters that yield the best match with the model waveform (with fixed parameters) defines $\Delta\boldsymbol{\lambda}_m$. In contrast, the statistical 1-σ errors $\Delta\boldsymbol{\lambda}_n$ are calculated via (4.34) with the phenomenological model [162] that is characterized by $\boldsymbol{\lambda} = (t_0, \phi_0, M, \eta, \chi)$. We checked that the inversion of the 5-dimensional Fisher matrix is accurate to 10^{-9}, i.e., $\Gamma\,\Gamma^{-1}$ and $\Gamma^{-1}\,\Gamma$ do not deviate from identity more than 10^{-9} in every component.

Our aim is not to present an exhaustive study of the parameter measurability throughout the entire parameter space, we merely want to relate our previously found $\Delta\boldsymbol{\lambda}_m$ to Fisher-matrix estimates. We therefore find it sufficient to present a few examples in Table 4.5 that bracket the parameter region in which we would trust our underlying model. Again, we refrain from considering negative spin parameters, as $\Delta\boldsymbol{\lambda}_m$ is possibly underestimated with our approach in this region (see the discussion of Fig 4.14). Similarly, considering systems with even higher total masses is generally interesting, but the effect of model uncertainties is reduced dramatically towards higher masses, so we shall leave this analysis to a dedicated study of statistical errors.

Nevertheless, interesting conclusions can be drawn from Table 4.5. Statistical errors

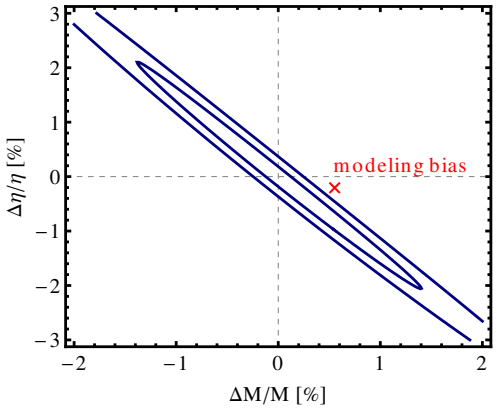

Figure 4.17: The 1-σ error ellipses of a GW from a $M = 20M_\odot$, $q = 4$, $\chi = 0.5$ system with SNR 10 (outer ellipse) and 20 (inner ellipse). Apart from M and η, the search also includes the model parameters t_0, ϕ_0 and χ, and the curves are obtained by minimizing the waveform distance with respect to those parameters. The modeling bias is adopted from the analysis around Fig. 4.12.

mostly rise towards higher total masses, suggesting that the ability to accurately extract the physical parameters of a detection is decreased. This might be expected from the simple fact that as M increases, the number of GW cycles in the detector band decreases, which means that less information exceeds the noise level. Higher mass ratios, on the other hand, do not seem to diminish our ability to identify the parameters of the system. The most interesting observation we can make in Table 4.5 is, however, that for the parameters M and η the noise-induced errors at SNR 10 are *in all cases much greater* than the modeling errors. As $\Delta\boldsymbol{\lambda}_n$ simply scales with the SNR, we can elaborate on these numbers and conclude that, in fact, when $\xi = |\Delta\lambda_n/\Delta\lambda_m|$ in Table 4.5, then only at an SNR of $10 \times \xi$ the modeling errors exceed the noise-induced uncertainties. For M and η we find ξ between 3 and 20 in the majority of cases, i.e., only at SNRs greater than 30 up to 200 the modeling uncertainty becomes the dominating source of error. This does not generally hold for the spin parameter χ as it affects the waveforms least in the inspiral part, hence rather large modeling errors are reported in Table 4.5 for $10M_\odot$ systems.

From a waveform modeling point of view, these results are very positive, as they seem to suggest that the parameter biases caused by model ambiguities are in many cases below the noise confusion and thus negligible. However, this is *not* equivalent to saying that model uncertainties do not lead to an additional *loss of information*, mainly because the parameter errors depend on the choice of parameters themselves.

Let us illustrate this point with a concrete example, and we chose a $20M_\odot$ system with mass ratio 4 and spin parameter $\chi = 0.5$. We learnt from Fig. 4.12 that a change in parameters as small as $\approx 0.6\%$ in the total mass M and -0.2% in the symmetric mass-ratio η caused a drop of the mismatch between the waveforms from roughly 15% to 1%. We would consequently expect that a single waveform family *alone* differs considerably between the two sets of parameters obtained after the full mismatch optimization (a more formal argument would relate the triangle inequality to mismatches, as we shall discuss in Chapter 5). Why does Table 4.5 still indicate that the 1-σ errors are much larger than the deviations just quoted?

The answer to this question is given in Fig. 4.17, where we plot the statistical error ellipses as defined by (4.33) together with the model bias reported before. We can clearly see that the parameter errors introduced by the ambiguous model are outside the 1-σ ellipse, implying that an ideal search model would be able to distinguish the target

parameter values from the red cross in Fig. 4.17. In that sense, the systematic errors *indeed exceed* the statistical errors. If we are only interested in the determination of M and η, however, we are anyway limited by the close degeneracy between these parameters that leads to the elongated error ellipses in Fig. 4.17. From this point of view, the little additional confusion from an uncertain model does not reduce our ability to measure M and η very much.

The close degeneracy between M and η is well known, and using the chirp mass

$$M_c = M\eta^{3/5} \tag{4.41}$$

instead of the total mass partly cures this problem so that M_c can be determined much more accurately than M. An alternative formulation of the fact illustrated in Fig. 4.17 is therefore that model uncertainties only weakly compromise the measurement of M and η but they considerably worsen our ability to determine, for instance, M_c.[4]

[4]Yet another way of looking at the problem is to follow the strategy we employ for the fitting factor optimization, where we first optimize over only $\{\phi_0, t_0, M\}$ before we perform a full optimization with respect to all parameters. A 3-dimensional Fisher matrix calculation for our chosen system yields $\Delta M \approx 0.1\%$, which is much smaller than the deviation in M we have to accept to decrease the mismatch error of the waveform families considerably.

Chapter 5

Conclusion and future prospects

5.1 Summary of our results

Predicting the GW signature of an inspiraling and merging BH binary in General Relativity is inevitably associated with analytical or numerical approximations to the full theory, and we have shown that both descriptions consistently predict the signal in their respective range of validity. Hence, analytical and numerical waveforms can be matched during the inspiral to construct a complete hybrid signal, and various methods to perform this matching have been introduced, both in the time and the frequency domain.

However, we found that the agreement between PN and NR is not perfect and it varies depending on the particular form of the PN approximant that is employed. Although both TaylorT1 and TaylorT4 (with incomplete spin terms at 3 and 3.5PN order retained) perform reasonably well over the parameter space of aligned spins and mass ratios less than 4, the final complete waveform is subject to several errors that potentially affect GW searches with such templates.

Here we estimated these errors by the distance between two approximate solutions for each physical configuration. One after another, we varied an ingredient to the construction of complete waveforms and found that the NR contribution as well as the hybridization procedure lead to acceptable errors in the final signal. The PN-induced uncertainty, on the other hand, turned out to clearly dominate the error budget, and we extensively analyzed the difference of standard PN approximants that are connected at some matching frequency to an NR-based merger and ringdown model.

We quantified these uncertainties by comparing the currently available 3.5PN (spinning contributions up to 2.5PN) versions of TaylorT1, TaylorT4 and TaylorF2 approximants. Introducing a simple algorithm that only requires amplitude information beyond the matching frequency, we first confirmed previous studies [45, 102, 128] that found that the mismatch error for fixed physical parameters greatly exceeds reasonable accuracy requirements, assuming typical NR waveform lengths.

Instead of demanding extremely long numerical simulations to overcome this uncertainty in the modeling process, we refined the understanding of the waveform error by adopting the actual data analysis strategy of detecting an unknown signal in noise-dominated interferometer data. In particular, assuming waveform families instead of

individual waveforms naturally redefines the concept of distance by allowing physical parameters to be varied in the mismatch calculation.

The results presented in Sec. 4.5 indicate that the GW signatures for many astrophysically relevant systems can in fact be well modeled by straightforward combinations of standard PN approximants and currently feasible NR simulations, covering $\lesssim 10$ orbits before merger. The accuracy has not yet reached a level such that detection and parameter estimation errors are limited only by the detector noise for high SNR events, and the intrinsic uncertainty of binary-BH models may exceed in some cases the anticipated deviations caused by non-BHs, making it impossible to identify them as such. Nevertheless, the reported disagreement among different models and biases in the parameters are certainly tolerable for the first GW detections that are likely to have low SNRs (~ 10). While this is true for systems with moderate spins, one has to keep in mind that even our idealized setting yields mismatch errors for high values of spins that are of the order of a few percent and increasing for higher mass ratios. Reducing the matching frequency poses unrealistic challenges for current NR codes, and either fundamentally different numerical approaches or advances in PN are needed to fully control the entire parameter space.

While the next spin-contributions in PN theory may become available in the near future to further improve the modeling of spinning systems (see the recent calculations of higher-order spin-orbit contributions [40, 109, 136]), unequal-mass nonspinning contributions at 4PN order are unlikely to be calculated with established techniques soon. However, as we discussed for a binary with mass-ratio 20:1, astrophysical expectations are that such systems only form with a high total mass, thereby reducing the impact of PN uncertainties. Even for 20:1 binaries, our results suggest that NR simulations of less than 10 orbits are sufficient.

In summary, we found that not single hybrid waveforms, but rather the embedding in the waveform manifold, results in templates accurate enough for detection, even with today's limited number of NR orbits. The uncertainty in physical parameters we had to accept for this tremendous increase in overlap is rather small, $\sim 1\%$ in mass and symmetric mass-ratio and ~ 0.1 at most for the spin parameter χ. For nearly equal-mass systems, the individual masses of the constituents are then only reliable to

$$\frac{\Delta m_i}{m_i} \approx \frac{\Delta M}{M} + \sqrt{\frac{\Delta \eta}{\eta}} \sim 10\% \,, \tag{5.1}$$

and it has to be decided whether this is good enough for astrophysical studies.

5.2 Discussion and future work

5.2.1 Limits and possible extensions of our approach

Of course, our results rely on a number of assumptions that are reasonable in the range where we apply them, but we shall collect and discuss their generalizations and limitations below.

First of all, our analyses are meant to provide a general concept of how to deal with modeling errors, instead of giving final answers. Especially, as we emphasized before, we do

not address the question of how accurate a particular waveform model is. The statements formulated here are based on selecting PN approximants that are compared with each other, and our choices were made to illustrate the *order of magnitude* one generally has to assume for our notion of error. This can be taken as a conservative estimate for all currently exsisting combinations of analytical and numerical relativity, because even a remarkable agreement in the overlapping region of both approaches does not necessarily diminish the uncertainty of many ambiguous choices that enter the modeling of (up to thousands of) GW cycles in the inspiral waveform. Nevertheless, one should keep in mind that a particular PN (or EOB)+NR combination can be much closer to the real waveform than estimated here, as well as the possibility that the PN ambiguity at consistent 3.5PN order generally underestimates the true error in the signal description.

Two further essential assumptions should be noted: We separated both the error of the hybridization procedure and any uncertainties beyond the matching frequency. Each turned out to be negligible, but care has to be taken when generalizing this statement. For instance, from Fig. 4.13 or Table 4.3 one might be tempted to conclude that actually very short NR waveforms are enough for modeling equal-mass, hardly spinning systems. This is certainly true from our results if the matching to PN can be done unambiguously. However, if there are too few cycles to align PN and NR signals properly, different matching procedures may lead to very different results. This aspect was not treated here as it can be checked separately, and it should only affect the resulting waveform for very short (< 5 orbits) NR simulations.

The other key assumption, the presence of exact high-frequency data, implies another important aspect to our results. Not only do we say that the error of the NR part of the wave is negligible (an assumption that could easily be dropped if the NR mismatch becomes significant) we also use waveform families that directly resemble PN/NR hybrids. In other words, the additional error that is introduced in the phenomenological fitting and interpolation process is not taken into account here. We merely state the fact here that *in principle* PN+NR combinations constitute sufficiently accurate target waveforms for the construction of template families.

An indication of how relevant these "interpolation errors" are is provided by the study of Damour, Nagar and Trias [82] who compared an EOBNR model [77] with phenomenological models [15, 16, 162], showing that even the mismatches optimized over physical parameters (excluding the spin) exceed 3% in some regions of the parameter space. At first sight, this might be surprising as the hybrids used to construct the models should be accurate enough for detection purposes (satisfying the 3% mismatch criterion). The difference between the final model and hybrids is also reported to be $\mathscr{M} \lesssim 2\%$ ($\lesssim 5\%$ for the PhenSpin model). It should be noted, however, that the triangle inequality reads

$$\|h_{\mathrm{model}} - h_{\mathrm{exact}}\| \leq \|h_{\mathrm{model}} - h_{\mathrm{hybrid}}\| + \|h_{\mathrm{hybrid}} - h_{\mathrm{exact}}\|, \tag{5.2}$$

which yields through the relation (4.5) and its assumptions

$$\mathscr{M}(h_{\mathrm{model}}, h_{\mathrm{exact}}) \leq \left(\sqrt{\mathscr{M}(h_{\mathrm{model}}, h_{\mathrm{hybrid}})} + \sqrt{\mathscr{M}(h_{\mathrm{hybrid}}, h_{\mathrm{exact}})}\right)^2. \tag{5.3}$$

Consequently, if the hybrids are accurate within, say, 2% mismatch and the model does not deviate by more than 2% from the set of hybrids, the resulting total uncertainty can

nevertheless only be bounded to 8%, which is far above the acceptable mismatch. It is clear from this rough estimation and the results from [82] that the interpolation of the final model has to be improved in the future, which can be done most easily by increasing the number of (NR/hybrid) waveforms it is constructed from.

Our error assessment can be complemented in many other ways. One obvious, yet involved extension is the completion of the parameter space by allowing arbitrary spin orientations that cause additional precession dynamics. Some steps towards building such hybrids have taken place already [47, 63, 142, 143, 166], but a deeper understanding of the waveform structure has to be gained before an extensive error analysis like the present one can be performed. Similarly, this study was restricted to the dominant spherical harmonic mode as it is crucial to understand and quantify the errors here first. Nevertheless, a final waveform model would have to include higher modes as well, and the algorithm we presented should be easily adaptable to these cases.

Implementing more PN approximants and repeating our analysis with pairwise comparisons of various flavors of PN and EOB will help to fully understand the spread of equivalent descriptions of the inspiral process. When more contributions to PN expansions become available the present analysis has to be repeated, hopefully reflecting the enhanced knowledge of the analytical approximation. This is especially true for spinning binaries, where calculations of higher-order PN contributions are expected in the next few years.

Finally and most interestingly, one should address the question of what kind of physics can be achieved given a certain performance of complete waveform models and, of course, given real GW detections with the upcoming generation of interferometers. It will be particularly important to analyze whether a certain disagreement between signal and model can be entirely explained by model uncertainties or if possibly unknown physical effects are the cause. This study serves as a first step to prepare for those kinds of questions.

5.2.2 Future gravitational waveform models and their applications

We want to conclude our work with some remarks about the possibly most urgent question of the waveform modeling community: How well are we prepared for the upcoming era of advanced detectors, and what needs to be done to improve the science output of GW detections?

The results presented here indicate that the theoretical basis is rather well developed, and waveform models are expected to advance steadily when more NR simulations become available and higher analytical corrections are determined. Certainly, the first direct GW detection will be a signal that clearly exceeds the detection threshold, and we will be able to see it because of the incredible sensitivity of the next generation detectors, independently of some remaining ambiguities in the employed signal templates. Considering the wealth of thoroughly constructed waveform families, we should also be able to deduce whether a detected signal satisfies our expectations of a compact-binary inspiral; and if so, we should be able constrain the parameters of the source to some extent. The work presented here provided some first estimates of the possible parameter accuracy if complete models are used.

The practical implementation of our knowledge and any much deeper analysis of

detected signals, however, still require some work to be done on the modeling and the data-analysis side. For instance, it is not obvious which final waveform family should ideally be used for the actual search. It has to be a well-understood balance of a simple and efficient model that nevertheless captures all the relevant characteristics of the expected signals throughout the parameter space.

Closely related is the question of how such models should be parameterized. The nonspinning families commonly use the physical parameters total mass and symmetric mass ratio to define the waveform. When the dominant effect of spins was added by considering aligned-spin configurations, it was found that one additional spin parameter is already sufficient to represent the entire family. The choice of this parameter relies on close degeneracies between signals of different physical scenarios, and although the mass-weighted total spin χ that is employed in the phenomenological models by Ajith *et al.* [16] and Santamaría *et al.* [162] might not be the final and optimal choice (see a different effective spin parameter in [10]), it shows the tendency for future representations of waveform models. Particularly, dealing with arbitrary precessing spins is not only challenging in the individual PN and NR descriptions, it will be of major importance to first understand the dominant characteristics in the complete signature that can actually be determined in a GW search (see, e.g., [51]). Neglecting other small contributions will both simplify the model and allow for an efficient search that constrains already the most important parameters. Work is underway to model precessing binaries with aligned-spin waveforms [10], expressed in an adapted coordinate frame [47, 142, 143, 166].

Another part of the parameter space that we might not be able to simulate with the same confidence are binaries with higher mass ratios ($q > 10$). The EOB description is an elegant formulation tailored to model this regime accurately, too, but in contrast to the comparable-mass regime we do note have the possibility to compare with a number of independent calculations, for example from NR. However, we have argued in Sec. 4.5.4 that astrophysical expectations are such that we would only have to model relatively high values of the total mass, which implies that rather short NR waveforms would be sufficient. Developing efficient methods to routinely make such simulations would be an important step to complement the parameter space we can model accurately.

Addressing the issues mentioned above will eventually help to identify the sources of detected GWs more accurately. This will improve our understanding of the population of compact binaries in the universe, the mass range they cover and the history of their formation. Beyond these astrophysical applications, there are questions concerning the fundaments of physics that could be answered, or constrained at least, by GW observations. For instance, is General Relativity the correct theory also in the strong gravity regime? There are tests proposed addressing this question that are based on a comparison of detected waveforms with highly accurate predictions from the theory [22, 23, 84, 121, 122, 203]. As we have detailed here, the assumption of *highly accurate* template waveforms might not be fulfilled with current models, simply because different, but equivalent approximations of the theory may differ already enough to mask the small deviations from General Relativity we would otherwise be able to measure.

Let us illustrate this last point with a concrete example. One generic test of deviations from Einstein's theory of gravitation is to test the PN expansion parameters, for example in

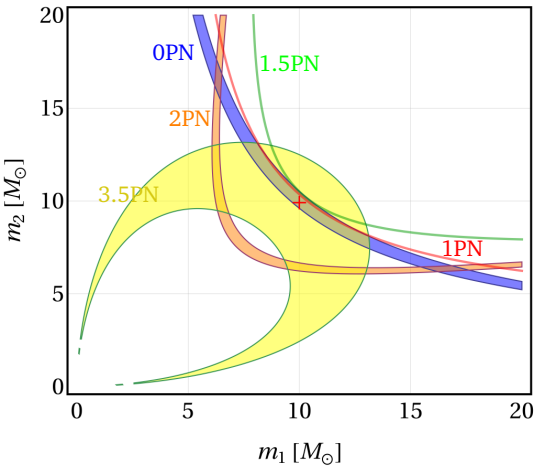

Figure 5.1: Test of General Relativity suggested in [22], applied to a TaylorT1+SpEC hybrid waveform. Each PN coefficient of the TaylorF2 phase was individually fitted (PN order as indicated), and the resulting mass range is illustrated in the plot. The width of the area is determined by the 1-σ fitting errors of each parameter. The true parameters are included as a red cross, and the result does not seem to be entirely consistent with General Relativity.

the TaylorF2 formulation (2.91). The test proposed by Arun *et al.* [22] assumes nonspinning systems and instead of determining only the two masses in a search, a third parameter corresponding to a PN coefficient is introduced as a free parameter to be determined in the matched-filter process. Such a search is repeated for each PN coefficient, while the others are given by the prediction of General Relativity, respectively. By overlaying the regions in the m_1-m_2 space that every PN parameter permits, we can find inconsistencies with the underlying theory.

As an illustration how much this test depends on the validity of PN predictions, we construct a TaylorT1 hybrid with the SpEC equal-mass waveform [2, 165]. Obviously, both descriptions are based on General Relativity. We then perform the test just described, and for illustration purposes (and simplicity) we do not assume a particular detector but determine the phase coefficients in multiple least-square fits. The frequency range we use corresponds to the interval $(10\,\mathrm{Hz}, f_{\mathrm{LSO}})$ for a binary with two $10M_\odot$-BHs. The result is shown in Fig. 5.1 where we include the 1-σ fitting error as a shaded area for each coefficient. As we see, the Newtonian-order coefficient and the 3.5PN-order coefficient are consistent with the system we simulated, but the 1PN and 1.5PN terms exhibit small biases, although they are well well determined. The 2PN contribution is far off the expected value. We do not include the 2.5 and 3PN terms here as they include logarithmic contributions that had to be treated separately. However, the conclusion we might be tempted to draw from Fig. 5.1 is that the signal is inconsistent with General Relativity, which is clearly not the case. With this very simplified example we do not mean to say that the proposed test is ineffective, one simply may have to modify the expected relation between physical parameters and expansion coefficients towards higher frequencies, as the optimal value is not necessarily the one predicted by the stationary-phase PN treatment.

For these and other tests of General Relativity we clearly need much more accurate models than currently exsisting, which brings us back to the requirement of hundreds of NR orbits to make the hybrid as accurate as possible. In that case, on the other hand, the NR uncertainty would most likely be the dominant source of error, and we have to carefully take all these considerations into account when estimating the potential power of such tests with GW data.

A similar caveat should be mentioned when, e.g., neutron stars are considered instead of

BHs. If the equation of state of the nuclear matter affects the GW signature strongly enough, we should in principle be able to extract it from GW observations by a discrimination from binary-BH templates. Indeed, various studies for binary neutron stars [83, 111] and BH-neutron-star binaries [146] address this question and conclude that particularly stiff equations of state could be detected, provided that the signal is loud enough. We learnt from the present study, however, that BH waveform models are still uncertain enough to possibly spoil such a sensitive measurement, and this modeling error is not reduced with increasing SNR of the signal.

We finally conclude that there are important issues to be resolved before we can take advantage of all opportunities GW observations offer. However, waveform models have well advanced within the last years, and this thesis provided an assessment of the current state of the art, but also developed a general framework of how to combine information both from analytical and numerical approximations and evaluate their accuracy. Taking these insights into account will be of great assistance in future developments and, eventually, the interpretation of GW data.

Acknowledgements

The work presented in this thesis is the result of countless discussions and exchanges with colleagues and friends. I am grateful to all of them.

In particular, I thank the Albert Einstein Institute and the International Max Planck Research School for giving me the chance to work in this stimulating environment and for the continued support that was provided. The people I had the privilege to work with greatly inspired me, and I am indebted to my supervisors Bernard Schutz and Badri Krishnan for their help. Every day I benefited from the pleasant atmosphere the people of the Gravitational-Waves group created, and I thank Pau Amaro-Seoane, Sofiane Aoudia, Stas Babak, Berit Behnke, Steve Drasco, Steffen Grunewald, my (sometimes extraordinary) office mate Michael Jasiulek, Alex Nielsen, Maria Alessandra Papa, Antoine Petiteau, Emma Robinson, Constanze Rödig, Lucía Santamaría, Ute Schlichting, Alberto Sesana and Shang Yu for that. Many of you have become more than "just colleagues" to me, and I gladly remember the peerless coffee break discussions, the conferences we attended together and, of course, the apple tree that will always be part of my life. It was also a pleasure to share the time with the Numerical-Relativity group here at the institute, and I am particularly grateful to my friends Philipp Mösta, Francesco Pannarale and Ian Hinder for the insights they shared with me.

Among the people that influenced me during my research for this thesis were not only members of my own institute, and I want to express my deepest gratitude to Mark Hannam and Sascha Husa, who supported me as if I was their own student. The time we spent discussing ideas, results, their presentation and many more was invaluable to me. I also thank Parameswaran Ajith, Marc Favata, Jocelyn Read, Michael Pürrer and Patricia Schmidt for useful discussions.

Visiting other institutes and working in different places was always a most pleasant experience, and I am grateful to the Universitat de les Illes Balears (Palma), the University of Vienna and Cardiff University for giving me that opportunity.

Zum Abschluss möchte ich mich, auch wenn es ein paar Worte nur schwerlich ausdrücken können, bei meiner Familie bedanken. Ohne euch gäbe es keine Sterne und keine Schwarzen Löcher! Meiner Frau Julia möchte ich für so viele Dinge danken. Vor allem, dass ich sie jetzt so nennen darf und dafür, dass sie immer für mich da ist, egal „wo" ich gerade bin.

Bibliography

[1] http://www.ninja-project.org/

[2] Waveforms are available at http://www.black-holes.org/Waveforms.html

[3] We acknowledge the useful discussion of that topic with Marc Favata (2011)

[4] J. Abadie *et al.* (LIGO Scientific Collaboration and Virgo Collaboration). *Predictions for the Rates of Compact Binary Coalescences Observable by Ground-based Gravitational-wave Detectors*. Class.Quant.Grav. **27**:173001 (2010), arXiv:1003.2480

[5] J. Abadie *et al.* (LIGO Scientific Collaboration). *A Gravitational wave observatory operating beyond the quantum shot-noise limit: Squeezed light in application*. Nature Phys. **7**:962 (2011), arXiv:1109.2295

[6] J. Abadie *et al.* (LIGO Scientific Collaboration and Virgo Collaboration). *Search for gravitational waves from binary black hole inspiral, merger and ringdown*. Phys.Rev. **D83**:122005 (2011), arXiv:1102.3781

[7] B. Abbott *et al.* (LIGO Scientific Collaboration). *LIGO: The Laser interferometer gravitational-wave observatory*. Rept.Prog.Phys. **72**:076901 (2009), arXiv:0711.3041

[8] T. Accadia, F. Acernese, F. Antonucci, P. Astone, G. Ballardin *et al.*. *Status of the Virgo project*. Class.Quant.Grav. **28**:114002 (2011)

[9] F. Acernese, M. Alshourbagy, P. Amico, F. Antonucci, S. Aoudia *et al.*. *Virgo status*. Class.Quant.Grav. **25**:184001 (2008)

[10] P. Ajith. *Addressing the spin question in gravitational-wave searches: Waveform templates for inspiralling compact binaries with nonprecessing spins*. Phys.Rev. **D84**:084037 (2011), arXiv:1107.1267

[11] P. Ajith and S. Bose. *Estimating the parameters of non-spinning binary black holes using ground-based gravitational-wave detectors: Statistical errors*. Phys.Rev. **D79**:084032 (2009), arXiv:0901.4936

[12] P. Ajith, M. Boyle, D. A. Brown, B. Brügmann, L. T. Buchman *et al.*. *The NINJA-2 catalog of hybrid post-Newtonian/numerical-relativity waveforms for non-precessing black-hole binaries*. Class.Quant.Grav. **29**:124001 (2012), 1201.5319

[13] P. Ajith *et al.*. *Data formats for numerical relativity waves* (2007), arXiv:0709.0093

[14] P. Ajith *et al.*. *Phenomenological template family for black-hole coalescence waveforms*. Class. Quant. Grav. **24**:S689 (2007), arXiv:0704.3764

[15] P. Ajith *et al.*. *A template bank for gravitational waveforms from coalescing binary black holes: I. non-spinning binaries*. Phys. Rev. **D77**:104017 (2008), arXiv:0710.2335

[16] P. Ajith *et al.*. *Inspiral-merger-ringdown waveforms for black-hole binaries with nonprecessing spins*. Phys. Rev. Lett. **106**:241101 (2011), arXiv:0909.2867

[17] B. Allen, W. G. Anderson, P. R. Brady, D. A. Brown and J. D. Creighton. *FINDCHIRP: An Algorithm for detection of gravitational waves from inspiraling compact binaries* (2005), arXiv:gr-qc/0509116

[18] K. Alvi. *Energy and angular momentum flow into a black hole in a binary*. Phys. Rev. **D64**:104020 (2001), arXiv:gr-qc/0107080

[19] M. Ando (TAMA Collaboration). *Current status of TAMA*. Class.Quant.Grav. **19**:1409 (2002)

[20] T. A. Apostolatos, C. Cutler, G. J. Sussman and K. S. Thorne. *Spin induced orbital precession and its modulation of the gravitational wave forms from merging binaries*. Phys.Rev. **D49**:6274 (1994)

[21] R. Arnowitt, S. Deser and C. W. Misner. *The Dynamics of General Relativity*. In L. Witten (editor), *Gravitation: An introduction to current research*, pp. 227–265. John Wiley, New York (1962), arXiv:gr-qc/0405109

[22] K. Arun, B. R. Iyer, M. Qusailah and B. Sathyaprakash. *Probing the non-linear structure of general relativity with black hole binaries*. Phys.Rev. **D74**:024006 (2006), arXiv:gr-qc/0604067

[23] K. Arun, B. R. Iyer, M. Qusailah and B. Sathyaprakash. *Testing post-Newtonian theory with gravitational wave observations*. Class.Quant.Grav. **23**:L37 (2006), arXiv:gr-qc/0604018

[24] K. G. Arun, A. Buonanno, G. Faye and E. Ochsner. *Higher-order spin effects in the amplitude and phase of gravitational waveforms emitted by inspiraling compact binaries: Ready-to-use gravitational waveforms*. Phys. Rev. **D79**:104023 (2009), arXiv:0810.5336

[25] K. G. Arun, B. R. Iyer, B. S. Sathyaprakash and P. A. Sundararajan. *Parameter estimation of inspiralling compact binaries using 3.5 post-Newtonian gravitational wave phasing: The non-spinning case*. Phys. Rev. **D71**:084008 (2005), arXiv:gr-qc/0411146

[26] A. Ashtekar and B. Krishnan. *Isolated and Dynamical Horizons and Their Applications*. Living Reviews in Relativity **7**(10) (2004), URL http://www.livingreviews.org/lrr-2004-10

[27] B. Aylott, J. G. Baker, W. D. Boggs, M. Boyle, P. R. Brady *et al.*. *Testing gravitational-wave searches with numerical relativity waveforms: Results from the first Numerical INJection Analysis (NINJA) project*. Class.Quant.Grav. **26**:165008 (2009), arXiv:0901.4399

[28] M. Babiuc, B. Szilagyi, J. Winicour and Y. Zlochower. *A Characteristic Extraction Tool for Gravitational Waveforms*. Phys.Rev. **D84**:044057 (2011), arXiv:1011.4223

[29] L. Baiotti, T. Damour, B. Giacomazzo, A. Nagar and L. Rezzolla. *Accurate numerical simulations of inspiralling binary neutron stars and their comparison with effective-one-body analytical models*. Phys.Rev. **D84**:024017 (2011), arXiv:1103.3874

[30] J. G. Baker, W. D. Boggs, J. Centrella, B. J. Kelly, S. T. McWilliams *et al.*. *Mergers of non-spinning black-hole binaries: Gravitational radiation characteristics*. Phys.Rev. **D78**:044046 (2008), arXiv:0805.1428

[31] J. G. Baker, J. Centrella, D.-I. Choi, M. Koppitz and J. van Meter. *Gravitational wave extraction from an inspiraling configuration of merging black holes*. Phys. Rev. Lett. **96**:111102 (2006), arXiv:gr-qc/0511103

[32] T. W. Baumgarte and S. L. Shapiro. *Numerical relativity and compact binaries*. Phys. Rept. **376**:41 (2003), arXiv:gr-qc/0211028

[33] K. Belczynski, V. Kalogera and T. Bulik. *A Comprehensive study of binary compact objects as gravitational wave sources: Evolutionary channels, rates, and physical properties*. Astrophys.J. **572**:407 (2001), arXiv:astro-ph/0111452

[34] E. Berti, V. Cardoso, J. A. González, U. Sperhake and B. Brügmann. *Multipolar analysis of spinning binaries*. Class. Quant. Grav. **25**:114035 (2008), arXiv:0711.1097

[35] E. Berti, V. Cardoso and A. O. Starinets. *Quasinormal modes of black holes and black branes*. Class.Quant.Grav. **26**:163001 (2009), arXiv:0905.2975

[36] E. Berti, V. Cardoso and C. M. Will. *On gravitational-wave spectroscopy of massive black holes with the space interferometer LISA*. Phys.Rev. **D73**:064030 (2006), arXiv:gr-qc/0512160

[37] G. D. Birkhoff. *Relativity and modern physics*. Harvard Univ. Press, Cambridge, Mass. (1923)

[38] L. Blanchet. *Gravitational Radiation from Post-Newtonian Sources and Inspiralling Compact Binaries*. Living Reviews in Relativity **9**(4) (2006), URL http://www.livingreviews.org/lrr-2006-4

[39] L. Blanchet, A. Buonanno and G. Faye. *Higher-order spin effects in the dynamics of compact binaries. II. Radiation field*. Phys.Rev. **D74**:104034 (2006), arXiv:gr-qc/0605140

[40] L. Blanchet, A. Buonanno and G. Faye. *Tail-induced spin-orbit effect in the gravitational radiation of compact binaries* (2011), arXiv:1104.5659

[41] L. Blanchet, T. Damour, G. Esposito-Farèse and B. R. Iyer. *Gravitational radiation from inspiralling compact binaries completed at the third post-Newtonian order*. Phys. Rev. Lett. **93**:091101 (2004), arXiv:gr-qc/0406012

[42] L. Blanchet, G. Faye, B. R. Iyer and S. Sinha. *The third post-Newtonian gravitational wave polarisations and associated spherical harmonic modes for inspiralling compact binaries in quasi-circular orbits*. Class. and Quant. Grav. **25**:165003 (2008), arXiv:0802.1249

[43] S. Bose, A. Gopakumar and M. Tessmer. *Gravitational wave data analysis implications of TaylorEt inspiral approximants for ground-based detectors: the non- spinning case* (2008), arXiv:0807.2400

[44] J. M. Bowen and J. York, James W. *Time asymmetric initial data for black holes and black hole collisions*. Phys.Rev. **D21**:2047 (1980)

[45] M. Boyle. *The Uncertainty in hybrid gravitational waveforms: Optimizing initial orbital frequencies for binary black-hole simulations* (2011), arXiv:1103.5088

[46] M. Boyle, D. A. Brown and L. Pekowsky. *Comparison of high-accuracy numerical simulations of black-hole binaries with stationary phase post-Newtonian template waveforms for Initial and Advanced LIGO*. Class. Quant. Grav. **26**:114006 (2009), arXiv:0901.1628

[47] M. Boyle, R. Owen and H. P. Pfeiffer. *A geometric approach to the precession of compact binaries*. Phys.Rev. **D84**:124011 (2011), arXiv:1110.2965

[48] M. Boyle *et al.*. *High-accuracy comparison of numerical relativity simulations with post-Newtonian expansions*. Phys. Rev. **D76**:124038 (2007), arXiv:0710.0158

[49] M. Boyle *et al.*. *High-accuracy numerical simulation of black-hole binaries: Computation of the gravitational-wave energy flux and comparisons with post-Newtonian approximants*. Phys. Rev. **D78**:104020 (2008), arXiv:0804.4184

[50] S. Brandt and B. Brügmann. *A Simple construction of initial data for multiple black holes*. Phys.Rev.Lett. **78**:3606 (1997), arXiv:gr-qc/9703066

[51] D. Brown, A. Lundgren and R. O'Shaughnessy. *Nonspinning searches for spinning binaries in ground-based detector data: Amplitude and mismatch predictions in the constant precession cone approximation* (2012), arXiv:1203.6060

[52] B. Brügmann *et al.*. *Calibration of Moving Puncture Simulations*. Phys.Rev. **D77**:024027 (2008), arXiv:gr-qc/0610128

[53] A. Buonanno, Y. Chen and T. Damour. *Transition from inspiral to plunge in precessing binaries of spinning black holes*. Phys. Rev. **D74**:104005 (2006), arXiv:gr-qc/0508067

[54] A. Buonanno, Y.-b. Chen and M. Vallisneri. *Detecting gravitational waves from precessing binaries of spinning compact objects: Adiabatic limit*. Phys.Rev. **D67**:104025 (2003), arXiv:gr-qc/0211087

[55] A. Buonanno, G. B. Cook and F. Pretorius. *Inspiral, merger and ring-down of equal-mass black-hole binaries*. Phys.Rev. **D75**:124018 (2007), arXiv:gr-qc/0610122

[56] A. Buonanno and T. Damour. *Effective one-body approach to general relativistic two- body dynamics*. Phys. Rev. **D59**:084006 (1999), arXiv:gr-qc/9811091

[57] A. Buonanno and T. Damour. *Transition from inspiral to plunge in binary black hole coalescences*. Phys. Rev. **D62**:064015 (2000), arXiv:gr-qc/0001013

[58] A. Buonanno, B. Iyer, E. Ochsner, Y. Pan and B. S. Sathyaprakash. *Comparison of post-Newtonian templates for compact binary inspiral signals in gravitational-wave detectors*. Phys. Rev. **D80**:084043 (2009), arXiv:0907.0700

[59] A. Buonanno, L. E. Kidder, A. H. Mroue, H. P. Pfeiffer and A. Taracchini. *Reducing orbital eccentricity of precessing black-hole binaries*. Phys.Rev. **D83**:104034 (2011), arXiv:1012.1549

[60] A. Buonanno *et al.*. *Toward faithful templates for non-spinning binary black holes using the effective-one-body approach*. Phys. Rev. **D76**:104049 (2007), arXiv:0706.3732

[61] A. Buonanno *et al.*. *Effective-one-body waveforms calibrated to numerical relativity simulations: coalescence of non-spinning, equal- mass black holes*. Phys. Rev. **D79**:124028 (2009), arXiv:0902.0790

[62] M. Campanelli, C. O. Lousto, P. Marronetti and Y. Zlochower. *Accurate evolutions of orbiting black-hole binaries without excision*. Phys. Rev. Lett. **96**:111101 (2006), arXiv:gr-qc/0511048

[63] M. Campanelli, C. O. Lousto, H. Nakano and Y. Zlochower. *Comparison of Numerical and Post-Newtonian Waveforms for Generic Precessing Black-Hole Binaries*. Phys.Rev. **D79**:084010 (2009), arXiv:0808.0713

[64] M. Campanelli, C. O. Lousto, Y. Zlochower, B. Krishnan and D. Merritt. *Spin Flips and Precession in Black-Hole-Binary Mergers*. Phys.Rev. **D75**:064030 (2007), arXiv:gr-qc/0612076

[65] S. M. Carroll. *Lecture notes on general relativity* (1997), arXiv:gr-qc/9712019

[66] S. M. Carroll. *Spacetime and geometry: An introduction to general relativity*. Addison-Wesley, San Francisco, USA (2004)

[67] J. M. Centrella, J. G. Baker, B. J. Kelly and J. R. van Meter. *The Final Merger of Black-Hole Binaries*. Ann.Rev.Nucl.Part.Sci. **60**:75 (2010), arXiv:1010.2165

[68] C. Cutler, T. A. Apostolatos, L. Bildsten, L. S. Finn, E. E. Flanagan *et al.*. *The Last three minutes: issues in gravitational wave measurements of coalescing compact binaries*. Phys.Rev.Lett. **70**:2984 (1993), arXiv:astro-ph/9208005

[69] C. Cutler and M. Vallisneri. *LISA detections of massive black hole inspirals: Parameter extraction errors due to inaccurate template waveforms*. Phys.Rev. **D76**:104018 (2007), arXiv:0707.2982

[70] T. Damour. *Coalescence of two spinning black holes: An effective one- body approach*. Phys. Rev. **D64**:124013 (2001), arXiv:gr-qc/0103018

[71] T. Damour, B. R. Iyer and A. Nagar. *Improved resummation of post-Newtonian multipolar waveforms from circularized compact binaries*. Phys.Rev. **D79**:064004 (2009), arXiv:0811.2069

[72] T. Damour, B. R. Iyer and B. Sathyaprakash. *A Comparison of search templates for gravitational waves from binary inspiral*. Phys.Rev. **D63**:044023 (2001), arXiv:gr-qc/0010009

[73] T. Damour, B. R. Iyer and B. S. Sathyaprakash. *Improved filters for gravitational waves from inspiralling compact binaries*. Phys. Rev. **D57**:885 (1998), arXiv:gr-qc/9708034

[74] T. Damour, B. R. Iyer and B. S. Sathyaprakash. *A comparison of search templates for gravitational waves from binary inspiral: 3.5-PN update*. Phys. Rev. **D66**:027502 (2002), arXiv:gr-qc/0207021

[75] T. Damour, P. Jaranowski and G. Schäfer. *On the determination of the last stable orbit for circular general relativistic binaries at the third post-Newtonian approximation*. Phys. Rev. **D62**:084011 (2000), arXiv:gr-qc/0005034

[76] T. Damour, P. Jaranowski and G. Schäfer. *Dimensional regularization of the gravitational interaction of point masses*. Phys. Lett. **B513**:147 (2001), arXiv:gr-qc/0105038

[77] T. Damour and A. Nagar. *An improved analytical description of inspiralling and coalescing black-hole binaries*. Phys. Rev. **D79**:081503 (2009), arXiv:0902.0136

[78] T. Damour and A. Nagar. *Relativistic tidal properties of neutron stars*. Phys.Rev. **D80**:084035 (2009), arXiv:0906.0096

[79] T. Damour and A. Nagar. *Effective One Body description of tidal effects in inspiralling compact binaries*. Phys.Rev. **D81**:084016 (2010), arXiv:0911.5041

[80] T. Damour, A. Nagar, E. N. Dorband, D. Pollney and L. Rezzolla. *Faithful Effective-One-Body waveforms of equal-mass coalescing black-hole binaries*. Phys. Rev. **D77**:084017 (2008), arXiv:0712.3003

[81] T. Damour, A. Nagar, M. Hannam, S. Husa and B. Brügmann. *Accurate Effective-One-Body waveforms of inspiralling and coalescing black-hole binaries*. Phys. Rev. **D78**:044039 (2008), arXiv:0803.3162

[82] T. Damour, A. Nagar and M. Trias. *Accuracy and effectualness of closed-form, frequency-domain waveforms for non-spinning black hole binaries*. Phys.Rev. **D83**:024006 (2011), arXiv:1009.5998

[83] T. Damour, A. Nagar and L. Villain. *Measurability of the tidal polarizability of neutron stars in late-inspiral gravitational-wave signals* (2012), arXiv:1203.4352

[84] W. Del Pozzo, J. Veitch and A. Vecchio. *Testing General Relativity using Bayesian model selection: Applications to observations of gravitational waves from compact binary systems*. Phys.Rev. **D83**:082002 (2011), arXiv:1101.1391

[85] A. Einstein. *Zur Algemeinen Relativitätstheorie*. Preuss. Akad. Wiss. Berlin, Sitzungsber. pp. 778–786 (1915)

[86] A. Einstein. *Die Grundlage der Allgemeinen Relativitätstheorie*. Ann. Phys. **49**:769 (1916)

[87] G. Faye, L. Blanchet and A. Buonanno. *Higher-order spin effects in the dynamics of compact binaries. I. Equations of motion*. Phys.Rev. **D74**:104033 (2006), arXiv:gr-qc/0605139

[88] L. S. Finn and D. F. Chernoff. *Observing binary inspiral in gravitational radiation: One interferometer*. Phys.Rev. **D47**:2198 (1993), arXiv:gr-qc/9301003

[89] E. E. Flanagan and T. Hinderer. *Constraining neutron star tidal Love numbers with gravitational wave detectors*. Phys.Rev. **D77**:021502 (2008), arXiv:0709.1915

[90] E. E. Flanagan and S. A. Hughes. *Measuring gravitational waves from binary black hole coalescences: 2. The Waves' information and its extraction, with and without templates*. Phys.Rev. **D57**:4566 (1998), arXiv:gr-qc/9710129

[91] H. Friedrich and A. D. Rendall. *The Cauchy problem for the Einstein equations*. Lect.Notes Phys. **540**:127 (2000), arXiv:gr-qc/0002074

[92] D. M. Gelino and T. E. Harrison. *GRO J0422+32: the lowest mass black hole?* Astrophys.J. **599**:1254 (2003), arXiv:astro-ph/0308490

[93] J. Goldberg, A. MacFarlane, E. Newman, F. Rohrlich and E. Sudarshan. *Spin s spherical harmonics and edth*. J.Math.Phys. **8**:2155 (1967)

[94] A. Gopakumar. *New Class of Gravitational Wave Templates for Inspiralling Compact Binaries* (2007), arXiv:0712.3236

[95] A. Gopakumar, M. Hannam, S. Husa and B. Brügmann. *Comparison between numerical relativity and a new class of post-Newtonian gravitational-wave phase evolutions: The Non-spinning equal-mass case*. Phys.Rev. **D78**:064026 (2008), arXiv:0712.3737

[96] E. Gourgoulhon. *3+1 formalism and bases of numerical relativity* Lecture notes (2007), arXiv:gr-qc/0703035

[97] J. Goussard, P. Haensel and J. Zdunik. *Rapid differential rotation of protoneutron stars and constraints on radio pulsars periods*. Astron.Astrophys. **330**:1005 (1998), arXiv:astro-ph/9711347

[98] K. Gröchenig. *Foundations of time-frequency analysis*. Applied and numerical harmonic analysis. Birkhäuser. ISBN 9780817640224 (2001)

[99] H. Grote (LIGO Scientific Collaboration). *The status of GEO 600*. Class.Quant.Grav. **25**:114043 (2008)

[100] M. Hannam. *Status of black-hole-binary simulations for gravitational- wave detection*. Class. Quant. Grav. **26**:114001 (2009), arXiv:0901.2931

[101] M. Hannam, S. Husa, B. Brügmann and A. Gopakumar. *Comparison between numerical-relativity and post-Newtonian waveforms from spinning binaries: the orbital hang-up case*. Phys. Rev. **D78**:104007 (2008), arXiv:0712.3787

[102] M. Hannam, S. Husa, F. Ohme and P. Ajith. *Length requirements for numerical-relativity waveforms*. Phys.Rev. **D82**:124052 (2010), arXiv:1008.2961

[103] M. Hannam, S. Husa, F. Ohme, B. Brügmann and N. O'Murchadha. *Wormholes and trumpets: The Schwarzschild spacetime for the moving-puncture generation*. Phys.Rev. **D78**:064020 (2008), arXiv:0804.0628

[104] M. Hannam, S. Husa, F. Ohme, D. Müller and B. Brügmann. *Simulations of black-hole binaries with unequal masses or nonprecessing spins: Accuracy, physical properties, and comparison with post-Newtonian results*. Phys.Rev. **D82**:124008 (2010), arXiv:1007.4789

[105] M. Hannam, S. Husa, D. Pollney, B. Brügmann and N. O'Murchadha. *Geometry and regularity of moving punctures*. Phys.Rev.Lett. **99**:241102 (2007), arXiv:gr-qc/0606099

[106] M. Hannam, S. Husa, U. Sperhake, B. Brügmann and J. A. Gonzalez. *Where post-Newtonian and numerical-relativity waveforms meet*. Phys.Rev. **D77**:044020 (2008), arXiv:0706.1305

[107] M. Hannam *et al.*. *The Samurai Project: verifying the consistency of black- hole-binary waveforms for gravitational-wave detection*. Phys. Rev. **D79**:084025 (2009), arXiv:0901.2437

[108] G. M. Harry (LIGO Scientific Collaboration). *Advanced LIGO: The next generation of gravitational wave detectors*. Class.Quant.Grav. **27**:084006 (2010)

[109] J. Hartung and J. Steinhoff. *Next-to-next-to-leading order post-Newtonian spin-orbit Hamiltonian for self-gravitating binaries* (2011), arXiv:1104.3079

[110] I. Hinder. *The Current Status of Binary Black Hole Simulations in Numerical Relativity*. Class. Quant. Grav. **27**:114004 (2010), arXiv:1001.5161

[111] T. Hinderer, B. D. Lackey, R. N. Lang and J. S. Read. *Tidal deformability of neutron stars with realistic equations of state and their gravitational wave signatures in binary inspiral*. Phys.Rev. **D81**:123016 (2010), arXiv:0911.3535

[112] S. A. Hughes, S. Marka, P. L. Bender and C. J. Hogan. *New physics and astronomy with the new gravitational wave observatories*. eConf **010630**:402 (2001), arXiv:astro-ph/0110349

[113] S. Husa, M. Hannam, J. A. Gonzalez, U. Sperhake and B. Brügmann. *Reducing eccentricity in black-hole binary evolutions with initial parameters from post-Newtonian inspiral*. Phys.Rev. **D77**:044037 (2008), arXiv:0706.0904

[114] P. Jaranowski and A. Królak. *Gravitational-Wave Data Analysis. Formalism and Sample Applications: The Gaussian Case*. Living Reviews in Relativity **15**(4) (2012), URL http://www.livingreviews.org/lrr-2012-4

[115] M. Jasiulek. *A New method to compute quasi-local spin and other invariants on marginally trapped surfaces*. Class.Quant.Grav. **26**:245008 (2009), arXiv:0906.1228

[116] N. K. Johnson-McDaniel, N. Yunes, W. Tichy and B. J. Owen. *Conformally curved binary black hole initial data including tidal deformations and outgoing radiation*. Phys.Rev. **D80**:124039 (2009), arXiv:0907.0891

[117] R. P. Kerr. *Gravitational field of a spinning mass as an example of algebraically special metrics*. Phys. Rev. Lett. **11**:237 (1963)

[118] L. E. Kidder. *Coalescing binary systems of compact objects to postNewtonian 5/2 order. 5. Spin effects*. Phys.Rev. **D52**:821 (1995), arXiv:gr-qc/9506022

[119] L. E. Kidder. *Using full information when computing modes of post-Newtonian waveforms from inspiralling compact binaries in circular orbit*. Phys.Rev. **D77**:044016 (2008), arXiv:0710.0614

[120] J. M. Lattimer and M. Prakash. *Neutron Star Observations: Prognosis for Equation of State Constraints*. Phys.Rept. **442**:109 (2007), arXiv:astro-ph/0612440

[121] T. Li, W. Del Pozzo, S. Vitale, C. Van Den Broeck, M. Agathos *et al.*. *Towards a generic test of the strong field dynamics of general relativity using compact binary coalescence* (2011), arXiv:1110.0530

[122] T. Li, W. Del Pozzo, S. Vitale, C. Van Den Broeck, M. Agathos *et al.*. *Towards a generic test of the strong field dynamics of general relativity using compact binary coalescence: Further investigations* (2011), arXiv:1111.5274

[123] L. Lindblom. *Use and Abuse of the Model Waveform Accuracy Standards*. Phys.Rev. **D80**:064019 (2009), arXiv:0907.0457

[124] L. Lindblom, J. G. Baker and B. J. Owen. *Improved Time-Domain Accuracy Standards for Model Gravitational Waveforms*. Phys.Rev. **D82**:084020 (2010), arXiv:1008.1803

[125] L. Lindblom, B. J. Owen and D. A. Brown. *Model Waveform Accuracy Standards for Gravitational Wave Data Analysis*. Phys. Rev. **D78**:124020 (2008), arXiv:0809.3844

[126] G. Lovelace, M. Boyle, M. A. Scheel and B. Szilagyi. *Accurate gravitational waveforms for binary-black-hole mergers with nearly extremal spins*. Class.Quant.Grav. **29**:045003 (2012), arXiv:1110.2229

[127] H. Luck (LIGO Scientific Collaboration). *The upgrade of GEO 600* (2010), arXiv:1004.0338

[128] I. MacDonald, S. Nissanke, H. P. Pfeiffer and H. P. Pfeiffer. *Suitability of post-Newtonian/numerical-relativity hybrid waveforms for gravitational wave detectors*. Class.Quant.Grav. **28**:134002 (2011), arXiv:1102.5128

[129] D. McKechan, C. Robinson and B. Sathyaprakash. *A tapering window for time-domain templates and simulated signals in the detection of gravitational waves from coalescing compact binaries*. Class.Quant.Grav. **27**:084020 (2010), arXiv:1003.2939

[130] S. McWilliams. *Applying numerical relativity to gravitational wave astronomy*. Ph.D. thesis, University of Maryland (2008)

[131] S. T. McWilliams. *The Status of Black-Hole Binary Merger Simulations with Numerical Relativity*. Class.Quant.Grav. **28**:134001 (2011), arXiv:1012.2872

[132] S. T. McWilliams, B. J. Kelly and J. G. Baker. *Observing mergers of non-spinning black-hole binaries*. Phys.Rev. **D82**:024014 (2010), arXiv:1004.0961

[133] B. Mikoczi, M. Vasuth and L. A. Gergely. *Self-interaction spin effects in inspiralling compact binaries*. Phys.Rev. **D71**:124043 (2005), arXiv:astro-ph/0504538

[134] C. Misner, K. Thorne and J. Wheeler. *Gravitation*, volume 1997. W. H. Freeman, San Francisco, USA. ISBN 0-7167-0344-0 (1973)

[135] A. H. Mroue, L. E. Kidder and S. A. Teukolsky. *Ineffectiveness of Pade resummation techniques in post-Newtonian approximations*. Phys.Rev. **D78**:044004 (2008), arXiv:0805.2390

[136] A. Nagar. *Effective one body Hamiltonian of two spinning black-holes with next-to-next-to-leading order spin-orbit coupling* (2011), arXiv:1106.4349

[137] E. Newman and R. Penrose. *An Approach to gravitational radiation by a method of spin coefficients*. J.Math.Phys. **3**:566 (1962)

[138] A. B. Nielsen, M. Jasiulek, B. Krishnan and E. Schnetter. *The Slicing dependence of non-spherically symmetric quasi-local horizons in Vaidya Spacetimes*. Phys.Rev. **D83**:124022 (2011), arXiv:1007.2990

[139] F. Ohme. *Analytical meets numerical relativity - status of complete gravitational waveform models for binary black holes*. Class. Quant. Grav. **29**:124002 (2012), arXiv:1111.3737

[140] F. Ohme, M. Hannam and S. Husa. *Reliability of complete gravitational waveform models for compact binary coalescences*. Phys.Rev. **D84**:064029 (2011), arXiv:1107.0996

[141] F. Ohme, M. Hannam, S. Husa and N. O. Murchadha. *Stationary hyperboloidal slicings with evolved gauge conditions*. Class. Quant. Grav. **26**:175014 (2009), arXiv:0905.0450

[142] R. O'Shaughnessy, J. Healy, L. London, Z. Meeks and D. Shoemaker. *Is J enough? Comparison of gravitational waves emitted along the total angular momentum direction with other preferred orientations* (2012), arXiv:1201.2113

[143] R. O'Shaughnessy, B. Vaishnav, J. Healy, Z. Meeks and D. Shoemaker. *Efficient asymptotic frame selection for binary black hole spacetimes using asymptotic radiation*. Phys.Rev. **D84**:124002 (2011), arXiv:1109.5224

[144] Y. Pan, A. Buonanno, M. Boyle, L. T. Buchman, L. E. Kidder *et al.*. *Inspiral-merger-ringdown multipolar waveforms of nonspinning black-hole binaries using the effective-one-body formalism*. Phys.Rev. **D84**:124052 (2011), arXiv:1106.1021

[145] Y. Pan *et al.*. *Effective-one-body waveforms calibrated to numerical relativity simulations: coalescence of non-precessing, spinning, equal-mass black holes*. Phys. Rev. **D81**:084041 (2010), arXiv:0912.3466

[146] F. Pannarale, L. Rezzolla, F. Ohme and J. S. Read. *Will black hole-neutron star binary inspirals tell us about the neutron star equation of state?* Phys.Rev. **D84**:104017 (2011), arXiv:1103.3526

[147] P. Peters and J. Mathews. *Gravitational radiation from point masses in a Keplerian orbit*. Phys.Rev. **131**:435 (1963)

[148] E. Poisson. *Gravitational waves from inspiraling compact binaries: The quadrupole-moment term*. Phys. Rev. **D57**:5287 (1998), arXiv:gr-qc/9709032

[149] D. Pollney, C. Reisswig, L. Rezzolla, B. Szilagyi, M. Ansorg *et al.*. *Recoil velocities from equal-mass binary black-hole mergers: A Systematic investigation of spin-orbit aligned configurations*. Phys.Rev. **D76**:124002 (2007), arXiv:0707.2559

[150] D. Pollney, C. Reisswig, E. Schnetter, N. Dorband and P. Diener. *High accuracy binary black hole simulations with an extended wave zone*. Phys.Rev. **D83**:044045 (2011), arXiv:0910.3803

[151] R. A. Porto and I. Z. Rothstein. *Next to Leading Order Spin(1)Spin(1) Effects in the Motion of Inspiralling Compact Binaries*. Phys.Rev. **D78**:044013 (2008), arXiv:0804.0260

[152] R. A. Porto and I. Z. Rothstein. *Spin(1)Spin(2) Effects in the Motion of Inspiralling Compact Binaries at Third Order in the Post-Newtonian Expansion*. Phys.Rev. **D78**:044012 (2008), arXiv:0802.0720

[153] F. Pretorius. *Evolution of binary black hole spacetimes*. Phys. Rev. Lett. **95**:121101 (2005), arXiv:gr-qc/0507014

[154] F. Pretorius. *Numerical relativity using a generalized harmonic decomposition*. Class.Quant.Grav. **22**:425 (2005), arXiv:gr-qc/0407110

[155] J. S. Read, C. Markakis, M. Shibata, K. Uryu, J. D. Creighton *et al.*. *Measuring the neutron star equation of state with gravitational wave observations*. Phys.Rev. **D79**:124033 (2009), arXiv:0901.3258

[156] C. Reisswig, N. Bishop, D. Pollney and B. Szilagyi. *Characteristic extraction in numerical relativity: binary black hole merger waveforms at null infinity*. Class.Quant.Grav. **27**:075014 (2010), arXiv:0912.1285

[157] C. Reisswig and D. Pollney. *Notes on the integration of numerical relativity waveforms*. Class.Quant.Grav. **28**:195015 (2011), arXiv:1006.1632

[158] C. Reisswig *et al.*. *Gravitational-wave detectability of equal-mass black-hole binaries with aligned spins*. Phys. Rev. **D80**:124026 (2009), arXiv:0907.0462

[159] C. S. Reynolds. *Astrophysics: Bringing black holes into focus*. Nature **455**:39 (2008)

[160] L. Rezzolla, P. Diener, E. N. Dorband, D. Pollney, C. Reisswig *et al.*. *The Final spin from the coalescence of aligned-spin black-hole binaries*. Astrophys.J. **674**:L29 (2008), arXiv:0710.3345

[161] L. Santamaría. *Coalescence of black-hole binaries: from theoretical source models to applications in gravitational-wave astronomy*. Ph.D. thesis, Universität Potsdam (2010)

[162] L. Santamaría *et al.*. *Matching post-Newtonian and numerical relativity waveforms: systematic errors and a new phenomenological model for non-precessing black hole binaries*. Phys. Rev. **D82**:064016 (2010), arXiv:1005.3306

[163] B. Sathyaprakash and B. F. Schutz. *Physics, Astrophysics and Cosmology with Gravitational Waves*. Living Reviews in Relativity **12**(2) (2009), URL http://www.livingreviews.org/lrr-2009-2

[164] M. A. Scheel, H. P. Pfeiffer, L. Lindblom, L. E. Kidder, O. Rinne *et al.*. *Solving Einstein's equations with dual coordinate frames*. Phys.Rev. **D74**:104006 (2006), arXiv:gr-qc/0607056

[165] M. A. Scheel *et al.*. *High-accuracy waveforms for binary black hole inspiral, merger, and ringdown*. Phys. Rev. **D79**:024003 (2009), arXiv:0810.1767

[166] P. Schmidt, M. Hannam, S. Husa and P. Ajith. *Tracking the precession of compact binaries from their gravitational-wave signal*. Phys.Rev. **D84**:024046 (2011), arXiv:1012.2879

[167] B. Schutz. *A First Course in General Relativity*. Cambridge University Press, 2nd edition. ISBN 9780521887052 (2009)

[168] K. Schwarzschild. *Über das Gravitationsfeld eines Massenpunktes nach der Einsteinschen Theorie*. Preuss. Akad. Wiss. Berlin, Sitzungsber. pp. 189–196 (1916), arXiv:physics/9905030

[169] M. Shibata, K. Kyutoku, T. Yamamoto and K. Taniguchi. *Gravitational waves from black hole-neutron star binaries I: Classification of waveforms*. Phys.Rev. **D79**:044030 (2009), arXiv:0902.0416

[170] M. Shibata and T. Nakamura. *Evolution of three-dimensional gravitational waves: Harmonic slicing case*. Phys.Rev. **D52**:5428 (1995)

[171] D. Shoemaker (LIGO Scientific Collaboration). *Advanced LIGO anticipated sensitivity curves*. https://dcc.ligo.org/cgi-bin/DocDB/ShowDocument?docid=2974

[172] D. Shoemaker, K. Smith, U. Sperhake, P. Laguna, E. Schnetter *et al.*. *Moving black holes via singularity excision*. Class.Quant.Grav. **20**:3729 (2003), arXiv:gr-qc/0301111

[173] D. Sigg (LIGO Scientific Collaboration). *Status of the LIGO detectors*. Class.Quant.Grav. **25**:114041 (2008)

[174] J. R. Smith (LIGO Scientific Collaboration). *The Path to the enhanced and advanced LIGO gravitational-wave detectors*. Class.Quant.Grav. **26**:114013 (2009), arXiv:0902.0381

[175] Spectral Einstein Code (SpEC). http://www.black-holes.org/SpEC.html

[176] U. Sperhake. *Binary black-hole evolutions of excision and puncture data*. Phys.Rev. **D76**:104015 (2007), arXiv:gr-qc/0606079

[177] U. Sperhake, E. Berti and V. Cardoso. *Numerical simulations of black-hole binaries and gravitational wave emission* (2011), arXiv:1107.2819

[178] R. Sturani, S. Fischetti, L. Cadonati, G. Guidi, J. Healy *et al.*. *Phenomenological gravitational waveforms from spinning coalescing binaries* (2010), arXiv:1012.5172

[179] R. Sturani *et al.*. *Complete phenomenological gravitational waveforms from spinning coalescing binaries*. J. Phys. Conf. Ser. **243**:012007 (2010), arXiv:1005.0551

[180] A. Taracchini, Y. Pan, A. Buonanno, E. Barausse, M. Boyle *et al.*. *A prototype effective-one-body model for non-precessing spinning inspiral-merger-ringdown waveforms* (2012), arXiv:1202.0790

[181] M. Tessmer and A. Gopakumar. *On the ability of various circular inspiral templates to that incorporate radiation reaction effects at the second post-Newtonian order to capture inspiral gravitational waves from compact binaries having tiny orbital eccentricities* (2008), arXiv:0812.0549

[182] S. A. Teukolsky. *Perturbations of a rotating black hole. 1. Fundamental equations for gravitational electromagnetic and neutrino field perturbations*. Astrophys.J. **185**:635 (1973)

[183] The LIGO Scientific Collaboration. http://www.ligo.org

[184] The Virgo Collaboration. https://wwwcascina.virgo.infn.it

[185] J. Thornburg. *Coordinates and boundary conditions for the general relativistic initial data problem*. Class.Quant.Grav. **4**(5):1119 (1987)

[186] W. Tichy and P. Marronetti. *A Simple method to set up low eccentricity initial data for moving puncture simulations*. Phys.Rev. **D83**:024012 (2011), arXiv:1010.2936

[187] T. Uchiyama, K. Kuroda, M. Ohashi, S. Miyoki, H. Ishitsuka *et al.*. *Present status of large-scale cryogenic gravitational wave telescope*. Class.Quant.Grav. **21**:S1161 (2004)

[188] H. Vahlbruch, M. Mehmet, S. Chelkowski, B. Hage, A. Franzen, N. Lastzka, S. Goßler, K. Danzmann and R. Schnabel. *Observation of Squeezed Light with 10-dB Quantum-Noise Reduction*. Physical Review Letters **100**(3):033602 (2008), arXiv:0706.1431

[189] B. Vaishnav, I. Hinder, F. Herrmann and D. Shoemaker. *Matched Filtering of Numerical Relativity Templates of Spinning Binary Black Holes*. Phys. Rev. **D76**:084020 (2007), arXiv:0705.3829

[190] M. Vallisneri. *Use and abuse of the Fisher information matrix in the assessment of gravitational-wave parameter-estimation prospects*. Phys.Rev. **D77**:042001 (2008), arViv:gr-qc/0703086

[191] J. Vines, E. E. Flanagan and T. Hinderer. *Post-1-Newtonian tidal effects in the gravitational waveform from binary inspirals*. Phys.Rev. **D83**:084051 (2011), arXiv:1101.1673

[192] R. M. Wald. *General Relativity*. University of Chicago Press, Chicago. ISBN 0-226-87032-4 (hardcover), 0-226-87033-2 (paperback) (1984)

[193] B. Walther, B. Brügmann and D. Müller. *Numerical black hole initial data with low eccentricity based on post-Newtonian orbital parameters*. Phys.Rev. **D79**:124040 (2009), arXiv:0901.0993

[194] J. Weber. *Observation of the Thermal Fluctuations of a Gravitational-Wave Detector*. Phys.Rev.Lett. **17**:1228 (1966)

[195] J. Weber. *Evidence for discovery of gravitational radiation*. Phys.Rev.Lett. **22**:1320 (1969)

[196] J. Weber. *Anisotropy and polarization in the gravitational-radiation experiments*. Phys.Rev.Lett. **25**:180 (1970)

[197] C. M. Will and A. G. Wiseman. *Gravitational radiation from compact binary systems: Gravitational wave forms and energy loss to second postNewtonian order*. Phys.Rev. **D54**:4813 (1996), arXiv:gr-qc/9608012

[198] Wolfram Research, Inc. *Mathematica*. http://www.wolfram.com/mathematica/ (2010)

[199] J. W. York, Jr. *Kinematics and dynamics of general relativity*. In L. Smarr (editor), *Sources of Gravitational Radiation*, pp. 83–126. Cambridge University Press, Cambridge (1979)

[200] J. W. York, Jr. In C. Evans, L. Finn and D. Hobill (editors), *Frontiers in numerical relativity*. Cambridge University Press. ISBN 9780521366663 (1989)

[201] N. Yunes, A. Buonanno, S. A. Hughes, M. Coleman Miller and Y. Pan. *Modeling Extreme Mass Ratio Inspirals within the Effective-One-Body Approach*. Phys. Rev. Lett. **104**:091102 (2010), arXiv:0909.4263

[202] N. Yunes, A. Buonanno, S. A. Hughes, Y. Pan, E. Barausse *et al.*. *Extreme Mass-Ratio Inspirals in the Effective-One-Body Approach: Quasi-Circular, Equatorial Orbits around a Spinning Black Hole*. Phys.Rev. **D83**:044044 (2011), arXiv:1009.6013

[203] N. Yunes and F. Pretorius. *Fundamental Theoretical Bias in Gravitational Wave Astrophysics and the Parameterized Post-Einsteinian Framework*. Phys.Rev. **D80**:122003 (2009), arXiv:0909.3328